



***The Human Cardiac Ryanodine Receptor  
Gating Behaviour: A Study of Mechanisms***

**By**

**Saptarshi Mukherjee**

**A thesis submitted for the award of Doctor of Philosophy in the  
Faculty of Medicine**

**September 2014**

**Institute of Molecular and Experimental Medicine**

**Wales Heart Research Institute**

**School of Medicine**

**Cardiff University**

## **DECLARATION**

This work has not been previously submitted in substance for any other degree or award at this or any other university or place of learning, nor is being submitted concurrently in candidature for any other degree or award.

Signed ..... Date .....

## **STATEMENT 1**

This thesis is being submitted in partial fulfillment of the requirements for the degree of PhD.

Signed ..... Date .....

## **STATEMENT 2**

This thesis is the result of my own independent work/investigation, except where otherwise stated. Other sources are acknowledged by explicit references.

Signed ..... Date .....

## **STATEMENT 3**

I hereby give consent for my thesis, if accepted, to be available for photocopying and for inter-library loan, and for the title and summary to be made available to outside organisations.

Signed ..... Date .....

## Acknowledgements

I would like to thank my supervisor Professor Alan Williams for giving me the opportunity to work on such an interesting project and for his valuable guidance throughout the duration of my PhD. I'm grateful to Dr Lowri Thomas, my co-supervisor (and 'go-to' person) for her continuous guidance and encouragement. I want to thank them both for always being approachable, for humouring me and patiently listening to all my ideas about new experiments (some feasible, some not so much!!). This work would not have been possible without their invaluable advice and support.

I would like to thank all my friends and colleagues (past and present) at WHRI and especially my lab for their help, advice and most of all, their company. I would also like to thank Mathew Davies and Bevan Cumbes for their technical help in protein purification and also Chloé Maxwell for sharing the burden/joy of the staff/student duality.

I would like to convey my gratitude to Professors David Colquhoun and Lucia Sivilotti of UCL (Pharmacology) for teaching me to think about channel gating in terms of mechanisms during 'the course' in summer of 2008. I would also like to thank Chris Nicolai (Senior Programmer, Sachs Lab, SUNY, Buffalo, USA) for his assistance in customising the QuB program for my RyR2 data through some masterful tweaking of Python codes.

During my training as a clinician, I realised that it was much more fun to create the knowledge than to merely apply it. I'm indebted to my parents for their unwavering support, understanding and encouragement all throughout my academic career, even when I switched from the analogue world of ECGs to the digital world of single channel currents! I thank my wife for her immense encouragement and support throughout my PhD and her patience during the writing of this thesis.

This research was supported by Cardiff University and the British Heart Foundation.

*"Nothing is too wonderful to be true, if it be consistent with the laws of nature; and in such things as these, experiment is the best test of such consistency".*

Laboratory journal entry # 10,040 (19 March, 1849); Michael Faraday. *The Life and Letters of Faraday* (1870) Vol II, p. 253. Edited by Dr Henry Bence Jones.

## **Summary**

Rhythmic contraction of cardiac myocytes is maintained by precisely controlled  $\text{Ca}^{2+}$  efflux from intracellular stores mediated by the cardiac ryanodine receptor (RyR2). Mutations in RyR2 result in perturbed  $\text{Ca}^{2+}$  release that can trigger arrhythmias. RyR2-dependent ventricular tachyarrhythmia is an important cause of sudden cardiac death, the mechanistic basis of which remains unclear. RyR2 dysfunction has also been implicated in other cardiovascular disorders such as heart failure and cardiomyopathy, thereby becoming an important target for putative drugs.

The massive size of RyR2 (~2.2 MDa) along with its intracellular location poses considerable challenges to studies aimed at understanding the mechanisms underlying channel dysfunction. Single channel studies of reconstituted RyR2 in artificial lipid bilayers have provided important insights into channel behaviour in response to various physiological ligands, toxins, drugs and biochemical modifications. However, the precise mechanisms by which RyR2 is activated by its primary physiological trigger, cytosolic  $\text{Ca}^{2+}$ , and the structural determinants of channel gating are yet unknown.

In this study, I aim to understand the actual physical reality of RyR2 gating behaviour using novel experimental approaches and analytical procedures. I have examined in detail, single channel kinetics of wild type purified recombinant human RyR2 (hRyR2) when activated by cytosolic  $\text{Ca}^{2+}$  in a precisely regulated minimal environment where the modulatory influence of factors external to the channel were minimised. This mathematical modelling of hRyR2 single channel behaviour will serve as a future experimental platform upon which the effects of disease causing mutations can be studied, as well as the influence of physiological modulators and potentially therapeutic compounds capable of stabilising mutant channel function.

Single channel studies of hRyR2 when modified by its archetypal ligand ryanodine in the absence of  $\text{Ca}^{2+}$  have uncovered an unusual voltage sensitive gating behaviour in this ligand-gated channel, providing further insights into the mechanisms underlying channel modification.

## **Publications**

Below is a list of my peer reviewed publications and conference abstracts including ones arising from the work contained in this thesis.

### ***Peer reviewed publications***

Mukherjee, S., Thomas, N. Lowri and Williams, Alan J. (2014). Insights into the gating Mechanism of the Ryanodine-Modified Human Cardiac  $\text{Ca}^{2+}$ -Release Channel (Ryanodine Receptor 2). *Mol. Pharmacol.* **86**:318-329.

Mukherjee, S., Thomas, N. Lowri and Williams, Alan J. (2012). A mechanistic description of gating of the human cardiac ryanodine receptor in a regulated minimal environment. *J. Gen. Physiol.* **140**:139-158.

### ***Published abstracts***

Mukherjee, S., Thomas, N. Lowri and Williams, Alan J. (2013). The Nature of  $\text{Ca}^{2+}$ -Controlled Gating in the Human Cardiac Ryanodine Receptor (hRyR2): A Zero  $\text{Ca}^{2+}$  Approach. *Biophys. J.* **104**(2):441a.

Mukherjee, S., Thomas, N. L., Maxwell, C.E. and Williams, A. J. (2011). Description of the gating behaviour of the human cardiac ryanodine receptor (hRyR2) by kinetic modelling and burst analysis under minimal conditions. *Proc. Physiol. Soc.* **23**:PC270.

Mukherjee, S., Thomas, N. Lowri., Guzadhur, L., Maxwell, C.E. and Williams, Alan J. (2010). Gating of the Purified Human cardiac Ryanodine receptor (hRyR2) in the Absence of Regulatory Accessory Proteins. *Biophys. J.* **98**(3):302a.

### ***Other peer reviewed publications***

Thomas, N. Lowri., Maxwell, C., Mukherjee, S. and Williams, Alan J. (2010). Ryanodine receptor mutations in arrhythmia: The continuing mystery of channel dysfunction. *FEBS Lett.* **584**:2153-2160.

Zissimopoulos, S., Viero C., Seidel, M., Cumbes, B., White, J., Cheung, I., Stewart, R., Jeyakumar, L. H., Fleischer, S., Mukherjee, S., Thomas, N. Lowri., Williams, Alan J. and Lai, F. Anthony. (2013). N-terminus oligomerization regulates the function of cardiac ryanodine receptors. *J. Cell Sci.* **126**:5042-5051.

## **List of abbreviations**

3D	Three-dimensional
[ <sup>3</sup> H]ryanodine	Tritiated ryanodine
ABF	Axon binary file format
ADP	Adenosine 5'-diphosphate
AKAP	A-kinase anchoring protein
AMP	Adenosine 5'-monophosphate
APS	Ammonium persulphate
ARVD	Arrhythmogenic right ventricular dysplasia
ATP	Adenosine 5'-triphosphate
AP	Action potential
BAPTA	1,2-bis(o-aminophenoxy)ethane-N,N,N',N'-tetraacetic acid
β-AR	Beta adrenergic receptor
BSA	Bovine serum albumin
[Ca <sup>2+</sup> ] <sub>cyt</sub>	Cytosolic calcium concentration
CaM	Calmodulin
CaMKII	Calmodulin/Calcium-dependent protein Kinase-II
cDMEM	Complete Dulbecco's Modified Eagles Medium
cDNA	Complementary deoxyribonucleic acid
CHAPS	3-[(3-cholamidopropyl)dimethylammonio]-1-propanesulfonate
CICR	Calcium-induced calcium release
CoMFA	Comparative molecular field analysis
CPVT	Catecholaminergic polymorphic ventricular tachycardia

CSQ	Calsequestrin
DAD	Delayed after-depolarisation
de-H <sub>2</sub> O	Deionised water
DIDS	4,4'-Diisothiocyanatostilbene-2,2'-disulfonic acid
DPM	Decays/disintegrations per minute
DTT	dithiothreitol
EC-Coupling/ECC	Excitation-Contraction Coupling
ECL	Enhanced chemiluminescent
EDTA	Ethylenediamine-tetra-acetic acid
EGTA	Ethyleneglycol-tetra-acetic acid
eGFP	Enhanced green fluorescent protein
FKBP	FK506 binding protein
HATC	Half-amplitude threshold crossing method
HEDTA	<i>N</i> -(2-Hydroxyethyl)ethylenediamine- <i>N,N,N'</i> -triacetic acid
HEK293	Human embryonic kidney 293 cell
HEPES	<i>N</i> -(2-Hydroxyethyl)piperazine- <i>N'</i> -(2-ethanesulfonic acid)
HMM	Hidden Markov Model
HSR	Heavy sarcoplasmic reticulum
IHBX	Inner-helix bundle crossover
IpTxa	Imperatoxin A
jSR	Junctional sarcoplasmic reticulum
KcsA	<i>Streptomyces lividans</i> potassium (K <sup>+</sup> ) channel
LB	Luria-Bertani medium
LL	Log-likelihood
LTCC	L-Type calcium channel

MIL	Maximum interval likelihood
MOPS	Morpholinopropanesulphonic acid
NaB	Sodium butyrate
NCX	Sodium-calcium exchanger
PC	L- $\alpha$ -phosphatidylcholine
pCa	Negative logarithm (base 10) of calcium concentration
PE	Phosphatidylethanolamine
PFR	Pore-forming region
PIPES	piperazine-N,N'-bis(2-ethanesulfonic acid)
PKA	Protein kinase A
PLB	Phospholamban
PMCA	Plasma membrane Ca <sup>2+</sup> -ATPase pump
PMSF	2-phenylmethyl-sulphonide fluoride
Po	Single channel open probability
PP1	Protein phosphatase 1
PP2A	Protein phosphatase 2A
PVDF	Polyvinylidene difluoride
REFER	Rate-equilibrium free energy relationship
hRyR2	Human Cardiac Ryanodine receptor
SDS-PAGE	Sodium Dodecyl Sulphate-Polyacrylamide Gel Electrophoresis
SERCA	Sarcoendoplasmic reticulum Ca <sup>2+</sup> -ATPase pump
SF	Selectivity filter
SOICR	Store-overload-induced calcium release
SR	Sarcoplasmic reticulum
T-tubule	Transverse tubule



TAE	Tris-acetate-EDTA buffer
TBS	Tris-buffered saline
TEMED	N,N,N',N'-tetramethylethylenediamine
TM	Transmembrane
TRD	Triadin
Tris	2-amino-2-hydroxymethyl-propane-1,3-diol
VGCC	Voltage-gated calcium channel
VT	Ventricular tachycardia
WT	Wild Type

## Contents

Title page	I
Declarations	II
Acknowledgements	III
Summary	IV
Publications	V
List of Abbreviations	VI
Table of Contents	X
List of Figures and Tables	XV

## Table of Contents

<b>Chapter 1.0</b>	<b>Introduction: Ryanodine receptor and its central role in cardiac calcium homeostasis and signalling</b>	<b>1</b>
1.1	The physiology of calcium signalling in the heart	2
1.1.1	Ca <sup>2+</sup> entry-induced Ca <sup>2+</sup> release is required for contraction	2
1.1.2	Termination of Ca <sup>2+</sup> release and efflux of Ca <sup>2+</sup> from the cytosol	6
1.1.3	Regulation of the key molecular players in ECC	7
1.2	The biophysical identity of the cardiac SR Ca <sup>2+</sup> release channel (RyR2)	8
1.2.1	Permeation properties of RyR2 channel pore	10
1.2.2	Architecture of the RyR2 conduction pathway	11
1.2.3	Structural determinants of RyR2 gating	12
1.3	Physiological regulation of RyR2 by ions, ATP, accessory proteins and cellular processes	14
1.3.1	Ca <sup>2+</sup> regulation of RyR2	15
1.3.2	Mg <sup>2+</sup> regulation of RyR2	17
1.3.3	Activation of RyR2 by adenine nucleotides	18
1.3.4	Modulation of RyR2 activity by regulatory accessory proteins	18
		X

1.3.5 RyR2 regulation by PKA and CaMKII mediated phosphorylation	21
1.4 Pharmacological modulators and exogenous ligands of RyR2	22
1.5 The role of RyR2 in cardiac pathophysiology	26
<b>Chapter 2.0 Materials and Methods</b>	<b>29</b>
2.1 Materials and Methods	30
2.2 RyR2 cDNA propagation and plasmid isolation	30
2.2.1 Buffers and reagents used for bacterial cell culture and propagation	30
2.2.2 Reagents for molecular biology	31
2.2.3 Propagation of plasmid DNA by transformation of bacterial cells	33
2.2.4 Miniprep: small scale eGFP- tagged hRyR2 plasmid DNA isolation	34
2.2.5 Maxiprep: large scale bacterial cell culture and plasmid DNA isolation	35
2.2.6 Determination of plasmid DNA yield and quality	35
2.3 Mammalian cell culture and transient heterologous expression of eGFP- tagged hRyR2	37
2.3.1 Media and reagents required for HEK293 cell culture and transfection	37
2.3.2 Reagents and buffers for hRyR2 protein isolation and purification	38
2.3.3 HEK293 cell culture and transfection	39
2.3.4 Isolation of mixed membrane microsomal vesicles from transfected HEK293 cells	40
2.3.5 Purification of recombinant eGFP- hRyR2	42
2.4 Biochemical and functional assays for recombinant hRyR2	44
2.4.1 List of reagents and buffers for SDS-PAGE and Western blot	44
2.4.2 Buffers and reagents for [ <sup>3</sup> H]ryanodine binding assay	45
2.4.3 SDS polyacrylamide gel electrophoresis	46
2.4.4 Western blotting	46
2.4.5 [ <sup>3</sup> H]ryanodine binding assay	48
2.5 Single channel studies of hRyR2 in a planar lipid bilayer system	49
2.5.1 Experimental milieu of RyR2: the cup and block system	49
2.5.2 Bilayer electronics and recording apparatus	50
2.5.3 Bilayer formation and hRyR2 incorporation	52
2.5.4 Single channel recording and analysis	55
2.6 Statistical methods	55

<b>Chapter 3.0</b>	<b>Optimisation of recombinant hRyR2 extraction and purification for single channel experiments: the solubility paradox</b>	<b>56</b>
3.1	Introduction	57
3.1.1	Purification and isolation of RyR2 using solubilisation	58
3.1.2	Understanding human RyR2 channel behaviour: the ideal experimental model	59
3.2	Key objectives	60
3.2.1	Additional objectives	60
3.3	Experimental procedures	61
3.3.1	Preparation of rabbit skeletal muscle heavy SR vesicles	61
3.4	Results	64
3.4.1	The first step: building up adequate starting material for optimisation and assays	64
3.4.2	Finding the ideal detergent concentration for recombinant hRyR2 solubilisation	65
3.4.2.1	Testing the outcome of the solubilisation process	66
3.4.3	Looking for the missing RyR2 after solubilisation: an unlikely location	68
3.4.4	Increasing the yield of purified RyR2: preventing protein loss from supernatant	72
3.4.5	Recombinant hRyR2 and endogenous FKBP 12.0 in HEK293 cells: do they interact?	75
3.5	Discussion	77
<b>Chapter 4.0</b>	<b>Improving the accuracy of RyR2 single channel data analysis using HMM-based programs</b>	<b>79</b>
4.1	Introduction	80
4.1.1	The key criterion: a memoryless system	80
4.1.2	Optimisation of single channel data: approaches	81
4.1.2.1	Threshold-crossing method	82
4.1.2.2	Time-course fitting method	82
4.1.2.3	Hidden Markov models (HMM)	83
4.2	Key objectives	84
4.3	Experimental procedures	85
4.4	Results	86
4.4.1	Data analysis using threshold-crossing method: drawbacks	86
4.4.2	Optimal technique for RyR2 single channel data analysis	86
4.4.3	HMM based analysis: QuB	88
4.4.4	Pre-processing of single channel data	90
4.4.5	Accurate detection of events: idealisation	94
4.4.6	Introducing the algorithms: workhorses of analysis programs	95

4.4.7	Idealisation of RyR2 single channel data: key steps	98
4.4.8	Model-based interpretation of single channel data using MIL	107
4.4.8.1	Building a putative gating scheme: key stages	108
4.4.8.2	Studying clusters of channel activity: burst analysis	114
4.4.8.3	Validation of kinetic scheme: model-based simulation	118
4.5	Discussion	120
<b>Chapter 5.0</b>	<b>The biophysical characterisation of single RyR2 response to its primary physiological trigger: cytosolic Ca<sup>2+</sup></b>	<b>121</b>
5.1	Introduction	122
5.1.2	The need for understanding RyR2 gating behaviour: employing minimal condition	123
5.1.3	Understanding RyR2 gating behaviour in terms of actual physical mechanisms	124
5.2	Key objectives	125
5.3	Experimental procedures	127
5.3.1	Single channel recording	127
5.3.2	Data analysis	128
5.4	Results	130
5.4.1	Activation of RyR2 by increasing [Ca <sup>2+</sup> ] <sub>cyt</sub>	132
5.4.2	Dwell time distributions point towards underlying mechanisms	136
5.4.3	Model-based description of RyR2 activation by [Ca <sup>2+</sup> ] <sub>cyt</sub>	139
5.4.4	Observed state transitions in terms of putative mechanisms	141
5.4.5	Transition rate constants and simulated data analysis: characterising Ca <sup>2+</sup> binding	143
5.4.6	Validation of kinetic schemes using model-based simulations	145
5.4.7	Study of bursts of RyR2 channel openings: examining ligand-bound kinetics	148
5.4.8	Putative mechanisms underlying the preopening isomerisation	152
5.5	Discussion	152
5.5.1	Physical interpretation of the kinetic scheme: novel insights into RyR2 gating	155
5.5.2	Unliganded channel activity: constitutive gating in RyR2	156
5.5.3	Gating independent of [Ca <sup>2+</sup> ] <sub>cyt</sub> : significance of flicker closing events	156
5.5.4	Pathophysiological relevance of RyR2 gating mechanism	157

<b>Chapter 6.0</b>	<b>Mechanistic basis of modified RyR2 gating behaviour: a zero Ca<sup>2+</sup> approach</b>	<b>160</b>
6.1	Introduction	161
6.2	Key objectives	164
6.3	Experimental procedures	165
6.3.1	Analysis of single channel data	166
6.3.2	Rate-equilibrium free energy relationship (REFER) and $\Phi$ value measurements	167
6.4	Results	169
6.4.1	Gating kinetics of ryanodine-modified RyR2 in the presence and absence of Ca <sup>2+</sup>	169
6.4.1.1	Unique voltage-dependence of ryanodine-modified RyR2	169
6.4.1.2	A detailed examination of the voltage dependence	172
6.4.1.3	Observe changes in channel activity: a true voltage dependent phenomenon	173
6.4.1.4	Mode-shifting of the ryanodine-modified channel	175
6.4.2	Mechanistic basis of ryanodine-modified channel gating	178
6.4.3	Model-based simulations to validate kinetic schemes	181
6.4.4	Modified RyR2 state transitions: from an energetics perspective	181
6.4.5	Effect of cytosolic Ba <sup>2+</sup> on ryanodine-modified RyR2 gating	185
6.4.6	Mechanism of action of Imperatoxin A: is it analogous to ryanodine?	186
6.5	Discussion	191
6.5.1	Study limitations	195
6.6	Implications of this study	196
<b>Chapter 7.0</b>	<b>A summary of findings: their implications and future directions</b>	<b>198</b>
7.1	Background	199
7.2	Overcoming issues with channel solubilisation and purification	199
7.3	Resolving mechanisms from single channel data: HMM based analysis	200
7.4	Mechanism of activation of hRyR2 by Ca <sup>2+</sup> cyt: kinetics reveal putative gates	201
7.5	Ryanodine-modified channel confirmation: new revelations	203
<b>Appendix I</b>		<b>204</b>
<b>References</b>		<b>207</b>

## List of figures and tables

### **Chapter 1**

Figure 1.1	Myocyte sarcolemma and sarcoplasmic reticulum geometry	3
1.2	Schematic representation of Ca <sup>2+</sup> release units	4
1.3	Schematic representation of actin-myosin interaction triggered by Ca <sup>2+</sup> binding	5
1.4	Schematic showing the major elements of CICR and [Ca <sup>2+</sup> ] <sub>i</sub> removal	6
1.5	Regulation of Ca <sup>2+</sup> handling in ECC	7
1.6	Cryo-EM reconstruction of RyR1 at 9.6 Å resolution	9
1.7	Predicted topology of the transmembrane region of RyR	11
1.8	RyR2 pore analogy model based on KcsA crystal structure	12
1.9	Putative determinants of RyR2 channel gating in the PFR	13
1.10	Interaction of RyR2 with its modulators in the cardiomyocyte	14
1.11	Hypothetical locations of the various types of Ca <sup>2+</sup> /Mg <sup>2+</sup> binding sites	16
1.12	A 3D model of RyR2 along with its regulatory accessory proteins	19
1.13	Effect of ryanodine modification on RyR2 single channel currents	23
1.14	3D line diagram of ryanodine structure showing the groups involved in altered ion conductance	23
1.15	Abnormal Ca <sup>2+</sup> handling leads to DADs	26
Table 1.1	Pharmacological modulation of RyR2 by drugs and toxins	25

### **Chapter 2**

Figure 2.1	Mammalian expression vector pcDNA3 used for cloning eGFP-tagged full length hRyR2	33
2.2	Restriction enzymes maps and digest patterns of plasmid DNA	36
2.3	eGFP tag as reporter of transfection efficiency of hRyR2 in HEK293 cells	40
2.4	Homogenisation of transfected HEK293 cells: microscopy	41
2.5	A linear regression analysis of the absorbance values (560 nm) of BSA serial dilutions	42
2.6	Sucrose density gradients containing hRyR2	44
2.7	Schematic diagram showing the principle of chemiluminescent protein (eGFP-hRyR2) detection in a Western blot	47
2.8	A schematic representation of the bilayer recording chambers	49
2.9	Schematic diagram of the bilayer recording chambers and associated electronics	51
2.10	A schematic diagram showing the fusion of membrane vesicles with	54

	an artificial planar lipid bilayer	
2.11	Perfusion of bilayer recording chamber	54
<b>Chapter 3</b>		
Figure 3.1	A process flowchart showing the various steps of hRyR2 expression, extraction and purification	63
3.2	HEK293 cells transfected by e-GFP tagged hRyR2 gene	65
3.3	Protein assay of supernatant samples from solubilisations using different concentrations of CHAPS	66
3.4	The graph shows the results of [ <sup>3</sup> H]ryanodine binding assays on the various samples of solubilised protein (supernatants) at different concentrations of CHAPS	67
3.5	Representative single channel traces when supernatant samples obtained using 0.4 and 0.6% CHAPS	68
3.6	Protein assay of pellet samples obtained after solubilisation using different CHAPS concentrations	69
3.7	[ <sup>3</sup> H]ryanodine binding assay of the pellet samples obtained after solubilisation using different levels of CHAPS	69
3.8	A representative single channel trace showing hRyR2 activity from 0.6% CHAPS solubilised pellet sample.	70
3.9	Western blot of eGFP-tagged hRyR2 from 0.2-1% CHAPS solubilised samples	71
3.10	A densitometric evaluation of the levels of hRyR2 protein detected in the pellet samples by the Western blot	71
3.11	Protein and [ <sup>3</sup> H]ryanodine binding assay results after solubilisation using 0.6% CHAPS followed by low speed centrifugation at 15,000g	72
3.12	[ <sup>3</sup> H]ryanodine binding assay to quantify the activity of rabbit skeletal RyR1 in heavy SR fraction	73
3.13	Comparison of amount of RyR1 activity between supernatant and pellet fractions at low (16,000g) and high speed (110,000 g) centrifugation post solubilisation	74
3.14	Representative single channel current trace showing rabbit skeletal RyR1 activity	75
3.15	The Western blot showing the putative interaction of FKBP with hRyR2 in HEK293 cells	76
<b>Chapter 4</b>		
Figure 4.1	Principle behind the 50% threshold crossing method	81
4.2	Time-course fitting of single channel data	83
4.3	Comparison of event detection using half-amplitude threshold crossing method and HMM	87
4.4	A flowchart showing the sequential steps of the single channel analysis method	89
4.5	The preprocessing interface and getting the raw data ready for idealisation in QuB	92
4.6	Preprocessing interface showing extracted single channel data ready	93



	for idealisation.	
4.7	Schematic showing the two basic components of raw single channel data	94
4.8	A block diagram showing the HMM-based signal processing method	95
4.9	Creating amplitude histograms using the preprocessing interface	98
4.10	Assigning the baseline for idealisation	99
4.11	Assigning the open level for idealisation	99
4.12	Closed and open current levels assigned to respective states in the <i>modelling</i> interface	99
4.13	The settings for idealising data using SKM	101
4.14	Idealised data obtained using the SKM algorithm	102
4.15	Low activity single channel data recorded at 250 nM $[Ca^{2+}]_{\text{cyt}}$ at +30 mV	103
4.16	Detection of brief opening events using re-estimation function in Idealize	103
4.17	Idealisation of low $P_o$ data using SKM algorithm with re-estimation off	104
4.18	Idealisation using Baum-Welch algorithm (Idl/base) and its settings	104
4.19	Idealised single channel data using Baum-Welch algorithm	105
4.20	Comparison of idealised single channel data with and without re-estimation	106
4.21	The MIL interface for modelling of single channel data	109
4.22	Building gating schemes using MIL	109
4.23	Adding states to the model with simultaneous fitting of dwell-time histograms	110
4.24	Error in fitting of data due to an incompatible kinetic scheme	111
4.25	Models ranked according to their maximum log likelihoods	112
4.26	The concept of critical time used in burst analysis	115
4.27	Analysis of single channel data in terms of bursts of openings	115
4.28	Idealised single channel data chopped into bursts	116
4.29	Plots showing closed times and open times within bursts	116
4.30	Burst lengths plotted according to their frequency of occurrence	117
4.31	Interburst intervals and burst length according to their order of appearance in the single channel data trace	117
4.32	Simulation of single channel data using putative gating model	118
4.33	Idealised simulated single channel data from the putative gating scheme	119
Table 4.1	Comparing kinetic parameters from HATC and HMM based idealisations	88
4.2	Idealisation with and without re-estimation of parameters	102
4.3	Comparing kinetic parameters from different idealisation algorithms with and without re-estimation	105

4.4	The best-fit parameters for the top-ranked kinetic scheme	111
4.5	Comparing kinetic parameters of experimental and simulated data	119
<b>Chapter 5</b>		
Figure 5.1	Mutational clusters of RyR2	122
5.2	Ca <sup>2+</sup> activation profiles for 12 hRyR2 channels (0-500 μM) showing functional variability at single molecule level	131
5.3	A single WT hRyR2 channel activation by [Ca <sup>2+</sup> ] <sub>cyt</sub>	133
5.4	Kinetic parameters of hRyR2 gating	135
5.5	Closed and open dwell-time histograms from a single representative channel recorded at various activating [Ca <sup>2+</sup> ] <sub>cyt</sub>	137
5.6	Kinetic schemes to describe hRyR2 gating behaviour during activation by [Ca <sup>2+</sup> ] <sub>cyt</sub>	141
5.7	Representative traces showing single channel data simulated using the kinetic model at various [Ca <sup>2+</sup> ] <sub>cyt</sub>	146
5.8	Kinetic parameters of simulated data	147
5.9	Single channel burst analysis	148
5.10	Closed dwell-time histograms of single channel bursts at various activating [Ca <sup>2+</sup> ] <sub>cyt</sub>	150
5.11	Kinetic scheme describing the ligand-bound gating behaviour (bursts)	151
5.12	Kinetic parameters of burst activity of WT hRyR2 at various activating [Ca <sup>2+</sup> ] <sub>cyt</sub>	151
5.13	Composite gating scheme proposed for hRyR2 activation by [Ca <sup>2+</sup> ] <sub>cyt</sub> represented as part of a larger mechanistic network	154
5.14	Comparison of the putative selectivity filter region of RyR2 with that of the KcsA	157
Table 5.1	Diverse experimental conditions in studies examining Ca <sup>2+</sup> activation of single RyR2 channels	126
5.2	Minimal conditions in single channel experiments with hRyR2	127
5.3	Time constants and relative areas for exponential fits of dwell-time histograms	138
5.4	Kinetic schemes ranked according to maximum likelihood values	139
5.5	Transition rates between states at different [Ca <sup>2+</sup> ] <sub>cyt</sub>	144
<b>Chapter 6</b>		
Figure 6.1	Structure of IpTxa	163
6.2	Conduction and gating of IpTxa-modified RyR2	163
6.3	Projection of Po values on Ca <sup>2+</sup> activation curve	165
6.4	Energy landscape diagram	168
6.5	Gating behaviour of ryanodine-modified RyR2 at zero Ca <sup>2+</sup>	170
6.6	Kinetic parameters of ryanodine-modified RyR2 gating	171
6.7	Study of ryanodine-modified RyR2 gating in the absence of activating Ca <sup>2+</sup> at various holding potentials reveals steep voltage	172

	dependence	
6.8	Representative single channel current traces showing the influence of membrane holding potential on ryanodine modified RyR2 gating under asymmetric ionic conditions	174
6.9	Voltage dependence of ryanodine modified RyR2 gating and direction of ionic flux	175
6.10	Spontaneous modal gating behaviour of ryanodine-modified RyR2 in the absence of $\text{Ca}^{2+}$	176
6.11	Fitting of closed and open dwell-time histograms with exponentials allow mechanistic interpretation of single channel data	177
6.12	Kinetic parameters from simulated single channel data validate gating models	182
6.13	REFER analysis and $\Phi$ (Phi)-value estimation from state transitions provides structural insights into mechanisms	184
6.14	Cytosolic $\text{Ba}^{2+}$ inhibition of ryanodine-modified channel $P_o$ also abolishes voltage dependence	186
6.15	Fitting of dwell-time histograms from single channel data reveal mechanisms of modified channel inhibition by cytosolic $\text{Ba}^{2+}$	187
6.16	Modification of RyR2 with Imperatoxin A in the presence and absence of activating $\text{Ca}^{2+}$	188
6.17	Double modification of RyR2 with ryanodine and IpTx <sub>a</sub> in the absence of $\text{Ca}^{2+}$ reveals mechanistic differences	190
6.18	The distribution of acidic and basic residues in the pore-forming region of RyR2 compared with KcsA	193
6.19	Schematic recapitulation of RyR2 gating behavior under different experimental conditions	197
Table 6.1	Parameters for exponential fits of open and closed time histograms	178
6.2	Rate constants optimised during fitting of histograms and model building	180
<b>Chapter 7</b>		
Figure 7.1	Cartoons figures summarising the putative channel conformations in the gating model for hRyR2	202
<b>Appendix I</b>		
A1	Representative hRyR2 single channel traces from experiments using mixed membrane microsomal preparations	204
A2	Atypical gating behaviour of hRyR2	204
A3	Dependence of backward as well as forward rates on ligand concentration suggests the possibility of ligand-dependent inhibition at high $[\text{Ca}^{2+}]_{\text{cyt}}$	205
A4	Detailed protocol for accurate buffering of free $[\text{Ca}^{2+}]$	206

## **Chapter 1.0**

**Introduction: Ryanodine receptor and its central role in cardiac calcium homeostasis and signalling**

## 1.1 The physiology of calcium signalling in the heart

The co-ordinated and controlled contraction of the heart in response to repetitive stimuli in the form of electrical depolarisation signals originating in the sinoatrial (SA) node is the primary function of cardiomyocytes. Ionised calcium in solution ( $\text{Ca}^{2+}$ ) is the major signalling molecule that transduces this electrical stimulus into systematic mechanical contraction of the cardiac chambers and forms the basis of an effective circulatory system. The important contribution of  $\text{Ca}^{2+}$  in cardiac contraction was first elucidated by the works of Sydney Ringer (Ringer 1883), since then this ubiquitous and versatile second messenger has been found to be involved in diverse functions such as electrical signalling, secretion, fertilisation, exocytosis, memory, gene transcription and apoptosis (Berridge et al. 2000). In this chapter I will focus on the biophysical aspects of  $\text{Ca}^{2+}$  signalling in the heart and its role in cardiac contraction.

### 1.1.1 $\text{Ca}^{2+}$ entry induced $\text{Ca}^{2+}$ release is required for contraction

In myocytes, the process of transduction of electrical signals (depolarisation of sarcolemma) into mechanical contraction is termed as Excitation-contraction coupling (ECC) (Fozzard 1977). This process is initiated by the spread of an action potential (AP) over the cardiomyocyte plasma membrane (sarcolemma) causing it to depolarise (resting membrane potential changes from  $\sim -90$  mV to  $\sim +20$  mV). This triggers the opening of L-type voltage-gated calcium channels (VGCCs) present on the sarcolemma and extracellular  $\text{Ca}^{2+}$  flows down its electrochemical gradient into the intracellular space, increasing the local intracellular  $\text{Ca}^{2+}$  ( $[\text{Ca}^{2+}]_i$ ) from a resting level of  $\sim 100$  nM within tens of microseconds (Lederer et al. 2013). In ventricular cardiomyocytes, L-type calcium channels (inward currents mainly mediated by  $\text{Ca}_v1.2$ ) are concentrated at specialised areas called ‘junctional zones’ (also known as dyads) where the sarcolemmal invaginations (T-tubules) come very close to sarcoplasmic reticulum (SR). This unique network of T-tubules (**Fig 1.1A**) in cardiomyocytes play a crucial role in the process of ECC by bringing the L-type calcium channels (LTCCs) in close apposition ( $\sim 15$  nm) to specialised arrays of  $\text{Ca}^{2+}$  release channels on the junctional SR membrane (**Fig 1.1B**) called ryanodine receptors (RyR2). The architecture of the dyads allow for local increases in  $\text{Ca}^{2+}$  (up to  $\sim 10$   $\mu\text{M}$ ) within the microdomains (dyadic clefts) due to the influx of extracellular  $\text{Ca}^{2+}$  through the LTCCs, which trigger the opening of RyR2

channels in order to release a large amount of  $\text{Ca}^{2+}$  from the intracellular stores (SR) into the cytoplasm (Tanskanen et al. 2007; Bers 2008; Fearnley et al. 2011).

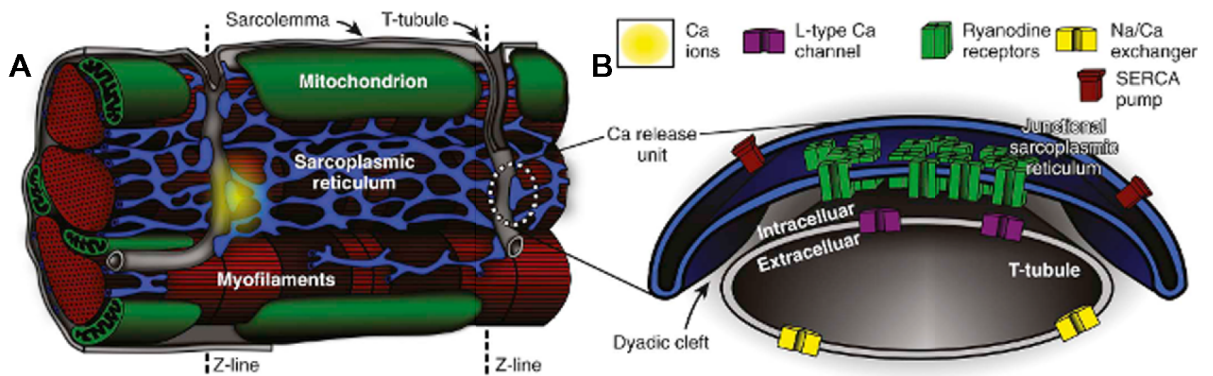


**Figure 1.1. Myocyte sarcolemma and sarcoplasmic reticulum geometry.** (A) Shows transverse tubules (T-tubules) as regular invaginations of the sarcolemma perpendicular to the long axis of the cell and their relationship to the junctional areas of the SR. The T-tubular lattice is crucial for the efficient spread of action potential and facilitates the spatiotemporal synchronisation of intracellular  $\text{Ca}^{2+}$  release. (B) is a magnified picture of the dyadic space where RyR2 clusters forming calcium release units (CRUs) situated on the junctional SR (jSR) are juxtaposed to the LTCCs in the T-tubules. The narrow space separating the jSR and T-tubules is called the dyadic cleft. Figure adapted from (Michailova et al. 2014).

The binding of  $\text{Ca}^{2+}$  to the RyR2 causes conformational changes in the channel protein causing it to ‘open’ leading to the efflux of  $\text{Ca}^{2+}$  from the SR stores into the myoplasm. These  $\text{Ca}^{2+}$  release events through a cluster of RyR2s are visualized as ‘ $\text{Ca}^{2+}$  sparks’ in imaging studies using  $\text{Ca}^{2+}$  sensitive dyes (Berridge et al. 2000; Brochet et al. 2012). The release of  $\text{Ca}^{2+}$  through one RyR2 recruits the neighbouring channels in the array and sets off a chain reaction of release events (**Fig 1.2B**) which sum up to a massive  $\text{Ca}^{2+}$  ‘wave’ that propagates through the cardiomyocyte and constitutes a  $\text{Ca}^{2+}$  transient. This phenomenon of global  $\text{Ca}^{2+}$  release from the SR stores triggered by a relatively small influx of extracellular  $\text{Ca}^{2+}$  through the LTCCs in response to membrane depolarisation is called  $\text{Ca}^{2+}$ -induced  $\text{Ca}^{2+}$  release (CICR) and constitutes the pivotal event in the process of ECC (Fozzard 1977; Fabiato 1983; Bers 2002). CICR causes a local rise of  $[\text{Ca}^{2+}]_i$  in the dyadic cleft to  $> 100 \mu\text{M}$  within a few milliseconds which then diffuses throughout the cytoplasm causing a global rise in  $[\text{Ca}^{2+}]_i$  to  $\sim 1 \mu\text{M}$  (Lederer et al. 2013; Fearnley et al. 2011). The organisation of RyR2 clusters in specialised 2D arrays (**Fig 1.2A**) for efficiently sensing and responding to a small  $\text{Ca}^{2+}$  signal through the LTCCs, is essential for the amplification of  $\text{Ca}^{2+}$  mediated signal in the form of CICR (Tanskanen et al. 2007; Franzini-Armstrong et al. 2005; Bers 2008; Yin et al. 2008; Fearnley et al. 2011).

This  $\text{Ca}^{2+}$  release from SR contributes to  $\sim 95\%$  of the  $\text{Ca}^{2+}$  entering the cytosol during ECC (Bers 2002).

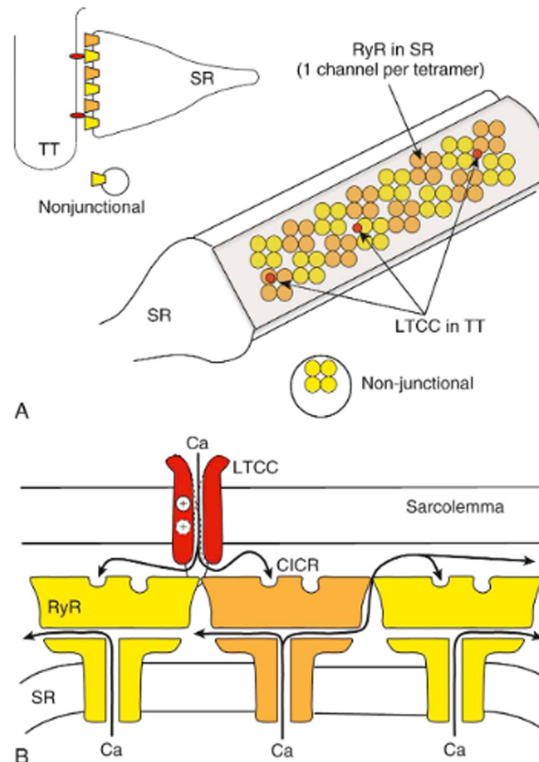


**Figure 1.2. Schematic representation of  $\text{Ca}^{2+}$  release units.** The concept of couplons or CRUs are shown in (A) where clusters of RyRs on junctional SRs are present in close proximity with L-type calcium channels on T-tubules. (B)  $\text{Ca}^{2+}$  release through RyRs induced by the influx of  $\text{Ca}^{2+}$  into the dyadic cleft through voltage-gated LTCCs and efflux through few RyRs activate the neighbouring release channels in a cascade like manner. Figure from (Bers 2004).

Recent electron tomographic studies and 3D reconstruction have revealed new information about the ultrastructure of the dyadic space (mean volume  $\sim 0.44 \times 10^{-12} \mu\text{L}$ ) that was found to have arrays of around 50 RyRs which are closely associated with  $\sim 10$ -25 LTCCs (Baddeley et al. 2009; Hayashi et al. 2009). In functional terms, these associations of LTCCs with clusters of RyR2s in the dyads are known as  $\text{Ca}^{2+}$  release units (CRUs) or couplons (Franzini-Armstrong et al. 1999) and approximately 20,000 of them are known to be present in a myocyte. The global increase in  $[\text{Ca}^{2+}]_i$  from the diastolic levels of  $\sim 100 \text{ nM}$  to  $\sim 1 \mu\text{M}$  during systole engages the contractile machinery of the cardiomyocytes to drive ventricular contraction. Myofilaments organised along the long axis of the myocyte into structures known as sarcomeres are the key elements in the process of  $\text{Ca}^{2+}$  induced contraction (Kobayashi et al. 2008). The sarcomeres comprise

myosin containing thick filaments that are surrounded by a hexagonal array of thin filaments (actin polymers and troponin/tropomyosin (Tn/Tm) units). The thin filament is bound to a Tn/Tm regulatory complex at every seventh actin filament. Tn is composed of three subunits: troponin C (TnC), troponin I (TnI) and troponin T (TnT). TnC binds to  $\text{Ca}^{2+}$ , which in turn causes a conformational change in an associated inhibitory subunit troponin I (TnI). This completely eliminates the inhibitory effect of TnI to enable the myosin thick filament to bind actin, thereby forming a cross-bridge (**Fig 1.3**). TnT has a constitutive interaction with Tm.

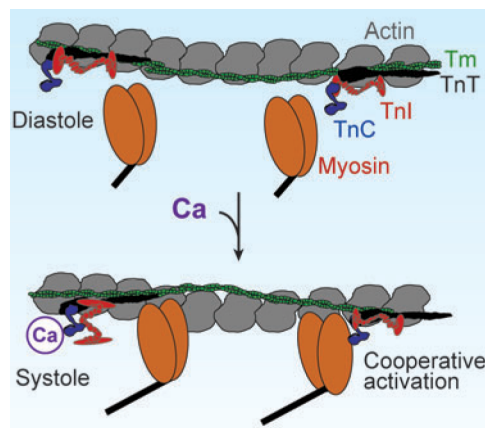


**Figure 1.3. Schematic representation actin-myosin interaction triggered by  $\text{Ca}^{2+}$  binding.** TnC binds  $\text{Ca}^{2+}$  at its N terminus and is then able to interact with the C terminus of TnI, pulling TnI off its site on actin and allowing Tm and TnT to roll deeper into the groove between actin monomers. This allows myosin to bind to actin and further shifts Tm-TnT deeper into the groove, enhancing  $\text{Ca}^{2+}$  binding and crossbridge formation at neighbouring sites and resulting in cooperativity. Figure adapted from (Bers 2008).

These repetitive actin-myosin interactions (using energy from ATP hydrolysis) enable the two filaments to slide relative to each other leading to shortening of the myocyte (Hernandez et al. 2001). The decline of  $[\text{Ca}^{2+}]_i$  leads to the dissociation of  $\text{Ca}^{2+}$  from TnC and cross-bridge detachment as the thick and thin filaments slide back to their original positions. This coordinated relative sliding motion of actin and myosin filaments over each other in groups of cardiomyocytes is the basis for contraction of the heart in a beat-to-beat basis. It should be remembered that the massive differences in resting levels of extracellular ( $\sim 2$  mM), intracellular ( $\sim 100$  nM) and SR ( $\sim 1$  mM)  $[\text{Ca}^{2+}]$  (Shannon and Bers 1997) favours the diffusion of  $\text{Ca}^{2+}$  down its electrochemical gradient through ion channels and hence becomes a very effective signalling ligand in myocytes.



### 1.1.2 Termination of $\text{Ca}^{2+}$ release and efflux of $\text{Ca}^{2+}$ from the cytosol

The cardiomyocytes need to relax after a contraction phase so the ventricular chambers can be refilled during the diastole and be prepared for the next contraction during systole. Therefore, after cytosolic  $\text{Ca}^{2+}$  has activated the contractile units, the positive feedback cycle of CICR is broken due to a significant depletion of SR  $\text{Ca}^{2+}$  content ( $[\text{Ca}^{2+}]_{\text{SR}}$ ) which causes the closure of RyR2 channels and termination of  $\text{Ca}^{2+}$  release (Zima et al. 2008). Experiments show that  $\text{Ca}^{2+}$  release terminates when  $[\text{Ca}^{2+}]_{\text{SR}}$  reaches  $\sim 400 \mu\text{M}$ , thereby diminishing the spatial gradient that exists between the cytosol and SR under resting condition (Picht et al. 2011). The excess  $\text{Ca}^{2+}$  is then rapidly removed from the cytosol in preparation of the next wave of membrane depolarisation. This process of depletion of  $[\text{Ca}^{2+}]_i$  to diastolic levels ( $\sim 100 \text{ nM}$ ) by extrusion into designated  $\text{Ca}^{2+}$  ‘sinks’ is carried out by four types of transporters: a) SR Ca-ATPase pump (SERCA) b) Na-Ca exchanger (NCX) c) Plasma membrane Ca-ATPase (PMCA) and d) mitochondrial Ca-uptake (Bers 2002). The contribution to  $[\text{Ca}^{2+}]_i$  decline in human cardiomyocytes is 70% and 28% by SERCA and NCX respectively (**Fig 1.4**) while the other two transporters play a minor role ( $\sim 1\%$  each).

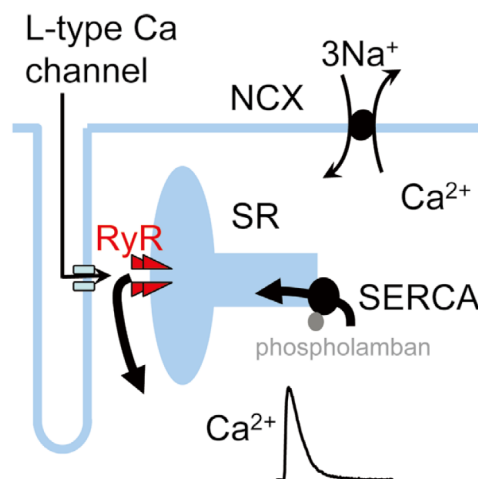


**Figure 1.4. Schematic showing the major elements of CICR and  $[\text{Ca}^{2+}]_i$  removal.** The RyR mediated  $\text{Ca}^{2+}$  release gives rise to  $\text{Ca}^{2+}$  transients and triggers contraction. The  $[\text{Ca}^{2+}]_i$  is then rapidly depleted by re-uptake through SERCA pump and the electrogenic NCX. For each  $\text{Ca}^{2+}$  extruded, the NCX allows in  $3 \text{ Na}^+$  and hence may constitute a depolarising current. Figure from (Eisner et al. 2009).

### 1.1.3 Regulation of the key molecular players in ECC

The key elements in the  $\text{Ca}^{2+}$  handling network of a cardiomyocyte are precisely regulated to maintain the fidelity of calcium cycling with each heartbeat. These regulatory pathways can rapidly alter the spatiotemporal aspects of cardiomyocyte  $\text{Ca}^{2+}$  signalling to acutely modulate cardiac output according to physiological demands. LTCCs can be deactivated by membrane repolarisation and inactivated by cytosolic  $\text{Ca}^{2+}$ .  $\text{Ca}^{2+}$ -dependent inactivation through calmodulin (CaM) acts as a negative feedback loop leading to termination of  $\text{Ca}^{2+}$  entry (Shaw and Colecraft 2013). The L-type channels can also be regulated by protein kinase A (PKA) mediated phosphorylation, downstream from  $\beta$ -adrenergic receptor ( $\beta$ -AR) stimulation that occurs as part of the fight-or-flight response. PKA-mediated phosphorylation promotes increased channel opening, thereby increasing  $\text{Ca}^{2+}$  influx and cardiac contractility (Catterall 2000).  $\text{Ca}^{2+}$ /CaM-dependent kinase II (CaMKII) can also phosphorylate LTCCs through Ca-CaM interaction and increase  $\text{Ca}^{2+}$  influx (Y. Wu et al. 2001).

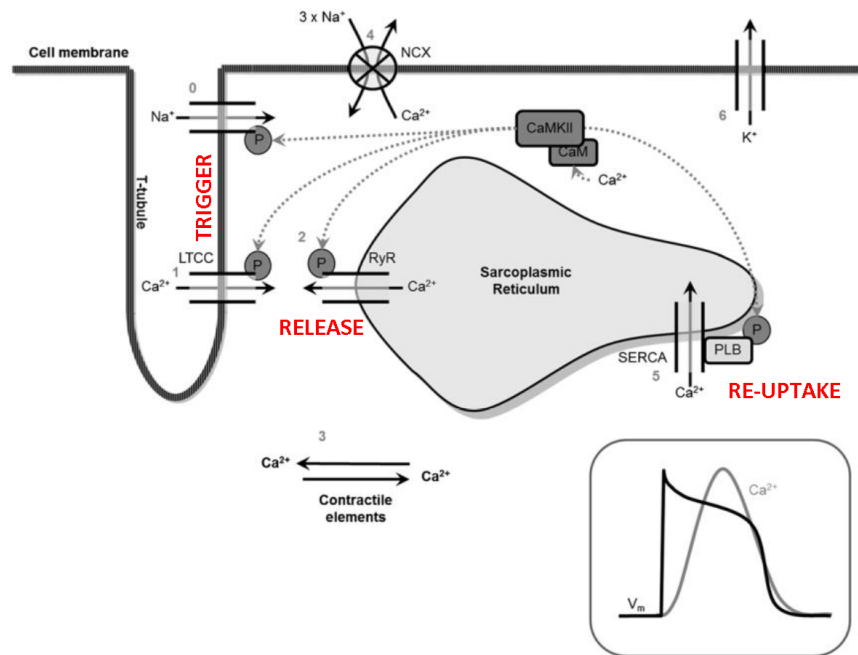


**Figure 1.5. Regulation of  $\text{Ca}^{2+}$  handling in ECC.** 0; Depolarisation spreads through the T-tubules and voltage gated  $\text{Na}^+$  channels open forming the upstroke, 1; this activates the VGCCs and  $\text{Ca}^{2+}$  enters the cell during plateau phase of AP (see inset) thereby triggering CICR, 2;  $\text{Ca}^{2+}$  efflux from RyR, 3;  $\text{Ca}^{2+}$  binding to contractile elements causing shortening of sarcomere, 4; NCX extrudes  $\text{Ca}^{2+}$  from the cell in exchange for  $\text{Na}^+$ , 5;  $\text{Ca}^{2+}$  re-uptake into the SR and store re-filling, 6; opening of  $\text{K}^+$  channels with outward flow of ions leading to repolarisation of membrane. The inset shows the temporal relationship of cardiac AP (black) and the  $\text{Ca}^{2+}$  transient (grey) during CICR. Modified from (Driessen et al. 2014).

Cardiac SERCA pumps (SERCA2a isoform) that are situated away from the junctional zones on the SR membrane play a key role in pumping  $\text{Ca}^{2+}$  back into the SR to replenish the stores for the next cycle of CICR (**Fig 1.5**). SERCA function is primarily regulated by its association with phospholamban (PLB). Unphosphorylated PLB in its depolymerised form can interact with SERCA and inhibit the pump by decreasing its affinity for  $\text{Ca}^{2+}$ . Both PKA and CaMKII mediated phosphorylation of PLB converts it to pentamer that is unable to associate with SERCA, enhancing pump activity and promoting  $\text{Ca}^{2+}$  accumulation in the SR (Kranias and Hajjar 2012). The NCX is mainly regulated by the thermodynamics of ionic gradients (cytosolic  $\text{Ca}^{2+}$  and  $\text{Na}^+$ ). The exchanger is activated by elevation in  $[\text{Ca}^{2+}]_i$  and exports  $\text{Ca}^{2+}$  from the cytosol to the extracellular space (forward mode) to prevent SR  $\text{Ca}^{2+}$  overload (Hilgemann et al. 1992). Under diastolic (low  $[\text{Ca}^{2+}]_i$ ) conditions it can operate in the reverse mode causing  $\text{Ca}^{2+}$  influx and  $\text{Na}^+$  extrusion. NCX can also be regulated by PKA and PKC mediated phosphorylation resulting in activation of the exchanger (Ruknudin et al. 2000). The  $\text{Ca}^{2+}$  release through RyR2 and its modulation forms the fundamental link between the electrical signals reaching the cardiomyocyte (action potential) and the mechanical effect (contraction). As different aspects of RyR2 channel behaviour form the subject of my study, I will now focus on introducing the current knowledge about channel function, its regulation and role in cardiovascular disease states.

## **1.2 The biophysical identity of the cardiac SR $\text{Ca}^{2+}$ release channel (RyR2)**

Ryanodine receptors (RyRs) perform the pivotal function of  $\text{Ca}^{2+}$  release from SR during the process of CICR. There are three mammalian isoforms of RyR (RyR1-3) that are found in a wide variety of tissues. RyR1 is primarily expressed in skeletal muscles; RyR3 which was first identified in the brain, is expressed in Purkinje cells, hippocampal neurons, diaphragm, lung, kidney etc. while in cardiac muscle, RyR2 is the predominantly expressed isoform that drives muscle contraction (Lanner et al. 2010).

RyR2s are the largest known ion channels (Otsu et al. 1990; Nakai et al. 1990) that are capable of conducting large amounts of ions for the rapid transient increases in  $[\text{Ca}^{2+}]_i$  required for cardiac contraction. The channels are named after a plant alkaloid ryanodine, which binds to RyRs with high affinity and specificity, displaying unique effects of its interaction with the open form of the channel. Ryanodine has proven to be vital tool for RyR channel identification and isolation (Inui et al. 1987; Imagawa et al. 1989). The RyR2 functions as a homotetrameric channel with each subunit having a molecular mass

of ~565 kDa (~5000 amino acids) and a total mass of ~ 2.2 MDa (Lanner et al. 2010). The detailed crystal structure of the channel hasn't yet been elucidated because of its massive size, however, some information has been obtained using cryo-electron microscopy (cryo-EM) (Sharma et al. 1998; Z. Liu 2002; Samsó et al. 2005; Samsó et al. 2009). The structures of all three isoforms are similar as the proteins share a high degree of sequence homology (~70%). Three-dimensional renderings of the cryo-EM structures show a mushroom-shaped (square-prism) protein with a four-fold symmetry (**Fig 1.6**). The RyR has a large N-terminal cytoplasmic domain (270 Å x 270 Å x 100 Å) that represents ~80% of the protein and a small transmembrane 'stalk' (120 Å x 120 Å x 60 Å) that contains the ion conducting pore (Van Petegem 2012).

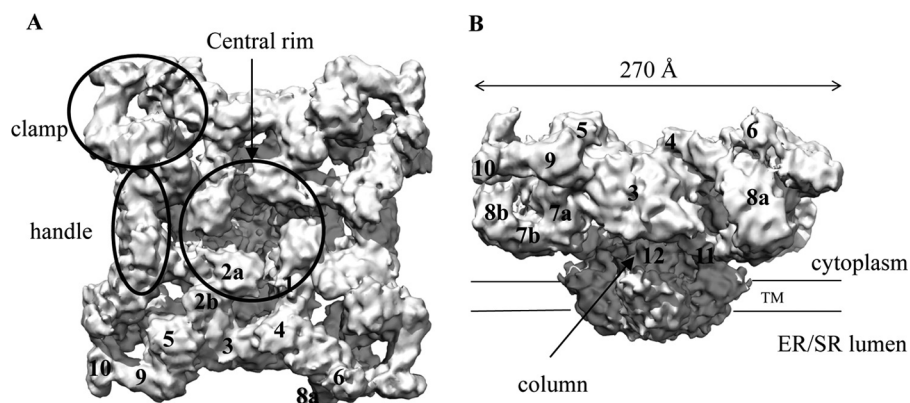


**Figure 1.6. Cryo-EM reconstruction of RyR1 at 9.6 Å resolution.** The top view (A) shows the large cytoplasmic domain and its mapped subdomains. The corners, known as 'clamps' are connected through the 'handle' domain that surrounds the 'central rim' domain around the central cavity. This nomenclature of channel parts (subdomains) aid structural description of the channel. The side view (B) shows the transmembrane domain (TM) which is embedded in the SR membrane and is connected to the large cytoplasmic domain through the 'column'. Figure derived from (Serysheva et al. 2008).

Confocal imaging of RyR  $\text{Ca}^{2+}$  fluxes and high affinity binding studies using [ $^3\text{H}$ ]ryanodine for measuring channel density and activity are two major approaches for studying channel function. However, the gold standard approach for biophysical and pharmacological characterisation of RyR is by reconstitution of isolated channels in artificial planar lipid bilayers as the channels are confined to regions of the cell that are inaccessible to conventional patch electrodes. The recordings of ionic currents flowing through single RyR channels incorporated in bilayers provide real-time description of the behaviour of channel molecules unlike the other approaches which provide information about populations of channels. Although bilayer electrophysiology is currently the only

technique that can provide detailed information about channel biophysics, one should remember that the RyR2 operates in a complex environment in the cell which is difficult to recreate during *in vitro* experiments.

### 1.2.1 Permeation properties of RyR2 channel pore

RyR2 is a  $\text{Ca}^{2+}$ -permeating,  $\text{Ca}^{2+}$ -activated channel that can mobilise enormous quantities of stored  $\text{Ca}^{2+}$  from the SR into the cytosol. Lipid bilayer experiments have confirmed that RyR2 like other isoforms, is a cation selective, divalent selective channel that has a higher unitary conductance for monovalent than for divalent ions (Lindsay et al. 1991; Tinker and Williams 1992). Unlike other types of calcium channels, the RyR is only modestly selective for divalent ions over monovalent (e.g.  $P_{\text{Ca}^{2+}}/P_{\text{K}^+} \sim 6$ ) (Tinker et al. 1992) whereas VGCCs have a much higher degree of discrimination ( $P_{\text{Ca}^{2+}}/P_{\text{K}^+} > 20$ ). The high ion permeation rate required to achieve the necessary  $\text{Ca}^{2+}$  flux during ECC may be the reason for this lack of selectivity as the channel pore gets very little time per ion to discriminate between them. RyR2 single channel conductance for the monovalent  $\text{K}^+$  is 723 pS in 210 mM symmetrical conditions whereas for  $\text{Ca}^{2+}$  its 135 pS under 210 mM bi-ionic conditions (Tinker and Williams 1992). This suggests that the channel pore has a higher affinity for divalent ions which permeate more slowly than monovalents. In comparison, the unitary  $\text{Ca}^{2+}$  conductance of the LTCC is  $\sim 8$  pS under 110 mM symmetrical  $\text{Ca}^{2+}$  (Rosenberg et al. 1988). The ion permeation through RyR follows Ohm's law (current proportional to membrane potential) where the channel behaves as a conductor/resistor without exhibiting any rectification. The dimensions of the pore forming region (PFR) of RyR have been estimated based on the relative permeability (with  $\text{K}^+$ ) of organic monovalent cations (of known radii), where the permeability declines with increasing radius of the cation (Tinker and Williams 1993). The minimum radius of RyR PFR has been estimated to be between 3.5 and 5 Å (Tinker and Williams 1993; Mead and Williams 2002a) while the length of the voltage drop across the channel pore is  $\sim 10$  Å as measured using blocking cations (bis-quaternary ammonium ions) of varying lengths (Tinker and Williams 1995). These parameters of the RyR PFR suggest a relatively shorter, wider and more flexible conduction pathway (Williams et al. 2001) when compared to other ion channels that are more selective but with much lower conductances (e.g. KcsA  $\text{K}^+$  channel).

## 1.2.2 Architecture of RyR2 conduction pathway

The C-terminal portion of RyR that contains the transmembrane domain also includes the PFR of the channel. Bioinformatics-based predictions, hydropathicity profiles and studies using fluorescent protein inserts along with protease digestions suggested that each subunit of RyR contains ~6-8 membrane spanning helices (Takeshima et al. 1989; Nakai et al. 1990; Du et al. 2002; Du et al. 2004; Ramachandran et al. 2013) (**Fig 1.7**) that are sufficient for forming the pore (Callaway et al. 1994). The identification of a putative selectivity filter motif GGGIGD (conserved between RyRs) that was found to be analogous to the ones occurring in  $K^+$  channels, located in a loop between the last two transmembrane (TM) helices was further evidence of this being the PFR of RyR (Balshaw et al. 1999).

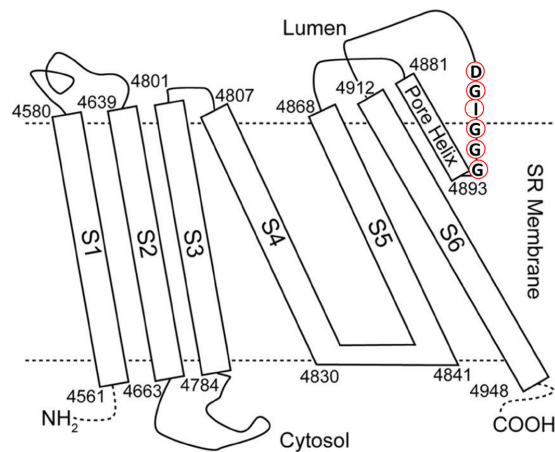


**Fig 1.7. Predicted topology of the transmembrane region of RyR.** TM helices were predicted using bioinformatics from RyR1 primary sequence (C-terminal) with both amino- and carboxy-termini facing the cytoplasm. The 6 TM segments are shown (S1-S6) where S5 and S6 are known as outer and inner (pore-lining) helix respectively. The S5 segment is connected to a short pore helix by a luminal loop which then connects to the pore-lining inner helix (S6) through a loop containing the selectivity filter motif (GGGIGD). Figure modified from (Ramachandran et al. 2013).

Using the detailed tertiary structure of the bacterial  $K^+$  channel KcsA (Doyle et al. 1998) as a template, a highly plausible model of the putative RyR2 PFR was constructed using the last two TM helices of RyR2 along with the luminal loop (Welch et al. 2004). This showed that the overall structural arrangement of the key elements of the RyR2 pore analogy model closely resembles the known structure of KcsA (**Fig 1.8**) and could contribute to channel function in a similar manner as in the  $K^+$  channel (Williams 2002). This supported the earlier evidence from single channels studies and  $Ca^{2+}$  release experiments where amino acid residues of the predicted selectivity filter (SF) region in

RyR2 were substituted leading to profound changes in the channel's conductance and the ability to discriminate between various cations (Zhao et al. 1999; Du 2001).

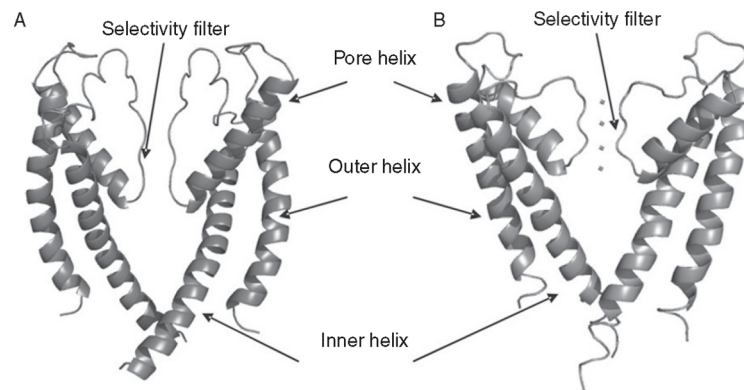


**Figure 1.8. RyR2 pore analogy model based on KcsA crystal structure.** (A) Ribbon diagrams showing the two transmembrane helices (from two subunits) forming the putative PFR model of RyR2 (Welch et al. 2004). The corresponding regions from the known structure of KcsA K<sup>+</sup> channel (used as template) are shown (B) along with the 4 binding sites for K<sup>+</sup> ions in SF (Doyle et al. 1998). The model predicts a more flexible and disordered SF region in the RyR2 model compared to KcsA that might account for higher rates of ion translocation and diminished discrimination between cations. Figure derived from (Carney et al. 2010).

### 1.2.3 Structural determinants of RyR2 gating

One of the most important characteristic of an ion channel is its ability to *gate*. A channel with only a pathway for permeant ions would be useless for cell signalling if it were to be continuously open or closed. The process of switching of an ion channel between conducting (activated/open) and non-conducting (inactivated/closed) states in response to specific triggers like changes in membrane potential, pH, ligand binding/unbinding etc. is known as gating. Structural information about the pore forming regions from the crystal structures of various types of K<sup>+</sup> and Na<sup>+</sup> channels (Y. Jiang et al. 2002; Kuo et al. 2005; Long et al. 2007; Tao et al. 2009; Payandeh et al. 2012) provide evidence in support of a generic organisation of the components of gating and permeation. Extensive functional studies on K<sup>+</sup> channels where key residues were substituted based on the structural models have revealed the identities of the major determinants of channel gating (Doyle 2004). The inner helix-bundle crossover (IHBX) region can act as a gate by bending away about a flexible glycine hinge to open when triggered by voltage or ligand (Yellen 2002). The metastable nature of the SF region can also contribute to channel gating by switching between a conducting open conformation and a collapsed non-conducting conformation such as that which occurs during C-type inactivation in KcsA (Cuello et al.

2010; Chakrapani et al. 2010). Gating at the SF region has been shown to be dependent on occupancy and coordination by  $K^+$  ions along with interaction of residues with water molecules (Cordero-Morales et al. 2006; Cuello et al. 2010; Ostmeyer et al. 2013).

Although detailed crystal structures of RyR2 PFR are not yet available, some assumptions can be made about the nature of the gate(s) based on the information from molecular modelling and functional studies (**Fig 1.9**). Mutation of key residues in the putative gate regions and comparison of single channel behaviour with wild type (WT) RyR2 can provide vital information regarding the determinants of gating.

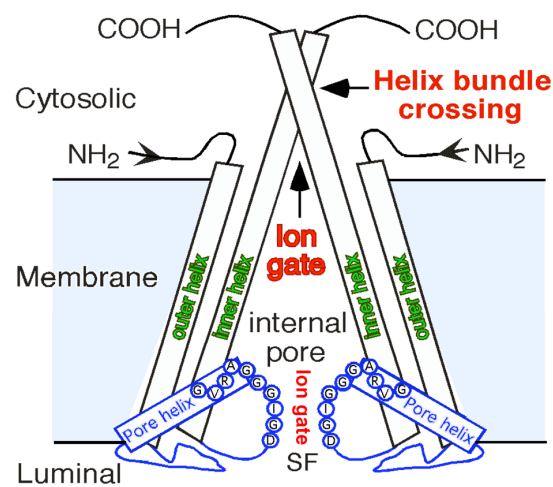


**Figure 1.9. Putative determinants of RyR2 channel gating in the PFR.** The cartoon shows the possible locations of gates in the RyR2 PFR (IHBX and SF regions) based on similarities of its homology model with structure-function information from of  $K^+$  channels. Figure modified from (W. Chen et al. 2014).

#### Contribution of this study

*One of the major aims of this study is to ascertain if the proposed structural similarities between the putative pore region of RyR2 and that of the  $K^+$  channel manifests into fundamental similarities in single channel gating behaviour.*



### 1.3 Physiological regulation of RyR2 by ions, ATP, accessory proteins and cellular processes

In the cardiomyocyte the RyR2 functions as a scaffold for a multitude of regulatory accessory proteins to form a macromolecular complex which acts as a ‘molecular switchboard’ that integrates a myriad of intracellular signals (**Fig 1.10**). The RyR2 is directly regulated by  $\text{Ca}^{2+}$ ,  $\text{Mg}^{2+}$  and ATP, which are its physiological ligands, as well as by cellular processes like phosphorylation, oxidation, nitrosylation etc. (Fill and Copello 2002; Lanner et al. 2010; Van Petegem 2012). These complex interactions with the channel enhance the versatility of the regulation of CICR *in vivo*. Although the functions of the individual accessory proteins are known, the effect of their complex interplay in the massive array of RyR2 macromolecular complexes *in situ* is still unclear.

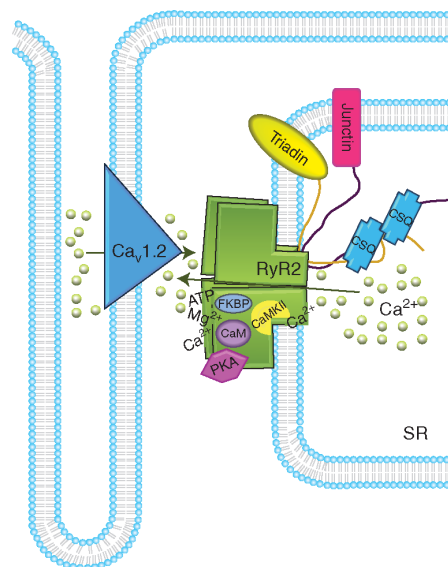


**Figure 1.10. Interaction of RyR2 with its modulators in the cardiomyocyte.** Cartoon figure shows interaction of RyR2 with luminal accessory proteins like calsequestrin (CSQ), junctin and triadin as well as by SR  $\text{Ca}^{2+}$  directly. The channel is regulated by FK506 binding proteins (FKBP), calmodulin (CaM), CaMKII and PKA on the cytoplasmic side along with  $\text{Ca}^{2+}$ ,  $\text{Mg}^{2+}$  and ATP. Figure from (Lanner et al. 2010).

### 1.3.1 Ca<sup>2+</sup> regulation of RyR2

Ca<sup>2+</sup> is the most potent and versatile physiological ligand of RyR2 as it can bind to cytosolic and luminal sides to activate or inactivate the channel and also permeate through the channel from the SR lumen to the cytosol. It can act alone or through other regulatory proteins to modify channel behaviour in a concentration and time- dependent manner. The effect of Ca<sup>2+</sup> on isolated RyR2 channels in planar lipid bilayers must be clearly understood before attempting to unravel the intricacies of the complex interactions that occur in the cardiomyocyte.

Cytosolic Ca<sup>2+</sup> (Ca<sup>2+</sup><sub>cyt</sub>) is the primary physiological trigger of RyR2 that initiates the process of CICR. Under diastolic conditions ([Ca<sup>2+</sup>]<sub>cyt</sub> ~ 100 nM), the rate of spontaneous activation of RyR2 clusters is negligible (~ 10<sup>-4</sup>/s) (Cheng et al. 1993). In single channel experiments done in the virtual absence of [Ca<sup>2+</sup>]<sub>cyt</sub>, the probability of opening of the channel (Po) is very low (< 10<sup>-5</sup>) where only constitutive channel openings are seen (Laver 2007; Mukherjee et al. 2012). Single channel experiments on RyR2s isolated from animal hearts show a sharp Ca<sup>2+</sup><sub>cyt</sub>- dependent (from 0 to 10 μM [Ca<sup>2+</sup>]<sub>cyt</sub>) increase in channel activity to a maximum Po of approximately 0.6 (Ashley and Williams 1990; Coronado et al. 1994; Meissner 1994). However, recent experiments using recombinantly expressed RyR2s have shown higher maximal activation (Po ~ 1) with increased [Ca<sup>2+</sup>]<sub>cyt</sub> (Tester et al. 2007; Mukherjee et al. 2012; Y. Liu et al. 2013). These varied results could be due to differences in experimental conditions employed in various studies (presence of Mg<sup>2+</sup>, ATP, caffeine, accessory protein interactions, luminal Ca<sup>2+</sup> concentration ([Ca<sup>2+</sup>]<sub>lum</sub>), phosphorylation status etc.). This increase in Po was demonstrated to be due to an increase in the frequency of openings and a decrease in time that the channel spends in the closed state (Sitsapasan and Williams 1994a). Calculated Hill coefficients of Ca<sup>2+</sup> activation were found to be > 1 (1-4), which suggests that binding of at least one Ca<sup>2+</sup> is required for channel opening and also some degree cooperativity between subunits during channel gating (Ashley and Williams 1990; Sitsapasan and Williams 1994a). Further increases in [Ca<sup>2+</sup>]<sub>cyt</sub> results in saturation of channel Po, and the RyR2 begins to inactivate beyond ~ 1-2 mM [Ca<sup>2+</sup>]<sub>cyt</sub> (Laver et al. 1995; Xu et al. 1996). This implies that Ca<sup>2+</sup> dependent inactivation is probably not the mechanism by which Ca<sup>2+</sup> release is terminated in cardiomyocytes as the peak global [Ca<sup>2+</sup>]<sub>i</sub> remains much lower than 1 mM during systole.

The finding that RyR2 can be directly regulated by  $\text{Ca}^{2+}$  in the SR, possibly through a luminal facing binding site for the ion was an interesting finding (Sitsapesan and Williams 1994b; I. Györke and S. Györke 1998). Tryptic digestion of luminal domains of RyR which possibly destroy the luminal  $\text{Ca}^{2+}$  binding sites was shown to abolish channel activation by  $[\text{Ca}^{2+}]_{\text{lum}}$  (Ching et al. 2000). However, it has also been suggested that  $[\text{Ca}^{2+}]_{\text{lum}}$  – dependent activation can occur when luminal  $\text{Ca}^{2+}$  flowing through the RyR2 act on binding sites situated on the cytosolic domain in a process termed as ‘ $\text{Ca}^{2+}$  feed-through’ (Laver 2007). Although it is not clear which mechanism is responsible for RyR2 activation by  $\text{Ca}^{2+}$  in SR, it has recently been suggested that it could be a combination of both (Laver 2009). The concept is further complicated by the finding that  $[\text{Ca}^{2+}]_{\text{lum}}$  can also regulate RyR2 activity indirectly by acting through luminal accessory proteins such as calsequestrin, triadin and junctin (I. Györke et al. 2004). A recent study has proposed that the putative gate formed by the IHBX in the PFR of RyR2 (**Fig 1.9**) is the location for a  $\text{Ca}^{2+}$  binding site that acts as a sensor for SR  $\text{Ca}^{2+}$  store (W. Chen et al. 2014). However, it is not clear how  $\text{Ca}^{2+}$  from the SR lumen can independently access the region in the pore when the channel is in a closed conformation. This makes the phenomenon of luminal  $\text{Ca}^{2+}$  sensing dependent on cytosolic  $\text{Ca}^{2+}$  binding and channel opening.

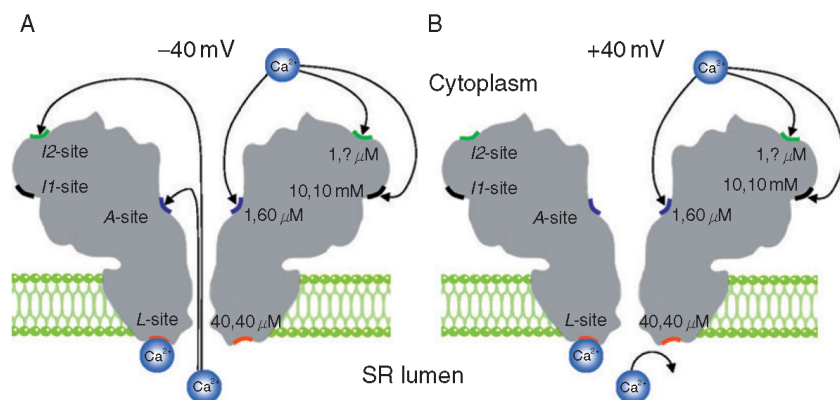


**Figure 1.11. Hypothetical locations of the various types of  $\text{Ca}^{2+}/\text{Mg}^{2+}$  binding sites.** (A) shows binding of  $[\text{Ca}^{2+}]_{\text{cyt}}$  on the high-affinity ( $\mu\text{M}$ ) activating site A which can also bind to  $[\text{Ca}^{2+}]_{\text{lum}}$  that feeds through the pore at negative holding potentials (luminal to cytosolic flux). The channel can be inhibited when  $\text{Ca}^{2+}$  (cyt/lum) binds to the high affinity ( $\mu\text{M}$ ) inhibition site I2 and also when  $[\text{Ca}^{2+}]_{\text{cyt}}$  the low-affinity (mM) inhibition site I1.  $[\text{Ca}^{2+}]_{\text{lum}}$  also activates the channel through the L site on the luminal side independently of  $\text{Ca}^{2+}$  feed-through (B) When the bilayer is held at positive potentials (cytosolic to luminal flux), no feed-through of  $[\text{Ca}^{2+}]_{\text{lum}}$  happens and the RyR2 is regulated by  $[\text{Ca}^{2+}]_{\text{cyt}}$  through cytosolic binding sites and by  $[\text{Ca}^{2+}]_{\text{lum}}$  acting through the luminal activation (L) site. Figure derived from (Laver 2009).

Based on RyR  $\text{Ca}^{2+}$  activation and inactivation data (cytosolic and luminal) from single channel studies, four types of  $\text{Ca}^{2+}$  binding sites have been proposed to explain the channel behaviour under various conditions (Laver 2007). Although this putative binding site-based phenomenological model (**Fig 1.11**) is useful for understanding the role of  $\text{Ca}^{2+}$  in channel regulation, it cannot be considered as a robust model for describing RyR2 gating behaviour. These experiments have used combinations of ligands (cytosolic  $\text{Ca}^{2+}$ , luminal  $\text{Ca}^{2+}$  and ATP) on sheep RyR2 which may or may not have associated accessory proteins and  $\text{Ca}^{2+}$  was buffered only using BAPTA for the whole range of  $[\text{Ca}^{2+}]$  ( $\sim 10 \text{ nM}$  to  $10 \text{ mM}$ ). These combinations complicate the final outcome of the experiments and make it difficult for lucid interpretation of single channel data in terms of mechanisms. Also, the current lack of detailed information about the structure of RyR2 and hence the nature and location of its  $\text{Ca}^{2+}$  binding sites makes understanding channel gating in terms of ligand binding unfeasible.

#### Contribution of this study

*The principal focus of this study is to understand, in terms of mechanisms, the behaviour of single RyR2 channels when activated by its primary physiological ligand  $\text{Ca}^{2+}_{\text{cyt}}$ . This work will aim to avoid the complications and pitfalls of the previous studies by conducting the experiments in a precisely regulated minimal environment where  $[\text{Ca}^{2+}]_{\text{cyt}}$  is unambiguously the only ligand acting on RyR2 in the complete absence of all accessory regulatory proteins.*

### **1.3.2 $\text{Mg}^{2+}$ regulation of RyR2**

Under diastolic conditions, the cardiomyocyte contains  $\sim 0.5 - 1.2 \text{ mM}$  free  $\text{Mg}^{2+}$  (Blatter and McGuigan 1986; Zahradníková et al. 2003) which has an important role of influencing the cytoplasmic and luminal  $\text{Ca}^{2+}$  dependencies of RyR2 activity *in situ* (Meissner and Henderson 1987; Laver and Honen 2008).  $\text{Mg}^{2+}$  is a potent inhibitor of RyR2 single channel activity and is known to act through three possible mechanisms (Laver et al. 1997). The divalent can bind to the A and L activation sites (**Fig 1.11**) and prevent  $\text{Ca}^{2+}$  binding to these sites, thus causing RyR2 inhibition by proxy as  $\text{Mg}^{2+}$  binding does not cause channel opening. The A site has  $\sim 50$ -fold higher affinity for  $\text{Ca}^{2+}$  than  $\text{Mg}^{2+}$ , while the L site has similar affinities for both divalents.  $\text{Mg}^{2+}$  can also directly inhibit the channel by binding to the I1 site (**Fig 1.11**) to close the channel (Laver et al. 1997).

### 1.3.3 Activation of RyR2 by adenine nucleotides

Millimolar levels of ATP have been shown to activate RyR2 in  $\text{Ca}^{2+}$  release, single channel and [ $^3\text{H}$ ]ryanodine binding studies (Meissner and Henderson 1987). The total diastolic level of ATP in a cardiomyocyte is  $\sim 3\text{-}5$  mM (Zahradníková et al. 2003) and is co-dependent with levels of  $\text{Mg}^{2+}$  due to its ability to buffer the divalent ion (Gusev and Niggli 2008). The by-products of ATP hydrolysis in the cell like ADP, AMP, cAMP can also potentiate the release of SR  $\text{Ca}^{2+}$  but have been shown to be less efficacious than ATP (Kermode et al. 1998). ATP activates RyR2 as a ligand (without being hydrolysed) by stabilising the open channel conformation (in the presence of  $[\text{Ca}^{2+}]_{\text{cyt}}$ ) that is seen as an increase in both frequency of openings and open durations (Xu et al. 1996; Kermode et al. 1998; Laver 2007). Recently, ATP has also been shown to sensitise the RyR2 to activation by  $[\text{Ca}^{2+}]_{\text{lum}}$  (Tencerova et al. 2012).

### 1.3.4 Modulation of RyR2 activity by regulatory accessory proteins

The versatility of the highly complex tetrameric assembly of the RyR2 channel protein is further enhanced by the company it keeps. The RyR2 channel by virtue of its massive size, fields a total of  $\sim 500,000$   $\text{\AA}^2$  surface area (Van Petegem 2012) that allows many independently regulated accessory proteins to dock and interact with the channel (**Fig 1.12**). The effect of the protein-protein interactions of some key regulatory proteins on RyR2 gating behaviour will be introduced here.

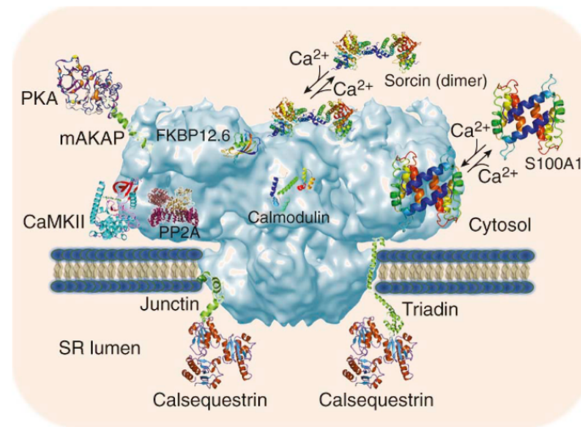


**Fig 1.12. A 3D model of RyR2 along with its regulatory accessory proteins.** A RyR 3D cryo-EM reconstruction is shown in pale blue onto which several regulatory proteins are docked (represented by their multicoloured crystal structures). The actual binding regions (from cryo-EM data) are shown for FKBP12.6 and calmodulin (Z. Liu 2002; Samsó et al. 2005). The positions of other proteins are hypothetical. Figure from (Valdivia 2014).

**Calmodulin** (CaM) is a ubiquitous and conserved 17 kDa  $\text{Ca}^{2+}$  binding protein (four EF-hand binding pockets) that can directly interact with RyR2, amongst other proteins and regulate their behaviour (Tang et al. 2002). The binding of CaM with  $\text{Ca}^{2+}$  causes conformational changes in the molecule that allows it to interact with and modulate the function of RyR2 by acting as a  $\text{Ca}^{2+}$  signal decoder (Saucerman and Bers 2012). It was the first peptide whose interaction with RyR was demonstrated by single channel experiments in lipid bilayers (Smith et al. 1989). In cardiomyocytes, CaM right-shifts the  $\text{Ca}^{2+}$  dependence of RyR2 activation and decreases channel activity at all  $[\text{Ca}^{2+}]_{\text{cyt}}$  (Balshaw et al. 2001; Yamaguchi et al. 2003). A recent study has shown that  $\text{Ca}^{2+}$ -CaM can also activate RyR2 under diastolic levels of  $[\text{Ca}^{2+}]_{\text{cyt}}$  (50-100 nM) (Sigalas et al. 2009). 3D reconstructions of cryo-EM structures of RyR1 and CaM (Samsó et al. 2005) suggest that the binding site may be located in subdomain 3 (**Figs 1.6 and 1.12**). Other similar  $\text{Ca}^{2+}$  binding proteins such as **sorcin** and **S100A1** (**Fig 1.12**) have been shown to associate with and inhibit RyR2 channels when  $[\text{Ca}^{2+}]_i$  increases in the cardiomyocyte (Lokuta et al. 1997; Farrell et al. 2003; Prosser et al. 2011). Recent studies have found that some CaM missense mutations could be associated with ventricular tachycardia and sudden cardiac death (Nyegaard et al. 2012; Crotti et al. 2013).

**FK506-Binding proteins 12 and 12.6** (FKBP12/12.6) are immunophilins that are expressed in most tissues and bind immunosuppressive drugs like FK506 and rapamycin. They have trans peptidyl-prolyl isomerase activity and also participate in other biochemical processes such as protein trafficking, protein folding, transcription and cell signalling (Lanner et al. 2010). The 12.6 kDa protein (FKBP12.6) has been shown to interact with and co-purify with RyR2 channels (Lam et al. 1995; Timerman et al. 1996; Masumiya 2002; George et al. 2003). Difference mapping of 3D reconstructions of RyR cryo-EM structures imply that FKBP12/12.6 docks between subdomains 3, 5 and 9 (**Figs 1.6 and 1.12**) on the channel (Samsó et al. 2005; Samsó et al. 2006). Under physiological conditions (in the absence of FK506/rapamycin) FKBP binds to RyR with high affinity (stoichiometry of 1 molecule per monomer of the channel) and stabilises the closed state (Ahern et al. 1994; Marx et al. 2000; Marx et al. 2001). However, in the presence of immunosuppressive drugs the FKBP12.6 dissociates from the RyR2 leading to increased channel activity. This phenomenon was also reported to occur in pathological conditions like heart failure and certain cardiac arrhythmias where increased phosphorylation of RyR2 (due to  $\beta$ -adrenergic drive) led to the dissociation of FKBP12.6 resulting in increased SR  $\text{Ca}^{2+}$  leak (Marx et al. 2000; Marx et al. 2001; Wehrens et al. 2003; Wehrens 2004b; Lehnart et al. 2006). However, both occurrence and the role of FKBP12.6 dissociation due to increased phosphorylation has been contested by other studies (D. Jiang 2005; N. Liu 2006; Guo et al. 2010) and remains a topic of debate (see (Thomas et al. 2007) for a review). Unlike FKBP12.6, FKBP12 has been shown to interact with RyR2 to activate the channel (Galfré et al. 2012), although it is mainly known as a regulator of RyR1 in the skeletal muscle (Ahern et al. 1997). In cardiac tissue, though FKBP12 is present in higher concentrations than FKBP12.6, the latter was found to have a much higher affinity for RyR2 and hence is the major regulator of the cardiac isoform of RyR (Timerman et al. 1996; Guo et al. 2010). These findings, in relation to the current study have been discussed further in **Chapter 3**. A recent study has shown FKBP12.6 to be a modulator of RyR1 in skeletal muscle (Venturi et al. 2014).

The luminal accessory protein **calsequestrin type 2** (CSQ2) expressed in the cardiac muscle acts as the principal  $\text{Ca}^{2+}$  buffer in the SR. It has a low affinity and high capacity for  $\text{Ca}^{2+}$  binding and exists in the SR as a mixture of monomers, dimers and various multimers (Beard et al. 2004; S. Györke and Terentyev 2008). It can bind  $\sim 40$ -50 calcium ions, albeit with low affinity ( $K_d \sim 1\text{mM}$ ) (Sanchez et al. 2012). When  $[\text{Ca}^{2+}]_{\text{SR}}$  exceed 1-10 mM, the monomers and dimers of CSQ form filamentous linear polymers

(Park et al. 2004). These CSQ2 polymers which are primarily located in the jSR are thought to act as stores of releasable  $\text{Ca}^{2+}$  that can promote myocyte contraction. In addition to serving as a  $\text{Ca}^{2+}$  buffer, CSQ2 can directly regulate RyR2 activity via protein-protein interactions that involve the anchoring proteins **triadin** (TRD1) and **junctin** (Jn) (see **Figs 1.10 and 1.12**) (S. Györke and Terentyev 2008). Single channel studies have also shown that TRD1 and Jn together can activate RyR2 channels in lipid bilayers at high  $[\text{Ca}^{2+}]_{\text{lum}}$  (5 mM) in the absence of CSQ2 (I. Györke et al. 2004). Therefore, CSQ2 along with TRD1 and Jn mediates the responsiveness of RyR2 to  $[\text{Ca}^{2+}]_{\text{SR}}$  by serving as luminal  $\text{Ca}^{2+}$  sensor (S. Györke and Terentyev 2008). Perturbed luminal  $\text{Ca}^{2+}$  sensing due to mutations in the *CASQ2* gene can lead to a life-threatening form of ventricular tachycardia (Lahat et al. 2001; di Barletta et al. 2006).

### **1.3.5 RyR2 regulation by PKA and CaMKII mediated phosphorylation**

The functional consequences of phosphorylation of RyR2 (Witcher et al. 1991; Uehara et al. 2002) in cardiac pathophysiology have in recent times, become a topic of considerable debate (George 2008; Thomas et al. 2010; Dobrev and Wehrens 2014). The RyR2 has been shown to possess anchoring sites (**Fig 1.12**) for kinases such as PKA and CaMKII and also phosphatases such as PP2A (Marx et al. 2000; Dobrev and Wehrens 2014). The ‘fight or flight’ response mediated by sympathetic stimulation via  $\beta$ -AR initiates a cascade of biochemical events that results in the activation of PKA. PKA mediated phosphorylation of RyR2 at residue Ser2808 have been shown to destabilise the closed state of the channel resulting in a ‘leaky’ phenotype (Marx et al. 2000; Wehrens et al. 2006). Ser2808 has also been shown to be a substrate for CaMKII mediated phosphorylation (Witcher et al. 1991). Another site (Ser2030) has been identified which could serve as the substrate for PKA mediated phosphorylation and has been designated as the primary phosphorylation site (Xiao 2005; Xiao et al. 2006). However, this has been disputed by (Wehrens et al. 2006; Huke and Bers 2008). In addition to these, residue Ser2815 has been shown to be a target for CaMKII dependent phosphorylation (Wehrens 2004a). Mutation Ser2815Ala that renders this site unphosphorylatable and prevents most, but not all, of the CaMKII effects on RyR2 (Wehrens 2004a; Respress et al. 2012) suggesting that S2815 is the major but not exclusive target for CaMKII. There are also reports of cross-talk between the phosphorylation sites, where knock-in mice carrying the mutation Ser2808Ala showed increased phosphorylation at Ser2814 site (Benkuský et al. 2007). Overexpression of CaMKII in transgenic mice caused enhanced



phosphorylation of RyR2 and PLB, and premature death (Maier 2003). Although the target sites for PKA and CaMKII are controversial and their interactions complex, phosphorylation mediated regulation of RyR2 offers a versatile control over ECC (Fischer et al. 2013; Marx and Marks 2013). It should also be noted that PKA and CaMKII mediated phosphorylation could also act on other elements of CICR (see **Fig 1.5**). SR  $\text{Ca}^{2+}$  release is precisely controlled by  $\text{Ca}^{2+}$  influx and SR  $\text{Ca}^{2+}$  load, both of which are enhanced by  $\beta$ -AR stimulation induced PKA-mediated phosphorylation of LTCCs and PLB associated with SERCA pump (Bers 2002).

#### **1.4 Pharmacological modulators and exogenous ligands of RyR2**

Due to its massive cytoplasmic domain offering numerous potential binding sites, RyR activity is amenable to modulation by a number of toxins and drugs (Mackrill 2010; Thomas and Williams 2012). However, no specific RyR2-targeted therapeutic compounds are yet available for treatment of cardiovascular disorders (although some are in clinical trials) despite this rich assortment of chemicals that modify the channel behaviour (McCauley and Wehrens 2011; Driessen et al. 2014). The two most important classes of toxins that profoundly alter RyR activity and bind to the channel with very high affinities are 1) ryanodine and related ryanoids and 2) calcins- a group of venom peptide toxins.

Ryanodine is a plant alkaloid which was first isolated from the South American shrub *Ryania speciosa* (Rogers and Koniuszy 1948) and was found to affect cardiac contractility by disrupting SR  $\text{Ca}^{2+}$  release (Sutko et al. 1985). The specific high-affinity interaction of ryanodine with the SR  $\text{Ca}^{2+}$  release channels of myocytes led to the isolation and identification of these channel proteins (Fleischer et al. 1985) that came to be known as ryanodine receptors (RyRs). Ryanodine has become the archetypal ligand of the RyR and has been used in a vast number of studies for biophysical characterisation of single channels in lipid bilayers and functional assessment of a population of RyR using [ $^3\text{H}$ ]ryanodine binding assays.

In single channel studies, (nM to low  $\mu\text{M}$ ) ryanodine binds on the cytosolic side to an open conformation of RyR and modifies the channel leading to profound alterations in ion permeation and gating (Tinker and Williams 1993; Lindsay et al. 1994). Unitary conductance of the channel is reduced to  $\sim 60\%$  (with  $\text{K}^+$  as the permeant ion) while the  $P_o$  increases drastically (**Fig 1.13**). However, at higher concentrations (100  $\mu\text{M}$  – 2 mM)

of ryanodine, the channel is completely inhibited (Tinker et al. 1996). These studies also show that ryanodine has a slow association ('On') rate and an even slower dissociation ('Off') rate such that after binding, the channel is irreversibly modified, at least in the time scales of single channel experiments.

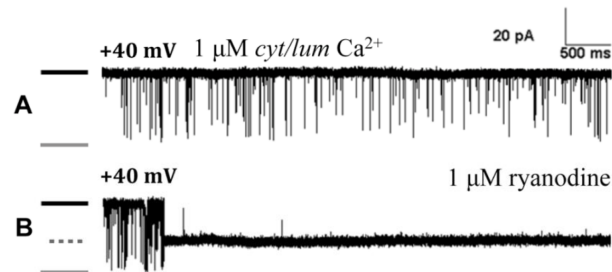


**Figure 1.13. Effect of ryanodine modification on RyR2 single channel currents.** (A) Single channel activity ( $P_o \sim 0.2$ ) of RyR2 when activated by  $1 \mu\text{M Ca}^{2+}$  (cytosolic/luminal). Single channel opening events are downward deflections from the baseline (shown by black bar) to the fully open current level (grey bar). The lipid bilayer was held at  $+40 \text{ mV}$  and  $\text{K}^+$  was the permeant ion. (B) Addition of  $1 \mu\text{M}$  ryanodine to the cytosolic side caused channel modification to a subconductance state ( $\sim 60\%$  of full open level current) which is marked by the grey dashed bar. Once modified,  $P_o$  rises irreversibly to  $\sim 1$  and the channel never opens to the full open level. Figure modified from (Mukherjee et al. 2014).

The altered rates of ion permeation in ryanodine-modified channels have been investigated in detail (Lindsay et al. 1994; Welch 2002). The specific structural aspects of the ligand (**Fig 1.14**) that are responsible for the altered conformation of the pore that resulted in subconductance states were identified (Welch et al. 1997).

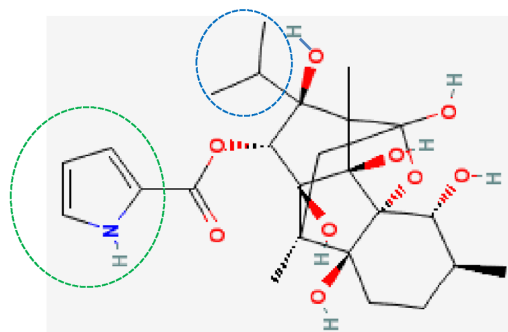


**Fig 1.14. 3D line diagram of ryanodine structure showing the groups involved in altered ion conductance.** The pyrrole ring (green circle) and the isopropyl group (blue circle) are together the major determinants of modified RyR channel conductance and affinity.

Functional analysis of RyR2 channels when modified with a range of synthetic analogues and natural congeners of ryanodine (ryanoids) showed marked differences in ionic conductances and affinity with changes in their chemical structure. These data along with comparative molecular field analysis (CoMFA), that correlates chemical structure with fractional conductance helped identify the orientation of the ligand in the high-affinity binding site of RyR and the functional groups responsible (Welch et al. 1997; Welch 2002). However, the mechanisms involved in the drastic change in RyR2 gating behaviour with modification by ryanodine still remains to be elucidated. Some studies have proposed that ryanodine acts by sensitising the RyR2 towards activation by  $\text{Ca}^{2+}$  (Masumiya et al. 2001; Du et al. 2001). However, a description of mechanism of action of ryanodine on RyR2 in terms of its interaction with the  $\text{Ca}^{2+}$  (another independent ligand) bound channel is not satisfactory and a robust and independent gating mechanism of the ryanodine-modified channel is needed.

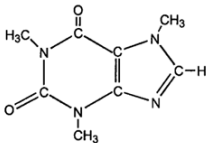
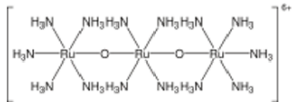
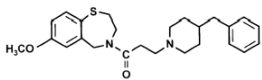
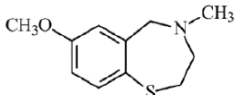
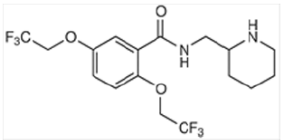
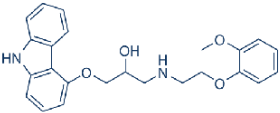
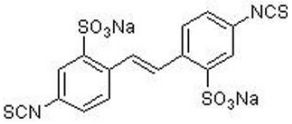
Toxins present in the venom of some scorpions have been shown to have qualitatively similar effects on RyR (Valdivia et al. 1991; Tripathy et al. 1998; Schwartz et al. 2009) where the channel exhibits sojourns to long-lasting subconductance states with altered gating behaviour. These toxins such as Imperatoxin (IpTxa), Maurocalcin (MCa), Hadrucalcin (HdCa) etc. are collectively known as *calcins* (Schwartz et al. 2009; Quintero-Hernández et al. 2013). However, unlike ryanodine, calcins have a faster ‘on’ rate and a much faster ‘off’ rate which makes channel modifications reversible (Tripathy et al. 1998). These characteristics are discussed in more detail in **Chapter 6** of this thesis.

Other important pharmacological modulators of RyR2 are listed in **Table 1.1** along with their modes of action.

#### Contribution of this study

*This study will examine in detail the mechanisms underlying the profound changes in RyR2 gating brought about by ryanodine modification and will aim to arrive at an independent gating model that will describe the action of this quintessential ligand. It will also probe the differences if any, between the gating behaviour of the subconductance states due to ryanodine and calcins (IpTxa).*

**Table 1.1. Pharmacological modulation of RyR2 by drugs and toxins**

Exogenous ligand	Mechanism of action	Salient features
<p style="text-align: center;"><b>Caffeine</b></p> 	<p>Increases channel <math>P_o</math> by increasing the sensitivity of RyRs towards <math>Ca^{2+}_{\text{cyt}}</math> (Rousseau E et al., 1989, Sitsapesan and Williams, 1990)</p>	<p>Routinely used for assessment of SR <math>Ca^{2+}</math> release in cells. Caffeine has low affinity (mM) and specificity for RyR but a fast association rate.</p>
<p style="text-align: center;"><b>Ruthenium red</b></p> 	<p>Decreases channel <math>P_o</math> of RyRs by producing ‘flickery’ block of channel (Ma J, 1993).</p>	<p>Membrane impermeable but has a moderately high affinity for RyRs. Was used in single channel activity for channel shut down. Non-specific.</p>
<p style="text-align: center;"><b>K201 or JTV-519</b></p> 	<p>Stabilises RyR2-FKBP12.6 interaction, thereby preventing diastolic <math>Ca^{2+}</math> leak (Wehrens XH et al., 2004).</p>	<p>Prevents <math>Ca^{2+}</math> overload-induced sudden cardiac cell death (Kaneko N, 1994). Direct effect on RyR2 ill-defined (Yamamoto T et al., 2008). Blocks other ion channels, SERCA and PKC in cardiomyocytes (Currie S, et al., 2011)</p>
<p style="text-align: center;"><b>S107</b></p> 	<p>Stabilises RyR2-FKBP12.6 interaction, thereby preventing <math>Ca^{2+}</math> leak (Bellinger AM et al., 2008, Lehnart SE et al., 2008).</p>	<p>May have higher affinity and specificity for RyR2 when compared with K201 (Lehnart SE et al., 2008).</p>
<p style="text-align: center;"><b>Flecainide</b></p> 	<p>Decreases <math>P_o</math> of RyR2 by open channel blockade (Hillard FA et al., 2010). However, this mechanism is controversial as it may act through <math>Na^+</math> channel block (Liu N et al., 2011).</p>	<p>Class IC antiarrhythmic that can also prevent arrhythmia in CPVT patients and mice (Wantabe H et al., 2009). Mechanism unclear. It is also a high affinity <math>Na^+</math> channel blocker.</p>
<p style="text-align: center;"><b>Carvedilol</b></p> 	<p>Reduces RyR2 <math>P_o</math> by decreasing the mean open times and increases frequency of closings (Zhou Q et al., 2011).</p>	<p>Combined action as <math>\beta</math>-blocker and RyR2 blocker. Prevents SOICR mediated CPVT tachyarrhythmia in mice.</p>
<p style="text-align: center;"><b>DIDS</b></p> 	<p>Increases RyR2 single channel current amplitude by ~ 8 -20% (‘superconductance’) and channel <math>P_o</math> (long openings). Modifies RyR2 irreversibly (Hill AP et al., 2002).</p>	<p>Negatively charged, membrane impermeable ligand. Modified channel gating is dependent of permeant ion and holding potential.</p>

## 1.5 The role of RyR2 in cardiac pathophysiology

Given the central role of RyR2 mediated SR  $\text{Ca}^{2+}$  release in maintaining the ordered and rhythmic activity of the heart, it's not surprising that functional alterations of RyR2 can seriously perturb the process of EC coupling leading to various cardiovascular disorders. Mutations in the human *RyR2* gene (mapped to chromosomal locus 1q42-43) have been shown to cause arrhythmogenic disorders like catecholaminergic polymorphic ventricular tachycardia (CPVT1) and arrhythmogenic right ventricular dysplasia (ARVD2) (Laitinen et al. 2001; Tiso et al. 2001; Kontula et al. 2005). These mutations result in destabilisation of the RyR2 channel protein leading to its increased sensitivity to  $\text{Ca}^{2+}$  activation and enhanced SR  $\text{Ca}^{2+}$  leak (Venetucci et al. 2012).

CPVT1 is an autosomal dominant disease characterised by adrenergically induced (e.g. during exercise or acute emotional stress) life-threatening ventricular tachycardia that may lead to syncope or even sudden cardiac death (van der Werf and Wilde 2013). The overwhelming majority of CPVT1 mutations (> 160 have been discovered till date and increasing) that have been functionally characterised are gain-of-function, causing uncontrolled release of SR  $\text{Ca}^{2+}$  during cardiac diastole leading to delayed after depolarisations (DADs) and cardiac arrhythmia (Medeiros-Domingo et al. 2009).

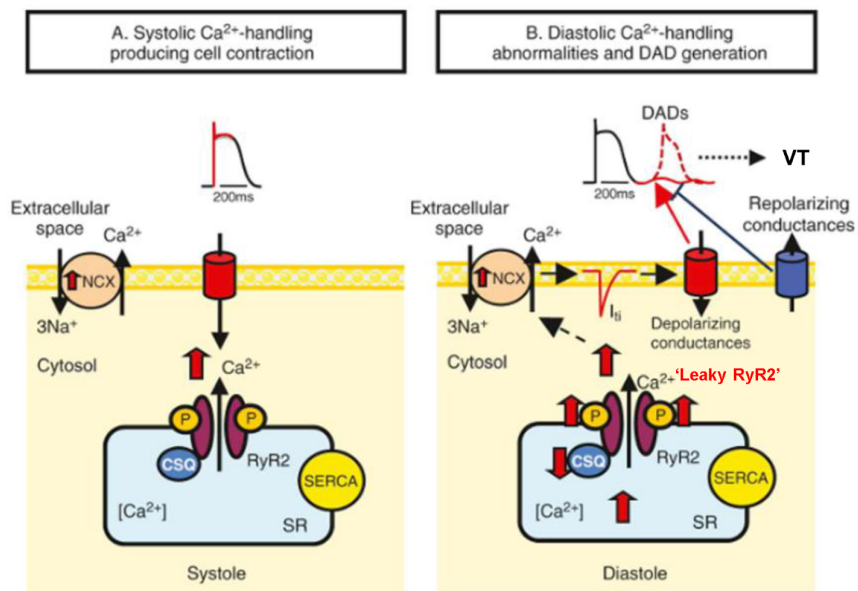


**Figure 1.15. Abnormal  $\text{Ca}^{2+}$  handling leads to DADs.** (A)  $\text{Ca}^{2+}$  influx occurs through LTCCs during the plateau phase of action potential that triggers CICR which initiates cellular contraction during systole. (B) Spontaneous  $\text{Ca}^{2+}$  release through leaky RyR2s elevate cytosolic  $\text{Ca}^{2+}$  during diastole and is pumped out by NCX leading to an inward depolarising  $\text{Na}^+$  current ( $I_{\text{Ni}}$ ) which underlie DADs. Phosphorylation (P) may play an important role. Figure from (Nattel et al. 2014).

The abnormally large quantity of  $\text{Ca}^{2+}$  that leaks out of the SR to the cytosol (spontaneous leak) during diastole is mainly pumped out by the NCX that generates an inward  $\text{Na}^+$  current ( $I_{\text{Ni}}$ ) that may cause transient depolarisation of the sarcolemma (**Fig 1.15**) after the completion of an action potential (DAD). If the DAD amplitude reaches the threshold for the activation of voltage-gated  $\text{Na}^+$  channels in the sarcolemma, an action potential is triggered which propagates through the myocardium as an extrasystolic (during diastole) beat. Repetitive extrasystoles form the basis of life-threatening of ventricular tachycardia (Venetucci et al. 2012). In addition to CPVT1, some RyR2 mutations have also been shown to be associated with sudden infant death syndrome (SIDS) (Tester et al. 2007).

Altered RyR2 function has been implicated in chronic hyperadrenergic states such as congestive heart failure (CHF) and related arrhythmia (Marx et al. 2000; Wehrens et al. 2006; Marks 2013). The main mechanism is a chronically reduced availability of SR  $\text{Ca}^{2+}$  during systole leading to decreased contractility of the heart. This is due to an aberrant diastolic leak of  $\text{Ca}^{2+}$  through RyR2 and insufficient re-uptake through SERCA (Blayney and Lai 2009). Abnormal RyR2 function has also been shown to be a pathological feature in mouse models of Alzheimer's disease (Chakroborty et al. 2009; B. Wu et al. 2013) and atrial fibrillation (Shan et al. 2012).

Although RyR2 mediated disorders have been studied *in vitro* and in animal models, the exact mechanism of channel instability that leads to abnormal  $\text{Ca}^{2+}$  leak is a matter of debate (Thomas et al. 2010; Priori and S. R. W. Chen 2011). The three main mechanisms that have been proposed are: 1) Enhanced PKA dependent “hyperphosphorylation” of RyR2 causing the dissociation of FKBP12.6 leading to enhanced channel activity (Marx et al. 2000), 2) Disease mutations causing destabilisation or ‘unzipping’ of a crucial interdomain regulatory interaction in RyR2 leading to leaky channels (Oda 2005) and 3) Mutations may enhance RyR2's luminal sensitivity to SR store overload-induced  $\text{Ca}^{2+}$  release (SOICR) (D. Jiang et al. 2004).

The lack of structural abnormalities in the heart, the sudden onset of potentially fatal arrhythmia occurring in the young and the lack of efficient therapeutic avenues have fuelled global research initiatives towards understanding the mechanistic basis of RyR2 dysfunction in CPVT1 and other RyR channelopathies. A substitution of even a single amino acid residue from a total of ~5000 present in each subunit of RyR2 (spanning the whole length of the sequence) is sufficient to perturb channel function and the majority of characterised mutations enhance channel activity. This implies that there must be a basic underlying mechanism by which localised perturbations (domains and subdomains)

in the channel due to point mutations are transmitted to the gating machinery leading to an increased propensity for gate opening. None of the proposed mechanisms of channel dysfunction can be reconciled with this central concept of global instability of RyR2.

*Contribution of this study*

*In this study, I plan to examine and quantify the inherent propensity of WT human RyR2 to open in the complete absence of activation by ligands external to the channel molecule. These unliganded constitutive opening events in WT RyR2 when compared with the ones in mutant channels can be used as a measure of the degree of mutation-induced perturbation of global RyR2 stability.*

## **Chapter 2.0**

### **Materials and Methods**



## 2.1 Materials and Methods

This chapter comprises of general descriptions of the methods used in production, isolation, quantification and functional assays of the human cardiac ryanodine receptor (hRyR2). The protocols that required optimisation and other specific techniques are described in the relevant results chapters. All techniques conformed to local safety guidelines included in the WHRI Health and Safety Handbooks.

All standard laboratory reagents and chemicals were of analytical grade and were obtained from **Sigma-Aldrich** unless otherwise stated. All solutions were prepared in the laboratory using de-ionised water (de-H<sub>2</sub>O) unless otherwise stated. All filtration was carried out using 0.2 µm syringe filters from Sartorius. All relevant reagents and buffers used in the protocols are listed below before the corresponding protocols.

## 2.2 RyR2 cDNA propagation and plasmid isolation

Sterile plasticware and glassware were obtained from Fisher Scientific and Greiner Bio-One. All glassware were thoroughly washed in detergent-free water and sterilised by autoclaving before use. Stringent aseptic precautions were employed in all bacterial cell culture work. Where possible, all work involving bacterial cultures were carried out in a Class I containment safety cabinet.

### 2.2.1 Buffers and reagents used for bacterial cell culture and propagation

**Ampicillin:** 100 mg/ml stock in de-H<sub>2</sub>O; filter sterilised and aliquots stored at -20°C.

**LB<sub>Amp</sub> broth:** 10 g/L Tryptone, 5 g/L yeast extract, 10 g/L NaCl. Autoclaved and allowed to cool before the addition of 100µg/ml of ampicillin.

**LB<sub>Amp</sub> agar:** 10g/L tryptone, 5g/L yeast extract, 10g/L NaCl, 15g/L agar. Autoclaved and allowed to cool before the addition of 100µg/ml of ampicillin.

**SOC medium:** 20 g/L Tryptone, 5 g/L yeast extract, 0.5 g/L NaCl, 0.18 g/L KCl, 0.95 g/L MgCl<sub>2</sub>. Solution is autoclaved and cooled before adding 0.4% glucose from stock solution.

### 2.2.2 Reagents for molecular biology

**Miniprep Resuspension buffer:** 50 mM Tris, 10 mM EDTA, 100 µg/ml RNase A, pH adjusted to 7.5 with HCl and filter sterilised.

**Miniprep Cell Lysis buffer:** 0.2 M NaOH, 1% (w/v) sodium dodecyl sulphate (SDS). Filter sterilised.

**Miniprep Neutralisation buffer:** 4.09 M Guanidine-HCl, 0.759 M acetic acid, pH adjusted to 4.2 with glacial acetic acid. Filter sterilised.

**Miniprep Column wash buffer:** 60 mM potassium acetate, 8.3 mM Tris-HCl (pH 7.5), 0.04 mM EDTA, pH adjusted to 8.0, 60% (v/v) ethanol.

**Restriction enzymes:** enzymes (*EcoRI*, *BamHI*, *BglIII*, and *HinDIII*) and appropriate buffers were obtained from New England Biolabs and were stored at -20°C.

**Agarose:** Molecular Biology grade from Eurogentec.

**EDTA:** 0.5 M of Na<sub>2</sub>EDTA stock prepared. pH adjusted to 10.0 with NaOH to dissolve EDTA. Once dissolved, pH adjusted to 8.0 using HCl.

**TAE buffer (50x):** 2 M Tris, 2 M acetic acid, 50 mM EDTA.

**DNA (gel) loading buffer (2x):** 50% (v/v) Glycerol, 5 ml 1xTAE & 0.25% (w/v) Orange G.

**DNA molecular weight markers (1kb):** obtained from Invitrogen, mixed with DNA loading buffer (2x) and aliquots stored at -20°C.

**Maxiprep Resuspension buffer P1:** 50 mM Tris (pH 7.5), 10 mM EDTA, 100 µg/ml RNase A.

**Maxiprep Lysis buffer P2:** 200 mM NaOH, 1% SDS (w/v).

***Maxiprep Neutralisation buffer P3:*** 3 M potassium acetate (pH 5.5).

***Equilibration buffer QBT:*** 750 mM NaCl, 50 mM MOPS, pH adjusted to 7.0, 15% isopropanol (v/v) and 0.15% Triton<sup>®</sup> X-100 (v/v).

***Wash buffer QC:*** 1M NaCl, 50 mM MOPS, pH 7.0, 15% isopropanol (v/v).

***Elution buffer QF:*** 1.25 M NaCl, 50 mM Tris, pH 8.5, 15% isopropanol (v/v).

### 2.2.3 Propagation of plasmid DNA by transformation of bacterial cells

The mammalian expression vector pcDNA3 (Fig 2.1) containing the full-length human RyR2 (hRyR2) cDNA which is tagged with eGFP at the N-terminus (pcDNA3-eGFP-hRyR2) was propagated in competent bacterial cells. The hRyR2 plasmid DNA was kindly provided by Dr C.H George and Dr Lowri Thomas at WHRI, Cardiff University (George et al. 2003). The huge size of the plasmid (21.22 kb) and its fragile nature prevents long-term storage in glycerol and must be propagated every time by bacterial transformation.

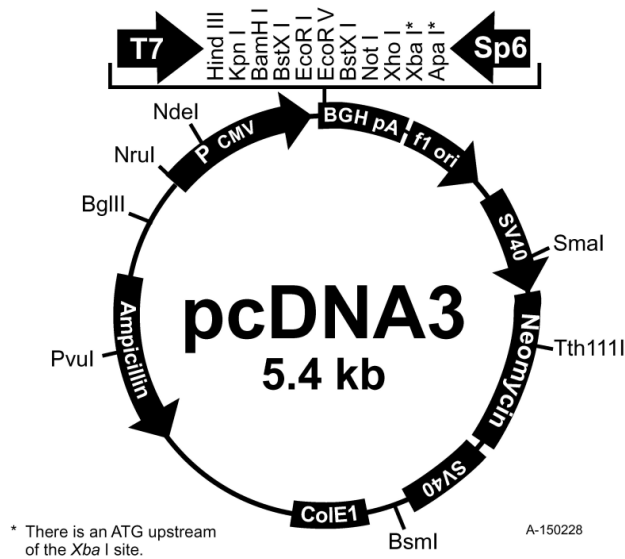


**Figure 2.1. Mammalian expression vector pcDNA3 used for cloning eGFP-tagged full-length hRyR2.** The vector contains Ampicillin resistance gene for positive selection in *E. coli* and Neomycin resistance gene for allowing selection of stably transformed mammalian cells. The vector was obtained from Invitrogen.

For this purpose, MAX Efficiency® Stbl2™ chemically competent cells (Invitrogen) were used for the amplification of full-length hRyR2 plasmid DNA. This strain of ‘super-competent’ *Escherichia coli* are optimised for the transformation of unstable inserts and produced a significantly higher yield of DNA than other types of cells like XL 10-Gold Ultracompetent cells (Aligent). Stringent adherence to transformation protocols was necessary for successful propagation of full-length hRyR2 plasmid DNA as the large size and fragile nature makes it prone to spontaneous intra-plasmid recombinations. MAX Efficiency® Stbl2™ cells were thawed on ice and 1 ng of the plasmid (pcDNA3-eGFP-hRyR2) was added to 50 µl of cells which were then incubated on ice for 30 minutes. Cells were heat-shocked for 25 seconds at 42 °C in a water bath without shaking and then

placed on ice for a further 2 minutes. SOC medium kept at room temperature (0.9 ml) was added to the cells and were incubated at 37 °C for 90 minutes, while shaking at 225 rpm. The cells were then spread onto LB<sub>Amp</sub> agar plates (100 µg/ml) and incubated overnight at 30 °C in a plate incubator (Heraeus). The plates were examined for colonies and individual colonies were picked, which were then inoculated into LB<sub>Amp</sub> broth (6 ml) before incubating at 30 °C for 16 hours (shaking at 225 rpm). The transformed bacteria were cultured at 30 °C for no more than 18 hours to minimise the likelihood of spontaneous plasmid DNA rearrangements (George et al. 2003). 3 ml from each of the cultures were centrifuged (20,000 g x 2 min) while the rest were diluted (1:2) using LB<sub>Amp</sub> broth and incubated at 30 °C (shaking at 225 rpm) for 4 hours prior to large scale bacterial cultures.

#### **2.2.4 Miniprep: small-scale eGFP-tagged hRyR2 plasmid DNA isolation**

Small-scale plasmid DNA isolation was carried out by the alkaline lysis method (Wizard® Plus SV Miniprep Plasmid purification kit; Promega) in which the plasmid DNA is purified from transformed bacterial cells. For this procedure, manufacturer's instructions were followed. Briefly, the pellets obtained from the culture of individual colonies after centrifugation were resuspended and lysed (using 250 µl of Resuspension and Cell lysis buffers respectively). The lysed cells were centrifuged (14,000 g x 10 min) at room temperature after adding the Neutralisation buffer (350 µl) to pellet any insoluble material. The cleared lysate was decanted into Wizard Miniprep spin columns containing silica gel DNA-binding membrane. The columns were centrifuged at 14,000 g for a minute while DNA binds to the silica membrane and the flowthrough was discarded. Column wash buffer (750 µl) was added to the columns and centrifuged again (14,000 g x 1 min). The supernatant was discarded and the wash step was repeated with the addition of 250 µl of wash buffer and centrifugation (14,000 g x 1 min). The flowthrough was discarded and the columns were spun again at 14,000 g for 2 minutes to dry the silica membrane. The columns were placed in collection tubes and DNA was eluted by adding 30 µl of nuclease free de-H<sub>2</sub>O and centrifuging at 14,000 g for 1 min. The DNA eluted was incubated with ~5-10 units of restriction enzyme EcoR1 along with the supplied buffer at 37°C for 2 hours (total reaction volume of 20 µl). The restriction digest products were run on an agarose gel and bands visualised by UV transillumination. This preliminary restriction enzyme mapping with EcoR1 was done to ensure that transformations were successful and no gross plasmid DNA rearrangements have

occurred. The individual cultures with appropriate EcoR1 restriction digest products (see **Fig 2.2** for correct patterns) were used to further inoculate large-scale bacterial culture for further amplification of plasmid DNA quantity.

### **2.2.5 Maxiprep: large-scale bacterial culture and plasmid DNA isolation**

The remaining Miniprep cultures that were incubated for further growth (see **2.2.2**) were used for large-scale inoculation of LB<sub>Amp</sub> broth (in 1:200 ratio) and the flasks (400 ml x 8) were incubated for 18 hours at 30 °C in a shaker-incubator (225 rpm). The cultures were centrifuged (10,000 g x 5 min) at 4 °C in an Avanti J-25 (Beckman Coulter) centrifuge using a JLA16.250 rotor. The supernatants were discarded and the pellets were used for large-scale purification of plasmid DNA using the alkaline lysis/ion-exchange method (Qiagen® Maxiprep kit) according to manufacturer's instructions. The pellets were resuspended in 20 ml of buffer P1 and divided into two 10 ml portions which were placed in centrifugation tubes (for Beckman JA25.5 rotor) before adding 10 ml of lysis buffer P2 to each tube and capped. The tubes were inverted a few times until the lysate clarified and 10 ml of neutralisation buffer P3 was added and kept on ice for 20 minutes. The tubes containing the lysate were then centrifuged at 20,000 g for 30 minutes (4 °C) in a JA25.5 rotor (Beckman) to remove the insoluble material. A Qiagen-tip 500 was equilibrated by 10 ml of buffer QBT that was allowed to empty by gravity flow after which the clear supernatant from the lysed cells was added. The column was then washed twice with 30 ml buffer QC and transferred to a 30 ml collection tube. Plasmid DNA from the column was eluted using 15 ml of buffer QF and 10.5 ml of isopropanol was added to the eluted DNA to precipitate overnight at -20 °C. The DNA was spun down by centrifugation (20,000 g x 30 min) at 4 °C and the supernatant was gently decanted. The pellet containing DNA was washed with 5 ml ethanol (70%) and subjected to centrifugation (20,000 g x 10 min) at 4 °C. After gently discarding the supernatant, the pellet was air dried for 10 minutes and then resuspended in about 500 µl of 10 mM Tris-HCl (pH 8.5).

### **2.2.6 Determination of plasmid DNA yield and quality**

Spectrophotometry is used to determine the concentration of plasmid DNA obtained using the Maxiprep method. The absorbance of UV light at 260 nm wavelength ( $Abs_{260}$ )

by a 1:50 dilution of DNA enabled the calculation of its concentration according to the equation:

$$\text{Abs}_{260} \times \text{dilution factor} \times 50 = [\text{DNA}] \text{ (ng/ml)}$$

Tryptophan and tyrosine residues present in proteins strongly absorb light at 280 nm wavelength ( $\text{Abs}_{280}$ ) and can be used as an indicator of contamination of the DNA sample by bacterial proteins. Therefore, the ratio  $\text{Abs}_{260}/\text{Abs}_{280}$  known as the optical density (OD) is used as an indicator of the purity of DNA and other nucleic acids.

The plasmid DNA was subjected to a panel of restriction enzyme digests and mapping (using NEB cutter 2.0) to ensure that no gross rearrangements had occurred within the plasmid during the process of transformation. Due to the large size of full-length RyR2 sequence and presence of multiple restriction sites, several restriction enzymes could be used for mapping. This produced distinct patterns when digested plasmid DNA was subjected to agarose gel electrophoresis due to the unique sizes of fragments (**Fig 2.2**).

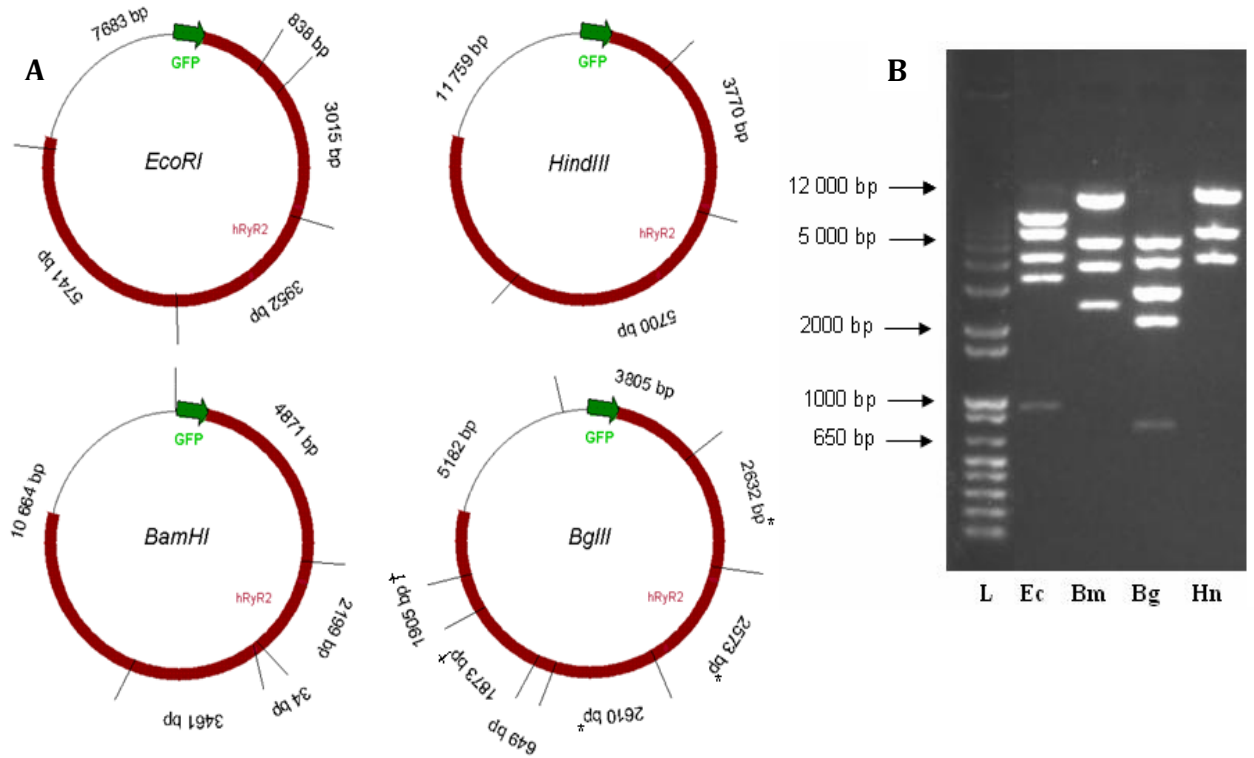


**Figure 2.2. Restriction enzymes maps and digest patterns of plasmid DNA.** **A** Shows restriction maps of pcDNA3-GFP-hRyR2 digested with the enzymes shown, fragment sizes are displayed between restriction sites (represented by a line), \* and †-these fragments cannot be resolved on the gel and run as one band. **B** shows the restriction digest pattern after agarose gel electrophoresis which is characteristic of eGFP-hRyR2 when cut with the enzymes mentioned in **A**. It shows DNA digested with Ec- *EcoRI*, Bm-*BamHI*, Bg-*BglII* and Hn-*HindIII*; L is the 1kb ladder with sizes marked.

For each reaction, 1 µg of DNA was mixed with 10 units of restriction enzyme (*EcoRI*, *BamHI*, *BglII* and *HinDIII*), 2 µl of corresponding 10x buffer and was made up to 20 µl with de-H<sub>2</sub>O. The reaction mix was incubated for 2 hours at 37°C and the restriction products were subjected to agarose gel electrophoresis to separate the DNA fragments. Briefly, the agarose was dissolved in 1 x TAE to form a 1% gel (w/v) and was allowed to cool down to about 50 °C before adding 0.01% (w/v) ethidium bromide. Once the gel was set, DNA samples were mixed with equal volumes of 2x DNA loading buffer and loaded onto the gel to run alongside 1kb DNA molecular weight marker. The gel was run at 80 V until the DNA fragments were sufficiently resolved which was indicated by the migration of the Orange G dye-front to ~75% of length of the agarose gel. The DNA fragments due to restriction enzyme digestions were visualised by UV transillumination (**Fig 2.2B**) and images captured with a Hamamatsu camera with Quantity One gel documentation software.

### **2.3 Mammalian cell culture and transient heterologous expression of eGFP-hRyR2**

HEK293 is an immortalised cell line that has been derived from human embryonic kidney cells (HEK). These adherent cells grow as plaques/monolayers, are easily transfected and exhibit epithelial cell like morphology. They were first described in 1977 and were created by transforming HEK cells with sheared Adenovirus 5 DNA (Graham et al. 1977). HEK293 cells show no endogenous expression of RyRs or luminal accessory proteins (S. R. Chen et al. 1997a; Stewart et al. 2008). Sterile cell culture plasticware was obtained from Nunc (Fisher Scientific), Greiner Bio-One and Corning. All cell culture media and reagents were obtained from Invitrogen. Saline (0.9%) and sterile water were purchased from Baxter Medical Supplies. Stringent aseptic precautions were taken in all mammalian cell culture work and they were done in the sterile environment of Microflow Class II containment cabinets.

#### **2.3.1 Media and reagents required for HEK293 cell culture and transfection**

***Complete Dulbecco's Modified Eagles Medium (cDMEM)***: obtained from Invitrogen, contains 10% (v/v) foetal calf serum, 2 mM glutamine and 100 µg/ml penicillin/streptomycin; all were filter sterilised before addition. The media were stored in the fridge at 4°C.



**Trypsin-EDTA:** 1x in HBSS devoid of calcium or magnesium; aliquots stored at -20°C.

**Hepes-buffered saline (HBS) 2x:** 280 mM NaCl, 10 mM KCl, 1.5 mM Na<sub>2</sub>HPO<sub>4</sub>, 10 mM glucose, 50 mM Hepes; pH adjusted to 7.05, filter sterilised and aliquots stored at -20°C.

**Calcium chloride:** 1M stock.

### 2.3.2 Reagents and buffers for hRyR2 protein isolation and purification

**Hypo-osmotic homogenisation buffer:** 20 mM Tris HCl, 1 mM EDTA, pH adjusted to 7.4 using HCl. 1 protease inhibitor tablet (Roche) was used for every 50 ml buffer.

**Cryoprotective buffer:** 0.4 M sucrose and 20 mM HEPES (pH adjusted to 7.4) along with 1:1000 protease inhibitor (PI) cocktail (Sigma).

**Micro BCA™ protein assay:** kit obtained from Thermo Scientific.

**Bovine serum albumin (BSA) standards:** diluted from 1 mg/ml stock to 10, 25, 50, 75, 100 and 200 µg/ml in de-H<sub>2</sub>O and stored at -20°C.

**Solubilisation base buffer (high salt):** 1 M NaCl, 0.15 mM CaCl<sub>2</sub>, 0.1 mM EGTA, 25 mM PIPES (pH adjusted to 7.4 using NaOH) to which protease inhibitor cocktail (Sigma-Aldrich) was added (1:1000). The complete solubilisation buffer contains, in addition to the base buffer, the detergent CHAPS and 2 mg/ml (0.3%) L- $\alpha$ -phosphatidylcholine (PC), that are added from a 10% CHAPS/PC stock (see **Chapter 3** for details).

**Gradient buffer:** 300 mM NaCl, 25 mM Tris HCl, 50 mM HEPES, 0.3 mM EGTA, 0.1 mM CaCl<sub>2</sub>, 0.3% (w/v) CHAPS, 0.15% PC and 2 mM DTT (pH 7.4).

**Sucrose solutions:** 5, 25 and 40% (w/v) sucrose, made up in gradient buffer.

### 2.3.3 HEK293 cell culture and transfection

HEK293 cells were routinely cultured in 75 cm<sup>2</sup> (T75) tissue culture flasks (Nunc or Greiner Bio-One) with filter caps and maintained in Complete Dulbecco's Modified Eagles Medium (cDMEM). Between passages, they were kept at 37°C, in 5 % CO<sub>2</sub> and ~80% humidity in a cell culture incubator (Fisher Scientific). Cells were routinely passaged when the culture approached full confluence (~90%) by detaching the cells from the flask surface by incubation with 2 ml Trypsin-EDTA. The action of Trypsin was terminated by adding 10 ml cDMEM and the cells were gently resuspended before counting them in a haemocytometer. The cells were recovered by centrifugation at 1000 rpm (Allegra 64R, Beckman) for 3 minutes and gently resuspending in 10 ml cDMEM by pipetting before seeding appropriate amounts of cells in T75 flasks. HEK293 cells were transfected with pcDNA3-GFP-hRyR2 so that they transiently overexpressed recombinant hRyR2 channel protein, which was then isolated and used in functional and biochemical assays. The transfection was achieved using a modified calcium phosphate DNA precipitation method (C. Chen and Okayama 1987) where a high DNA:cell ratio is used. T75 flasks were seeded with ~4 x 10<sup>6</sup> HEK293 cells approximately 24 hours prior to transfection. For transient transfection of HEK293 cells with eGFP-hRyR2 which stably express FKBP12.6, ~6 x 10<sup>6</sup> cells were seeded 24 hours prior to transfection (see **Chapter 3**). pcDNA3-GFP-hRyR2 plasmid DNA (28 µg) was mixed with 1 M CaCl<sub>2</sub> (259 µl) and the volume made up to 1050 µl using sterile de-H<sub>2</sub>O. This mixture was added, a drop at a time to 2x HBS (1050 µl) in a 50 ml Corning tube which was being vortexed continuously for proper mixing. The resulting transfection complex was incubated for 25 minutes to allow fine particles of DNA precipitates to form (O'Mahoney and Adams 1994). The total mixture was then added to the culture in a drop-wise manner whilst gently swirling the medium for mixing. The cells were then incubated for 24 hours before a gentle wash with normal saline (prewarmed to 37°C) and replacing the culture media with fresh cDMEM. The addition of 2 mM sodium butyrate (NaB) to the culture media at this stage was found to enhance the expression of recombinant hRyR2 protein, although the exact mechanism by which gene expression is regulated by NaB is unknown. The cells were incubated for a further period of 24 hours before visualising them using fluorescence microscopy to ascertain the levels of eGFP-hRyR2 expression (**Fig 2.3 and 3.2**). The hRyR2 was tagged at the N-terminus by eGFP to allow for the monitoring of the efficiency of transfection (George 2003), while having no observable

effect on hRyR2 localisation and function (Thomas et al. 2004; Thomas et al. 2005; Wang et al. 2007; Mukherjee et al. 2012). The imaging was done using a Zeiss fluorescence microscope which employs a Xenon lamp light source (peak excitation:  $\sim 488$  nm) and a  $515 \pm 30$  nm band-pass filter. The cells were harvested at 48 hours post transfection using trypsin-EDTA and centrifugation at 1000 rpm for 5 minutes at  $4^{\circ}\text{C}$ . Using this method for transfection, RyR2 expression levels of  $\sim 60\%$  were consistently achieved. Considering the massive sizes of the plasmid DNA and the translated hRyR2 protein, this level of expression is outstanding and resulted in adequate amounts of channels for downstream assays.

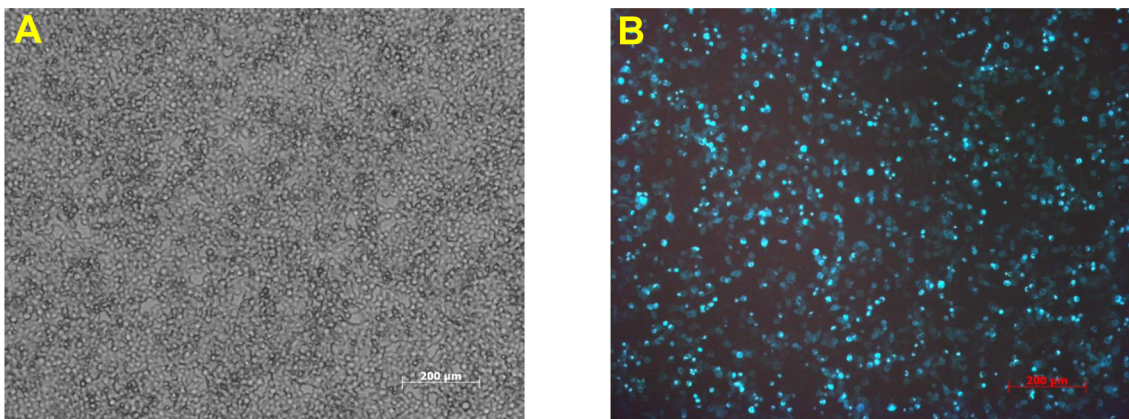


**Figure 2.3. eGFP tag as a reporter of transfection efficiency of hRyR2 in HEK293 cells.** A and B shows the bright-field and fluorescent (eGFP) images respectively, of HEK293 cells that were transiently transfected with pcDNA3-GFP-hRyR2 (at 48 hours post-transfection).

#### **2.3.4 Isolation of mixed membrane microsomal vesicles from transfected HEK293 cells**

The transfected cells were harvested and the pellets obtained from the above process were resuspended in chilled hypo-osmotic homogenisation buffer (1 ml of buffer/  $1 \times 10^6$  cells) and left on ice for 30 min to lyse the cells. Physical disruption of the resuspended cells were carried out (on ice) by passing them 15 times through a 23G needle and further homogenised using a Teflon glass homogeniser (10x strokes). It was found that passing the cell suspension through the 23G needle (inner dia.  $\sim 0.34$  mm, BD) was a crucial step (**Fig 2.4**) that aids the release of the intracellular proteins (including hRyR2). This manual process of syringing the cell suspension through a 23G needle was later mechanised (from July 2009) using a custom-built device made by R.A Montgomery (NHLLI, Imperial College, London).

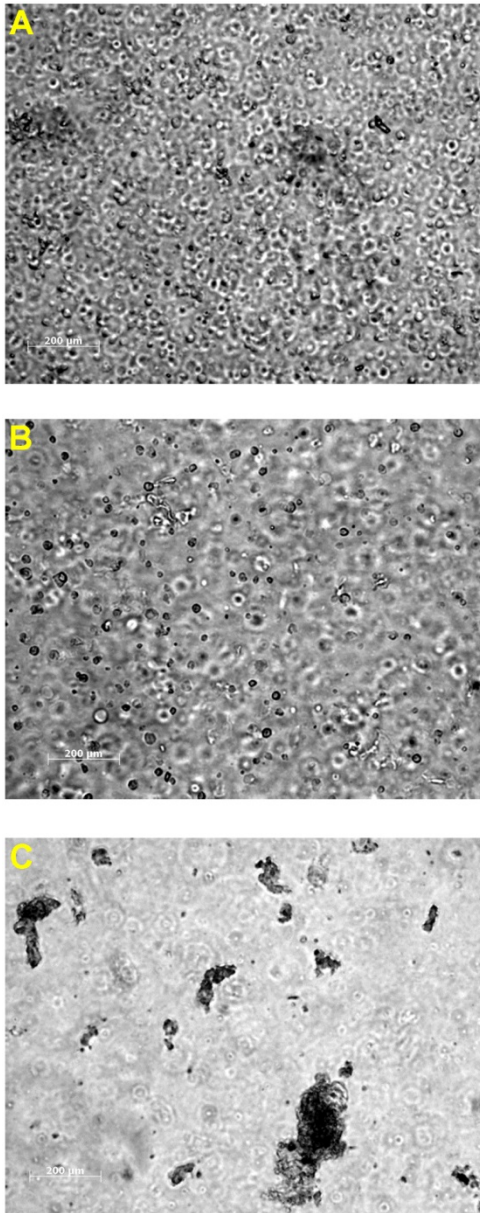


**Figure 2.4. Homogenisation of transfected HEK293 cells: microscopy.** (A) Shows the resuspended cells in the homogenisation buffer. Most cells still have intact cell membranes. (B) Mechanical disruption of the cells using just the Teflon glass homogeniser (10x strokes) without passing the cells through the needle. Some cells still retain their cellular morphology while others seem to have lysed. (C) Shows the state of the resuspended cells after first passing through the 23G needle (15x) and then using the homogeniser. Cells have completely lysed with no recognisable cellular morphology, only cell debris seen. Therefore, for successful disruption of cell membranes and release of hRyR2, it was necessary to pass the cell suspension repeatedly through the needle. Scale bar: 200 µm.

After mechanical disruption of the cells, the homogenate was centrifuged at 1500 rpm for 15 minutes at 4°C (Allegra 64R, Beckman) and the pellets containing cellular debris were discarded. The supernatant was collected and centrifuged at 100,000 g for 90 minutes at 4°C in an Optima L-90K ultracentrifuge (Beckman Coulter) with a previously chilled 50.2ti rotor. The supernatant was carefully decanted out and discarded while the pellets (containing mixed membrane microvesicles) were thoroughly resuspended in ~400 µl of cryoprotective buffer before snap freezing the aliquots (30 µl) in liquid N<sub>2</sub> and storing at -80°C until needed.

Before freezing the mixed membrane protein preparation, its protein content was determined using the micro bicinoninic acid (BCA) colourimetric assay. For this procedure, manufacturer's guidelines were followed (Micro BCA™ protein assay kit). Briefly, three dilutions of the protein sample (1/20, 1/50 and 1/100) and the serial

dilutions of BSA (10-200  $\mu\text{g/ml}$ ) were mixed with appropriate reagents included in the kit. These were then incubated in a 96 well plate at 37°C for 30 minutes that resulted in the mixture changing its colour to various shades of blue-purple. The coloured reaction product is formed by the chelation of two molecules of BCA with one cuprous ion. The BCA/copper-amino acid complex is water-soluble and exhibits a strong linear absorbance at  $\sim 560$  nm, directly proportional to increasing protein concentration. After incubation, the absorbance values of the samples at 560 nm ( $\text{Abs}_{560}$ ) were read using a plate reader (Multiscan EX from Labsystems) to generate a standard plot of BSA protein concentrations (**Fig 2.5**). The equation of the linear regression was used to determine the protein concentration of the sample from its  $\text{Abs}_{560}$ .

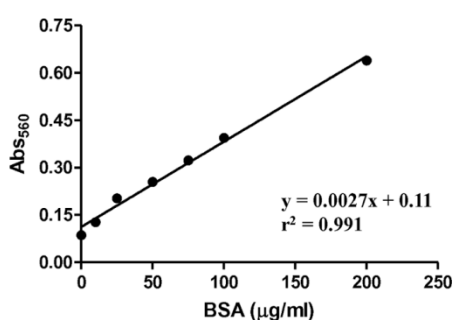


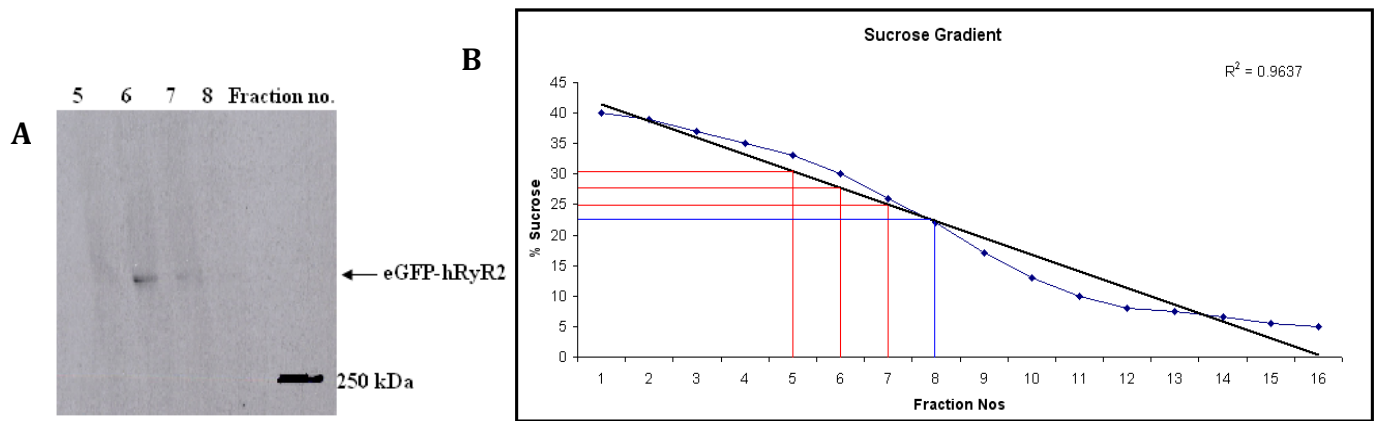
**Figure 2.5.** A linear regression analysis of the absorbance values (560 nm) of BSA serial dilutions. The straight line equation from the standard plot is used to determine the value of the protein conc. of the mixed membrane prep (x) when its  $\text{Abs}_{560}$  is known (y). In this case it was calculated to be 10.5 mg/ml.  $r^2$  value gives the goodness-of-fit.

### 2.3.5 Purification of recombinant eGFP-hRyR2

Purification and isolation of the hRyR2 channels from the mixed membrane preparation involved the solubilisation of the protein using a detergent-lipid system followed by a density gradient ultracentrifugation to separate the solubilised membrane proteins. The process of detergent solubilisation is a critical step that determines the final yield of purified channels and the feasibility of various functional assays. High levels of detergent could easily degrade the RyR2 channel protein, whereas less than adequate levels could lead to low yield of purified channels and contamination by other membrane associated proteins. For this reason, the various steps of this process were carefully optimised for achieving a high yield of purified hRyR2 and are described in **Chapter 3**.

The supernatant obtained after centrifugation of the solubilised mixed membrane protein preparation (**Chapter 3**) was carefully layered onto a continuous sucrose density gradient

containing protease inhibitors (1:1000). For making the sucrose gradient, 5%, 25% and 40% (w/v) sucrose solutions (made up in gradient buffer) were allowed to mix on a rotary agitator for an hour at 4°C. This was used to create a sucrose density gradient (5-25%) in polyallomer centrifugation tubes (Beckman-Coulter) by a linear gradient maker (Fisons Scientific, MSE) connected to a peristaltic pump (Masterflex LS from Cole Parmer). The continuous gradients were created by the gradual dilution of 25% sucrose with the 5% sucrose solution and they also had a 5 ml cushion at the bottom (40% sucrose). The tubes were gently placed inside a chilled SW32.1 swing-out rotor without disturbing the gradients and centrifuged at 100,000 g for 17 hours at 4°C inside an Optima L-100XP ultracentrifuge (Beckman Coulter). After the completion of ultracentrifugation, the bottoms of the polymer tubes containing the sucrose density gradients were punctured using a wide bore needle (tube piercer, BD) and typically ~1 ml fractions were collected using a peristaltic pump (M2V, Shuco Scientific Ltd) and a custom-made controller (made by R.A Montgomery, NHLI). The complete fraction collection set-up was placed inside a small refrigerated compartment (4-8°C). The sucrose densities in each of the collected fractions were measured using a (0-50%) sugar refractometer (Bellingham and Stanley Ltd.) to identify the fraction having a density of 28% sucrose. According to previous studies it was determined that the RyR2, because of its massive size when compared to other cellular proteins, should be present at this sucrose density (28%) and in a relatively purified state (Lai et al. 1988; Anderson et al. 1989). The sucrose densities in each of the 1 ml fractions obtained from the gradient were plotted and it was found that in an undistorted gradient, fractions 5 or 6 typically corresponds to the 28% sucrose density (**Fig 2.6**). These fractions were tested for the presence of purified hRyR2 in single channel studies after incorporation in planar lipid bilayers before being aliquoted (25 µl) and snap frozen in liquid N<sub>2</sub>. The fractions containing purified channels were stored at -80 °C until used.



## 2.4 Biochemical and functional assays for recombinant hRyR2

The hRyR2 present in the mixed membrane protein preparations was typically detected and quantified using SDS-PAGE and Western blot techniques, while functional assays of purified RyR2 channels include [<sup>3</sup>H]ryanodine binding studies (populations of channels) and single channel experiments (single molecules). These three techniques will be broadly described in this chapter while specific adaptations of the protocols will be addressed in the relevant results chapters.

### 2.4.1 List of reagents and buffers for SDS-PAGE and Western blot

**Tris buffer (stacking):** 0.5 M, pH 6.8.

**Tris buffer (resolving):** 1.5 M, pH 8.8.

**Sodium Dodecyl Sulphate (SDS):** 10% (w/v), prepared freshly before each use.

**SDS-PAGE running buffer:** 25 mM Tris, 310 mM Glycine, 0.5% (w/v) SDS.

**Acrylamide (40%):** bis-solution 37.5:1, obtained from BioRad.

***Ammonium persulphate (APS):*** 10%, freshly prepared solution before use.

***SDS-PAGE sample buffer (5x):*** 0.06 M Tris (pH 6.8), 2% (w/v) SDS, 10% (v/v) glycerol, 0.005 M EDTA, 0.25 % (w/v) bromophenol blue and 10% (v/v)  $\beta$ -mercaptoethanol.

***Molecular weight markers:*** Pre-stained markers (Kaleidoscope), obtained from BioRad.

***Transfer buffer (Semi-dry):*** 48 mM Tris, 39 mM glycine, 0.375% (w/v) SDS.

***Tris-buffered saline (TBS), 1x:*** 20 mM Tris, 137 mM NaCl (pH 7.6).

***TBS-T buffer:*** TBS (1x), 0.1% (v/v) Tween-20.

***TBS-T-Milk blocking solution:*** 5% (w/v) non-fat dried milk (Marvel) was dissolved in TBS-T buffer.

***Enhanced Chemiluminescence detection:*** ECL kit obtained from GE Healthcare.

#### **2.4.2 Buffers and reagents required for [<sup>3</sup>H]ryanodine binding assay**

***Ryanodine binding buffer:*** 1M KCl, 25 mM PIPES, 1 mM EGTA, 1 mM HEDTA, 1 mM NTA (pH adjusted to 7.4 using KOH).

***CaCl<sub>2</sub>:*** 20 mM stock.

***Ryanodine:*** 1 mM stock, made up in ryanodine binding buffer. Ryanodine obtained from Abcam Biochemicals, UK.

***[<sup>3</sup>H]ryanodine (1  $\mu$ M):*** obtained from PerkinElmer.



### **2.4.3 SDS polyacrylamide gel electrophoresis**

SDS-PAGE along with a Western blot analysis has been traditionally used to determine the levels of protein expression (Laemmli 1970). A 4% polyacrylamide resolving gel is suitable for very large proteins like RyR2, while much smaller proteins such as FKBP12/12.6 can be run on a 15% gel. The 4% separating gel for a large Hoefer casing and tank was prepared as follows: 3 ml of 40% bis-Acrylamide, 7.5 ml Tris resolving buffer, 300  $\mu$ l of 10% SDS, 150  $\mu$ l of 10% APS, 19.04 ml de-H<sub>2</sub>O and 15  $\mu$ l TEMED. The total volume of the mixture was 30 ml. Freshly prepared APS and TEMED were added last as they act as catalysts for the polymerisation of bis-acrylamide. The gel casing was assembled and gel poured according to manufacturer's instructions (Hoefer) and allowed to set while the stacking gel (4%) was made up. The stacking gel for a large gel casing and tank was made up as follows: 1.2 ml of 40% bis-Acrylamide, 3 ml Tris stacking buffer, 120  $\mu$ l of 10% SDS, 60  $\mu$ l of 10% APS, 7.62 ml de-H<sub>2</sub>O and 12  $\mu$ l TEMED. The total volume of the stacking gel mixture was 12 ml, which was poured over the already set resolving gel followed by the insertion of the plastic 'comb' for making the loading spaces. Typically, 100  $\mu$ g hRyR2 protein samples (mixed membranes) were incubated along with sample loading buffer containing SDS for 20 minutes at 42°C to linearise the protein molecules by adding negative charges so that they migrate according to their respective sizes. After the stacking gel had set, the protein samples were loaded alongside the pre-stained molecular weight markers (Kaleidoscope, Bio-Rad) and the electrophoresis was carried out inside the running buffer in the Hoefer gel tank. For the first 1 hour, electrophoresis was carried out at 0.04 Ampere (constant current) till the markers and the dye front migrated to the end of the stacking gel, after which a 0.01 Ampere constant current was used. The gel was run overnight till the dye front had run off the gel with only the top two coloured markers (typically 250 and 110 kDa) remaining. The RyR2 monomer with a size of ~565kDa ran much slower than the highest protein molecular weight marker 250 kDa (myosin).

### **2.4.4 Western blotting**

The separated proteins on the resolving gel were transferred onto a Polyvinylidene difluoride (PVDF) membrane (Immobilon-P), obtained from Millipore using a semi-dry blotting method. The PVDF membrane was cut to size and soaked for a minute in 100% methanol before being allowed to soak in the semi-dry transfer buffer along with pre-cut

blotting papers. The Bio-Rad semi-dry blotting apparatus was assembled according to the manufacturer's instructions after carefully removing the gel from the tank. The transfer was carried out in a cold room (4°C) at 0.4 Ampere constant current for 2 hours, taking care to limit the voltage to 25 V. On completion of transfer (pre-stained molecular weight markers are seen on the membrane), the membrane was blocked with TBS-T-Milk (5%) blocking buffer overnight at 4°C in a cold room. This was followed by treating the membrane overnight at 4°C with an anti-eGFP primary antibody (B-2, mouse monoclonal; Santa Cruz) at a dilution of 1:1000 in TBS-T-Milk buffer. The membrane was then washed three times (15 minutes each) with diluted TBS-T-Milk (1%) buffer. This was followed by exposing the membrane for 2 hours to a horseradish peroxidase (HRP)-conjugated goat anti-mouse secondary antibody (1:10,000) diluted in TBS-T-Milk (1%) buffer at room temperature. The membrane was then washed 5 times with TBS-T buffer for 10 minutes each to remove the unbound secondary antibody and the bands were visualised by enhanced chemiluminescence detection (ECL, GE Healthcare). The procedure was carried out in accordance with the manufacturer's instructions. The conjugated HRP catalyses a reaction that oxidises luminol (present in the ECL kit) which in turn emits light at 428 nm wavelength and can be detected by exposing a light sensitive autoradiography X-ray film (GE Healthcare). The basic principles underlying this process are shown in **Fig 2.7**.

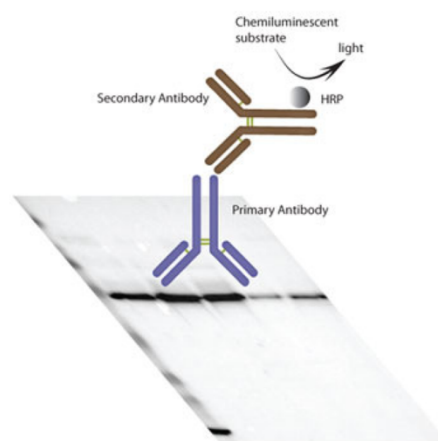


**Figure 2.7. Schematic diagram showing the principle of chemiluminescent protein (eGFP-hRyR2) detection in a Western blot.** The anti-eGFP mouse primary antibody (blue) binds to the eGFP in the protein band containing hRyR2. The secondary goat anti-mouse antibody with conjugated HRP (brown) then binds to the primary. The HRP catalyses the oxidation of luminol by peracid. Oxidised luminol emits light in the far blue range due to decay from an excited state. This light is detected by sensitive X-ray film. Therefore, hRyR2 is detected by proxy using an antibody probe for its tag (eGFP). Diagram from Sigma-Aldrich.

#### 2.4.5 [<sup>3</sup>H]ryanodine binding assay

The tritium-labelled ryanodine binding assay has been extensively used to examine the effects of various ligands on RyR2 channel activity. As ryanodine binds to the open conformation of RyR2, this assay could provide information about the average activity of a population of channels. For this assay, typically 50 µg samples of mixed membrane preparations or 100 µg samples of solubilised protein are used. Accurate measurement of protein concentrations (Micro BCA assay) in the samples along with quantification of RyR2 levels (Western blot) prior to the binding assay is useful in eliminating any effects of heterogeneous expression of hRyR2 after transfection. The protein samples were mixed with the ryanodine binding buffer and incubated along with appropriate amounts of [<sup>3</sup>H]ryanodine (10 nM for 50 µg sample) at 37 °C for 90 minutes. The free Ca<sup>2+</sup> level was adjusted to 100 µM using CaCl<sub>2</sub> and buffers according to MaxChelator software for maximal activation of hRyR2. Non-specific binding was determined from duplicate assays where there was a 1000-fold excess of unlabelled ryanodine (10 µM). There were two replicates each for the specific and non-specific binding reactions. After terminating the reaction by diluting the mixture by ice cold binding buffer, the samples were filtered through Whatman glass-fibre filters (GF/F) which were pre-soaked in ryanodine binding buffer. The [<sup>3</sup>H]ryanodine-bound hRyR2 were retained in the filter material after washing with binding buffer to remove excess unbound [<sup>3</sup>H]ryanodine. The filters corresponding to each of the samples were placed in vials containing scintillant liquid (Ultima Gold; PerkinElmer) and vortexed before being placed in a scintillation counter (tri-Card 2100 TR; Packard Bioscience). The radioactive decay is counted in terms of disintegrations per minute (dpm); this was used (after subtracting non-specific dpm values) along with the specific activity of the radio-ligand and protein content of the sample to find the molar concentration of [<sup>3</sup>H]ryanodine binding (pmol/mg).

## 2.5 Single channel studies of hRyR2 in a planar lipid bilayer system

The ability to observe the current flow through single ion channels has revolutionised our understanding of the biophysical aspects of channel gating behaviour (Neher and Sakmann 1976). Further improvements in experimental design and electronics along with the development of analytical methods have made it possible to interpret the real-time dynamics of these single molecules in terms of actual physical mechanisms (Hamill et al. 1981; Colquhoun and Hawkes 1981). Single channel experiments on RyR2 are not possible using conventional patch clamp techniques as its intracellular location prevents access to patch pipettes. Therefore, the incorporation of single isolated RyR2s in artificial planar lipid bilayers (Holmberg and Williams 1989) are currently the only method to observe channel gating in response to various ligands in real-time. The basic experimental setup of a bilayer recording rig has two main components: 1) the channel and its environment and 2) the electronics and recording system.

### 2.5.1 Experimental milieu of RyR2: the cup and block system

Two fluid-filled chambers corresponding to the cytosolic (*cis*) and luminal (*trans*) sides of RyR2 are connected through a small hole (diameter: 200  $\mu\text{m}$ ). The *cis* chamber is formed by a styrene copolymer cup with a cylindrical cavity that is drilled close to one edge, giving rise to a thin septum. An artificial planar lipid bilayer is formed by spreading phospholipid dispersions across a 200  $\mu\text{m}$  precision-drilled hole at the centre of the thin septum (Fig 2.8A).

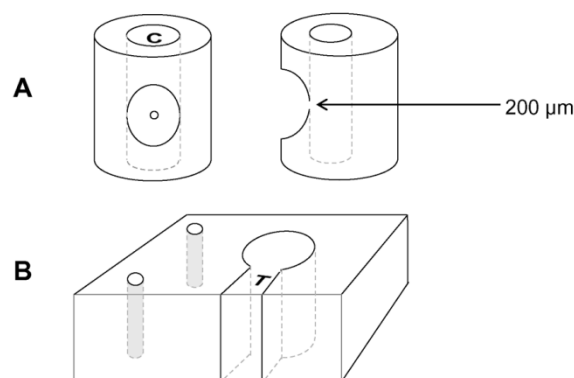


**Figure 2.8. A schematic representation of the bilayer recording chambers. (A)** The cup with its cylindrical cavity forms the *cis* chamber (marked as 'C'). A 200  $\mu\text{m}$  hole drilled on the front of the cup connects the chambers (shown in a lateral profile view). **(B)** The cup fits into a cavity in the block that leaves a rectangular *trans* chamber (T) in front of the hole in the cup. Two smaller cylindrical holes (grey) are drilled on one side of the block to accommodate 3M LiCl solutions, agar salt bridges and Ag/AgCl connecting electrodes.

The rectangular perspex block has a cavity for slotting in the cup with its hole facing towards the front. The rectangular space created by this arrangement in front of the cup forms the *trans* chamber (**Fig 2.8B**). The volumes of recording solution that are typically added to the *cis* and *trans* chambers are 500  $\mu\text{l}$  and 1000  $\mu\text{l}$  respectively. The front surface of the block is made of a clear glass sheet glued to the block polymer to provide an unobstructed view of the *trans* chamber and the front surface of the *cis* chamber bearing the hole.

### 2.5.2 Bilayer electronics and recording apparatus

Mechanical noise-induced distortions of the bilayer is minimised by fixing the cup-block arrangement including the head-stage electronics (with its connections) on a heavy lead block that was placed on a vibration isolation table. Ambient electromagnetic interference from surrounding devices is minimised by enclosing the setup inside an aluminium box with a lid that acts as a Faraday cage. The small magnetic stirrer (a circular magnet attached to a motor) was incorporated in the lead block below the cup-block arrangement so that solutions in the chambers could be efficiently mixed using small magnetic beads. The *cis* and *trans* recording solutions are connected to two small cylindrical wells in the block filled with 3 M LiCl using agar salt bridges (**Fig 2.9A**). The salt bridges were made by filling thin glass capillaries (heat bent to shape) with 2% (w/v) agar dissolved in 3 M LiCl. The electrical connection between the wells and the head amp is made using silver wire electrodes coated by silver chloride (Ag/AgCl). Most of the electronic components (**Fig 2.9B**) of the bilayer setup were designed and custom-built by R.A Montgomery (NHLI, Imperial College, UK). The head amplifier works as a very sensitive current-to-voltage converter, converting picoampere (pA) currents flowing through a RyR2 channel into voltage signals which can then be sampled. It has an operational amplifier (Op-Amp) that works as the I-V converter (10 mV/pA sensitivity) and can clamp the bilayer at a desired voltage (using a negative feedback loop). The desired external command voltage ( $V_c$ ) is relayed to the bilayer from the controller through the head stage amplifier (**Fig 2.9B**). A very high value (10 G $\Omega$ ) feedback resistor ( $R_f$ ) is connected in parallel with the Op-Amp to allow for the measurement of miniscule amounts of ionic current (pA) flowing through a single RyR2 channel (**Fig 2.9B**). The output voltage  $V_o$  from the head amplifier passes to a second stage differential amplifier which subtracts the clamp voltage  $V_c$  (**Fig 2.9B**). The final output voltage signal (V) is split and passed through two analogue filters: 5 kHz (built by R.A Montgomery) and 1

kHz (Frequency Devices, USA) low-pass 8-pole Bessel filters. This helps get rid of the high frequency electronic noise that distorts the actual biological signal from the channels.

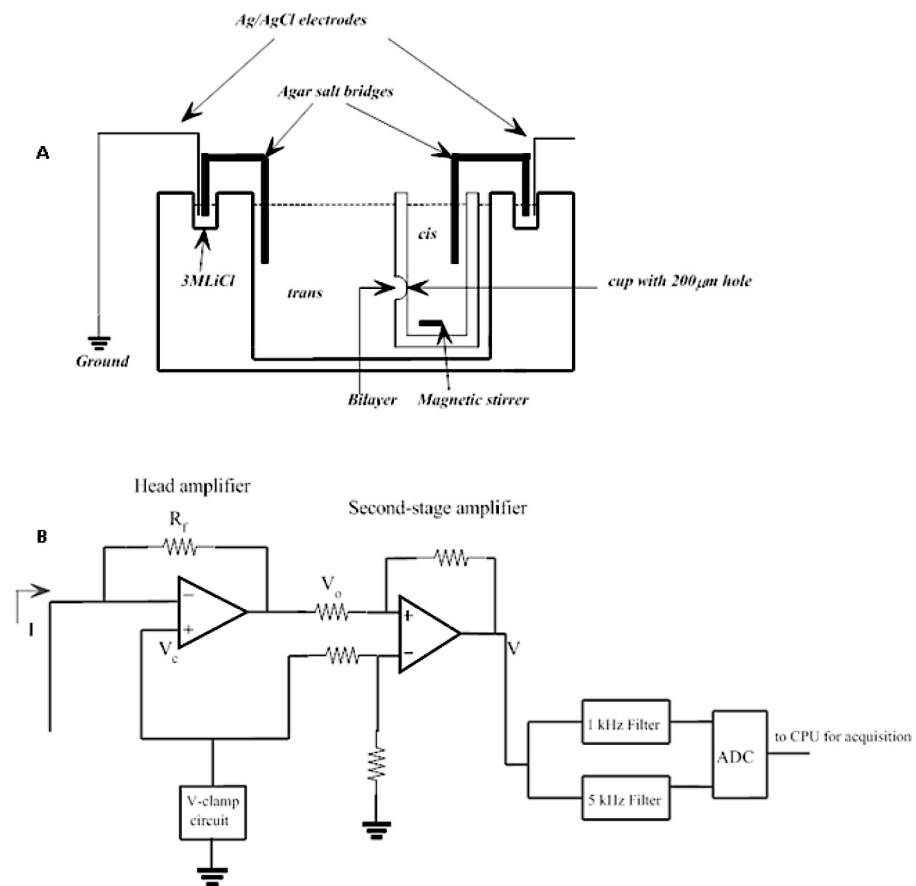


**Figure 2.9. Schematic diagram of the bilayer recording chambers and associated electronics.** (A) shows a schematic section of the cup-block assembly with the electrical connections between the chambers and the head amplifier. The electrode connected to the *cis* chamber continues in the electronic circuit diagram (B) delivering current  $I$  to the head amplifier.  $I$  is the current from the bilayer;  $R_f$  is the 10 G $\Omega$  feedback resistor;  $V_c$  is the clamped (command) voltage;  $V_o$  the output voltage; the amplifiers are represented as triangles (standard). Here  $V_o = -I.R_f + V_c$ . and  $V = -I.R_f$ . ADC is the analogue to digital converter (PCI-6036E, National Instruments). The filters are analogue 8-pole low-pass Bessel filters of the values as shown.

The filtered analogue voltage signals are converted to digital signals using an analogue-to-digital converter (ADC) PCI 6036E obtained from National Instruments, TX, USA. During the digitisation, the signals are sampled at 20 kHz with a sampling interval of 50  $\mu$ s. The recordings were acquired through the acquisition software Acquire v5.0.1 (Bruxon, Seattle, USA) and displayed in real-time on the computer screen. The temporal resolution of the recording system depends on the rise time of the head amplifier and the filtering used.

### 2.5.3 Bilayer formation and hRyR2 incorporation

During single channel experiments, the *trans* chamber is always held at virtual ground, while the *cis* chamber is ‘clamped’ at different voltages relative to the ground (**Fig 2.9**). The recording chambers can be isolated from the electronics if required, by using a magnetised reed switch that allows the manipulation of recording solutions without damaging the bilayer. Planar phospholipid bilayers were formed using purified bovine heart phosphatidylethanolamine PE (Avanti, Alabaster, USA) that was stored as a stock solution in chloroform (50 mg/ml) at  $-80^{\circ}\text{C}$ . Small aliquots were taken out before experiments and the chloroform was evaporated under a stream of  $\text{N}_2$ . The dried lipid was then resuspended in the solvent *n*-decane at a final concentration of 35 mg/ml. A small amount of the lipid suspension is taken on the back of a ‘painting stick’ (made by cutting a disposable plastic Pasteur pipette) and deposited around the aperture of the hole in the *cis* chamber and allowed to dry. The cup hole is then said to be ‘primed’ for the formation of planar lipid bilayers. The cup is then slotted into the block such that the hole faces the *trans* chamber and the required ionic solutions are added to both chambers. Typically, the starting solution in both chambers for all experiments was 210 mM KCl, 20 mM HEPES (pH adjusted to 7.4 using KOH) containing  $\sim 1\ \mu\text{M}$  contaminant  $\text{Ca}^{2+}$ . A small quantity of the lipid suspension was used to coat the tip of the painting stick which was dragged gently across the hole on the *cis* side in an upward direction. The hydrophobic coating of the copolymer wall surface created by previous priming helped in dispersing a layer of lipid across the 200  $\mu\text{m}$  hole. The initial lipid film is usually several  $\mu\text{m}$  thick and is in dynamic equilibrium with a thick annulus of lipid surrounding the hole that acts as a reservoir (Mueller et al. 1962). The chemical and thermodynamic property of lipid (Plateau-Gibbs border suction) causes it to migrate from the hole towards the periphery, thereby spontaneously thinning into a planar lipid bilayer which is  $\sim 3\text{-}5\ \text{nm}$  thick (White 1986; Nagle and Tristram-Nagle 2000; Laver 2001). The lipid bilayer (insulator) along with ionic solutions on either side (conductors), effectively act as a capacitor that can charge up and discharge with changes in membrane potential. As the capacitance of a lipid film is inversely proportional to its thickness, the formation of a bilayer can be monitored by measuring the capacitance spikes due to charging and discharging of the membrane. A square wave pulse (oscillating between  $\pm 4\ \text{mV}$ ) applied to the lipid membrane during the process of bilayer formation is seen as an increase in the capacitance spike as the thickness of lipid decreases. The thinning of lipid can also be

aided by 'dry painting' across the hole to remove any excess lipid, thereby shifting the equilibrium of lipid volume between the central region and annulus.

Membrane vesicles containing reconstituted hRyR2 obtained from either mixed membrane or purified protein preparations are added in small quantities (1-3  $\mu\text{l}$ ) to the *cis* chamber solution for incorporation of channels into the bilayer. The fusion of membrane vesicles with the lipid bilayer was facilitated by the creation of a hyperosmotic gradient from the *cis* to the *trans* chamber. This was achieved by the addition 3 M KCl aliquots (2 x 100  $\mu\text{l}$ ) into the *cis* chamber causing a net movement of water molecules into the vesicle lumen from the surrounding solution. The rise of the intravesicular pressure causes them to swell and burst while being pushed towards the bilayer (due to osmotic gradient from *cis* to *trans*) resulting in the incorporation of any channels present in the vesicles (**Fig 2.10**) The vigorous stirring of the *cis* chamber solution using a magnetic stirrer increases the probability of membrane vesicles to come near the vicinity of the lipid bilayer, thereby aiding vesicle fusion and channel incorporation. During all additions of ionic solutions, ligands and channel protein, the recording chambers were isolated from the head stage electronics by sliding a magnet over the reed switch, thus preventing the bilayer from breaking. The bilayer was held at 0 mV under these asymmetric ionic conditions (*cis* to *trans* gradient) such that any incorporation of hRyR2 can be visualised in the form of single channel current fluctuations due to the diffusion of  $\text{K}^+$  ion down its electrochemical gradient. Once a channel had incorporated, symmetric ionic conditions were restored by the perfusion of the *cis* chamber with 210 mM KCl solution (**Fig 2.11**) using a peristaltic pump (Shuco International, London). The RyR always incorporates into the bilayer in a fixed orientation such that its large cytosolic domain faces the *cis* chamber while the luminal side points into the *trans* chamber (Sitsapesan and Williams, 1994a; Laver, 2001). This can be easily verified by adding 5 mM EGTA to the *cis* chamber to achieve nominally zero  $\text{Ca}^{2+}$  conditions that result in channel shutdown (no activating ligand present). The addition of 1  $\mu\text{M}$  ryanodine to the *cis* chamber should modify the channel by binding from the cytosolic side of RyR2 (**Chapter 1**).



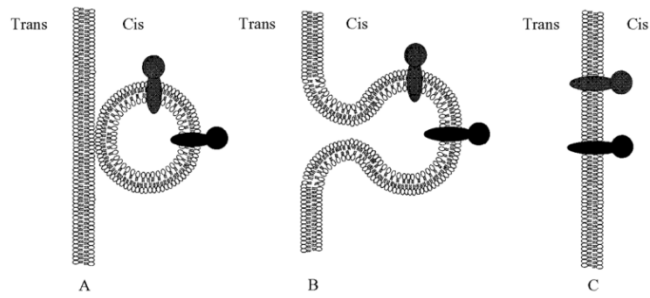


**Figure 2.10. A schematic diagram showing the fusion of membrane vesicles with an artificial planar lipid bilayer.** (A) Shows the adherence of a vesicle with the lipid bilayer during the pre-fusion state. (B) The cis-trans high osmotic gradient causes the swelling of vesicles and promotes fusion with the bilayer. (C) After fusion is complete, the channel protein presents in the vesicle are aligned such that the domain facing outwards (e.g. hRyR2 cytosolic domain) now face the cis chamber in which the vesicles were added. Figure from (Williams 1994).

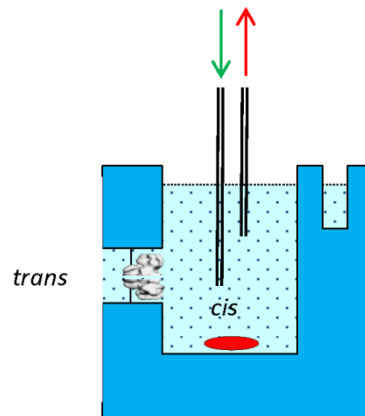


**Figure 2.11. Perfusion of bilayer recording chamber.** The schematic diagram shows the arrangements of fresh solution input (green arrow) and waste output (red arrow) glass tubes used for perfusion of the *cis* chamber. During the volume exchanges, it's important to maintain the surface of the liquid above the level of the hole to prevent the bilayer from breaking.

#### 2.5.4 Single channel current recording and analysis

The various experimental conditions employed in order to study different aspects of hRyR2 gating behaviour are described in the methods sections of relevant results chapters. Data from recordings where only a single ion channel had incorporated were further analysed as it becomes difficult to interpret, in terms of mechanisms, kinetic information from multiple channels in the bilayer. The single channel data were recorded on a computer after digitisation and were later inspected using Review software (Bruxon, Seattle, USA). The kinetic parameters of channel activity were calculated after analysis of the current fluctuations due to the opening and closing of hRyR2. The various techniques used for data analysis and the ones most suitable for my experiments including their optimisation for RyR2 data are described in detail in **Chapter 4**.

#### 2.6 Statistical methods

In this study, all data are represented as mean  $\pm$  standard error of mean (S.E.M) and Student's *t* test was used as a test of significance where  $p < 0.05$  was considered significant. Prism 5.0 (GraphPad Software Inc.) and MS Excel were used for plots and statistical analyses. The absolute error bars when plotted on a logarithmic scale become asymmetric. To avoid this, I have used the relative logarithmic error that is symmetrical in our log-log energetics plots (**Fig. 6.13, Chapter 6**). The relative log error  $\Delta z \approx 0.434(\Delta x/x \text{ or } \Delta y/y)$ , where  $\Delta x$  and  $\Delta y$  are the absolute errors on the x and y axes respectively ( $\Delta x$  and  $\Delta y$  are assumed to be small) (Baird 1962).

## **Chapter 3.0**

### **Optimisation of recombinant hRyR2 extraction and purification for single channel experiments: the solubility paradox**

### 3.1 Introduction

Biophysical characterisation of the RyR2 at a single molecule level is central to our understanding of the mechanism of perturbed channel function in disease states brought about by mutations. The ‘gold standard’ approach for obtaining an accurate description of RyR2 channel gating behaviour in real-time when activated by its physiological trigger cytosolic calcium ( $[Ca^{2+}]_{cyt}$ ) is by studying the channel molecule after its incorporation in artificial planar lipid bilayers. Ryanodine receptor-rich heavy SR membrane fractions isolated from native sources (animal cardiac tissue) have been used in single channel experiments (Ashley and Williams 1990; Rosales et al. 2004; H. Chen et al. 2013). The advantages of using native preparations are 1) animal hearts can be relatively easy to obtain and 2) the high yield of protein that significantly increases the probability of channel incorporation in the bilayer. However, using RyR2 from native sources also poses significant challenges. Native SR membranes contain numerous  $Cl^-$  selective channels and  $K^+$  channels apart from RyR which might interfere with single channel current recordings by distorting the baseline current level. The massive flux of  $Ca^{2+}$  from the SR into the cytosol through RyR2 channels during CICR (see **Chapter 1**) could momentarily set up a potential difference across the SR membrane. A counter-current of  $K^+$  from the cytosol into the SR through trimeric intracellular cation-selective (TRIC) channels in the SR membrane could help offset this membrane potential by compensating for the net loss of positive charges from the  $Ca^{2+}$  stores (Pitt et al. 2010; Venturi et al. 2013). However, the role of TRIC channels as a carrier for counter-current across the SR has been disputed by another study (Guo et al. 2013). To minimise the distortive activities of these channels, ionic solutions incorporating calcium-HEPES/Tris-HEPES, cesium methanesulfonate ( $CsCH_3SO_3$ ),  $Ba^{2+}$  etc. are sometimes used ( $Ca^{2+}$  and  $Ba^{2+}$  can permeate only through the RyR pore but not  $K^+$  channels) including conducting experiments at or near the reversal potential for  $Cl^-$  (Fill and Copello 2002). The RyR is modulated by several key accessory proteins in the myocyte (**Chapter 1**), some of which may or may not be co-isolated along with the receptor in the heavy SR fraction. Unless the presence/absence of these regulatory proteins in the isolated fractions can be confirmed and their possible interactions with RyR in the bilayer quantified, it’s very difficult to unambiguously interpret the single channel data from  $[Ca^{2+}]_{cyt}$  activation experiments. Therefore, for a clear understanding of the mechanisms underlying the activation of RyR2 by  $[Ca^{2+}]_{cyt}$ , the channel activity should be at first studied in isolation, in an environment where possible effects of these accessory proteins are absent.

### 3.1.1 Purification and isolation of RyR2 using solubilisation

RyR2 like most membrane proteins is not soluble in aqueous solutions. Special synthetic systems are therefore required for *in vitro* studies where RyR2s reside in surroundings that satisfy their high hydrophobicity. Membrane proteins can be purified into lipid-detergent micelles where the hydrophobic regions of the protein are solvated with the nonpolar groups available in a dispersed lipid solution (Seddon et al. 2004). This process is known as solubilisation that results in *proteoliposomes* from which the channels can be reconstituted back into artificial planar lipid bilayers and their single channel activity monitored. Solubilisation of RyR2 using the detergent-lipid pair of 3-[(3-cholamidopropyl)dimethylammonio]-1-propanesulfonic acid (CHAPS; a non-denaturing zwitterionic detergent) and Phosphatidylcholine (PC) has been shown to provide a good yield of purified functional channels (Pessah et al. 1986; Anderson et al. 1989). This approach ensures that only purified RyR2 are present in lipid bilayers in the absence of accessory regulatory proteins. However, the process of using detergents and lipids as surfactants to extract RyR from its native environment in the SR and its subsequent manipulation for single channel experiments is nontrivial and requires careful optimisation steps. RyR2 has been purified from HSR fractions sourced from cardiac tissues of various mammalian species (sheep, pig, dog, rat, mouse etc.) and although the single channel studies have revealed vital information about channel behaviour, interspecies variation does exist. These variations in regulation of the channel by  $\text{Ca}^{2+}$ ,  $\text{Mg}^{2+}$  etc. could translate into differences in EC coupling in the heart (Bers 2002; Walweel et al. 2014). Species-specific differences in cardiac cycle are manifestations of spatiotemporal variation of calcium signalling in the cardiomyocytes. As  $\text{Ca}^{2+}$  release through RyR2 forms an integral part of the  $\text{Ca}^{2+}$  signalling 'toolbox', interspecies differences in channel function are to be expected. As current studies are becoming increasingly focussed on understanding the effect disease causing mutations in RyR2 and the search for putative therapeutic compounds that could stabilise channel function, the need for upgrading to the human RyR2 isoform has become imminent in order to make the findings more relevant.

### 3.1.2 Understanding human RyR2 channel behaviour: the ideal experimental model

RyR2 channels from human cardiac tissue have been used previously in some studies where they were mostly obtained from explanted hearts from patients or from cadavers (Holmberg and Williams 1989). Human pancreatic acinar cells have also been found to express RyR2 and were sourced from cadaveric donors (Lewarchik et al. 2014). However, in most cases it is difficult to consistently obtain cardiomyocytes from human hearts that are completely free of any pathology for functional characterisation of normal RyR2 gating behaviour. Human RyR2 channels recombinantly expressed in mammalian cell lines can be solubilised using detergent-lipid systems and purified for single channel functional studies after reconstitution into planar lipid bilayers. Using this approach, the major challenge is to routinely obtain functional RyR2 channels after solubilisation with yields sufficient enough to do feasible single channel experiments.

Although eGFP-tagged recombinant human RyR2 expressed in HEK293 cells have been purified for single channel experiments in the lab (**Chapter 2**), the yield of functional channels was not satisfactory. Regular incorporation of functional single channels in lipid bilayers for every reasonable volume of protein preparation added to the *cis* chamber during each experiment is a must for conducting feasible studies and achieving consistency among data sets. In this chapter, I will highlight the experimental approaches that were employed in order to identify the problems in RyR2 solubilisation and purification steps leading to low channel yield and the methods adopted to correct them.

## 3.2 Key objectives

1. Examination of the key steps in RyR2 solubilisation process to identify the factor(s) responsible for sub-optimal yield of channels used in single channel experiments.
2. Once identified, use a range of conditions to optimise the steps such that purified RyR2 channel protein devoid of other contaminant channels ( $\text{Cl}^-$ ,  $\text{K}^+$ ) is obtained in sufficient quantities for feasible single channel studies.

### 3.2.1 Additional objectives

Studying the single channel gating behaviour of RyR2 in a regulated minimal environment in the absence of any interaction with its accessory proteins (see **Chapter 1**, Introduction) that may modulate channel gating is one of the key aims of this work (**Chapter 5**). It is therefore essential to ensure that RyR2 does not associate with any endogenously expressed accessory proteins in the HEK293 system.

HEK293, being non-excitabile cells, do not have endogenous RyR2 and its associated luminal accessory proteins required as a part of EC coupling machinery (S. R. Chen et al. 1997a; Stewart et al. 2008). However, HEK293 cells are known to endogenously express FKBP12.0 but not FKBP12.6 (Xiao 2004). Although FKBP12 is not known to interact with RyR2 in the cardiomyocyte due to much lower affinity than FKBP12.6 (Timerman et al. 1996; Guo et al. 2010), some studies have shown otherwise (Jeyakumar et al. 2001; Galfré et al. 2012). The nature of interaction, if any, between recombinant RyR2 with endogenous FKBP12.0 in HEK293 should therefore be investigated and characterised.

### 3.3 Experimental procedures

The experimental methods concerning the propagation of *hRyR2* cDNA in bacteria and its subsequent transfection in HEK293 cells to overexpress the channel protein have been described in detail in the previous chapter (**Materials and Methods, Chapter 2**). The protocols for experiments that test the biochemical and functional aspects of the extracted RyR2 channel protein like the Western Blot assay, [<sup>3</sup>H]ryanodine binding assay and single channel experiments have also been described in **Chapter 2**. For the Western blot analysis of FKBP12/12.6 interactions with hRyR2, the resolving gel used for SDS-PAGE was 15% and the primary antibody used was anti-FKBP12 (1:1000; rabbit polyclonal; obtained from Affinity Bioreagents) that also detects FKBP12.6. All other steps remained the same as those used for detection of eGFP-hRyR2 (**Chapter 2**). The process of solubilisation of RyR2 and its purification using the detergent-lipid system will be elucidated here, as the optimisation of this process is the major focus of this chapter.

#### 3.3.1 Preparation of rabbit skeletal muscle heavy SR vesicles

Some of the steps involved in recombinant hRyR2 protein solubilisation process that were optimised in this study were further verified by repeating the optimal protocols in another system where the channel protein yield was significantly higher. The high yield of RyR1 channels from native tissue facilitated easy detection of the channel activity in assays so that differences in outcomes between the optimised and suboptimal methods could be easily discerned. RyR1s present in heavy SR fraction isolated from rabbit skeletal muscle tissue were solubilised by repeating the same protocols and conditions as that used for RyR2. This procedure served as a form of control for the optimisation process.

Rabbit skeletal muscle heavy SR vesicles containing RyR1 were prepared as previously described (Inui et al. 1987; Meng et al. 2009). Briefly, 40 gm of back muscle from New Zealand white rabbits (euthanised in accordance with UK Home Office regulations and the Guide for the Care and Use of Laboratory Animals issued by the NIH) was homogenised on ice along with 200 ml of solution A1 (0.3 M Sucrose, 10 mM HEPES, 0.5 mM EDTA, 2 mM PMSF and 1:1000 protease inhibitor (PI) cocktail (Sigma) in an Ultra-Turrax blender. The homogenised muscle was centrifuged for 15 min at 11,000g in an Optima LX-90 (45ti rotor) at 4°C. This was done to remove the cell debris and connective tissue. The supernatant was again centrifuged at 110,000g for an hour at 4°C



using the same centrifuge and rotor. The pellet obtained was re-suspended in 40 ml of buffer A2 (buffer A1 + 0.65 M KCl) and incubated on ice for 1 hr. It was then re-pelleted (110,000g x 1hr at 4°C) and re-homogenised in 30 ml of buffer A3 (buffer A1 without EDTA). Sucrose step gradients were prepared in 6 tubes (from bottom to top: 45% (w/v), 38%, 32%, 27% sucrose) using a solution containing 0.65 M KCl, 10 mM HEPES, PI cocktail 1:1000 (pH 7.0). The re-suspended pellet was layered onto the sucrose density gradients in 5ml aliquots and the tubes were centrifuged for 16 hours in a Beckman centrifuge with an SW32ti (swing-out) rotor (70,000g) at 4°C. The gradients were carefully removed from the centrifuge and kept on ice. There was a dense white band formed by the heavy SR fraction at the interface of 38% and 45% sucrose layers. The upper layers were removed from all the tubes using a tap suction pump and the bands were carefully collected using a pipette. About 60 ml of the heavy SR fraction in sucrose was collected which was then diluted with twice the volume of buffer A1 and centrifuged at 110,000g for 1 hour at 4°C in a 45ti rotor. The resulting pellets were re-suspended in buffer A3 and protein assay was performed using the micro BCA method (**Chapter 2**). The heavy SR fraction containing RyR1 channels was aliquoted, snap frozen in liquid nitrogen and stored at -80°C until required.

#### **Buffers used for preparation of rabbit skeletal muscle heavy SR vesicles**

**Buffer A1:** 0.3 M Sucrose, 10 mM HEPES, 0.5 mM EDTA, 2mM PMSF and 1:1000 protease inhibitor (PI) cocktail ( pH 7.0).

**Buffer A2:** Buffer A1 + 0.65 M KCl.

**Buffer A3:** Buffer A1 without EDTA.

**Sucrose density gradient buffer:** 0.65 M KCl, 10 mM HEPES, PI cocktail 1:1000 (pH 7.0)

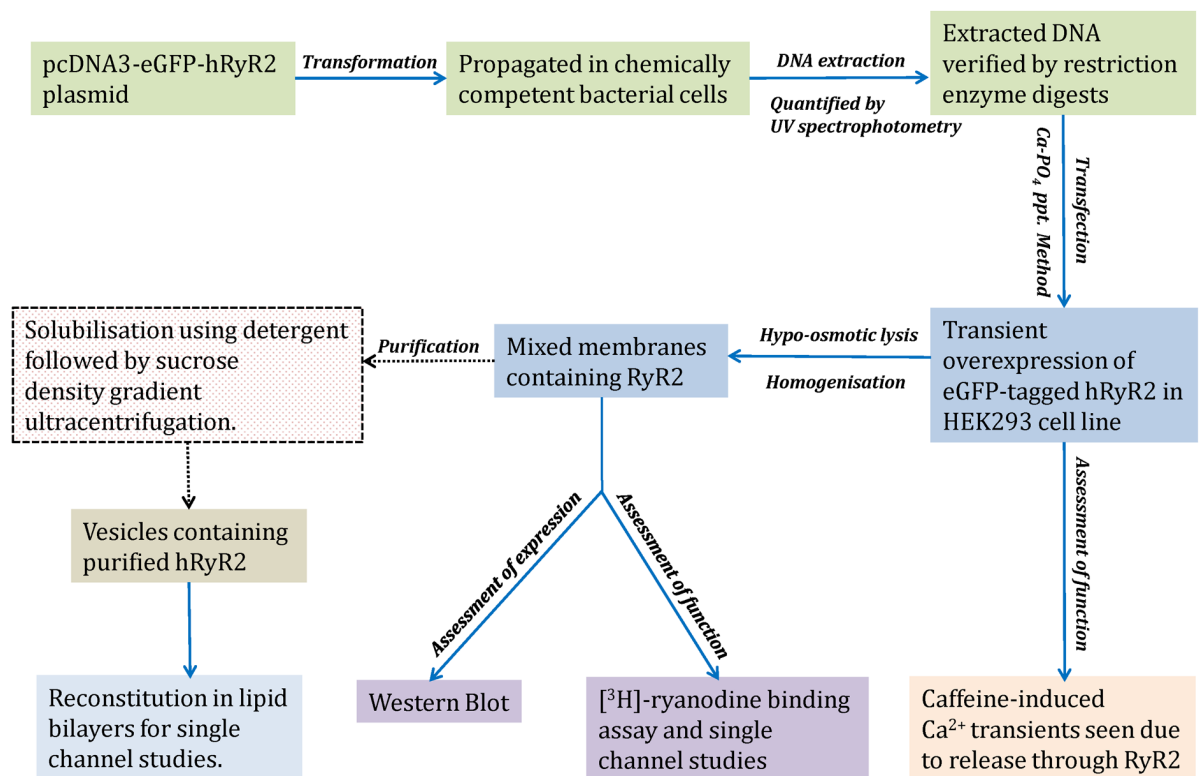


**Figure 3.1. A process flowchart showing the various steps of hRyR2 expression, extraction and purification.** The major sequential steps are shown along with the different assays done to verify plasmid fidelity, protein expression and channel function. The purification step (box with dashed outline) was responsible for low yield of RyR2 for single channel studies and required optimisation. Other key steps have been described in detail in **Chapter 2**.

### 3.4 Results

The purpose of this study was to unravel the reasons behind consistently low yields of purified recombinant human RyR2 and optimise the conditions of channel purification. The flowchart in **Fig. 3.1** shows the key steps involved in expression and purification of hRyR2 from HEK293 cells. The eGFP-tagged channel was efficiently expressed by the HEK293 cells (**Chapter 2**) and its function *in situ* (caffeine-induced  $\text{Ca}^{2+}$  release) was verified in previous studies using the same experimental system (Thomas et al. 2004). The mixed membrane microsomal vesicles prepared by lysis and homogenisation of HEK293 cells overexpressing RyR2 (**Chapter 2**) were subjected to biochemical and functional assays and were found to contain adequate amounts of channels for feasible experiments. As mentioned earlier, single channel current recordings from mixed membrane preparations with  $\text{K}^+$  as the permeant ion often have distorted baselines due to the activity of non-RyR2 channels (see **A1** in **Appendix I** for example traces). However, as the major aim of my work was to characterise the single channel gating behaviour of purified RyR2 under minimal conditions, the need for functional channels to incorporate into lipid bilayers consistently was of paramount importance. The strategy to address this issue of suboptimal yield of purified channels should therefore involve a systematic dissection of the key steps involved in the process of solubilisation of RyR2 protein from mixed membrane preparations.

#### 3.4.1 The first step: building up adequate starting material for optimisation and assays

In order to be able to apply different conditions in the solubilisation steps and assess their outcomes, a large amount of starting material in the form of mixed membrane protein preparation was necessary. HEK293 cells were grown in 18 T75 flasks and transfected using the calcium phosphate precipitation method to overexpress hRyR2 channels (as described in Chapter 2). The cells were imaged prior to harvesting and although the confluency of cells were slightly variable, the transfection efficiency was relatively good ( $58 \pm 9\%$ ; n=6 flasks) as shown in **Fig. 3.2 A-D**. The total number of cells harvested after transfection was 291 million which were then lysed and homogenised to produce a mixed membrane preparation. The combined protein yield was 19.32 mg at a concentration of 3.32 mg/ml and was the starting material for a series of experiments aimed at optimisation of the RyR2 purification process.

### 3.4.2 Finding the ideal detergent concentration for recombinant hRyR2 solubilisation

The detergent-lipid combination of CHAPS and L- $\alpha$ -phosphatidylcholine (PC) sourced from soybean (Avanti, Alabaster, USA) has been found to be particularly suitable for solubilisation of RyR from both native and recombinant sources.

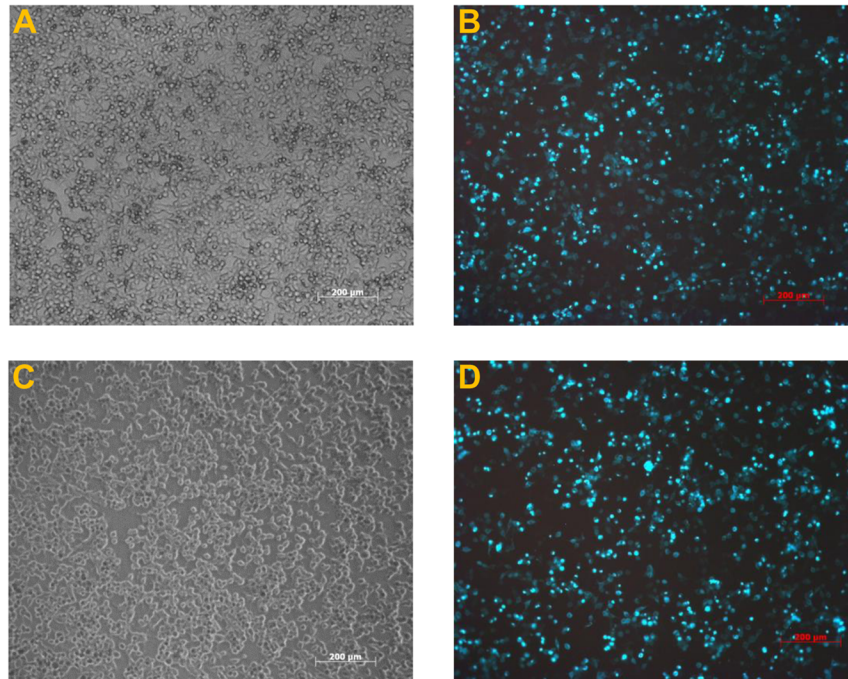


**Figure 3.2. Figures A-D showing bright field and fluorescent images of HEK293 cells transfected by e-GFP tagged hRyR2 gene.** In A, the culture is more confluent (~90%) than in B (~60%) but the eventual efficiency of transfection shown by eGFP fluorescence in B and D respectively are similar (~65%).

The concentration of detergent used plays a crucial role in determining if the protein will be adequately extracted from the membranes and excess detergent could lead to denaturation of the channel protein. The amount of detergent needed for optimal protein extraction depends on the critical micellar concentration (CMC), aggregation number, temperature and nature of the membrane and the detergent (le Maire et al. 2000; Lichtenberg et al. 2013). The CMC for the zwitterionic detergent CHAPS ranges from 0.3-0.6% (w/v) but various concentrations have been used for solubilising RyR in previous studies (0.5%: (Sitsapesan and Williams 1994a); 1%: (Du 1998); 1.5%: (S. R. W. Chen et al. 1997b)). However, as no previously published studies were available for recombinant human RyR2 channels, the concentration of CHAPS used in the lab to solubilise the channel protein was 0.4%, which was not the optimal amount. This study therefore used a range of detergent concentrations to solubilise the same amount of

protein to ascertain the optimal conditions for the purification of recombinant hRyR2 channels expressed in HEK293 cells.

The mixed membrane (microsomal) preparation was solubilised at a protein concentration of 2mg/ml using 0.2%, 0.4%, 0.6%, 0.8% and 1% (w/v) CHAPS along with 0.2% (w/v) PC. The solubilisation base buffer was made up using 1M NaCl, 0.15 mM CaCl<sub>2</sub>, 0.1 mM EGTA and 25 mM PIPES along with 1: 1000 PI cocktail at pH 7.4 to which appropriate amounts of CHAPS-PC were added. The microsomal preparation was solubilised on ice for 1 hour with constant stirring after which the samples were spun at 110,000g in an Optima TLX ultracentrifuge (TLA-100.4 rotor, Beckman Coulter) for 1 hour at 4°C. The soluble RyR2 channel protein should be retained in the supernatant while the insoluble materials forming the pellet are usually discarded. The supernatant was aliquoted in tubes containing cryoprotective 250 mM sucrose solution (0.4 M sucrose and 20 mM HEPES; pH 7.4) with 1:1000 PI cocktail and snap frozen in liquid nitrogen to be stored at -80°C until needed. The pellets were not discarded in this instance and were re-suspended in 250 mM sucrose solution (with PI cocktail) made up using solubilisation base buffer (without CHAPS-PC) and stored at -80°C.

#### 3.4.2.1 Testing the outcome of the solubilisation process

The amounts of solubilised protein present in the supernatant fractions were measured using the micro BCA method (**Chapter 2**) and the results are shown in **Fig 3.3**. The amount of soluble protein present in the supernatant samples showed a rising trend with increasing detergent concentration, which was expected as higher amounts of CHAPS, should facilitate solubilisation.

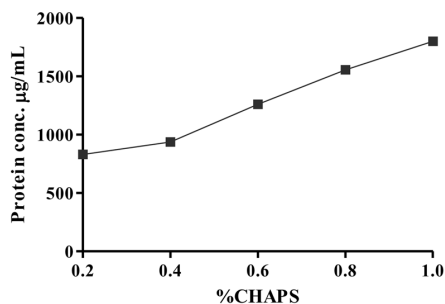


**Figure 3.3. Protein assay of supernatant samples from solubilisations using different concentrations of CHAPS.** The black squares show that the amount of protein released by solubilisation increases with increasing CHAPS concentration. The protein concentration in each sample solubilised was 2mg/ml.

A tritium-labelled ryanodine ( $[^3\text{H}]$ ryanodine) binding assay (see **Chapter 2** for detailed protocols) was carried out on supernatant samples obtained from these solubilisations, such that the level of functional RyR2 could be quantified. The reactions contained 100  $\mu\text{g}$  of protein from each solubilisation and the RyR2 channels present were activated using 100  $\mu\text{M}$  free  $\text{Ca}^{2+}$  present in the binding buffer. **Fig. 3.4** shows the specific binding of the protein samples solubilised using different detergent concentrations. The amount of RyR2 channels appeared to be lower at 0.2% and 1% CHAPS concentrations which probably are as a result of incomplete solubilisation and channel protein denaturation respectively.

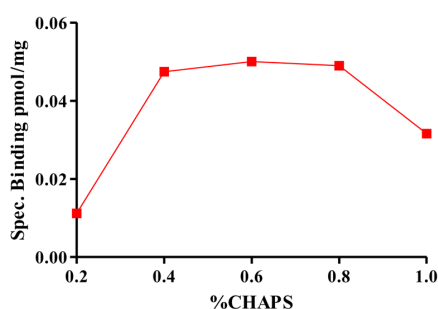


**Figure 3.4.** The graph shows the results of  $[^3\text{H}]$ ryanodine binding assays on the various samples of solubilised protein (supernatants) at different concentrations of CHAPS. The red squares show specific binding levels of  $[^3\text{H}]$ ryanodine as a measure of hRyR2 activity. This was higher at 0.4-0.8% CHAPS range.

The next step was to ascertain if the of RyR2 channels were functionally intact and could exhibit gating after incorporation into planar lipid bilayers (see **Chapter 2** for detailed methods). For this, the supernatant samples solubilised with 0.4%, 0.6% and 0.8% CHAPS were tested as they had the highest readings from the  $[^3\text{H}]$ ryanodine binding assays. Numerous small conductance channels incorporated (possibly  $\text{Cl}^-$  and  $\text{K}^+$  channels) within a minute after addition of 2  $\mu\text{l}$  of the 0.4% CHAPS solubilised sample but no RyR2 channel activity was noted even after 10 minutes (see **Fig 3.5A** for a representative trace). This process was repeated in four additional experiments with up to 8  $\mu\text{l}$  of sample added to the cis chamber but no RyR2 channel activity was seen. RyR2 channel activity was seen in only two out of five experiments with the 0.6% CHAPS solubilised sample within 3 minutes of addition of 4  $\mu\text{l}$  of prep. However, the baseline current level was ‘junky’ (distorted) and could be as a result of incorporation of protein fragments into the bilayer that are not ion channels (**Fig. 3.5B**). The 0.8% CHAPS

solubilised sample was used in two experiments where up to 10  $\mu\text{l}$  of prep was added and no channel activity was noted after 10 min of wait along with constant stirring of the *cis* chamber to facilitate channel incorporation. The presence of a large amount of smaller channels (e.g.  $\text{Cl}^-$ ,  $\text{K}^+$  etc.) and protein debris is a concern but can be easily remedied by using sucrose density gradient ultracentrifugation to purify the RyR2 channel protein based on its large size. However, the major issue is the lack of sufficient amount of RyR2 in the samples after the solubilisation process for conducting feasible single channel experiments and the further inevitable loss of a portion of channel protein during purification process, compounds this problem.

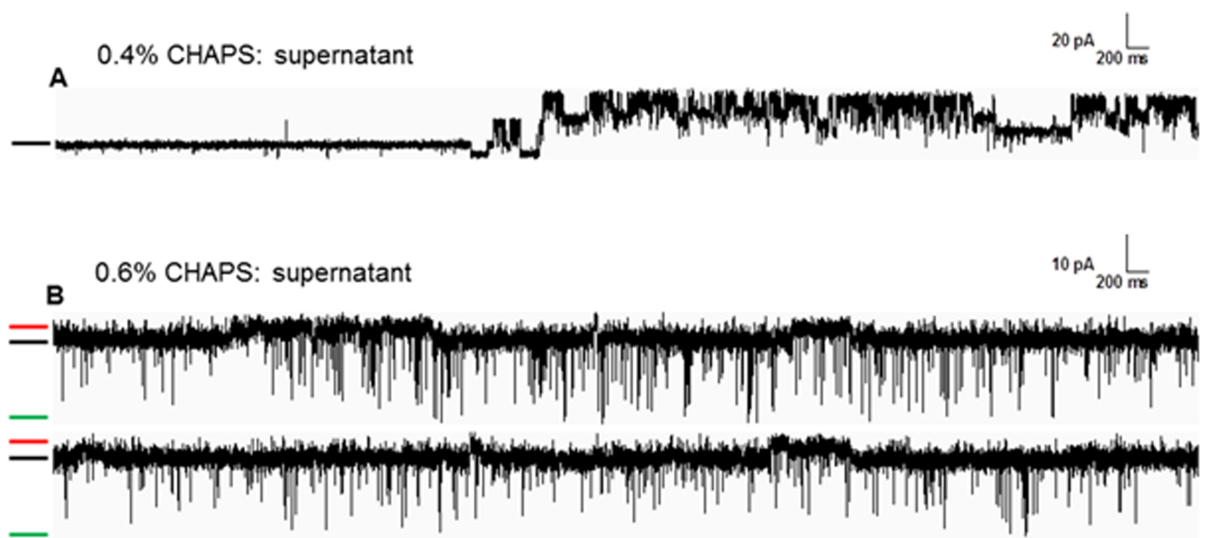


**Figure 3.5.** A and B shows representative single channel traces when supernatant samples obtained using 0.4 and 0.6% CHAPS respectively were tested. When 0.4% CHAPS solubilised sample was added, simultaneous incorporation of numerous small conductance  $\text{K}^+$  channels (? TRIC) were seen instead of hRyR2 (A). The black bar denotes the closed level from which the openings are seen. Trace B shows the incorporation of a single hRyR2 in the bilayer from the 0.6% CHAPS solubilised supernatant sample along with a  $\text{Cl}^-$  channel as contaminant, distorting the baseline current level. The black bar depicts the baseline from which RyR2 channel openings are downward deflections to the fully open level shown by green bar. The red bars show the open level of the  $\text{Cl}^-$  channel. The experiments were done with symmetrical 210 mM KCl solutions at +30 mV holding potential (see Chapter 2 for details).

### 3.4.3 Looking for the missing RyR2 after solubilisation: an unlikely location

From the assays it was evident that a major portion of the RyR2 protein was being lost during the process of solubilisation, irrespective of the concentration of detergent used. There are two possible reasons for this outcome: 1) majority of the channel protein resides in the pellet and not the supernatant obtained after post-solubilisation spin or 2)

The RyR2 channels are being degraded during the solubilisation process. The pellet samples obtained previously for the different concentrations of CHAPS were assayed for their protein concentration (**Fig. 3.6**). The amounts of protein that were sedimented in the pellets showed a decreasing trend with increasing CHAPS concentration, which complements the results obtained for the supernatant samples (**Fig. 3.3**).

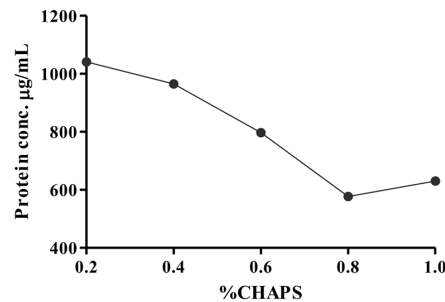


**Figure 3.6. Protein assay of pellet samples obtained after solubilisation using different CHAPS concentrations.** The pellet samples show decreasing protein levels with increasing CHAPS concentrations (black circles), roughly complementing the levels seen in the supernatants. The highly compact nature of the pellets obtained after solubilisation prevented their adequate re-suspension and may lead to slight errors in estimations.

[<sup>3</sup>H]ryanodine binding assays were done on the pellets using the same method as that of the supernatant samples (**Fig. 3.7**). The amounts of RyR2 present in the pellet samples were found to be ~ 20 fold more than those in the corresponding supernatant samples. This result was surprising as RyR2 was expected to be a completely soluble protein and present in the supernatant fraction after centrifugation instead of being pelleted.

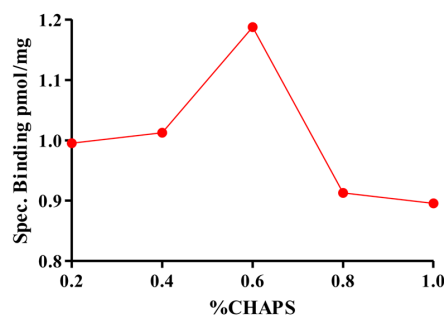


**Figure 3.7. [<sup>3</sup>H]ryanodine binding assay of the pellet samples obtained after solubilisation using different levels of CHAPS.** The red circles show hRyR2 channel activity in the form of specific binding where 0.6% CHAPS results in the highest amount of active channels in the pellet.



The 0.6% pellet sample (highest reading in binding assay) was tested in lipid bilayer experiments where single RyR2 channel activity was seen within 30 seconds of addition of 2  $\mu$ l of prep to the cis chamber and no  $K^+/Cl^-$  channel activity was observed (see trace in **Fig. 3.8**). This was repeated in four more experiments where channel incorporation was observed each time confirming the presence of adequate amounts of functional channels in the pellet samples.



**Figure 3.8.** A representative single channel trace showing hRyR2 activity from 0.6% CHAPS solubilised pellet sample. RyR2 single channel activity was seen without any distortion of current levels due to incorporation of other types of channels. The closed and the open levels are shown by black and green bars respectively. The recording was done at 0 mV with a *cis* to *trans*  $K^+$  gradient where the channel is being activated by contaminant  $Ca^{2+}$  present in KCl (see Chapter 2 for detailed methods).

This unexpected phenomenon was further verified by running the supernatant and pellet samples on a gel (SDS-PAGE) and then Western blotting to detect RyR2 (see **Chapter 2** for detailed methods). The sample volumes were at first reduced by  $\sim 5.5$  times using a vacuum concentrator (SpeedVac<sup>TM</sup>, Thermo Scientific) to increase the protein concentration such that volumes containing 100  $\mu$ g of protein could be loaded on each lane of the gel. The Western blot in **Fig. 3.9** show that the RyR2 present in the supernatants (for all detergent concentrations) were not high enough to be detected by the antibody but the pellet samples had sufficient amounts channel protein.

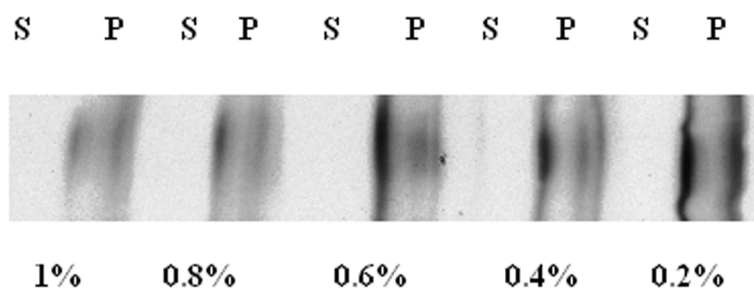


**Figure 3.9. Western blot of eGFP-tagged hRyR2 from 0.2-1% CHAPS solubilised samples.** S and P mark the lanes for supernatant and pellet samples respectively. The amounts of RyR2 protein present in the supernatant samples were not high enough to be detected.

Also, the level of RyR2 detected for 1% CHAPS pellet sample was the lowest by visual inspection and this corroborates the radiolabelled ryanodine binding data (**Fig. 3.7**). The protein samples obtained after volume reduction using vacuum concentrator had turned viscous probably due to the 250 mM sucrose previously added as a cyroprotective agent before storing the samples at  $-80^{\circ}\text{C}$ . The samples were not homogeneously dispersed in the loading buffer and resulted in the loaded samples not running as distinct horizontal bands on the gels as is usual in a typical Western blot. Because of this, accurate densitometric evaluation of the bands obtained in the Western Blot for comparison of the amount of protein obtained in different pellet fractions was not possible. Quantity One software (Bio-Rad) was nevertheless used for obtaining empirical values of the relative band intensities due to the various pellet samples (**Fig. 3.10**).

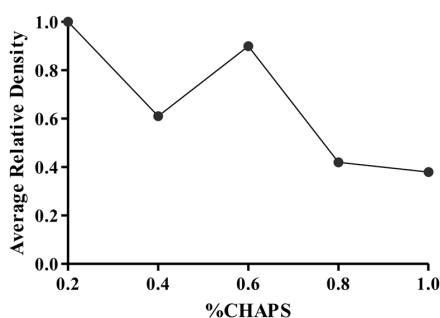


**Figure 3.10. A densitometric evaluation of the levels of hRyR2 protein detected in the pellet samples by the Western blot.** The data seems to qualitatively agree with the findings in [ $^3\text{H}$ ]ryanodine binding assay (**Fig 3.7**) except at 0.2% CHAPS where it's unusually high. This may be partly due to high amounts of sucrose present in the loaded sample leading to an anomalous gel run or non-specific binding of antibodies.

### 3.4.4 Increasing the yield of purified RyR2: preventing protein loss from supernatant

This study suggests that RyR is probably not a completely soluble protein and some parts of this massive-sized channel might be inherently insoluble, thereby preventing most of it from remaining in the supernatant fraction after centrifugation at 110,000 g. Although the exact reason for this phenomenon is interesting and demands further investigation, it's beyond the scope of my current study which focusses on understanding the nature of gating of the purified channel. Therefore, the immediate aim was to find a way to retain most of the RyR2 protein in the supernatant for achieving higher yields of purified channels and successful single channel experiments.

The mixed membrane microsomal preparation was again solubilised at 2mg/ml, this time only using 0.6% CHAPS as the highest total ryanodine binding value (supernatant + pellet; **Figs. 3.4 & 3.7**) was obtained at this detergent concentration. To prevent the loss of RyR2 protein in the pellet, post-solubilisation centrifugation speed was reduced from usual speed of 110,000 g in the Optima TLX ultracentrifuge (Beckman Coulter) to 15,000 g, while all other conditions were unchanged. The protein assay and subsequent [<sup>3</sup>H]ryanodine binding assay results are shown in **Fig. 3.11A** and **B** respectively. The low speed spin resulted in more than two-thirds of the RyR2 protein being retained in the supernatant and this translated into higher probabilities of channel incorporation during single channel experiments (see Discussion).

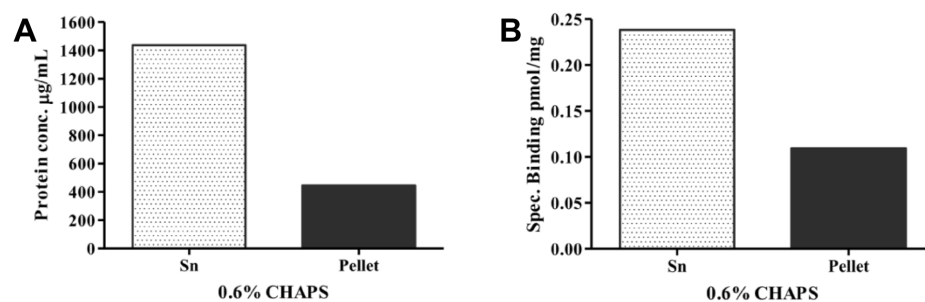


**Figure 3.11. Protein and [<sup>3</sup>H]ryanodine binding assay results after solubilisation using 0.6% CHAPS followed by low speed centrifugation at 15,000 g.** (A) shows the protein concentrations in the supernatant (Sn) and Pellet fractions after the low speed spin. (B) shows that major fraction of hRyR2 protein was retained in the supernatant (Sn).

As the mixed membrane preparation was already a month old during this final assay and its aliquots had been thawed and re-frozen once before for the previous solubilisations

and assays, the total amount of functional channels (supernatant + pellet) appeared to be reduced (see **Figures 3.4 & 3.7**) probably due to protein degradation as might've been expected. Although other cellular proteins along with RyR are likely to be present in the supernatant, the sucrose gradient ultracentrifugation step should effectively separate the RyR2 based on its significantly larger size and result in a relatively purified protein sample.

As mentioned earlier, native sources of RyR (from animal tissues) yield far greater amounts of channels than recombinant expression systems. For this reason, a rabbit skeletal muscle heavy SR preparation containing RyR1 was used for testing the efficacy of the newly optimised conditions for solubilisation. The higher channel density should generate data plots showing stark differences in RyR2 content in the pellets and supernatants when the low and high speeds are compared. Using the methods described above, 40 grams of skeletal muscle generated a total of 22.6 mg of protein in the form of heavy SR preparation (2.83 mg/ml). Increasing amounts of protein (0, 25, 50, 100 and 200  $\mu\text{g}$ ) were used in [ $^3\text{H}$ ]ryanodine binding assay to quantify RyR1 activity (**Fig. 3.12**). The calculated average specific activity was  $4.375 \pm 0.15$  pmol/mg of sample (n=4), which was much higher compared to that obtained from the HEK293 cells ( $\sim 0.9$  pmol/mg in unsolubilised mixed membrane preparation).

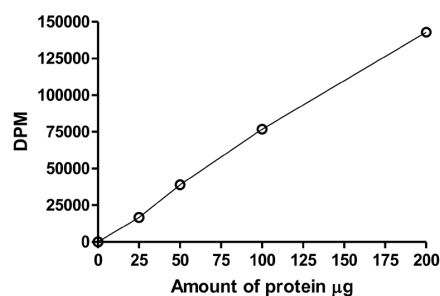


**Figure 3.12. [ $^3\text{H}$ ]ryanodine binding assay to quantify the activity of rabbit skeletal RyR1 in heavy SR fraction.** There is a proportional increase in binding (disintegrations/min) with increasing amounts of prep used in the assay. The average specific activity was calculated to be  $4.375 \pm 0.15$  pmol/mg (n=4) of heavy SR fraction.

Solubilisation using 0.6% CHAPS was carried out (in duplicate) on the heavy SR prep as before and resulting two samples were spun at 16,000 g and 110,000 g and their outcomes were compared using the [ $^3\text{H}$ ]ryanodine binding assay. As expected, the maximum counts of channel activity were detected in the supernatant from the low-speed

spin and the pellet from the high speed spin as shown in **Fig. 3.13** confirming the previous observations that suggest that the RyR is not a completely soluble protein.

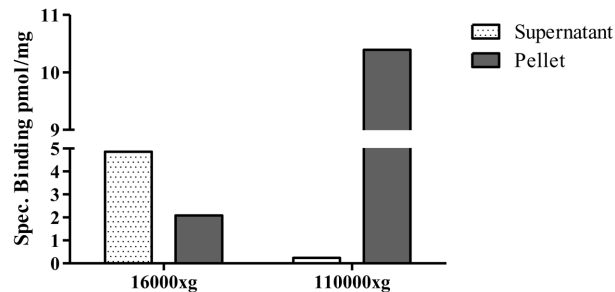


**Figure 3.13. Comparison of amount of RyR1 activity between supernatant and pellet fractions at low (16,000g) and high-speed (110,000 g) centrifugation post solubilisation.** The bar graphs confirm the previous finding in the case of hRyR2 above that high-speed centrifugation results in the majority of the solubilised RyR protein to be retained in the pellet which is partially rescued by lowering the speed to 16,000 g.

The supernatant obtained from the low speed spin was purified using sucrose density gradient ultracentrifugation (**Chapter 2**) and the different fractions obtained at various sucrose densities were tested on planar lipid bilayers for channel activity. Numerous RyR1 channels were simultaneously incorporated into the bilayer within a minute of addition of 2  $\mu$ l of protein fraction obtained at 26% sucrose density as expected (**see Chapter 2**) and there were no  $\text{Cl}^-$  or  $\text{K}^+$  channel activity observed (**Fig. 3.14**). The optimisation exercise was therefore successful in unravelling the reason behind suboptimal yield of purified recombinant hRyR2 channels, resulting in changes in the solubilisation protocol to remedy the issues.



**Figure 3.14. Representative single channel current trace showing rabbit skeletal RyR1 activity.** High density of purified RyR1 obtained from solubilisation 0.6% CHAPS followed by low speed centrifugation allowed for simultaneous incorporation of multiple RyR1 channels (at least 6 channels are seen in the trace). The black bar marks the level where all channels are closed and green bars denote each open level. The experiments were conducted at 0 mV holding potential and a *cis* to *trans* K<sup>+</sup> gradient.

### 3.4.5 Recombinant hRyR2 and endogenous FKBP12.0 in HEK293 cells: do they interact?

The interaction between RyR2 and FKBP12.6 in cardiomyocytes is well established but there have been some recent reports of the channel's interaction with FKBP12 (Galfré et al. 2012), which is better known for its interaction with the skeletal isoform (RyR1). The aim of the following experiments was to ascertain if recombinantly expressed hRyR2 interacts with the endogenously expressed FKBP12 in HEK293 cells and whether it plays any role in modifying channel gating when mixed membrane microsomal preparations are used in single channel experiments. HEK293 cells do not endogenously express RyR2, FKBP12.6 or any of the luminal accessory proteins seen in myocytes (S. R. Chen et al. 1997a; Xiao 2004; Stewart et al. 2008).

Two cellular sources were used for the mixed membrane microsomal preparations: 1) HEK293 cells stably expressing FKBP12.6 protein along with endogenous FKBP12 (cells were provided by Dr. N.L Thomas) and 2) FKBP12.6 expressing stable HEK293 cells that were co-transfected with eGFP-tagged WT hRyR2 cDNA (see **Chapter 2** for methods). The last step of the mixed membrane preparation involves a high-speed spin that results in the pelleting of the membrane fraction containing proteins (e.g. ion

channels) that are membrane-bound while the supernatant is formed by the already soluble cytosolic proteins. In this study, both the pellet and the membrane fractions were retained for analysis using a SDS-PAGE and Western blots (see **Chapter 2**).

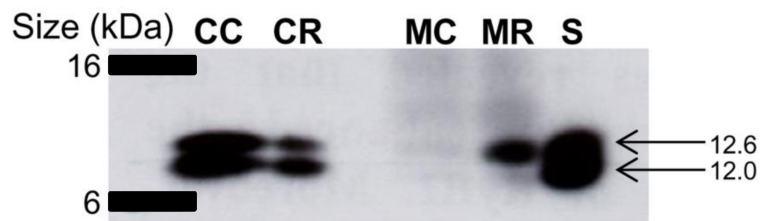


**Figure 3.15. The Western blot showing the putative interaction of FKBP with hRyR2 in HEK293 cells.** CC and MC are cytosolic and membrane fractions respectively from HEK293 cells stably expressing FKBP12.6 along with endogenous FKBP12.0. The lack of RyR2 results in both FKBP12.6 and FKBP12.0 being retained in the cytosolic fraction (CC). CR and MR are the cytosolic and membrane fractions from the above cells which were additionally transfected to express recombinant hRyR2. The presence of RyR2 and its interaction with FKBP12.6 results in the latter being present in the membrane fraction (MR). The absence of FKBP12.0 in MR suggests that it probably doesn't interact with recombinant hRyR2 in HEK293 cells. The ladder is marked corresponding to 16 and 6 kDa size. Lane S is a protein sample known to contain both the FKBP12.6 and FKBP12.0 and serves as a positive control for the other lanes.

**Fig. 3.15** shows the Western blot of the membrane and cytosolic fractions from the two types of cells. CC and MC depict the cytosolic and membrane fractions respectively from the control cells (HEK293 cells stably expressing FKBP12.6 protein along with endogenous FKBP12). As both FKBP12 and 12.6 are cytosolic proteins, they are present in the cytosolic fraction CC as expected but as there are no RyR2s present in the cells to interact with, the membrane fractions are devoid of both FKBP12 and 12.6 (lane MC). CR and MR represent the cytosolic and membrane fractions obtained from the control cells that were co-transfected with hRyR2. In other words, the intracellular membranes had RyR2 available to interact with FKBP12 and 12.6. As before, both the FKBP12 and 12.6 were present in the cytosolic fraction (CR) but only FKBP12.6 was detected in the membrane fraction MR. This suggests that hRyR2 can interact with FKBP12.6 and pull it down in the membrane fraction (pellet) but not with endogenously expressed FKBP12 in HEK293 cells. However, this may not be the case in native cardiomyocytes where the levels of FKBP12 are much higher than those of 12.6, although the former has a lower affinity for RyR2 (Timerman et al. 1996; Guo et al. 2010). Therefore, mixed membrane microsomal preparations from HEK293 cells with recombinantly expressed hRyR2 are free of FKBP12/12.6 interactions (See **Section 5.5**, p. 152).

### 3.5 Discussion

The steps involved in the solubilisation process were systematically dissected in order to understand the reasons behind sub-optimal yield of purified hRyR2 for single channel experiments. A CHAPS concentration of 0.6% in the solubilisation buffer was found to be ideal for mixed membrane microsomal preparation from HEK293 cells containing hRyR2, releasing adequate amounts of protein from the cellular membranes while avoiding denaturation at higher detergent levels. However, a major portion of the 'solubilised' RyR2 protein was still being lost with the high-speed centrifugation at the end of the process at 110,000 g. This was an unexpected finding as unlike other membrane proteins and ion channels, RyR even when freed by detergent solubilisation from the cellular membranes was still not a completely soluble entity. The tendency of the channel to come out of the supernatant during centrifugation may be due to the insoluble nature of some exposed domains of the protein which result in aggregation of the protein and its appearance in the pellet fraction. A high-speed spin after solubilisation is routinely employed during the process of purification of RyR from native heavy SR membranes obtained from animal tissues and seems to pose no problems with channel yield as previous studies have shown (Anderson et al. 1989). The very high density of RyR present in heavy SR preparations from native sources ensures a reasonably good presence of channels in the supernatant even after most of them have been pelleted (0.25 pmol/mg in **Fig. 3.13**). In comparison, the starting density of recombinantly expressed RyR is much lower and when the major portion of it is discarded in the pellet after the high-speed spin, the single channel experiments become unfeasible.

Using the low speed spin at 15,000 g after solubilisation of the mixed membrane preparation ensures that the major portion of the RyR2 protein is retained in the supernatant, which could then be purified using a sucrose density gradient centrifugation. The high yield of purified hRyR2 obtained using this optimised technique has been successfully implemented in all subsequent studies done in our lab (Mukherjee et al. 2012; Euden et al. 2013; Zissimopoulos et al. 2013; Mukherjee et al. 2014) including the ones presented as a part this thesis. In a previous study, the use of CHAPS at 1% (w/v) to solubilise native RyR2 was shown to abolish very high (~10-15 mM)  $[Ca^{2+}]_{cyt}$  induced channel inhibition (Laver et al. 1995) but as this is not a physiologically relevant  $[Ca^{2+}]_{cyt}$  range in the cardiomyocyte, it was not considered in this study (range of nominally zero to 500  $\mu$ M).



It is also useful to review the post solubilisation centrifugation speeds used by other studies that have used recombinant purified RyR channels expressed in HEK293 cells for comparison. The only other group that has extensively used purified recombinant RyR channels expressed in HEK293 cells (animal isoforms) in single channel experiments is Dr S.R Wayne Chen's lab in the University of Calgary, Canada. Their early work on  $\text{Ca}^{2+}$  sensitivity of mouse recombinant single RyR2 channels (P. Li and S. R. Chen 2001) uses the high-speed (~100,000g) post-solubilisation centrifugation, the protocols for which were established in their previously published studies (S. R. W. Chen et al. 1997b; Zhao et al. 1999). Their subsequent studies have since then referred to (P. Li and S. R. Chen 2001) for the solubilisation process (Masumiya et al. 2001; D. Jiang 2002; D. Jiang et al. 2004). However, in the supplementary information associated with (D. Jiang et al. 2004), a low speed centrifugation at 16,000g is mentioned. This was a surprising finding as the main text of the article still refers to (P. Li and S. R. Chen 2001) for the solubilisation protocols (using the high-speed spin). Nevertheless, the reason for this abrupt switchover by this group from high to low speed centrifugation was not elaborated upon in any of their published studies and no data was provided to support this change in protocol. All studies emanating from that group have since used 16,000g speeds (30 min at 4°C) for the preparation of solubilised lysate (D. Jiang et al. 2007; Y. Liu et al. 2013; W. Chen et al. 2014).

Although the optimisation steps in this study have corrected the problem of suboptimal yield of purified channels, the exact reason underlying the anomalous solubility of detergent solubilised RyR still remains unknown. Further investigations, such as examining channels in supernatant and pellet fractions using cryo-EM for visualisation of the actual physical state of the channel molecules might assist in our understanding of the nature of the problem.

## **Chapter 4.0**

**Improving the accuracy of RyR2 single channel data analysis  
using HMM based programs**

## 4.1 Introduction

The precise control of ion permeation through the channel pore is critical for normal functioning of the cell and organ systems. There are definite structural elements in the channel pore known as ‘gates’ that act as intermittent barriers to the flow of ions- a process known as gating. The function of ion channels has been studied in terms of the behaviour of these gates (gating kinetics), which can be quantified by single channel experiments. The incorporation of RyRs in planar lipid bilayers in order to examine the gating of individual channels is the only method of studying, in real-time, the dynamics of a single channel molecule.

However, it was found that the gating behaviour of any single ion channel was not deterministic: it varied randomly over time even when the experimental conditions remained unchanged. RyR gating like many other processes including radioactive decay, Brownian motion, stock market fluctuations etc., is a stochastic process that can only be described in probabilistic terms. The foundations of single channel analysis lie in the robust application of probability theory and statistics: (Colquhoun and Hawkes 1977; Colquhoun and Hawkes 1981) and (Colquhoun and Sigworth 1995).

### 4.1.1 The key criterion: a memoryless system

During the process of state transition, the ion channel passes through numerous conformations that involve the stretching and bending of a vast number of chemical bonds within the protein molecule. This happens until at some point the channel finds itself in a conformation that is very close to the transition state and flips from one state to another by crossing the energy barrier. These bending and stretching events around bonds are so numerous that the channel does not ‘remember’ a particular sequence of such events that has led to a conformational pathway for that state transition. Thus ion channel gating can be modelled as a memoryless *Markov* process in which the state transitions between conformations are independent of the previous history of the system and depend only on the present state the channel is in. Single channel data can therefore be analysed via Markov modelling to unravel underlying gating mechanisms.

#### 4.1.2 Optimisation of single channel data: approaches

It is essential to know the amplitude of a single channel event and the amount of time the channel spends at that amplitude level, known as the *dwell time*. So for a channel like WT (wild type) RyR2 which opens to only one conductance level, the ideal trace would consist of a sequence of dwell time intervals with an amplitude of 0 pA (corresponding to the closed level) and another series of dwell times corresponding to the open state. Generating a train of such closed and open events from the raw single channel data trace is known as *Idealisation* and is the first step of data analysis. The detection and characterisation of single channel events is made difficult by the presence electronic noise along with the actual data signal. Although shielding of the experimental set-up inside a Faraday cage and low-pass filtering improves the signal-to-noise ratio (SNR) to some extent, (see **Chapter 2**) the accurate resolution of actual gating events from the raw trace still poses a significant challenge. One can approach this problem in various different ways and each of the techniques has its own advantages and caveats.

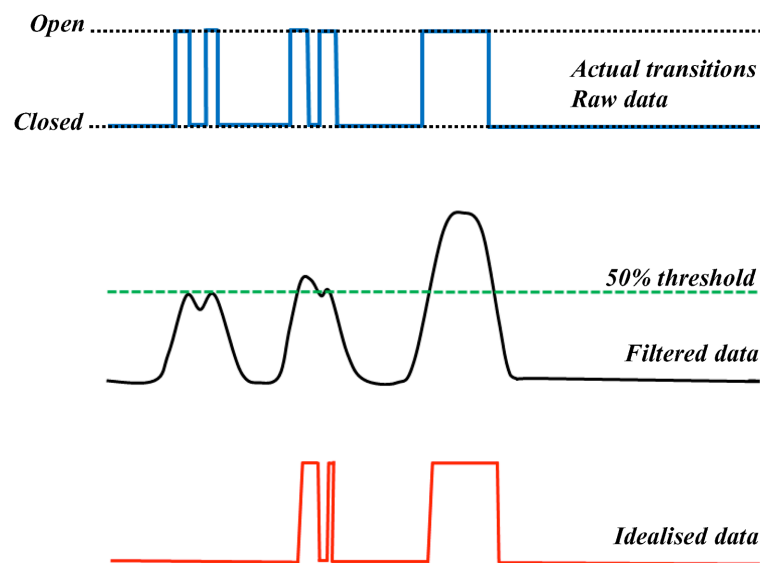


**Figure 4.1. Principle behind the 50% threshold crossing method.** This schematic shows the actual data drawn in blue where the closed and open current levels are shown using black dashed lines. After applying a low-pass filter, the brief opening events are further attenuated and the half-amplitude line (green, dashed) fails to pass through all the data points. The idealised data is drawn in red and shows that the first two brief opening events are missed as they no longer reach the fully open level after filtering. Diagram adapted from (Colquhoun and Hawkes 1995).

#### 4.1.2.1 Threshold-crossing method

In this method of analysis an event is detected when the current deflection (due to channel opening) from the baseline (closed level) crosses a pre-set threshold value that is usually halfway (50%) between closed and open channel amplitudes (**Fig 4.1**). This method is fast but there are a few pitfalls:

- a) The threshold-crossing method cannot be used to detect events unambiguously if the data contains multiple open conductance levels.
- b) Brief events that do not reach the set threshold are missed, giving rise to an idealised data trace with loss of detail. As a rule of thumb, only events longer than 1.5 x rise time of the filter can be detected with sufficient accuracy.
- c) Baseline drift and unstable channel amplitudes if present in the single channel traces can give erroneous results using this method.

Although this method of optimisation of data can be quick and can also be automated, the validity of the fits to the data should be checked by visual inspection. Examples of these analysis programs are pClamp software (Molecular devices) and TAC (Bruxton).

#### 4.1.2.2 Time-course fitting method

Every single channel transition in the data trace is individually examined and each amplitude is fitted as seen on the screen. The experimentally determined step response function is used to fit the trace to estimate simultaneously both durations and amplitude. Although this method is considerably slower than the 50% threshold-crossing method, it's much more accurate. Brief events can be fitted accurately using time course fitting and it also provides better estimates of current amplitude than threshold-crossing. Also, as data are fitted as seen on screen, multiple single channel opening levels can be measured without ambiguity (**Fig 4.2**). The Single Channel ANalysis (SCAN) program written in the laboratory of David Colquhoun at UCL, London (<http://www.ucl.ac.uk/Pharmacology/dcpr95.html#scan>) is the only available software employing the time-course fitting method.

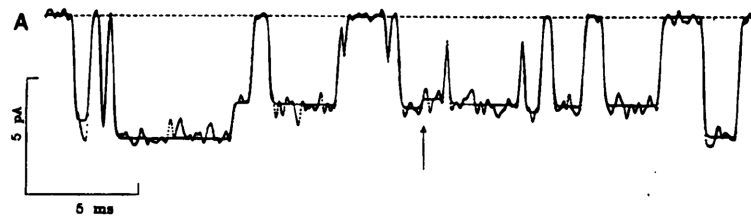


**Figure 4.2. Time-course fitting of single channel data.** The directly fitted idealised data (black lines) is overlaid on the single channel current time course where each event is fitted as observed (Colquhoun and Hawkes 1995) .

#### 4.1.2.3 Hidden Markov models (HMM)

HMM based analysis techniques have long been used in the field of digital signal processing where the goal is to extract the real signal from a set of imperfect measurements. It has found applications in such diverse areas as speech recognition, target tracking in defence systems and bioinformatics. A Markov model (Elliott et al. 1995) describes a dynamic process characterized by a finite number of discrete states where the actual biological signal is accompanied with extraneous noise. Only instantaneous transitions between states are possible, with the probability of transition proportional to a rate constant. When the state of the process cannot be observed or measured directly, except through another noisy variable, the Markov model is called *hidden* (Rabiner and Juang 1986; Juang and Rabiner 1991). HMMs are employed when the observations do not unambiguously show which state the system is in at any given moment.

By starting with a simple  $C \leftrightarrow O$  (closed-open state) gating scheme, the HMM based forward-backward, Baum-Welch and SKM algorithms can be used to accurately detect single channel data resulting in idealised traces. The visual inspection of an idealised data trace overlaid on the channel recording allows the verification of accurate event detection and correct assignment of state (closed, open). This method is inferior to the former method for channel traces with multiple subconductance levels. The QuB suite of analysis programs developed in SUNY, Buffalo, USA (<http://www.qub.buffalo.edu/>) uses HMM based algorithms for estimation of single channel kinetics, generating gating models and simulation of data using the models.

## 4.2 Key Objectives

After optimisation of the procedure for purification of recombinant hRyR2, the next step is to study the effect of ligands at the single channel level and to understand the mechanisms behind the changes in gating behaviour. A single channel data analysis technique that is both sensitive to the subtle changes in channel gating as well as fast enough to analyse thousands of events under different experimental conditions is essential. In this chapter, I will explain why some techniques of RyR2 single channel data analysis are better suited for my requirements than others and how various obstacles were overcome to arrive at an optimised technique that was ideal for my needs. In doing so, I will try to avoid, as far as possible, mathematical jargon but aim to convey the essential message that would be of use to the physiologist.

### 4.3 Experimental procedures

The single channel data used in the optimisation process was generated using the experimental protocols described in detail in the Methods section (**Chapter 2**). Two sets of data were used in this chapter to elucidate various the analytical steps: 1) channel with higher Po which was activated using  $1\mu\text{M} [\text{Ca}^{2+}]_{\text{cyt}}$  at +30 mV holding potential and 2) low Po channel under sub-activating  $[\text{Ca}^{2+}]_{\text{cyt}}$  (250 nM), also at +30 mV holding potential. The permeant ion was  $\text{K}^+$  from 210 mM symmetrical solutions (*cis/trans*).



## 4.4 Results

### 4.4.1 Data analysis using threshold-crossing method: drawbacks

Single channel data from previous studies on RyR2 looking at the effect of various ligands and biochemical processes on channel gating have been routinely analysed using half-amplitude (50%) threshold-crossing method (HATC) (Tester et al. 2007; Marjamaa et al. 2011). While it's a fast, user-friendly and hence popular technique, it does not provide the desired level of accuracy needed for further analysis and modelling of data to reveal mechanisms underlying channel gating in RyR2. This method was used for a preliminary analysis of single channel data from experiments where purified hRyR2 was progressively activated by increasing  $[Ca^{2+}]_{cyt}$ . The quality of event detection and accuracy of kinetic parameters like, open and closed times, open probability etc. at low and high  $[Ca^{2+}]_{cyt}$  were not satisfactory (**Figs. 4.3 A and C**). Brief opening events when  $P_o$  was low and shorter flicker closing events at higher  $P_o$  were particularly missed (**see section 4.4.3**). This would potentially result in erroneous fits of dwell-time histograms and incorrect reaction mechanisms.

### 4.4.2 Optimal technique for RyR2 single channel data analysis

The low quality of outcomes from single channel data analysis using HATC method engendered a search for a better approach to looking at my data. As mentioned earlier, time-course fitting of data using the SCAN program could give the most accurate results and the idealised trace should be the closest approximation of the original current trace. For an understanding of the fundamental concepts behind time-course fitting technique and single channel analysis in general, I attended the summer graduate course titled 'Understanding Ion Channel Currents In Terms Of Mechanisms' in July 2008. Prof. David Colquhoun and his colleagues run this course in UCL where SCAN and other associated software are being developed (<http://www.onemol.org.uk/>). Although this course proved invaluable in providing me with an understanding of how mechanistic information could be gleaned from single channel data, unfortunately I was not able to use time-course fitting technique for my work. The reasons for this were as follows: a) the data files from the acquisition software Acquire (Bruyton) were not compatible with the SCAN software. I was unable to retrieve the file formats from Bruyton and the developers of SCAN were unable to assist and b) time-course fitting requires visual inspection of every event in the trace for effective fitting of the data points. This is a very

slow process and in the proposed studies, a faster method was needed to utilise several thousand events over different ligand concentrations for building accurate gating models. HMM method of analysis is another approach to this problem and was found to be better suited for analysis of RyR2 single channel data.

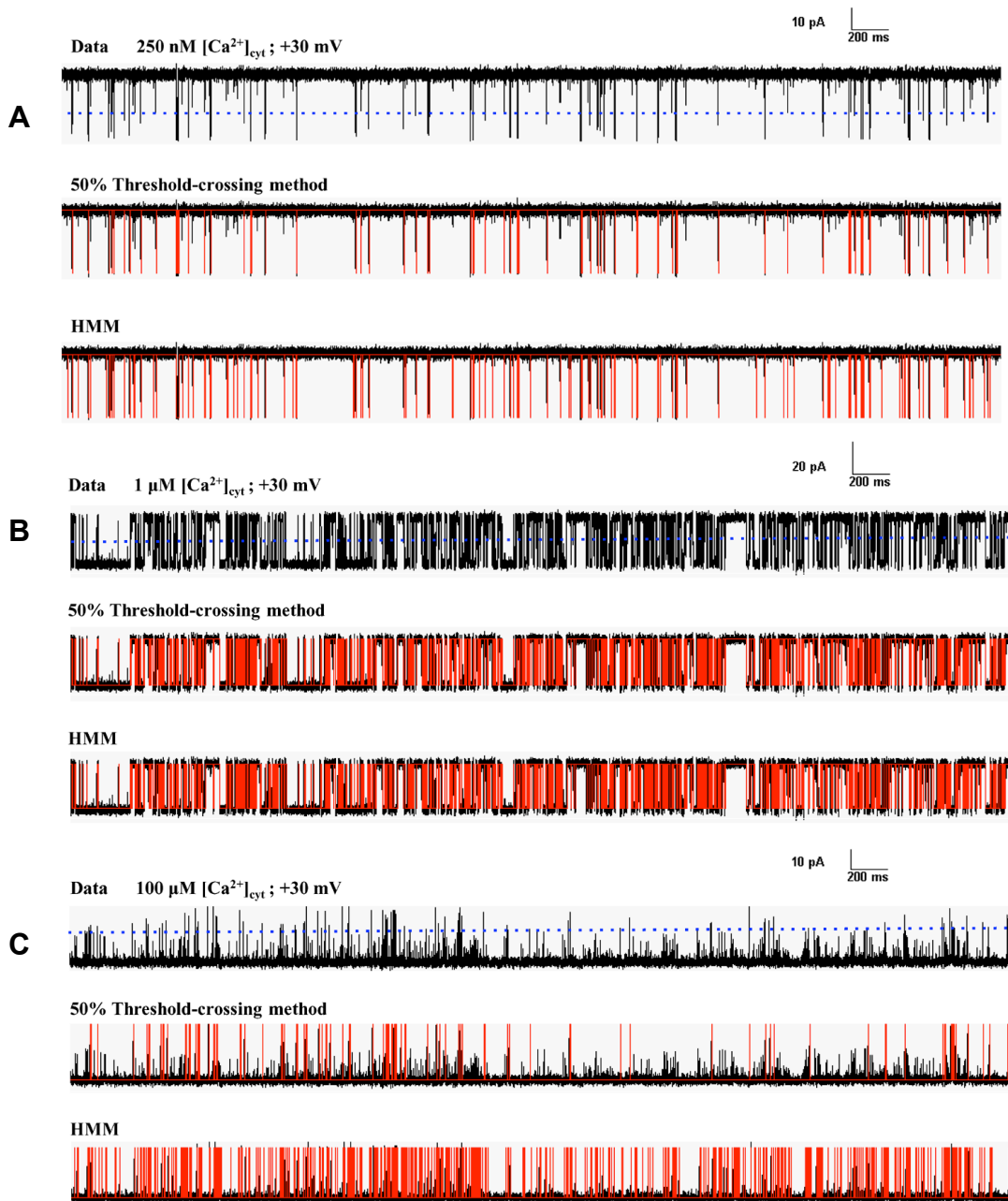


**Figure 4.3. Comparison of event detection using half-amplitude threshold crossing method and HMM.** Data recorded under low and high  $\text{Ca}^{2+}$  conditions when analysed using 50% threshold crossing resulted in many undetected brief events compared to HMM based analysis (A and C respectively). At intermediate  $[\text{Ca}^{2+}]_{\text{cyt}}$  (1  $\mu\text{M}$ ), both methods were equally effective as most events reached the full conductance level (B). In all data traces the openings are downward deflections from the baseline on top and the blue dotted line marks the half-amplitude level. See **Table 4.1** for kinetic parameters.

#### 4.4.3 HMM based analysis: QuB

The QuB suite of analysis programs use HMM based algorithms for detection of single channel events with the eventual aim of fitting kinetic mechanisms onto the data. The programs were written using Python, a powerful programming language that is compact, fast and easy to debug. Preliminary analyses were done on representative stretches of single channel data at various levels of channel activity (**Figs. 4.3 A, B and C**) and the results were compared with ones obtained using HATC method (**Table 4.1**). The superiority of HMM based analysis over HATC method is evident upon visual inspection of idealised traces (red) fitted on the actual data. Most of the brief opening and closing events that are missed by the HATC method when the channel activity is low and high respectively are correctly identified as events using the HMM method. This ensured that the majority of state transitions were accurately identified and that the gating model derived from the single channel data was an accurate representation of RyR2 behaviour.

**TABLE 4.1**

$[Ca^{2+}]_{cyt}$ /Method	Closed Events	Open events	Closed time (ms)	Open time (ms)	Open probability
250 nM/HATC#	78	77	38.72	0.45	0.0145
250nM/HMM	171	170	16.55	0.4	0.0264
1 $\mu$ M/HATC	479	478	3	2.15	0.4688
1 $\mu$ M/HMM	489	488	3	1.95	0.4757
100 $\mu$ M/HATC	102	103	0.2	17.2	0.9955
100 $\mu$ M/HMM	533	534	0.3	4.77	0.9600

# Half-Amplitude Threshold-crossing method

In the following sections I will highlight the sequence of steps required to reach a *mechanistic end-point* starting from raw single channel current traces and how each step was optimized for RyR2 data. A general overview of the whole process is necessary before each of the steps is described in detail. The sequential steps are shown in the form of a flowchart which will be followed through with the progression of this section (**Fig 4.4**). The raw single channel traces need to be “pre-processed” for the software to recognise the data files where artefacts on the traces are removed if present and homogeneity of data is ensured. The data are then idealised using appropriate algorithms

and various kinetic parameters are calculated. This generates a sequence of open and closed dwell-times that are then fitted with sums of exponentials based on a given kinetic scheme that is used by the HMM based MIL (maximum interval likelihood) program to optimize the rate constants of the transitions while simultaneously maximizing the likelihood of the fit. Once an appropriate kinetic scheme is attained, it should provide information about the various states and the transitions between them. The gating model should convey a mechanistic view of the transitions and is validated by running simulations using the kinetic schemes. The simulated data can be idealised and its kinetic parameters compared with those of the original data to verify if the model is an accurate description of the data.

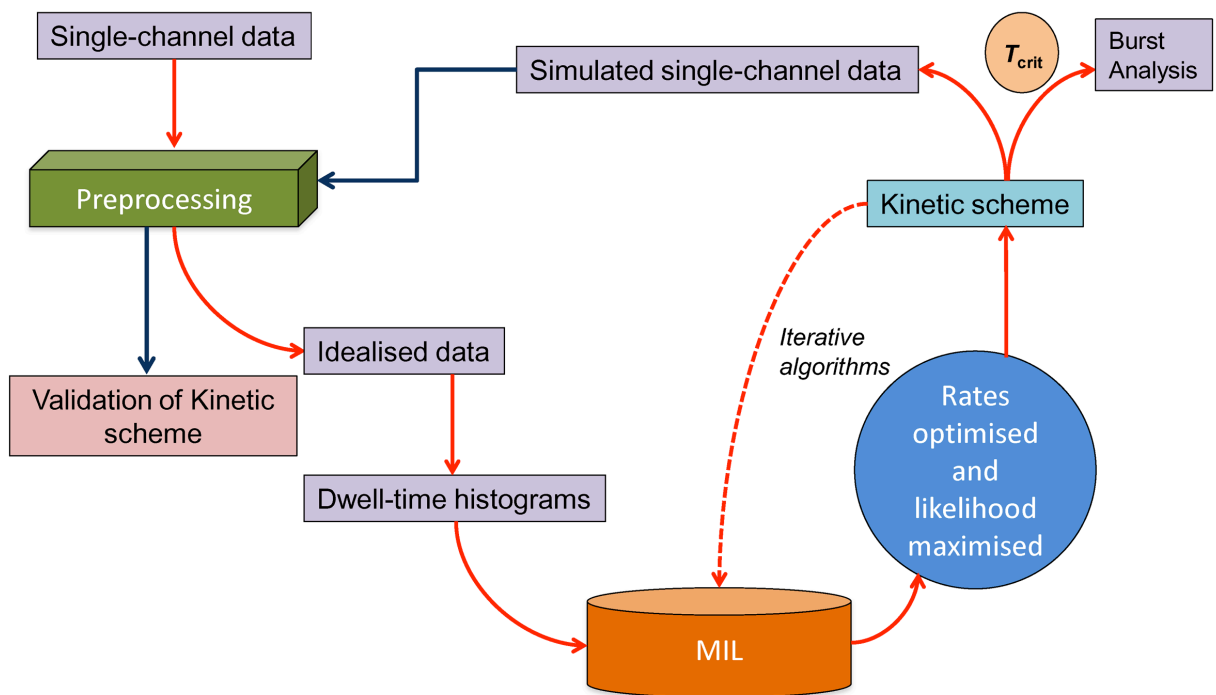
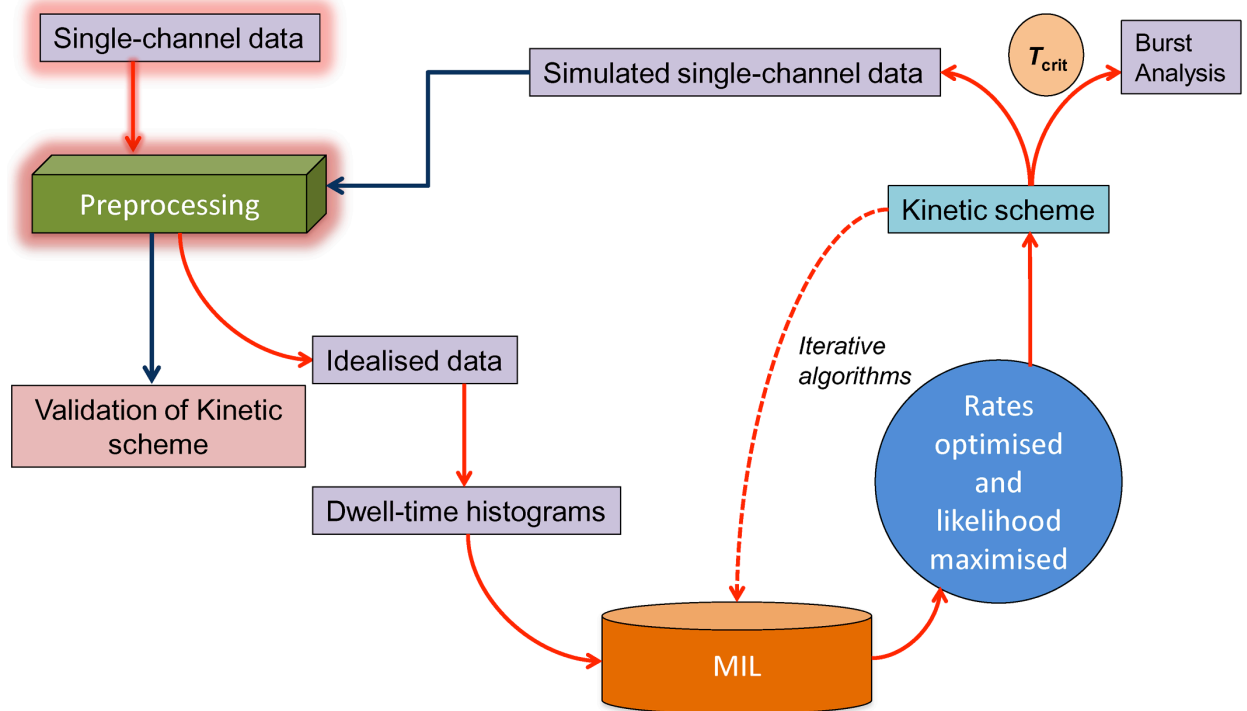


**Figure 4.4. A flowchart showing the sequential steps of the single channel analysis method.** This chart will be used to follow-through using highlights, in a logical sequence, the various steps of analysis as they are optimised and discussed in this chapter.



#### 4.4.4 Pre-processing of single channel data

Pre-processing involves getting the data ready for analysis using HMM based algorithms. The single channel data acquisition program Acquire (Bruxton) generated .acquire data files whose format was not recognized by the QuB analysis programs (v1.5.0.19). To overcome this problem, the .acquire files were first opened using another Bruxton program called Review and exported as ABF (Axon Binary Format) data files. The signal filtered at 5 kHz (analogue) before digitization was isolated and the appropriate sweep was selected using Clampfit 8 software (Axon Instruments) and saved as individual .abf files. These .abf files were then converted to QDFs (QuB data files) using custom software called ABFtoQDF written by the QuB programmers. The QuB suite version 1.5.0.19 was used to analyse and model all single channel data generated by  $\text{Ca}^{2+}$  dependent activation of purified human RyR2 (Results Chapter 5). Collaboration with QuB programmers allowed the direct measurement of ‘interburst’ intervals (v1.5.0.37) and later, recognize all ABF files directly (v1.5.0.39) when they modified the Python codes running the QuB suite. These improvements along with faster computation abilities

of later versions prompted me to use version 2.0.0.14 released in August 2012 and this was used for analysis of data from ryanodine and toxin-modified RyR2 (**Chapter 6**).

The data file (.abf) is opened in the *Preprocessing* interface (opened using the side button marked 'Pre' and shown by a red arrow) of QuB (**Fig 4.5 A**) and visually inspected for artefacts such as unusual noisy interludes, interference from 50 Hz AC hum and its odd harmonics, capacitance spikes occurring while switching the polarity of holding potential and serious baseline drifts. These artefacts are deleted along with periods of channel activity that are not typical of the channel gating behaviour for that particular experimental condition. For example, unusually long periods of closings or openings that stand out from the rest of the trace are probably due to modal shifts in RyR2 gating and should be removed before analysis if their overall proportion is low (<10% of the total duration of trace). This is necessary to maintain homogeneity in the single channel data required for the derivation of consistent kinetic models that accurately describe typical channel behaviour for a set of experimental conditions. It satisfies the essential Markov assumption that the rate constants of state transitions (transition probabilities) do not change with time in a memoryless system. In this chapter, I will use a section of current trace (~ 30 seconds) where a single RyR2 was activated using  $1\mu\text{M} [\text{Ca}^{2+}]_{\text{cyt}}$  at +30 mV holding potential in order to demonstrate the optimisation techniques that were developed for analysing data from my experiments using QuB.

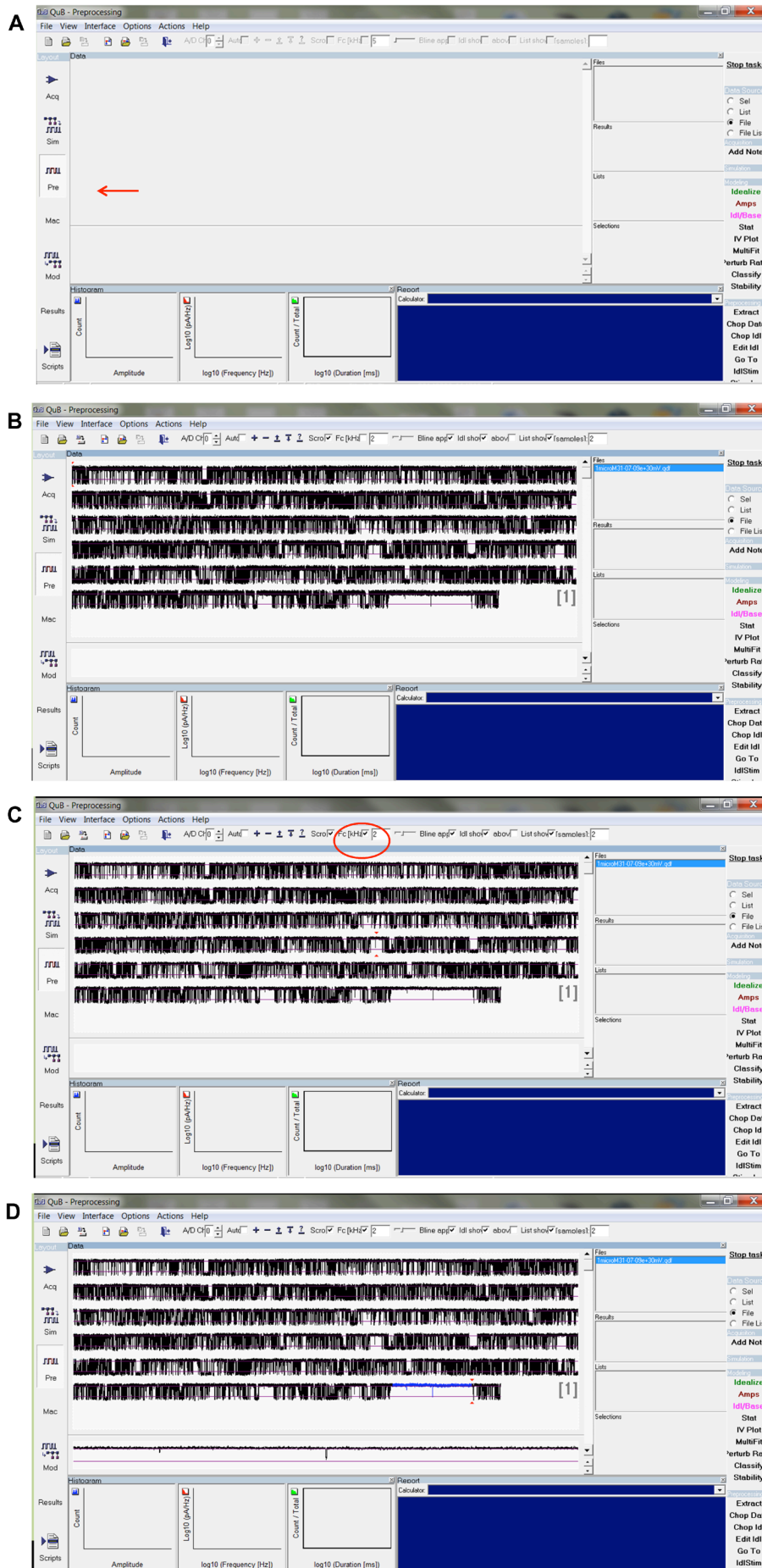
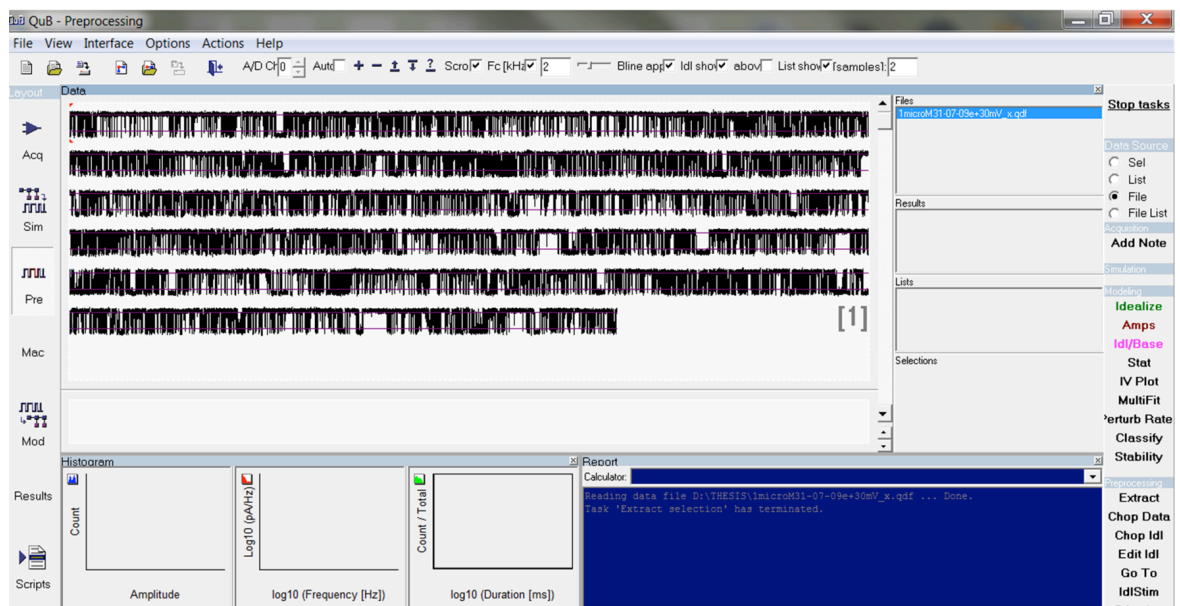


Figure 4.5. The preprocessing interface and getting the raw data ready for idealisation in QuB.

**Figure 4.5 B** shows the raw data file opened in the preprocessing interface, although the use of a digital Gaussian filter after sampling of data is not desirable as it would lead to a loss of detail, a 2 kHz filter was applied for better visualisation of the traces (**Fig 4.5 C**; red circle). The analysis programs used for idealisation of the trace ignored this low-pass filter by using appropriate settings (see next section). On inspection, the current trace looks homogenous apart from a small segment near the end (**Fig 4.5 D**, highlighted in blue) where the channel shows very low  $P_o$  (channel openings are downward deflections from the baseline), which is atypical and is due to modal shift in gating. This low  $P_o$  segment of 0.78s in duration (total data ~30s) was deleted to maintain homogeneity and allow accurate mechanistic interpretation of data (**Fig 4.6**). After deletion of any data points or when there are multiple sweeps displayed as separate traces, the whole file must be ‘extracted’ to a QDF file to prevent corruption of the traces and splice all the segments into a continuous trace. This is done using the *Extract* function on the lower right panel and the file is saved with a ‘\_x’ at the end of the filename as default to differentiate it from the original raw ABF data file.



**Figure 4.6. Preprocessing interface showing extracted single channel data ready for idealisation.** The file format is now in QDF format (QuB data file) which can easily be recognised by the software for further analysis.



#### 4.4.5 Accurate detection of events: idealisation

Like all ion channels, the RyR passes through a continuum of conformational states during the process of gating and in reality all state transitions are almost instantaneous. However the detection of single channel events as manifestations of such state transitions is inherently limited by the sensitivity and bandwidth of instruments currently available. Therefore, the most stable conformational states (which the channel molecule visits most often) are detected by analysis of data and the underlying mechanisms can be described using a kinetic model. HMM based algorithms are a powerful way of detecting the sequence of events in a noisy single channel trace (**Fig 4.7**).

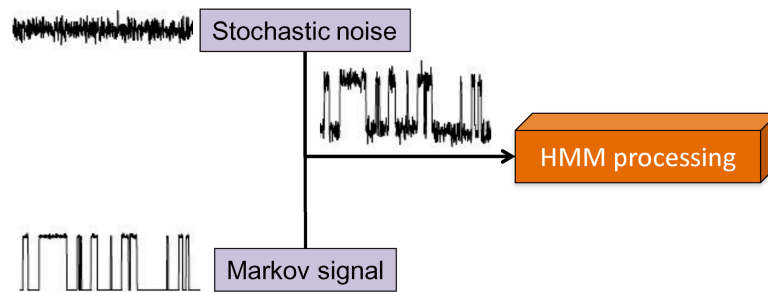


**Figure 4.7. Schematic showing the two basic components of raw single channel data.** The HMM-based algorithms consider these two components of stochastic noise and the actual biological signal hidden in it (a Markov process).

In an ideal world, one would like to find the kinetic model (theory) with the highest likelihood of being true given the data that is observed (conditional probability; **Eqn. 4.1**) However, this is a very difficult task as there is no prior information about the various kinetic parameters and the sequence of states from the data. It is easier if the thought processes are reversed and we start with a simple initial kinetic model (theory) and try to find the likelihood of the observed data set being correct given the model (**Eqn. 4.2**). The various algorithms perform iterative calculations to maximize the likelihood (probability of observing data given a model) and arrive at an optimal kinetic scheme.

$$P_{\text{theory}} = \text{Prob}\{\text{theory} \mid \text{data}\} \quad (4.1)$$

$$P_{\text{data}} = \text{Prob}\{\text{data} \mid \text{theory}\} \quad (4.2)$$

#### 4.4.6 Introducing the algorithms: workhorses of analysis programs

In effect, the *idealisation* procedure finds the most likely state sequence (MLSS) given the sampled data and a starting model. It then uses the MLSS to re-estimate the parameters of the model. I will briefly introduce some of the salient features of some of the algorithms that are used to a) find the MLSS and b) estimate the parameters so that it provides a logical basis for justifying their use in particular situations when they arise later in this Results section.

The fundamental concept behind analysis is that for a starting model, the probabilities of all possible pathways between adjacent data points in the trace are calculated, both forward and backward, and the true current levels are derived from the highest probabilities. As the initially supplied model and parameters were just guesses, there will be mismatch between the actual data and the model. Using a revised model, the observation sequence is compared again with this new model and this iterative process continues until maximum likelihood is reached. The ***Forward-Backward*** method is a dynamic programming algorithm which calculates the data likelihood and is based on the above mentioned concept (Baum et al. 1970). It is also described as an optimal filter-soother algorithm for discrete time dynamic models with discrete states. This iterative process by which the signal model is compared with the data leading to the model parameters being re-estimated and improved is shown as a flowchart (**Fig 4.8**).

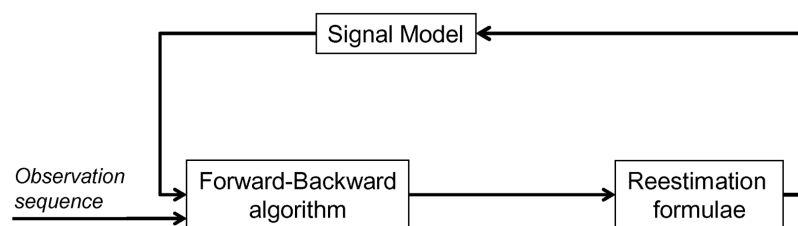


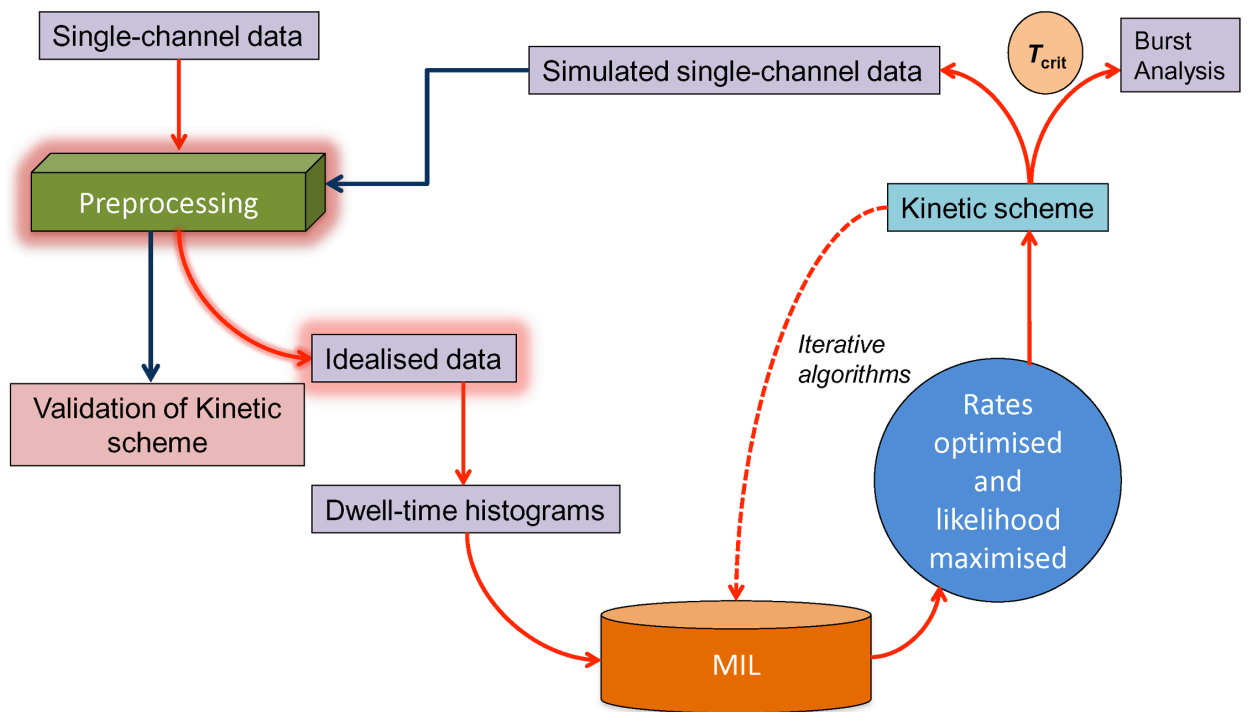
**Figure 4.8.** A block diagram showing the HMM-based signal processing method. The observation sequence (train of single channel events) is processed on the basis of the initial signal model where the forward and backward variables for every state are calculated at each discrete time point. These variables are then used to revise the parameters of the signal model based on the reestimation formulae with each iteration and is repeated many times. Adapted from *Signal Processing Based on Hidden Markov Models*, Biological Membrane Ion Channels (Krishnamurthy and Chung 2007).

The *Viterbi* algorithm (Viterbi 1967) finds the most likely sequence of states and is similar to the forward step of the Forward-Backward method. This algorithm works best for idealising data with a good signal to noise ratio. Apart from single channel data analysis, it finds wide applications in the fields of telecommunications, speech recognition, DNA analysis and radio astronomy.

The *Expectation-Maximisation* (EM) finds the maximum likelihood parameters using an iterative algorithm that alternates between two basic steps and was first described by (Dempster et al. 1977). The expectation step (E) finds the most likely sequence of steps given the data and parameter estimates by calculating the expected value of log-likelihood function. The maximisation (M) step then finds a new parameter estimate to maximise the expected log-likelihood of the data. These steps are repeated until the program converges to a maximum.

The *segmental k-means* (SKM) for HMMs is a dynamic programming algorithm that uses a Viterbi function to perform the expectation step (Qin and L. Li 2004). A maximisation step then re-estimates the parameters from the data and the sequence found by the expectation step. This procedure is fast and is set as the default analysis program in QuB. The SKM assumes the noise is Gaussian and the state transitions are instantaneous. This method works well when the signal to noise ratio is good in the raw data and the complete data likelihood is strongly peaked in favour of one sequence of states.

The *Baum-Welch* algorithm uses the Expectation-Maximisation method to perform maximum likelihood parameter estimation in HMMs (Baum et al. 1970; Rabiner and Juang 1986). The expectation step uses the Forward-Backward algorithm for finding the state sequence and the maximization step uses *re-estimation* formulae to obtain new parameter estimates. The estimation stipulates how the model parameters should be revised, given the forward and backward variables. It is a powerful algorithm (although computationally expensive and slower) which estimates state transition probabilities (not transition rates) and can be used even where the signal-to noise ratio is poor to deliver accurate results.



#### 4.4.7 Idealisation of RyR2 single channel data: key steps

1. The data is extracted to a QDF file and opened in the pre-processing interface of QuB software as described earlier. The whole file is then used to create an all-points amplitude histogram (Fig 4.9; red arrow). The data can be exported to an Excel spreadsheet and the distributions fitted using Gaussian curves for an accurate estimate of single channel current amplitude.

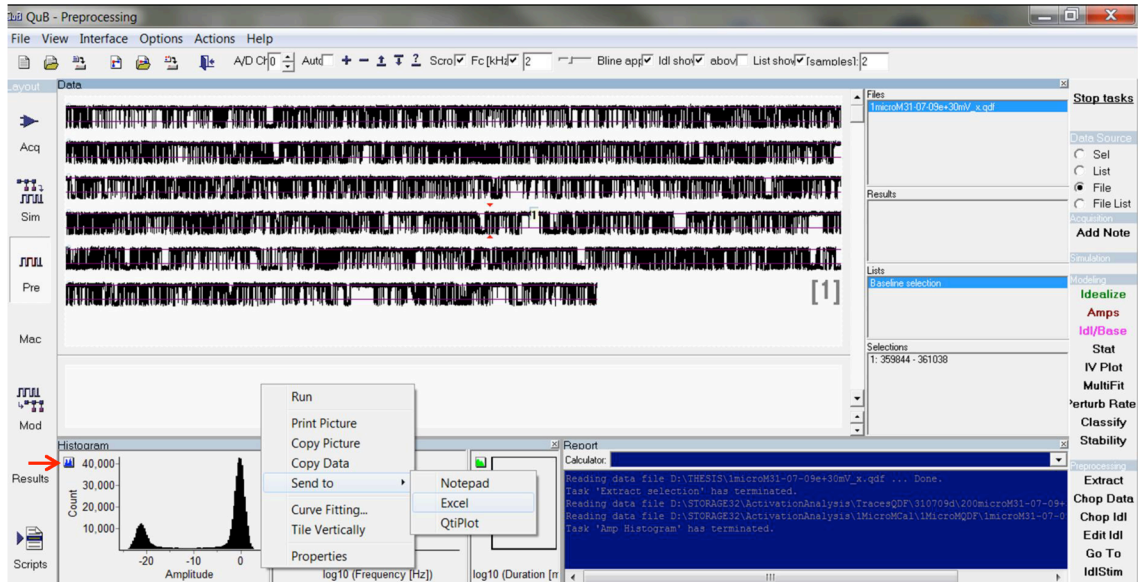


**Figure 4.9. Creating amplitude histograms using the preprocessing interface.** The red arrow marks the button for launching the create histogram function.

2. A segment of the closed level of the trace is selected as the baseline which has no obvious opening events. These points (highlighted blue in Fig 4.10) are then used to set the baseline using the root-mean-square value of the baseline noise and this is marked by the purple line. The setting of a correct baseline is critical as this provides the program with information regarding the closed level. The open level is similarly selected by highlighting using the cursor, a continuous sequence of points on a fully open current level with no obvious closings (Fig 4.11).

3. These closed and open current levels are then assigned to the Class 1 (black) and Class 2 (red) states respectively in the initial C $\leftrightarrow$ O model used for analysis. This is done by switching to the *Modelling interface* (Fig 4.12; red arrow) and selecting 'grab' on the menu by right clicking on the respective model classes (1, 2). This ensures that the algorithms know the starting values of the baseline and the fully open channel current level. The forward and backward rate constants are 1000s<sup>-1</sup> by default and are left as such.

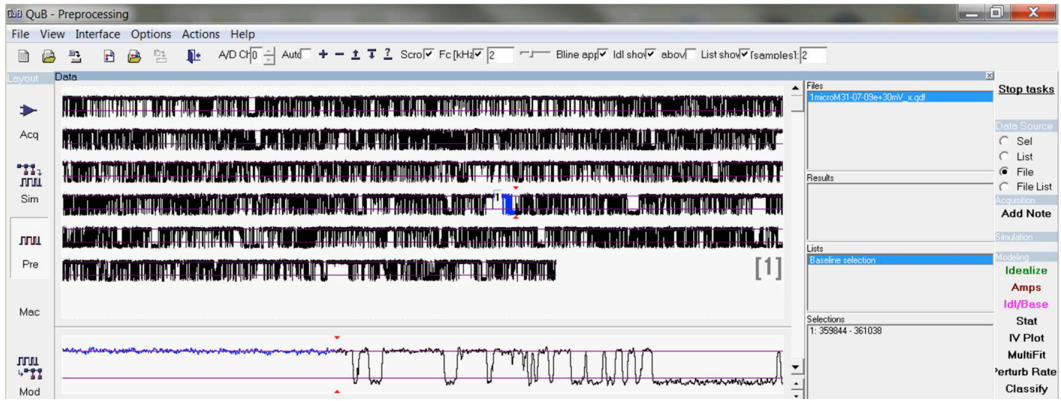


Figure 4.10. Assigning the baseline for idealisation. The closed level current is assigned by selecting an appropriate section of the trace (blue).

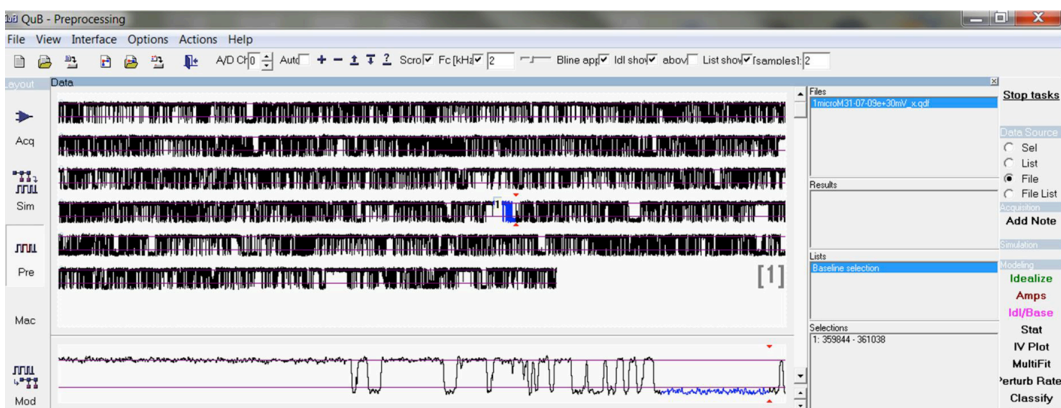


Figure 4.11. Assigning the open level for idealisation. The fully open level current is assigned by selecting an appropriate section of the trace (blue).

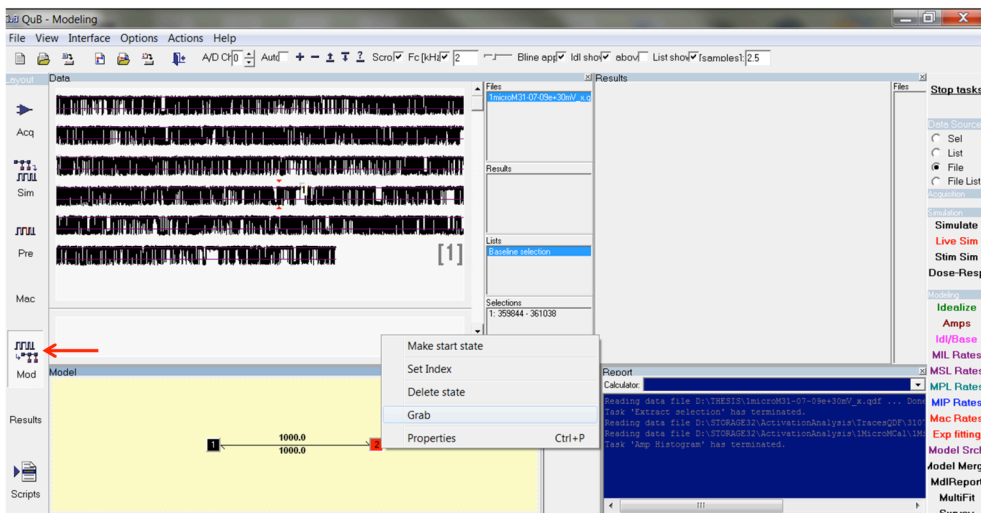


Figure 4.12. Closed and open current levels assigned to respective states in the modelling interface.

4. Before the various algorithms can be run to idealise the data set, it is important to impose an acceptable resolution such that even the briefest of the transitions are clearly distinguished from the baseline noise. The set resolution should at the same time ensure that as few as possible real transitions are missed. This cut-off duration is known as the *dead time* ( $T_d$ ) and all events with durations longer than this will be considered as true events and those shorter will be missed. Choosing an appropriate dead time is critical as an incorrectly set resolution might distort the dwell time distributions leading to an error prone kinetic model that is not representative of the data.

$$\sqrt{\frac{1}{f_c^2}} = \sqrt{\frac{1}{f_1^2} + \frac{1}{f_2^2} + \dots + \frac{1}{f_n^2}} \quad 4.3$$

$$T_r \approx 0.3321/f_c \quad 4.4$$

The first step is to determine the final filter cut-off frequency ( $f_c$ ) of the experimental set-up from which the rise-time ( $T_r$ ) of the filter is calculated. From **equations 4.3** and **4.4** (Colquhoun and Hawkes 1995) we get 5 kHz as the  $f_c$  (as only a 5 kHz low-pass 8-pole Bessel filter was used) and 66  $\mu$ s as the rise time. As a low pass filtered event of duration  $2T_r$  reaches ~99% of the original amplitude, a  $T_d$  set around this value should be a reasonable level of temporal resolution. Most of the single channel data sets from my experiments were well idealised using this resolution but at very low or high channel activity with brief opening and closing events respectively, a shorter dead time was better suited for accurate detection of events.

5. **Figure 4.13** shows the *Idealize* window with the appropriate settings for running the idealisation program using the SKM algorithm. The whole file is used for the analysis and the 2 kHz digital Gaussian filter is ignored using the setting: None- use original data. Incorporating the filter in analysis is not necessary for good data traces as it might distort the transitions. The right end of the topmost panel shows the dead time setting as a box marked `td[samples]` which expresses the value as multiples of the sampling interval (marked by red circle in **Fig 4.13**). As the single channel data were digitised at 20 kHz (sampling interval is 50  $\mu$ s), a dead time of 125  $\mu$ s was imposed which is 2.5 times the sampling rate. The re-estimation algorithm improves the accuracy of event detection considerably when the majority of events in the data set are clear transitions between the fully closed and open levels as seen in the current file being analysed. The SKM

idealisation algorithm is run with 100 iterative steps (default) and the output is an idealised trace (red) overlaid on the raw trace (**Fig 4.14**). The fidelity of the output must be well scrutinised by expanding random segments of the trace (panel below the data box) to satisfy oneself that the events picked up by the program are true events and not artefacts. It is also crucial to ensure that many putative true events are not missed by the idealisation process and this process is partly dependent on the judgement of the user. Therefore, it is important to know what RyR2 single channel data might look like under various experimental conditions and going through many data sets certainly helps. For example, in **Fig 4.14**, the small downward deflections from the base line (marked by green arrows) may look like putative opening events but I am satisfied that in this instance, they are indeed noisy artefacts as judged by the SKM algorithm.

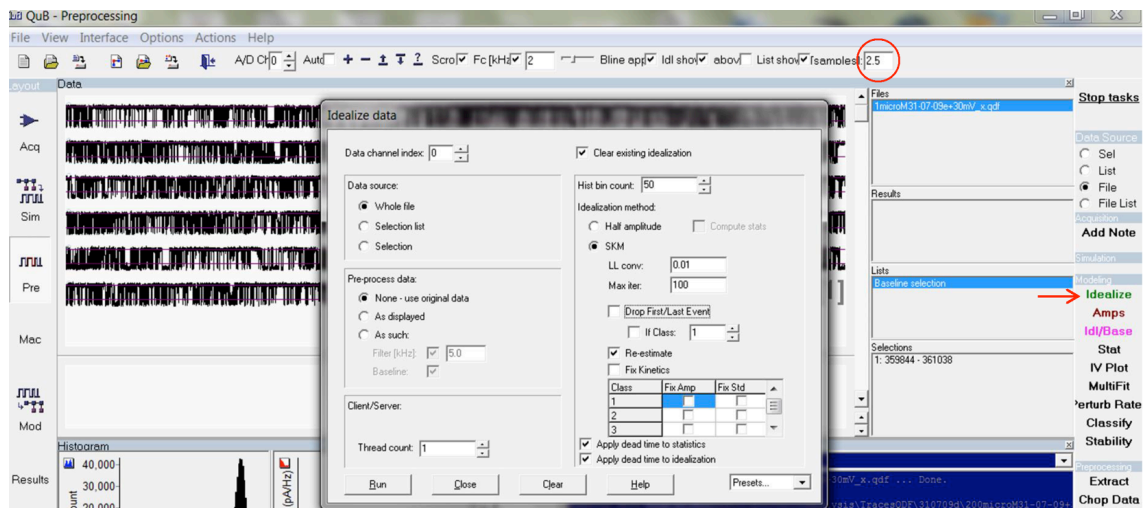


**Figure 4.13.** The settings for idealising data using SKM. The dead time is entered in the window marked with the red circle.

6. The kinetic parameters of idealised data are displayed under the Segments tab in the Results interface. **Table 4.2** compares the parameters obtained by running the SKM with and without the re-estimation function on single channel data where RyR2 was activated by  $1\mu\text{M} [\text{Ca}^{2+}]_{\text{cyt}}$ . An expanded portion of a random segment of data trace shows that by using re-estimation, more true events are picked up during idealisation. While in this instance it does not significantly change the  $P_o$  value, there is a difference in the closed and open times, which might alter the final kinetic scheme.



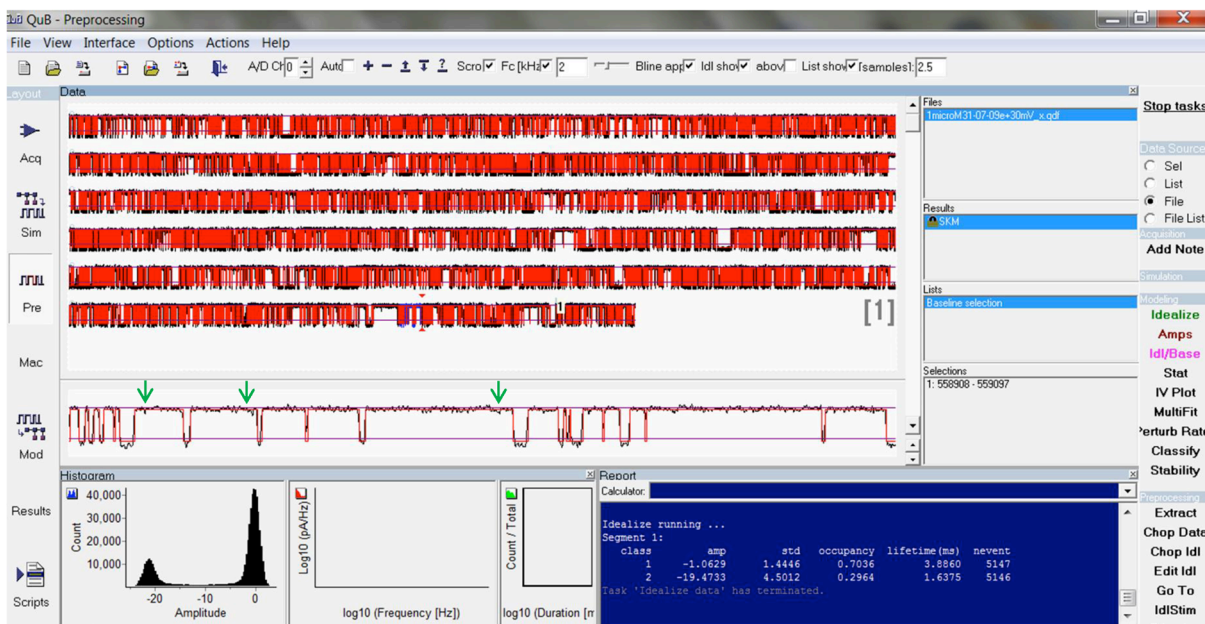


**Figure 4.14. Idealised data obtained using the SKM algorithm.** The idealised data are shown in red, overlaid on the actual single channel current trace (black). The arrows mark baseline artefacts that have not been recognised as true events.

**TABLE 4.2**

Algorithm ± Re*	Closed Events	Open events	Closed time (ms)	Open time (ms)	Open probability
SKM + Re*	5063	5062	2.15	0.8	0.2902
SKM	4030	4029	2.95	0.9	0.2909

Re\* Re-estimation

7. The idealisation process becomes more difficult in cases where single channel events are very brief and do not reach the full open or closed levels. This happens when RyR2 channel  $P_o$  is very low or high respectively and it requires modification of the program settings. To illustrate the problem and how it is overcome, I will use a 35 s segment of single channel data where the channel was activated by 250 nM  $[Ca^{2+}]_{cyt}$  at +30 mV holding potential. **Fig 4.15** shows the data opened in the preprocessing interface and there are only a few opening events that are long enough to reach the fully open current level. During analysis it was found that using a shorter dead time of 75  $\mu$ s (1.5 x sampling interval) resulted in more brief events being detected than the usual Td of 125  $\mu$ s when the channel  $P_o$  was very low or very high. The re-estimation function when used along with the SKM algorithm detected significantly more events than when re-estimation was switched off (**Figs 4.16** and **4.17**). The re-estimation of parameters with

each iteration results in the program significantly underestimating the open level current amplitude (the red lines of idealisation don't reach the full amplitude in **Fig 4.16**). This happens because the overwhelming number of very brief events in the trace compared to the few which reach the full open level forces the program to re-estimate the actual open state current level. However, as I'm interested in the gating kinetics of RyR2 and not the precise amplitude of current through the channel (the amplitude is accurately measured from all-point histograms), this is not an inconvenience and is a small price to pay. This kind of single channel data along with their associated underlying gating mechanisms cannot be accurately studied using the traditional HATC method.

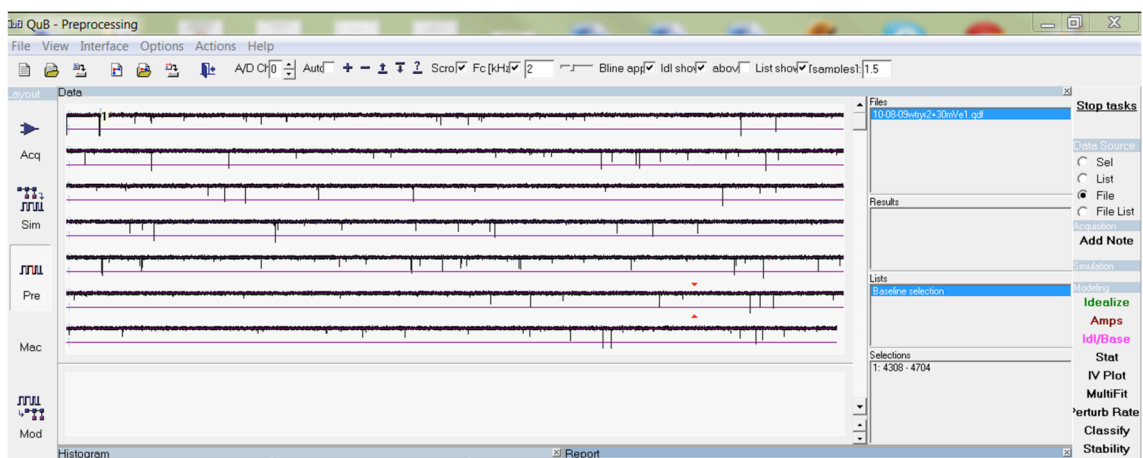


**Figure 4.15. Low activity single channel data recorded at 250 nM  $[Ca^{2+}]_{cyt}$  at +30 mV.**

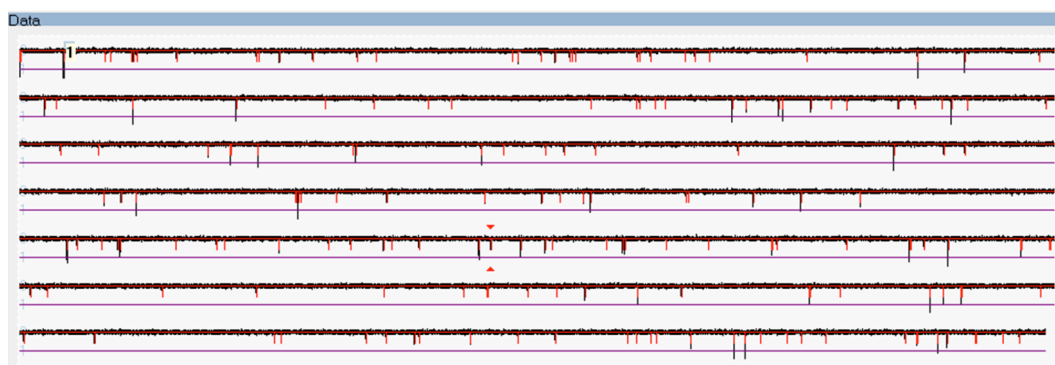


**Figure 4.16. Detection of brief opening events using re-estimation function in Idealize. The idealised trace (red) shows that even brief opening events that don't reach the full open level are detected.**

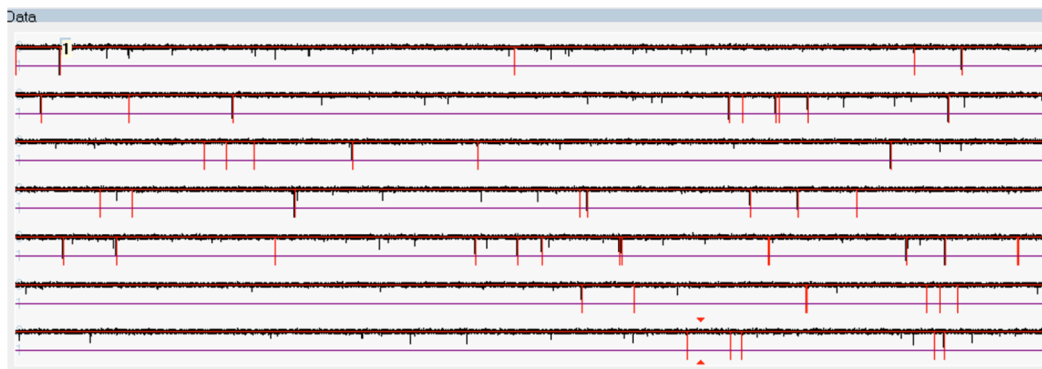


**Figure 4.17. Idealisation of low Po data using SKM algorithm with re-estimation turned off.** Most of the brief opening events were not detected when re-estimation was turned off.

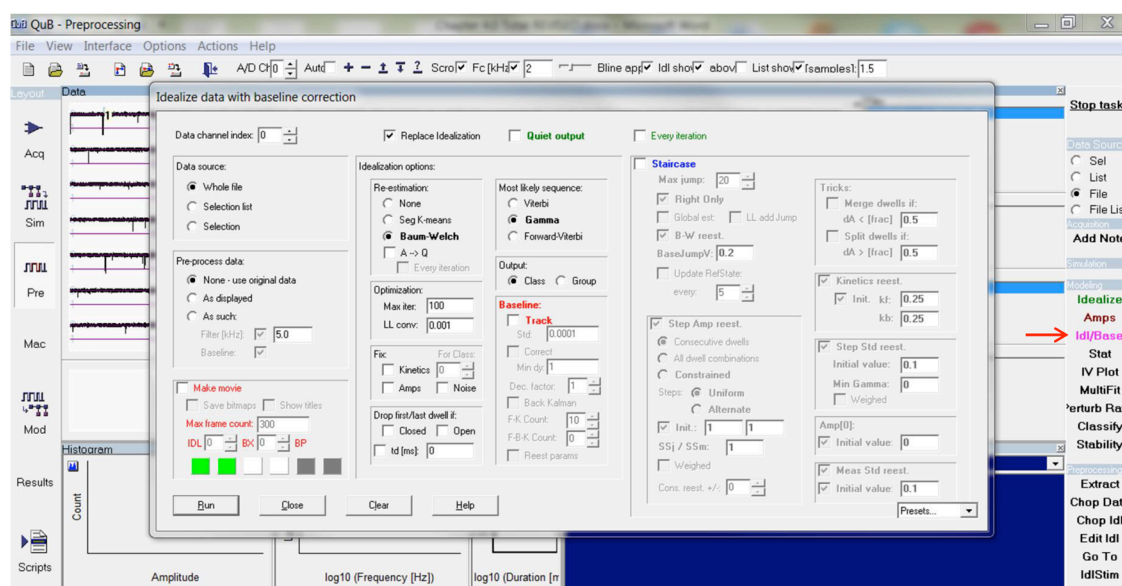


**Figure 4.18. Idealisation using Baum-Welch algorithm (Idl/base) and its settings.**

8. The Baum-Welch algorithm using the re-estimation formulae can also be used efficiently in cases when the signal to noise ratio is low or the event durations are very brief. This is accomplished by selecting the *Idl/Base* function from the right side preprocessing panel (Fig 4.18; marked with a red arrow) which opens the settings box for this method of idealisation. Again, the whole file is selected and the original raw data are used without any digital filtering. The Baum-Welch function is selected with Gamma as the most likely sequence (a maximisation method) and the program is run for 100 iterations. If there is a baseline drift, selecting the Track function will result in the Kalman filter algorithm tracking the baseline to correct for the drift.

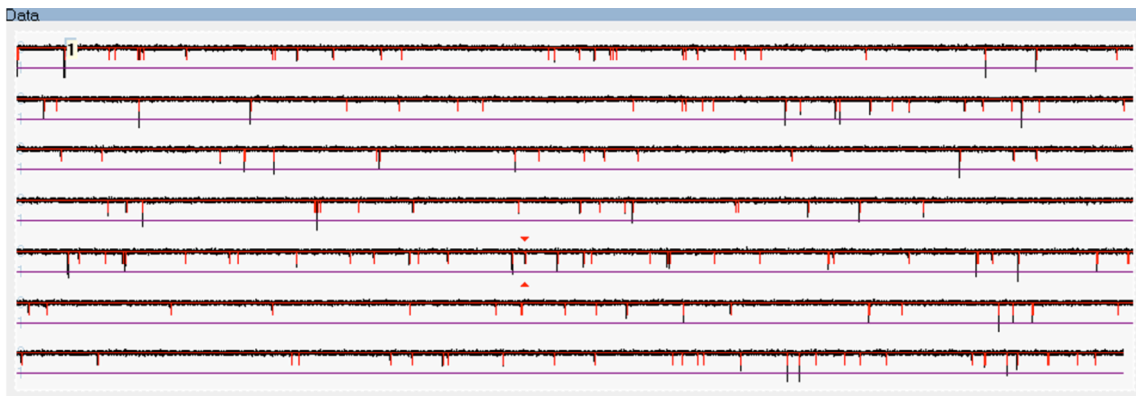


**Figure 4.19. Idealised single channel data using Baum-Welch algorithm.** Brief opening events were accurately detected using this method.

**TABLE 4.3**

$[Ca^{2+}]_{cyt}$ /Algorithm	<i>Re-estimation</i> +/-	Closed Events	Open events	Closed time (ms)	Open time (ms)	Open probability
250 nM/SKM*	+	167	166	141.4	0.3	0.00145
250nM/SKM#	+	177	176	131.35	0.25	0.00148
250 nM/SKM*	-	46	45	474.92	0.25	0.00033
250nM/SKM#	-	50	49	403.77	0.25	0.00035
250 nM/B-W	+	184	183	131	0.25	0.00151
250nM/HATC	n.a	43	42	503	0.25	0.00031

\*  $T_d = 125 \mu s$

#  $T_d = 75 \mu s$

**B-W** Baum-Welch

The idealised result is shown in **Fig 4.19** and the kinetic parameters from the various idealisation trials mentioned above are compared in **Table 4.3**. The two best outcomes and their underlying analysis conditions are shaded in grey. The importance of re-estimation is emphasised using **Figs. 4.20A** and **B** where expansions of the idealised trace obtained in **Figs. 4.16** and **4.17** respectively are shown. Idealisation with re-estimation turned off produced results similar to that obtained when HATC method was used (**Table 4.3**). It should be noted that the Idl/Base method of idealisation is computationally expensive and is considerably slower when compared with the SKM algorithm. The former needed about 3.5 min to idealise 30s worth of data while SKM took only 10 s to complete on a PC with a 2.27 GHz processor and 4GB RAM. In practical analysis of records, 2-3 minutes of data consisting of tens of thousands of

events are used for each experimental condition, making SKM a better-suited method unless the Baum-Welch re-estimation is needed.

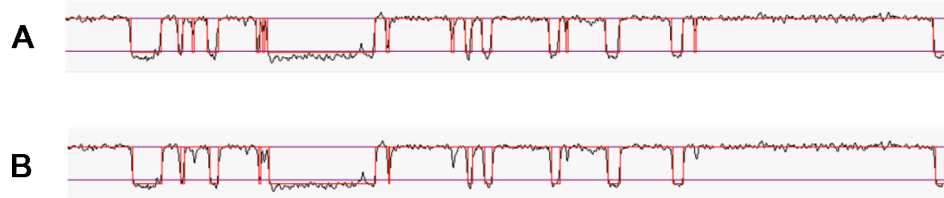
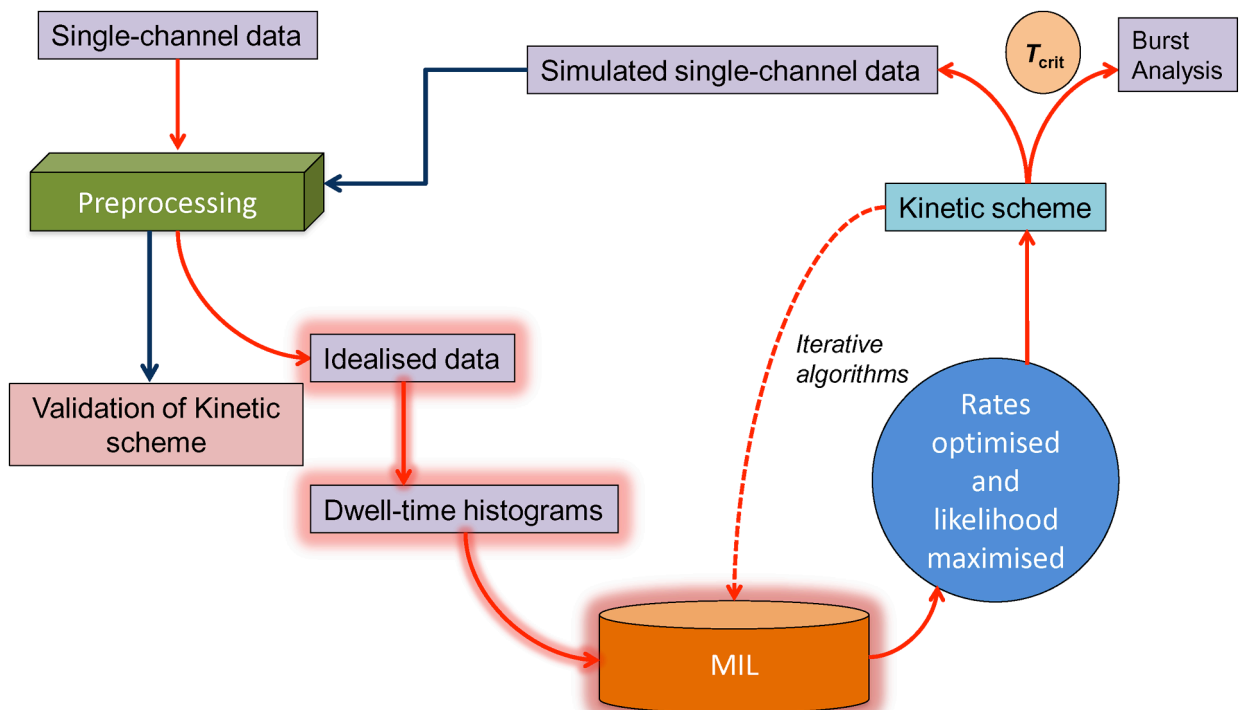


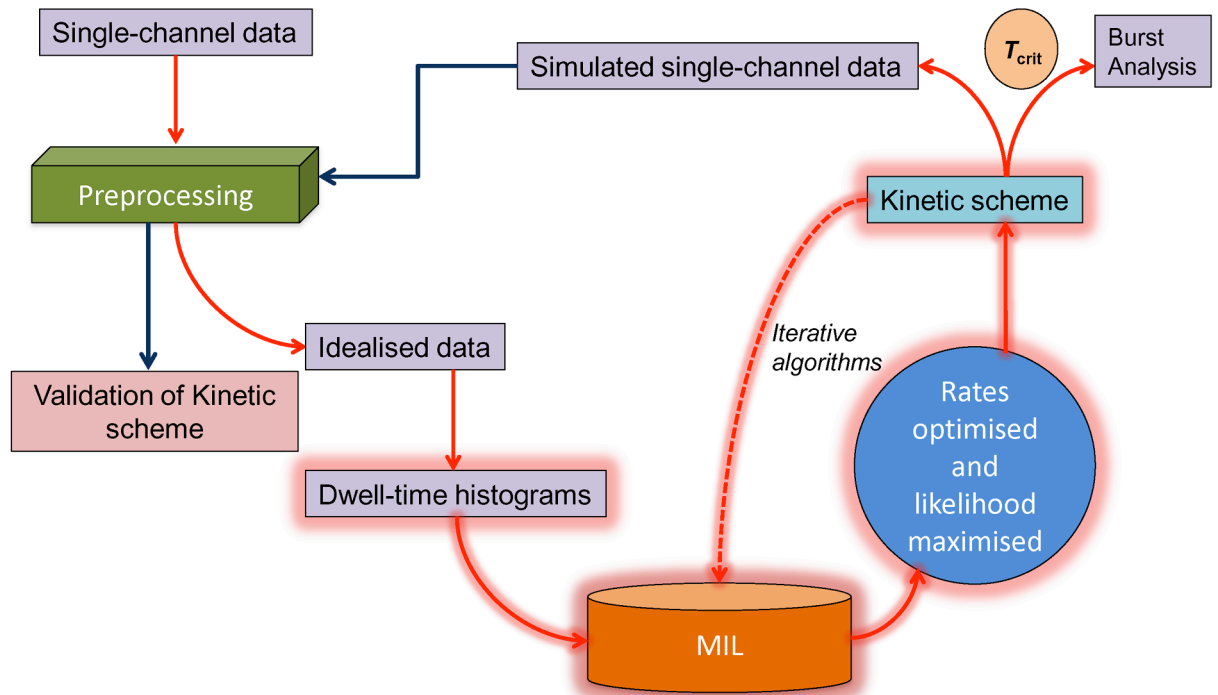
**Figure 4.20. Comparison of idealised single channel data with and without re-estimation.** A portion of the data idealised using SKM with re-estimation turned on (**Fig 4.16**) is shown on an expanded time base in (**A**). The same segment of data is shown after idealisation without re-estimation (**Fig 4.17**) while all other settings remained the same (**B**). Many brief opening events which didn't reach the full open current level were missed (**B**).



#### 4.4.8 Model-based interpretation of single channel data using MIL

The idealisation process allows the creation of frequency histograms of the number of closed and open intervals vs. their durations. The area under the curve between any two time values gives the probability of observing an interval with a dwell time between those values (Colquhoun and Hawkes 1994). Markov models describing channel behaviour predicts that dwell time histograms are comprised of sums of exponential components where the total number of closed and open components is equal to the number of closed and open states visited by the channel (Colquhoun and Hawkes 1982; Shelley and Magleby 2008). My aim is to gain an insight into the actual physical basis for the origins of the exponential components in order to unravel underlying mechanisms behind state transitions in the RyR2. In this section I will briefly describe the basic theory underlying the MIL fitting process.

The maximum interval likelihood (MIL) program of QuB software is used to derive a kinetic model to describe the RyR2 gating behaviour while simultaneously fitting the dwell-time histograms with mixtures of exponentials while optimising the rate constants of the transitions. Given a connection scheme and single channel data, the MIL finds the most likely rate constants. It does this by maximising the continuous time likelihood of a dwell time sequence and performs a first order correction of missed events due to the dead time applied (Qin et al. 1996). Starting with an initial kinetic scheme, a closed or an open state was sequentially added, ensuring that the maximum log likelihood (LL) value change by at least 5 upon every state added. This was repeated until the fit of the probability distribution was sufficiently good and further additions of states to the model did not change the LL value significantly. Here the likelihood is defined as the sum likelihood, over all state sequences that match the data. MIL uses a gradient search to adjust the rate constants until likelihood reaches a maximum. This represents the absolute value of the maximum log likelihood at convergence of the program and is a positive value, increasing with every significant addition of closed or open state to the kinetic scheme.



#### 4.4.8.1 Building a putative gating scheme: key stages

1. After idealisation of raw single channel data using appropriate algorithms and ensuring the accuracy of event detection, the MIL model optimisation window is opened by clicking on MIL rates in the Modelling interface of QuB (**Fig 4.21**, shown by red arrow). Again, as before, the whole file is selected along with smooth binning and square root ordinate. This use of the Sigworth and Sine transform (Sigworth and Sine 1987) of the plot has several advantages over a linear histogram: a) exponential components appear as peaked functions in the display; b) the position of the peak in each component corresponds directly to its time constant; c) the height of each peak corresponds to the total number of events in that component; and d) the expected statistical scatter in the data is of constant magnitude throughout this type of display. The single channel data used for this procedure is that obtained by activating the RyR2 by  $1\mu\text{M}$   $[\text{Ca}^{2+}]_{\text{cyt}}$  at +30 mV that has been idealised using SKM method (**Fig 4.14**).

2. The MIL program was run with the initial C $\leftrightarrow$ O scheme with a dead time of 125  $\mu\text{s}$  (2.5 x sampling interval) and the fits of the dwell time histograms were inspected (**Fig 4.22**). The fits of the closed and open time histograms are suboptimal and can be further improved by the addition of more states in the kinetic model. Note the initial LL value (50908) and the optimised rate constants. The LL value is found under the 'Summary' tab of MIL results window (**Fig 4.22**, blue arrow)

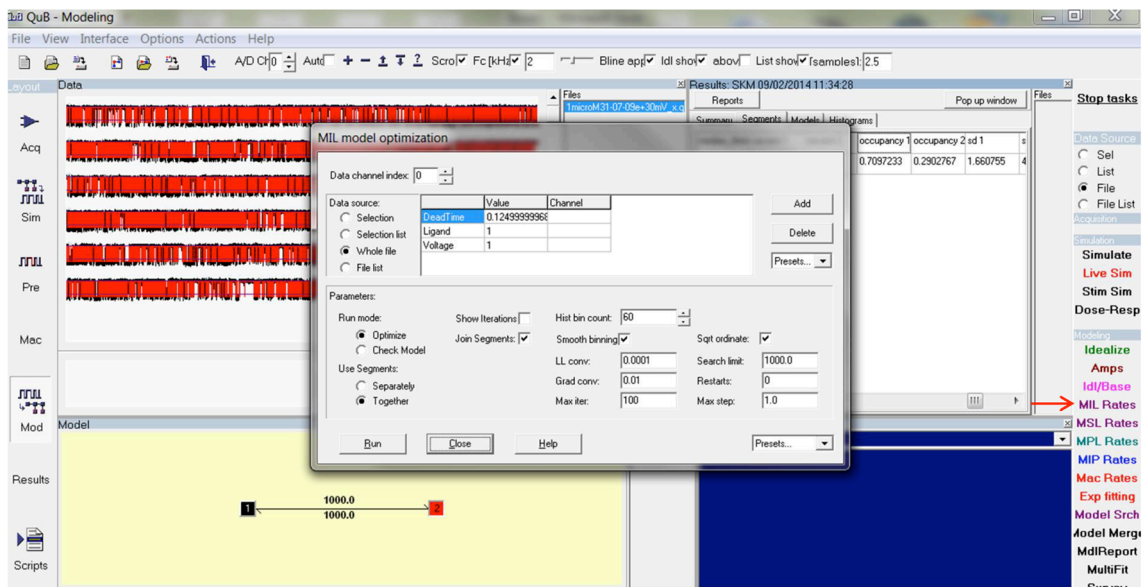


**Figure 4.21. The MIL interface for modelling of single channel data.** The appropriate settings for running the MIL program and optimisation of rate constants are shown.

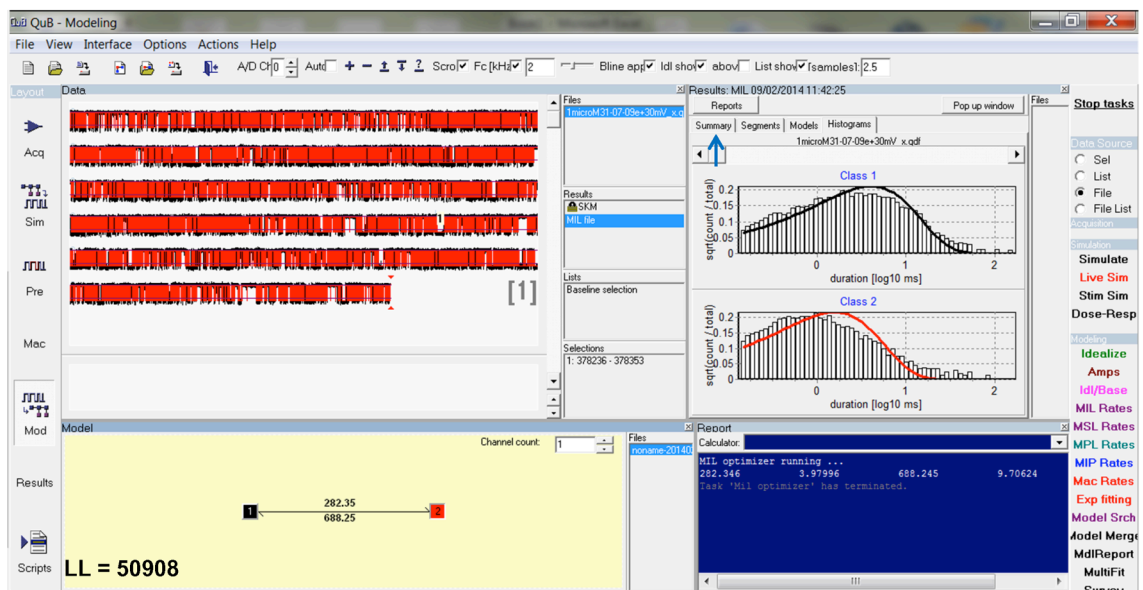


**Figure 4.22. Building gating schemes using MIL.** The result of the first run using a simple two state scheme is shown along with its log likelihood (LL) and the optimised rate constants. The exponential fits of closed and open dwell time histograms (black and red respectively) don't look adequate, hence more states are needed.

3. Another closed state (black box labelled 3) was connected to the initial closed state (1) by clicking on the Model window and the MIL program was run again. The LL value improved significantly ( $>5$  LL values) and the fit of the closed time histogram was better (Fig 4.23A). More open and closed states were added to the kinetic scheme and the rate constants were optimised until the LL value stopped changing and the overall fits of both



closed and open time histograms looked appropriate (**Figures 4.23 B-D**). The fits and LL values (**Fig 4.23 D**) show that a gating model with a minimum of three closed and open states each can adequately describe the single channel kinetic of RyR2 under these particular experimental conditions. The final kinetic scheme (LL 52068) is saved as a QMF (QuB model file) and stored for future analysis.

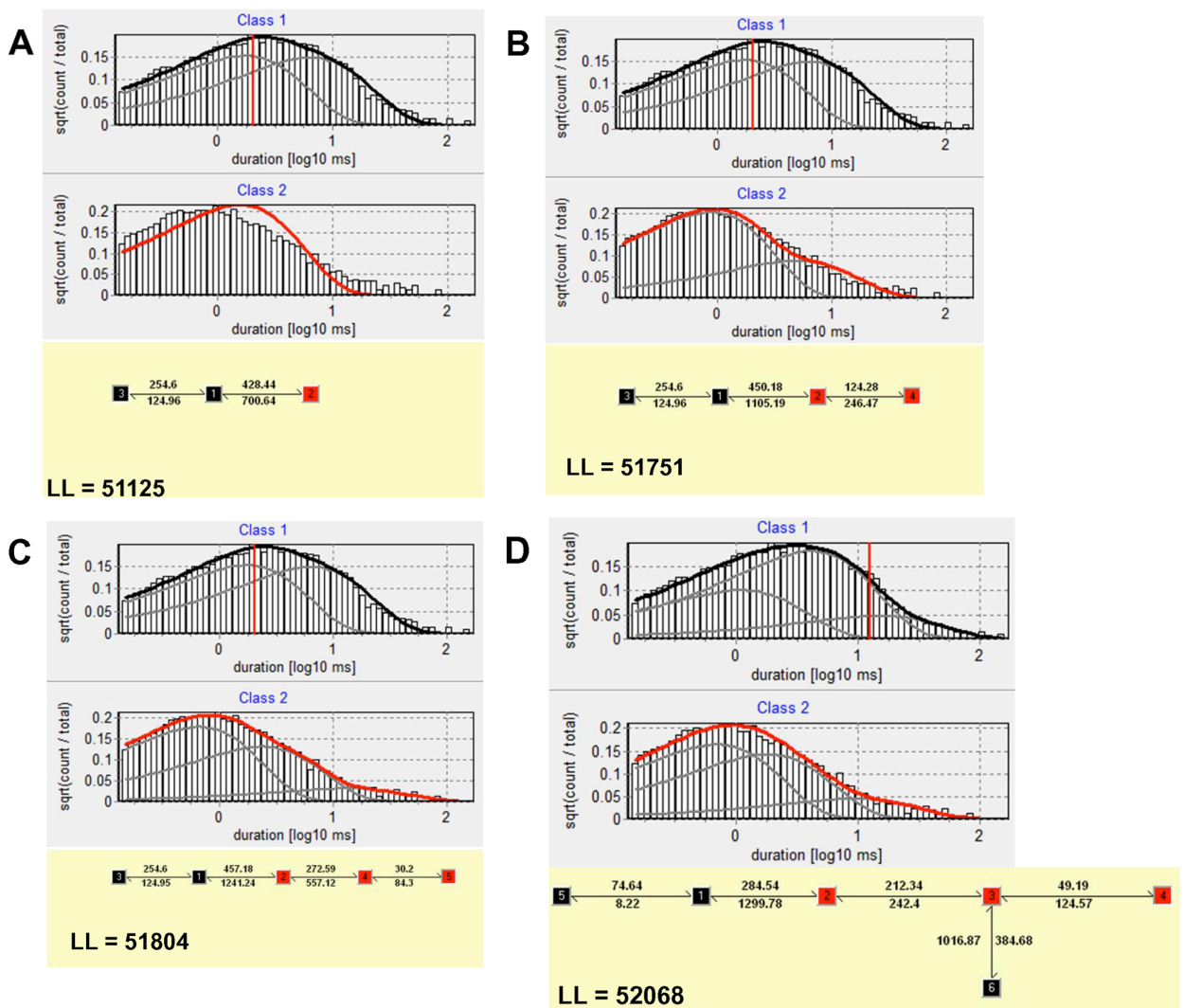


**Figure 4.23. Adding states to the model with simultaneous fitting of dwell-time histograms.** (A-D) show the improvements in the fits along with significant increase in the maximum log likelihood when new closed and open states are sequentially added to build up a gating model. The rate constants of the state transitions are optimised after each step. The time constants and area under the exponential fits (from the final model shown in D) corresponding to the closed states (5, 1 and 6; black boxes) and open states (2, 3 and 4; red boxes) are shown in **Table 4.4** below.

**TABLE 4.4**

CLOSED (class 1)			OPEN (class 2)		
STATE	$\tau$ (ms)	Amp (%)	STATE	$\tau$ (ms)	Amp (%)
5	14.24	5	2	0.66	52.1
1	3.93	74.3	3	1.73	43.4
6	1	20.7	4	9.1	4.5

$\tau$  time constant of exponential component

Amp area under exponentials

The best-fit parameters for this final model (time constants and areas under individual exponentials) are shown in **Table 4.4**. A detailed report in the form of a Word document can be generated for each run of the MIL program by clicking on the Reports button above the histogram windows. An inappropriate kinetic model will result in the failure of the MIL program to converge and provide optimised rate constants. For example, the addition of another open state (7) to the previous model (**Fig 4.23 D**) results in grossly erroneous fits and absurd rate constant values (**Fig 4.24**).

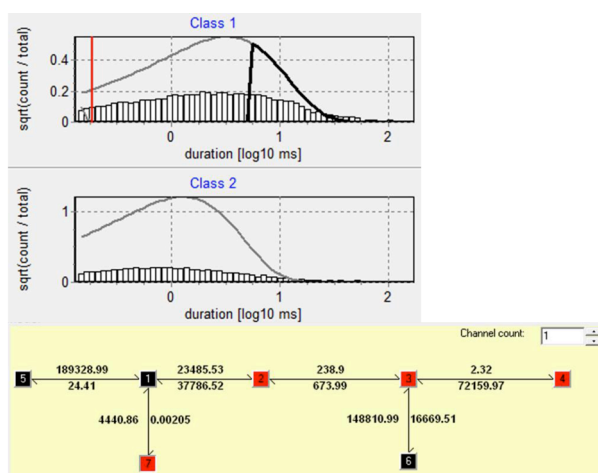


**Figure 4.24. Error in fitting of data due to an incompatible kinetic scheme.** An inappropriate starting model results in the non-convergence of the MIL program run.

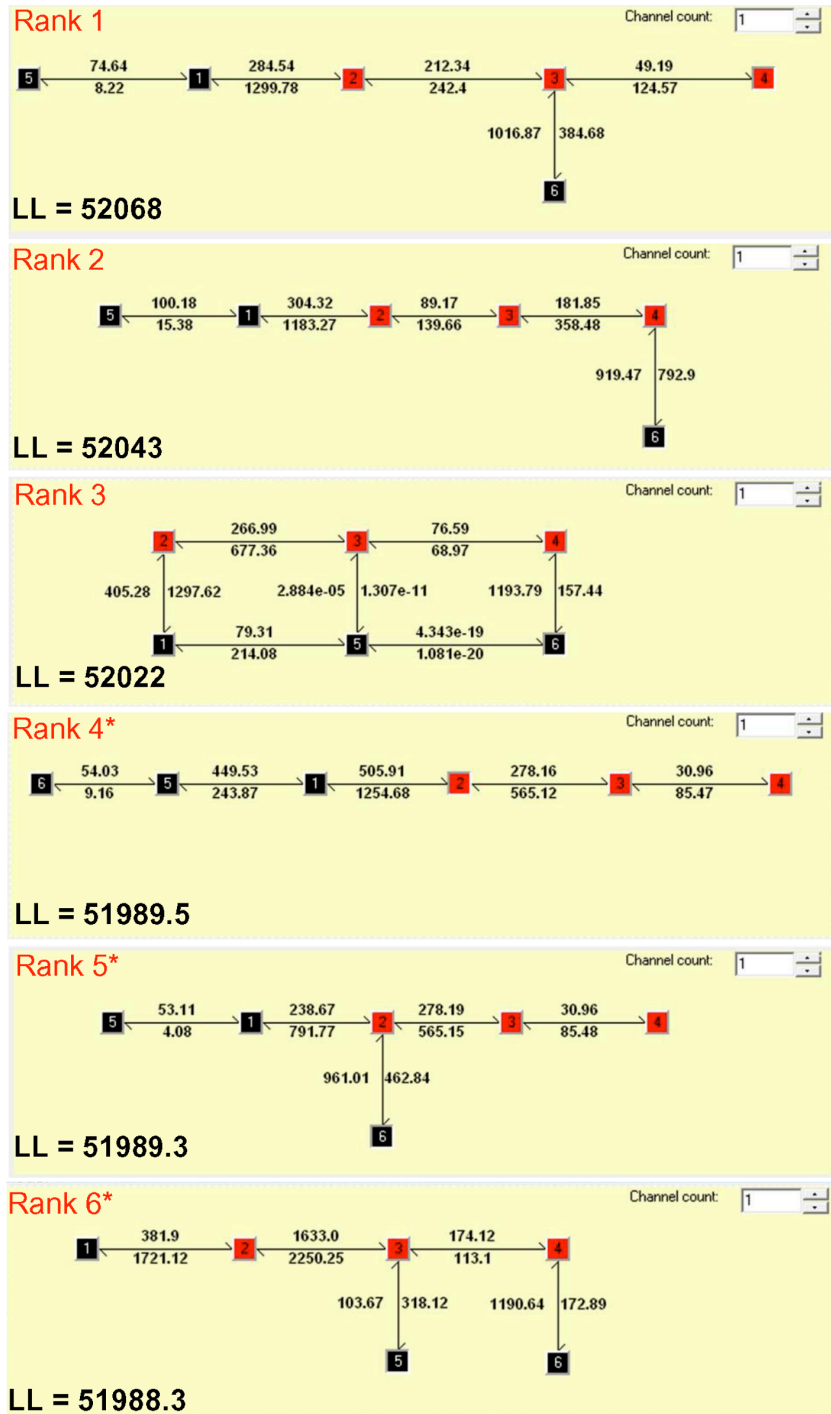
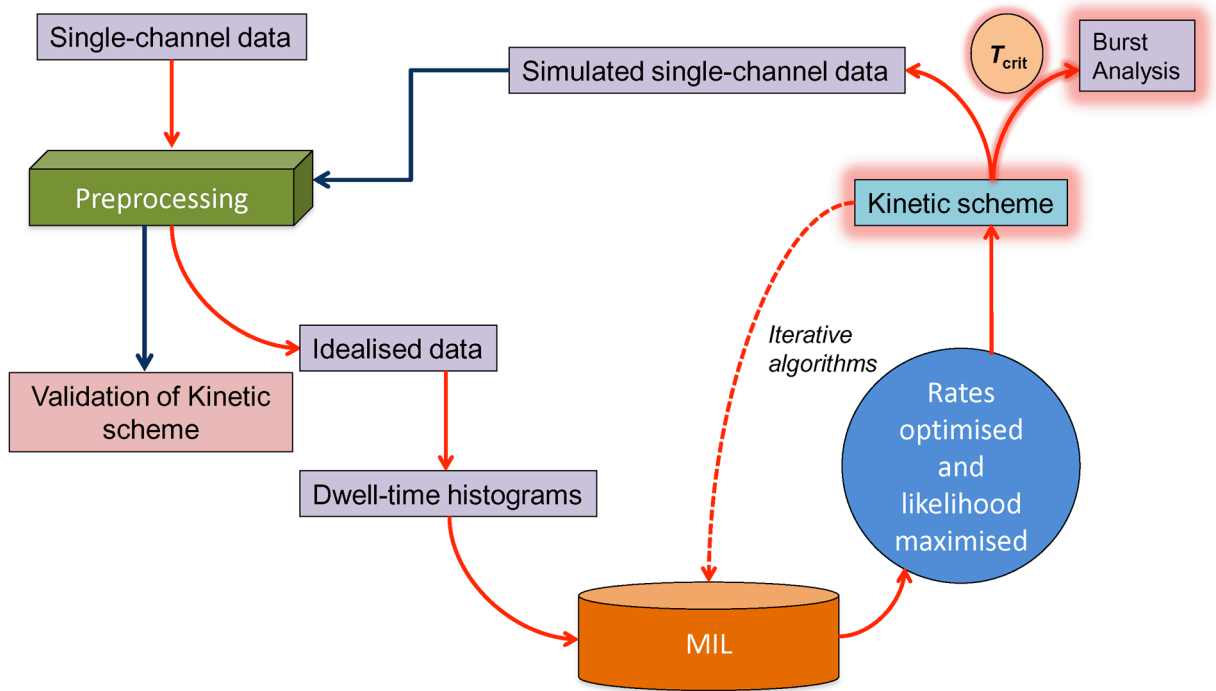


**Figure 4.25. Models ranked according to their maximum log likelihoods.** This shows that different kinetic schemes are possible with the same number of closed and open states (3 each) but the ones having the highest LL values should also make mechanistic sense in order to be a putative gating model.

4. Models with equal numbers of closed and open states but connected differently may have similar LL values making them equally likely. Therefore, it is important to check if different connection schemes can offer better fits of the histograms with higher LL values. This can be done manually if the total numbers of states are low by changing the way various states are connected and checking the LL after each run of MIL program. If the topology of the kinetic scheme is complicated, an automated but computationally intensive model search program may be run using the *Model Srch* button in the lower right panel. Various possible kinetic schemes with high LL derived using manual model searches are ranked in **Fig 4.25**. The branched linear scheme derived in the previous steps is the most likely gating model (rank 1) while looped models (rank 3) are not preferred as some of the optimised rate constants are absurdly low, thereby making those transitions (between states 3 and 5; 5 and 6) very unlikely. This model therefore, in reality, is almost kinetically similar to the one with rank 2 in terms of topology. However if schemes incorporating loops are ranked higher with realistic rate constants, it's important to ensure that microscopic reversibility holds true. In a cyclical model, the product of the rate constants in the clockwise direction should be equal to the product going in the anticlockwise direction and thus suitable constraints can be imposed during model fitting (Colquhoun et al. 2004). The kinetic models with ranks 4-6 are almost equally likely in terms of their LL values. The final gating model (rank 1) can be again used as a kinetic template with accurate rate constants for re-idealising the raw data to further increase the accuracy of the parameters such as  $P_o$ ,  $T_c$  and  $T_o$ . The search for an adequate model that can best describe the RyR2 gating behaviour does not end with the output of the MIL program. The mechanistic appropriateness of a particular gating scheme must be evaluated by the user in terms of actual physical meaning of state transitions and QuB has very limited role to play in terms of model choice.



#### 4.4.8.2 Studying clusters of channel activity: burst analysis

The gating activity of various types of ion channels has been shown to be comprised of bursts of rapid openings and closing events separated by relatively longer interburst closings (Colquhoun and Hawkes 1982). As bursts are known to occur when the channel is ligand bound and are terminated by the dissociation of the ligand, study of burst kinetics may provide valuable information about channel gating behaviour. Mathematically, bursts of openings are defined as being separated by closed durations equal to or greater than a cut-off critical time ( $T_{crit}$ ). For each analysed data set,  $T_{crit}$  was determined by the MIL program such that an equal number of long and short closed time intervals were misclassified (Magleby and Pallotta 1983; Clapham and Neher 1984). This is represented by **Eqn. 4.5** where  $\tau_1$  is the time constant of the longest shut-time component and  $\tau_2$  is the time constant of the component that immediately follows this one in the closed time distribution whereas  $amp_1$  and  $amp_2$  respectively are the areas under those exponential components.

$$amp_1 \times e^{-\frac{\tau_{crit}}{\tau_1}} = amp_2 \times \left( 1 - e^{-\frac{\tau_{crit}}{\tau_2}} \right) \quad 4.5$$

The red vertical line on the closed time histogram which equally divides the area of overlap (green area in **Fig 4.26**) between the two adjacent closed time distributions indicates the  $T_{crit}$ .

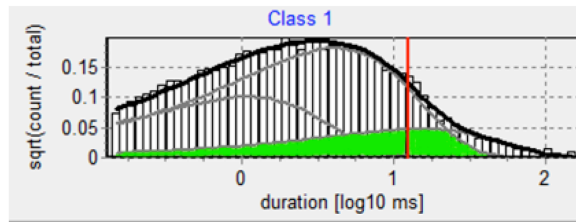


**Figure 4.26. The concept of critical time used in burst analysis.** Closed time histograms with exponential fits showing the area of overlap between the two adjacent distributions (green) and the red line dividing the area marks the position of  $T_{crit}$ .

For the segment of data being analysed, the  $T_{crit}$  value from the outcome of the MIL program was 12.74 ms. This is used to chop the idealised data into bursts using the *Chop Idl* function in the lower right preprocessing panel (**Fig 4.27**; shown with red arrow). For my analyses, I have decided to only consider bursts with at least three opening events and that is indicated in the settings panel.

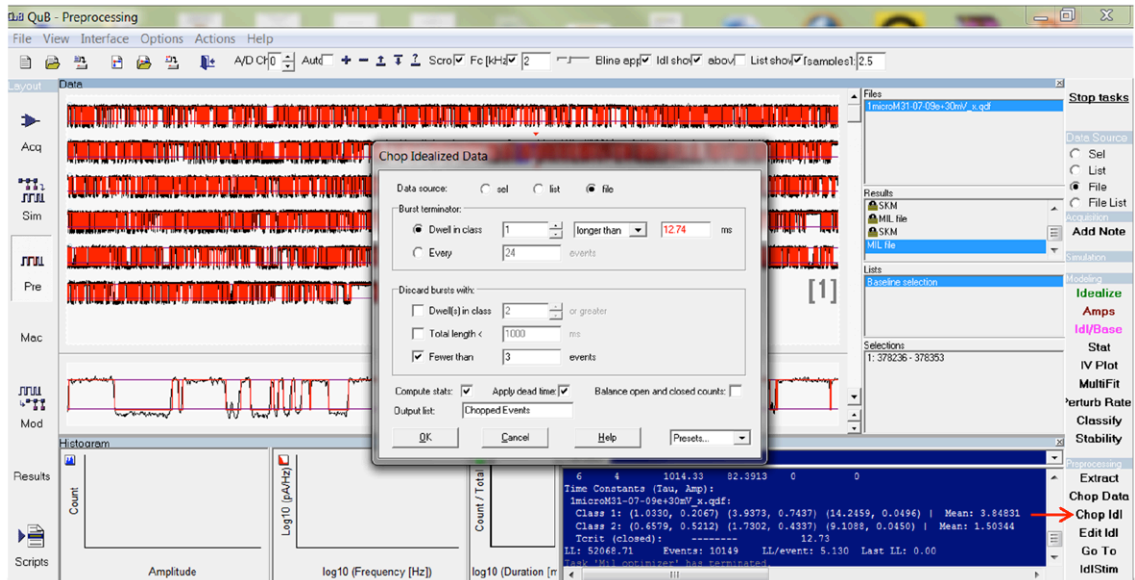


**Figure 4.27. Analysis of single channel data in terms of bursts of openings.**  $T_{crit}$  from MIL is used to define bursts using Chop Idl in the preprocessing interface.

The idealised data were chopped into 230 bursts and the kinetic parameters for each of them were separately available as a list (Fig 4.28). In this figure burst #116 is randomly selected from the list and it is displayed separately in the panel below the data. The closed and open times within each burst (Fig 4.29 A and B respectively) and burst lengths (Fig 4.30) are plotted as count vs. durations (ms). These parameters can also be plotted according to their sequence in the trace. The interburst intervals and burst lengths (ms) were plotted according to their order of occurrence in the trace in Figs. 4.31 A and B respectively. The scatter plots prove that the channel gating behaviour seen in the data is indeed homogenous with no obvious atypical segments and modal gating.

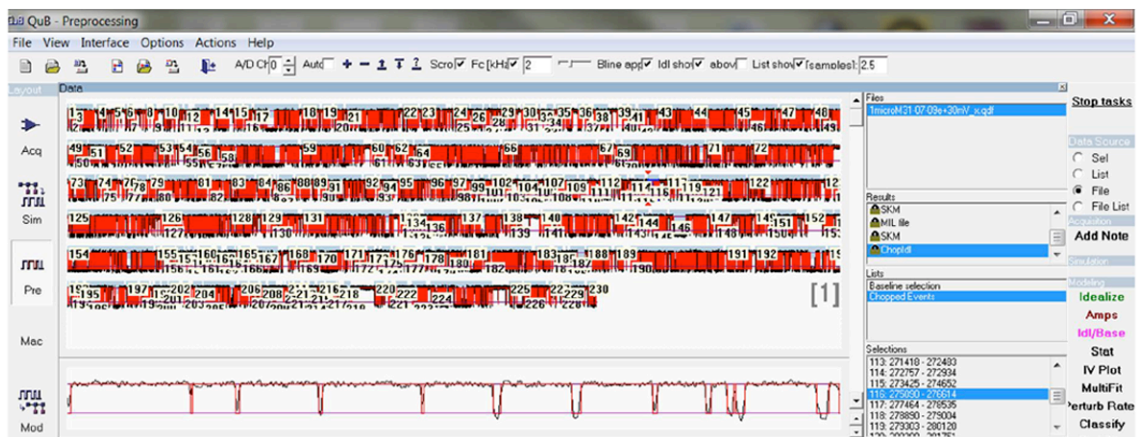


Figure 4.28. Idealised single channel data chopped into bursts. 230 bursts of openings were found and #116 is randomly expanded in the panel below to show the openings within that burst.

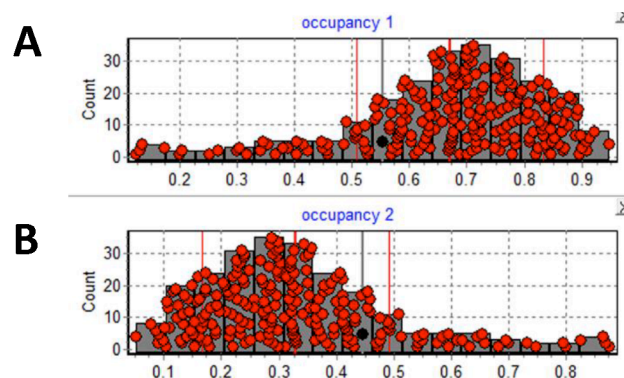
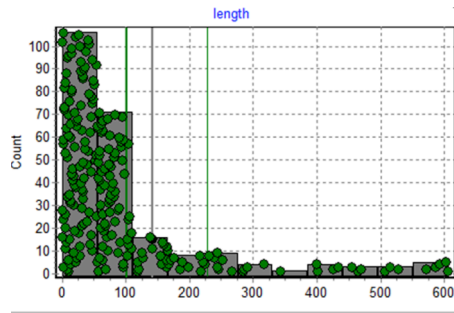
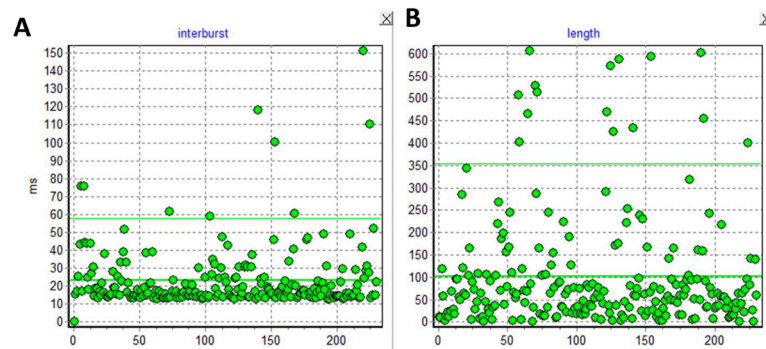


Figure 4.29. Plots showing closed times (A) and open times (B) within bursts (milliseconds).

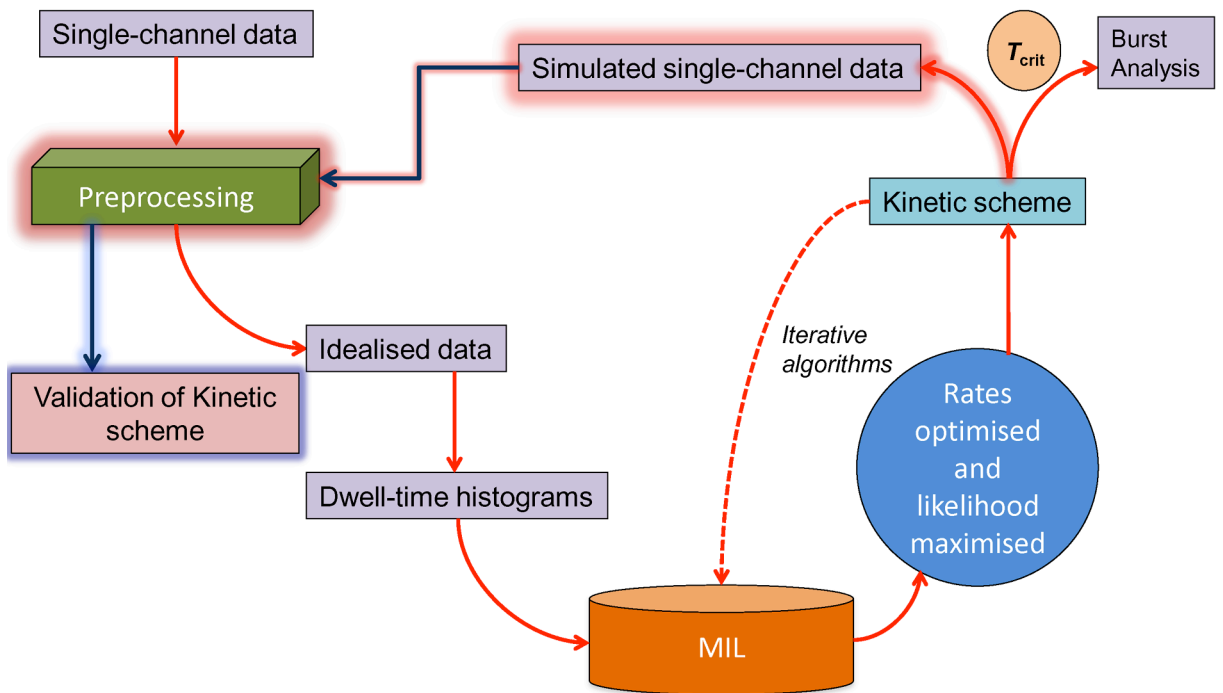


**Figure 4.30.** Burst lengths (ms) are plotted according to their frequency of occurrence. Most bursts have durations up to 100ms in this data.



**Figure 4.31.** Plots showing Interburst intervals (A) and burst length (B) according to their order of appearance in the single channel data trace. The majority of the interburst intervals (A) range from 12.57 ms ( $T_{crit}$ ) to about 25 ms, while majority of bursts are up to 100 ms in length. The scatter plots look homogenous without any unusual clustering which indicates the absence of atypical gating periods in these data.





#### 4.4.8.3 Validation of kinetic scheme: model-based simulation

The putative gating model obtained from the MIL program with its optimised rate constants was used to simulate single channel data to check if it replicated the experimental data. This validation was necessary to ensure that the direct mechanism fitting of single channel data successfully generated a plausible mechanistic model. The kinetic model file was selected and the Simulate button from the right Simulation panel (Fig 4.32; labelled with red arrow) clicked to generate a required length of stochastically simulated data.

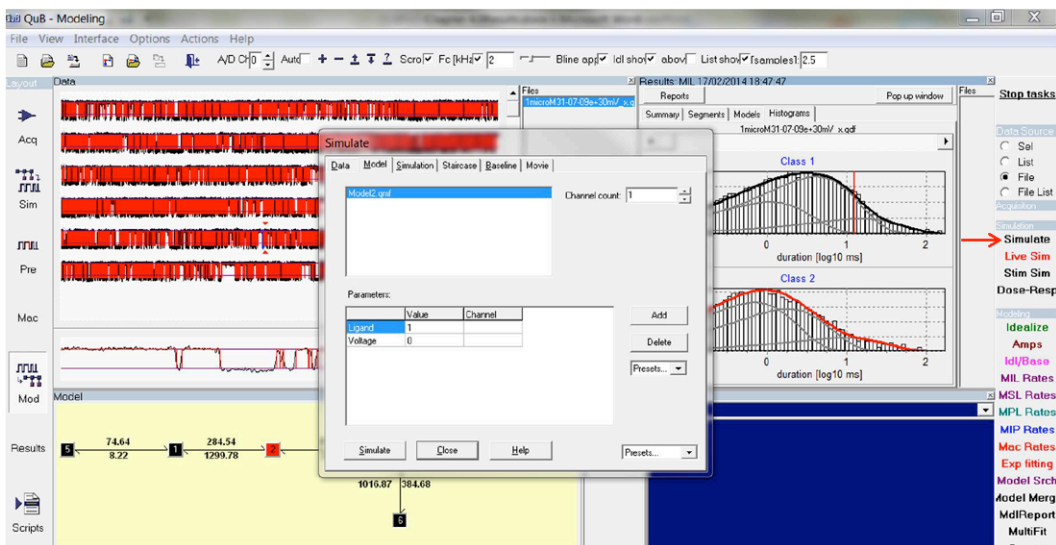
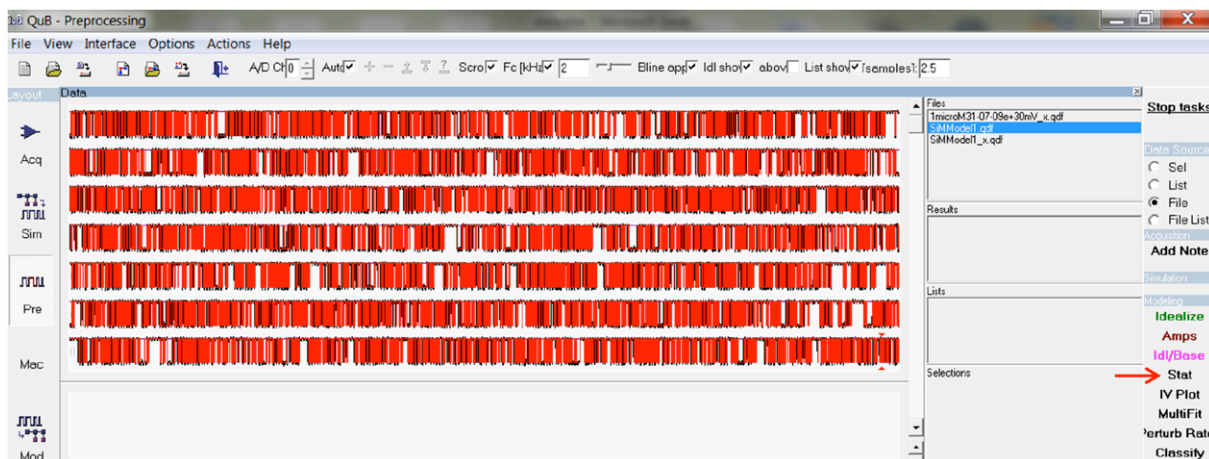


Figure 4.32. Simulation of single channel data using putative gating model.



**Figure 4.33. Idealised simulated single channel data from the putative gating scheme (Fig 4.25, Rank 1).** Kinetic parameters of the simulated data were computed using Stat function (red arrow) and compared with those from the experimental data (Table 4.5).

The simulated data thus generated were saved as a separate file and kinetic parameters calculated using the Stat (statistics) function in the right hand panel (preprocessing interface), which idealises the simulated trace (Fig 4.33; red arrow). In this example, the simulated data look very similar to the original data traces and the kinetic parameters are comparable (Table 4.5). The settings also allow customisable noise elements to be used in the simulation to mimic the actual traces.

**TABLE 4.5**

Data source	Closed Events	Open events	Closed time (ms)	Open time (ms)	Open probability
Experimental	5063	5062	2.15	0.8	0.2902
Simulated	5104	5103	2.27	0.87	0.293

## 4.5 Discussion

These analytical exercises involving RyR2 single channel data with varying levels of channel activity played a key role in the design of effective protocols for accurate quantification of channel gating behaviour. The HMM based programs permit the extraction of a wealth of information from single channel traces if appropriate algorithms with correct settings are employed. It is essential to understand the fundamental concepts underlying the analysis techniques in order to use them judiciously. Analysis of data emanating from various experiments involving RyR2 required considerable customisation of program settings that required extensive trials. The key steps involved in making the QuB program suitable for analysis of RyR2 has been described in this chapter. This provided me with powerful analytical tools to detect and describe mathematically, subtle changes in RyR2 gating behaviour with changing experimental conditions in the studies that follow.

## **Chapter 5.0**

**The biophysical characterisation of single RyR2 response to its primary physiological trigger: cytosolic Ca<sup>2+</sup>**

## 5.1 Introduction

Rhythmic contraction of cardiomyocytes is sustained by precisely controlled  $\text{Ca}^{2+}$  efflux from the SR stores that plays a pivotal role in the functional coupling between excitation of the sarcolemma and activation of the contractile apparatus. The pathophysiology of disease-induced perturbations of RyR2 mediated  $\text{Ca}^{2+}$  efflux have become a topic of intense investigation in recent years (Thomas et al. 2010; Venetucci et al. 2012; Belevych et al. 2013; Dobrev and Wehrens 2014). CPVT1 is an inherited autosomal dominant disease due to point mutations in the *RYR2* gene (>160 have been found till date and increasing), characterised by life-threatening adrenergic (exercise/emotional stress) mediated polymorphic ventricular tachyarrhythmia that could lead to sudden cardiac death (Leenhardt et al. 2012). RyR2 mutations have also been shown to be associated with hypertrophic cardiomyopathy, dilated cardiomyopathy, arrhythmogenic right ventricular dysplasia, atrial fibrillation and epilepsy (see **Chapter 1** for details). The CPVT1 related point mutations are mostly (~80%) found to be clustered into four regions in the channel protein (N terminal, central and two C-terminal regions; (Venetucci et al. 2012), most of the ones that have been characterised happen to be gain-of-function mutations (**Fig 5.1**). These cause instability in the channel protein leading to spontaneous aberrant  $\text{Ca}^{2+}$  release events (arrhythmogenic) that are not triggered by action potentials (Priori and S. R. W. Chen 2011). It is therefore interesting that mutation of only 1 out of 4,967 amino acid residues is sufficient to cause perturbed  $\text{Ca}^{2+}$  release regardless of their loci. Although several theories have been proposed, the underlying mechanisms of abnormal  $\text{Ca}^{2+}$  handling in RyR2 related channelopathy is a topic of active debate and investigation (see **Chapter 1**).

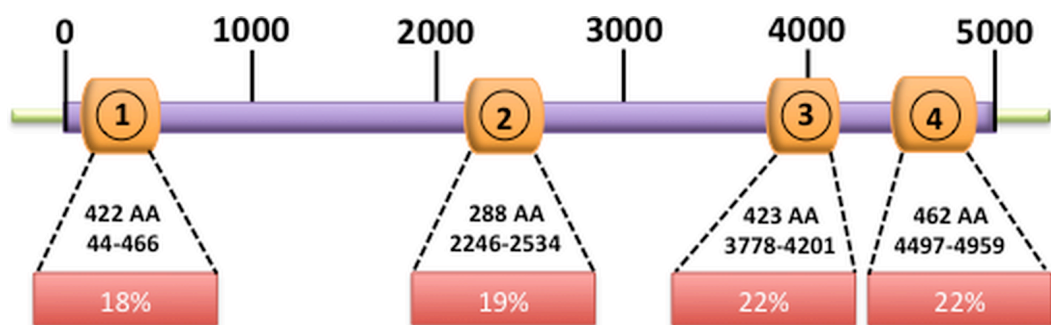


**Figure 5.1. Mutational clusters of RyR2.** The orange cylinders represent the clusters in the N-terminal region (1), central (2) and C-terminal regions (3&4) of RyR2. The amino acid (AA) ranges of the clusters are shown along with the percentages of reported mutations occurring in each cluster. Adapted from (Priori and S. R. W. Chen 2011).

### 5.1.2 The need for understanding RyR2 gating behaviour: employing minimal conditions.

An important approach to unravelling the mechanisms underlying aberrant RyR2 behaviour is to understand the effect of regulatory proteins and cellular processes as well as the direct consequences of mutations on the gating mechanisms of RyR2, but before this can be done, it is essential to have an accurate description of the gating kinetics of the wild type (WT) channel. As described in **Chapter 4**, real-time dynamics of RyR2 at a molecular level have been studied by incorporating them into planar lipid bilayers and recording the current flowing through individual channels. Published results have been obtained from channels incorporated into bilayers from several sources including native heavy SR preparations from animal tissues (Ashley and Williams 1990; W. Liu et al. 1998), intracellular membrane vesicles of cells in which recombinant RyR2 has been expressed (P. Li and S. R. Chen 2001; Tester et al. 2007) and channels purified from membrane preparations containing either native or recombinant channels (Lindsay et al. 1994; W. Chen et al. 2014). RyR2 incorporated from native SR membrane vesicles may or may not retain regulatory accessory proteins while many of these accessory proteins are absent from the cells in which recombinant RyR2 is expressed. In addition, the procedures used in the purification of RyR2 from membrane preparations are likely to separate the channel from other components of the channel complex. RyR2 function can also be modulated by many cellular regulatory agents including ATP,  $Mg^{2+}$ , cytosolic and luminal  $Ca^{2+}$  and by other cellular processes such as oxidation, phosphorylation, nitrosylation etc. (see **Chapter 1**). Also, most single channel studies examining the response of RyR to a large spectrum of  $[Ca^{2+}]_{cyt}$  have used only EGTA or BAPTA as calcium chelators (thereby offering a limited 'good' buffering range), leading to inaccurate final levels of free  $Ca^{2+}$ . It is therefore unsurprising that there are inconsistencies in the results from various groups as combinations of different starting material, permeant ions and modulatory factors have been used in single channel experiments and the models derived from such disparate data are similarly prone to discrepancies and hence are rarely comparable (Ashley and Williams 1990; Schiefer et al. 1995; Saftenku et al. 2001; Rosales et al. 2004; Zahradník et al. 2005; Laver 2007). Some of the previously published studies involving activation of RyR2 by  $[Ca^{2+}]_{cyt}$  are summarised in **Table 5.1** which illustrates the disparate experimental conditions.

Therefore, it is essential to first characterise the gating behaviour of the human RyR2 channel (hRyR2) in a minimal environment, isolated from accessory proteins where the sole activating ligand is cytosolic  $Ca^{2+}$  ( $[Ca^{2+}]_{cyt}$ ), such that the intrinsic mechanisms

involved in the modulation of open probability can be revealed. This novel approach will allow us to mathematically describe, in terms of a kinetic model, the behaviour of isolated RyR2 in response to  $[Ca^{2+}]_{cyt}$ . This will in turn provide a platform for modelling of the effects of physiological regulatory factors and dissecting out the mechanistic nature of the perturbations in mutant channels causing cardiovascular pathology.

### **5.1.3 Understanding RyR2 gating behaviour in terms of actual physical mechanisms**

The sophisticated HMM based tools for single channel data analysis that I adapted for RyR2 (**Chapter 4**) will be used for an accurate description in terms of putative kinetic models of single RyR2 behaviour when activated exclusively by  $[Ca^{2+}]_{cyt}$ . However, the lack of detailed RyR2 structural information makes it difficult for us to directly relate the observed state transitions to definite conformations during channel gating. Whereas in  $K^+$  channels, with the availability of crystallographic structural information, accurate structure-function correlation has been feasible (Doyle et al. 1998; Y. Jiang et al. 2002; Kuo et al. 2005; Long et al. 2007; Tao et al. 2009). However, ion permeation studies and structural modelling of the RyR2 pore region suggests several similarities (**Fig 1.8, Chapter 1**) with equivalent regions of the  $K^+$  channels (Williams et al. 2001; Williams 2002; Welch et al. 2004) and this information could point towards possible similar structural components of the RyR2 gating mechanism when seen in the light of single channel data.

## 5.2 Key Objectives

1. Combinations of disparate experimental conditions involving several external modulatory factors have prevented the unambiguous description of RyR2 gating behaviour in response to  $\text{Ca}^{2+}$ . This lack of consensus has prompted this study in which single channel gating kinetics of purified human RyR2 when activated solely by  $[\text{Ca}^{2+}]_{\text{cyt}}$  will be examined in detail under a stringently regulated environment where the modulatory influence of factors external to the channel are minimised.
2. HMM based programs (optimised in Chapter 4) will be employed to accurately detect changes in RyR2 gating behaviour with changing  $[\text{Ca}^{2+}]$ , resulting in gating models that convey in terms of actual physical mechanisms, the various state transitions observed.
3. RyR2 behaviour will also be compared with that of  $\text{K}^+$  channels for unravelling possible fundamental similarities in gating kinetics as their putative pore regions have been shown to be analogous.



**TABLE 5.1. Diverse experimental conditions in studies examining  $Ca^{2+}$  activation of single RyR2 channels.**

	<b>Published study</b>	<b>RyR2 channel protein source</b>	<b>Permeant ion</b>	<b>Range of <math>[Ca^{2+}]_{cyt}</math> and buffer used for RyR2 activation</b>	<b>Luminal <math>Ca^{2+}</math></b>	<b>Accessory proteins</b>	<b>Other ligands (activation/inhibition)</b>	<b>Single channel event detection method</b>
1	<i>Ashley and Williams 1990 J Gen Physiol.</i>	Sheep ventricular muscle (native) HSR vesicles	$Ca^{2+}$ (luminal-cytosolic)	0.1-100 $\mu M$ free $Ca^{2+}$ . Buffered using EGTA.	54 mM $Ca^{2+}$	May be present	1 mM ATP	50% threshold crossing
2	<i>Li and Chen 2001 J Gen Physiol.</i>	Purified recombinant mouse RyR2 & purified from canine native HSR.	$K^{+}$ current driven by voltage (luminal-cytosolic).	106 nM to 10.5 mM with 5 intermediate $Ca^{2+}$ conc. EGTA used as sole buffer.	Not specified.	Absent	Caffeine, ATP and $Mg^{2+}$ and ryanodine	50% threshold crossing
3	<i>Rosales, R.A et al. 2004 J Gen Physiol.</i>	Canine ventricular muscle heavy SR microsomes	$Cs^{+}$ current driven by voltage. ?Direction	1, 10 and 100 $\mu M$ $Ca^{2+}$ . Buffer used: unknown	20 $\mu M$ $Ca^{2+}$	May be present	None	HMMs and MCMC methods
4	<i>Tester, D.J et al. 2007 Heart Rhythm.</i>	Recombinant human RyR2 co-expressed with FKBP12.6 in HEK293 cells. Microsomal prep.	$Ba^{2+}$ current from luminal-cytosolic using 53 mM <i>trans</i> $Ba^{2+}$ .	From 90 nM to 5 $\mu M$ $Ca^{2+}$ buffered using EGTA.	Not specified	FKBP12.6	Some channels were PKA phosphorylated	50% threshold crossing
5	<i>Marjamaa, A et al. 2011 Int J of Cardiol.</i>	Recombinant human RyR2 co-expressed with FKBP12 in HEK293. Microsomal prep.	$Ba^{2+}$ current from luminal-cytosolic using 53 mM <i>trans</i> $Ba^{2+}$ .	350 nM, 700 nM & 1 $\mu M$ $Ca^{2+}$ buffered using EGTA.	Not specified	FKBP12	Some channels were PKA phosphorylated	50% threshold crossing
6	<i>Chen, H et al. 2013 J Gen Physiol.</i>	Rat & mouse heavy SR microsomes.	$Cs^{+}$ primary charge carrier (+40 mV <i>trans-cis</i> )	0.1 to 1000 $\mu M$ $Ca^{2+}$ buffered using EGTA.	1 mM or 0.1 mM $Ca^{2+}$	-/+ CASQ	$Mg^{2+}$ , ATP	50% threshold crossing

### 5.3 Experimental procedures

The optimisation of protocols for expression and purification of recombinant WT hRyR2 have been discussed in detail in **Chapters 2** and **3**. The purification step ensures the absence of interacting regulatory proteins such as FKBP12.6 (**Chapter 3**) and myocyte specific proteins calsequestrin, junctin and triadin that are absent in HEK293 cells (Stewart et al. 2008). The features of the minimal experimental conditions that were ensured in this study are summarised in **Table 5.2** below.

**TABLE 5.2. Minimal conditions in single channel experiments with hRyR2**

Experimental Conditions	References and notes
Cytosolic Ca <sup>2+</sup>	Stringently controlled using a cocktail of EGTA, HEDTA and NTA. Range:~0.7nM to 500μM.
Luminal Ca <sup>2+</sup>	Maintained at 50nM with EGTA as buffer.
Redox state	DTT used as reducing agent in protein isolation and purification protocols.
Luminal accessory proteins	HEK293 cells are devoid of Calsequestrin. Junctin and Triadin are also absent (myocyte proteins). Stewart et al., 2008.
FKBP12.6	No endogenous FKBP12.6 in HEK293 cells. See <b>Chapter 3</b> for data.

#### 5.3.1 Single channel recording

Formation of planar lipid bilayers for the incorporation of single channels has been explained in **Materials and Methods (Chapter 2)**. Briefly, an osmotic gradient was created by the addition of two aliquots (100 μl each) of 3 M KCl to the *cis* chamber to which the purified hRyR2 were then added. On stirring, hRyR2 incorporates into the bilayer in a fixed orientation such that the *cis* chamber corresponds to the cytosolic face of the channel and the *trans* chamber to the luminal face. After channel incorporation, symmetrical ionic conditions were re-instated by perfusion of the *cis* chamber with 210mM KCl. A holding potential of +30 mV was used for all single channel experiments.

Unlike most previous studies looking at the activation of RyR2 by  $\text{Ca}^{2+}$  (see **Table 5.1**), the free  $[\text{Ca}^{2+}]$  (cytosolic and luminal) was stringently regulated in this study using a cocktail of chelators and  $\text{CaCl}_2$ . EGTA, HEDTA and NTA were used at appropriate concentrations such that good buffering was maintained across the whole range of activation (according to MaxChelator, <http://www.stanford.edu/~cpatton/maxc.html>). EGTA provides adequate buffering at nM concentrations, HEDTA at  $\mu\text{M}$  and NTA at high  $\mu\text{M}$  to mM free  $\text{Ca}^{2+}$  (Patton et al. 2004). This was further verified using a calcium probe (Orion, Thermo Scientific). The luminal side (*trans* chamber) was buffered at 50 nM  $\text{Ca}^{2+}$  and free  $[\text{Ca}^{2+}]_{\text{cyt}}$  was gradually increased in steps from nominally zero  $\text{Ca}^{2+}$  ( $\sim 740$  pM) to 500  $\mu\text{M}$  in the *cis* chamber by the addition of  $\text{CaCl}_2$  aliquots (from a 20 mM  $\text{CaCl}_2$  stock solution in 210 mM KCl) to progressively activate the hRyR2. The steps of addition of  $\text{Ca}^{2+}$  buffers and aliquots of  $\text{CaCl}_2$  to achieve various final free  $[\text{Ca}^{2+}]$  are shown in detail in A4 (**Appendix I**). A previous study had reported the possible influence of  $\text{Cl}^-$  on RyR1 channel activity where increasing cytosolic  $[\text{Cl}^-]$  enhanced  $[\text{}^3\text{H}]$ -ryanodine binding (Meissner et al. 1997). The reason for this  $\text{Cl}^-$  sensitivity of RyR2 is unclear as no further studies have since examined this phenomenon at a single channel level. Nevertheless, KCl has been routinely used as recording solution in single channel studies where  $\text{K}^+$  as the permeant ion offers high signal-to-noise ratio and the data obtained from such experiments are in agreement with studies where other solutions were used. The incorporation of only a single channel in the bilayer was verified at the end of each experiment by examining the current traces where the hRyR2 was maximally activated by high *cis*  $\text{Ca}^{2+}$ . All experiments were performed in the ambient temperature range of  $21 \pm 2^\circ\text{C}$ .

### 5.3.2 Data analysis

The single channel data acquisition methods were explained in **Chapter 2** and HMM based data analysis techniques were discussed in the previous chapter (**Chapter 4**). Single channel current traces of 2-3 minutes were idealised using the SKM based program (Idealise function) and also Idl/Base function in QuB (in case of noisy data) which utilises the iterative HMM-based Baum-Welch expectation maximization algorithm while tracking baseline using a Kalman filter. Idealisation of the single channel current recordings results in the calculation of kinetic parameters such as the mean amplitude, the open probability ( $P_o$ ), median open ( $T_o$ ) and closed ( $T_c$ ) durations. A dead time of 75-120  $\mu\text{s}$  was imposed during idealisation and an initial two state  $\text{C} \leftrightarrow \text{O}$

scheme was used. As explained previously (**Chapter 4**), shorter dead times were suitable for detection of short-lived single channel events which dominate current traces at very low or high  $[Ca^{2+}]_{\text{cyt}}$ .

In spite of there being no substantial evidence relating to the number, location and architecture of the activating  $Ca^{2+}$  binding sites on cytoplasmic domain of RyR2, some of the previous gating models have made prior assumption of there being four identical binding site per channel (one per subunit) (Saftenku et al. 2001; Zahradník et al. 2005). Therefore, the current study avoids imposing kinetic constraints based on a prior assumption of an arbitrary number of  $Ca^{2+}$  binding sites to avoid bias. Moreover, it is also not known whether such  $Ca^{2+}$  binding sites are functionally independent or if there is a cross talk.

Data sets from single channel experiments used in this study (n=12) were acquired both by me (n=8) and Dr N.L Thomas (n=4) who is also my PhD co-supervisor. This served as a robust quality control to minimise the chances of errors due to experimental and analytical variations. These channels were derived from 4 separate purified hRyR2 protein preparations made from transfections done at different times; this ensured that any biological heterogeneity, if present, will be revealed and incorporated in the results.

## 5.4 Results

Like all ion channels, individual RyR2s show an inherent variability at the single molecule level. Random thermodynamic fluctuations occur within each channel while it globally passes through a spectrum of possible conformations. Therefore, at the single channel level, no two individual RyR2s are exactly the same in terms of kinetic parameters but when many such channels are examined over a sufficiently long period of time, they show some striking similarities in gating behaviour. In this study, data from 12 single channels were analysed and various kinetic parameters were determined using the methods explained in **Chapter 4 (Fig 5.2)**. Data from 8 different single channels over the whole range of  $\text{Ca}^{2+}$  activation were further analysed in detail to establish a putative kinetic model that would account for the major features of the  $[\text{Ca}^{2+}]_{\text{cyt}}$ -dependent kinetics of hRyR2. There is an overall similarity in the shape of the resulting  $\text{Ca}^{2+}$  activation curve with similar kinetic parameters (**Fig 5.4**) but the absolute values ( $\text{EC}_{50}$ , Hill slope, transition rate constants etc.) showed a degree of variability as is to be expected given that each channel is a distinct single functional molecule. Thus in some instances for clarity, data pertaining to the gating schemes are shown for one representative channel (channel 1 in **Fig 5.2**).

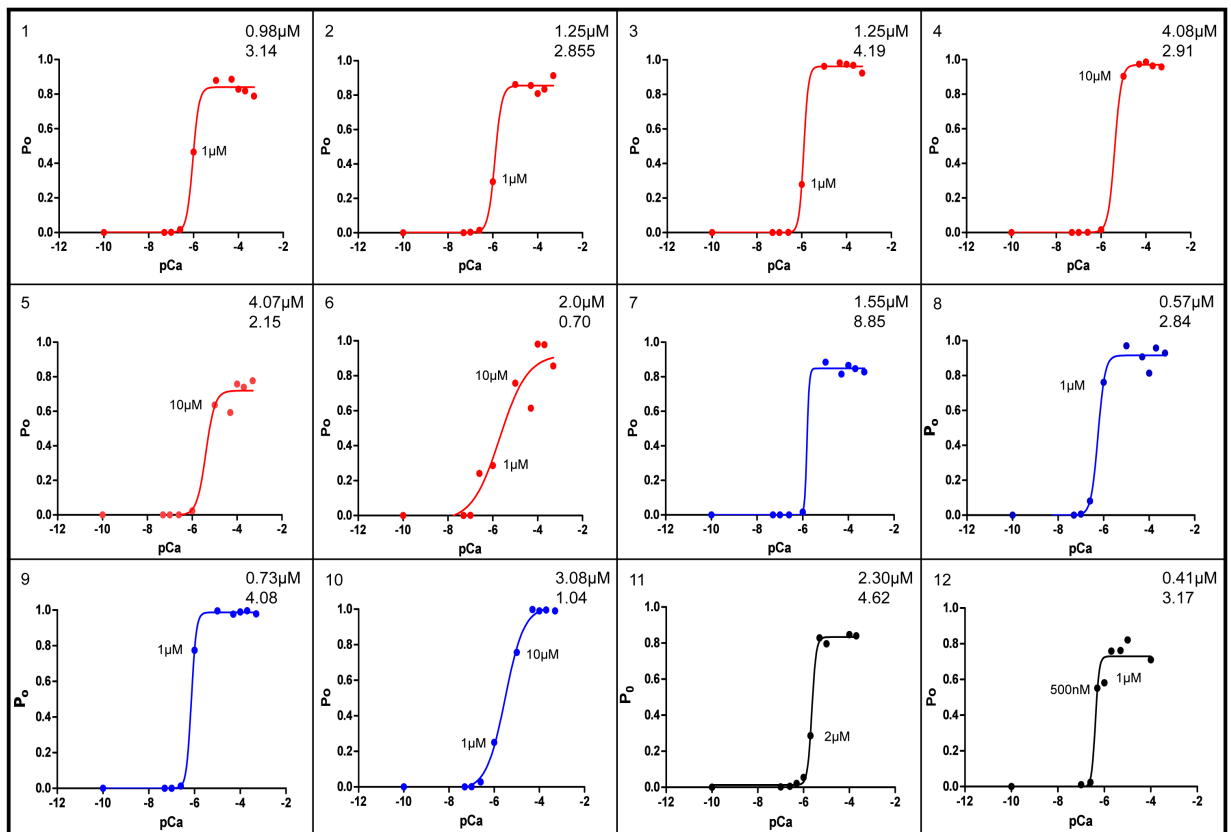


**Figure 5.2.  $\text{Ca}^{2+}$  activation profiles for 12 hRyR2 channels (0-500  $\mu\text{M}$ ) showing functional variability at single molecule level.** These are colour coded as follows: Red – channels recorded at 0, 0.05, 0.1, 0.25, 1, 10, 50, 100, 200 and 500  $\mu\text{M}$   $[\text{Ca}^{2+}]_{\text{cyt}}$ , and were all analysed by Maximum interval likelihood (MIL) fitting. Blue – channels recorded at the same concentrations as above, but data either showed periods of modal gating at  $P_o \geq 0.8$  resulting in increased  $T_o$  values (channels, 8, 9 and 10 see Figure 2C) or did not exhibit any intermediate open probabilities (channel 7) and were therefore not included in any further analysis. Black – channels recorded at additional intermediate concentrations (0, 0.1, 0.25, 0.5, 1, 2, 5, 10, and 100  $\mu\text{M}$   $[\text{Ca}^{2+}]_{\text{cyt}}$  (and 200  $\mu\text{M}$  for channel 11)  $[\text{Ca}^{2+}]_{\text{cyt}}$ , and were also analysed by Maximum interval likelihood fitting. Individual  $\text{EC}_{50}$  and Hill coefficient measurements are given in each top right-hand corner.

#### 5.4.1 Activation of RyR2 by increasing $[Ca^{2+}]_{cyt}$

Single channel current recordings from twelve individual WT hRyR2 channels were analysed in total for Po, To and Tc measurements. Each channel was studied at 10-13 different  $[Ca^{2+}]_{cyt}$  levels ranging from nominally zero to 500  $\mu$ M (0, 0.05, 0.1, 0.25, 0.5, 1, 2, 5, 10, 50, 100, 200 and 500  $\mu$ M  $[Ca^{2+}]_{cyt}$ ). The luminal  $Ca^{2+}$  was 50 nM and the bilayer was held at +30 mV for all experiments. The channels showed a sharp increase in Po with increasing  $[Ca^{2+}]_{cyt}$  as seen in the representative steady-state current traces (**Fig 5.3**). The current amplitude progressively decreases with increasing  $[Ca^{2+}]_{cyt}$  as the relative permeability of  $Ca^{2+}$  is approximately six times that of  $K^+$ . As  $Ca^{2+}$  increasingly occupies the pore, the current amplitude decreases due to the lower conductance of  $Ca^{2+}$  compared to  $K^+$  (Williams et al. 2001).

The rise in Po was more than 100-fold (**Fig 5.4 A**) with a 10-fold rise in  $Ca^{2+}$  (100 nM - 1  $\mu$ M) but less than a 4-fold rise was seen with a further increase in  $[Ca^{2+}]_{cyt}$  (1  $\mu$ M - 10  $\mu$ M). An increase in  $Ca^{2+}$  beyond  $\sim$ 10  $\mu$ M sees the channel Po reach saturation levels ( $0.89 \pm 0.025$ , n=12). The dependence of Po on cytosolic  $Ca^{2+}$  for the 12 individual channels is shown in **Figure 5.2**. Preliminary analyses (of channels 1-10) established that the cytosolic  $Ca^{2+}$  activation profile of hRyR2 is steep (occurs over a very narrow range). Using these conditions, the majority of plots had only one or two points on the activation phase and the  $Ca^{2+}$  concentrations at which these points occurred showed a degree of channel-to-channel variation. In an attempt to obtain more data points in this rising phase of the relationships, (such that more intermediate channel conformations could be resolved) I carried out additional experiments (channels 11 and 12, **Fig 5.2**), which included intermediate  $Ca^{2+}$  concentrations (500 nM, 2  $\mu$ M and 5  $\mu$ M). However, even when these intervening  $Ca^{2+}$  concentrations were included, the steep dependence of Po on cytosolic  $Ca^{2+}$  (a necessity for RyR2 to function as an effective  $Ca^{2+}$ -release channel during excitation-contraction coupling) meant that for any individual channel it was not possible to acquire more than 2 points of different Po on the rising phase of the curve.

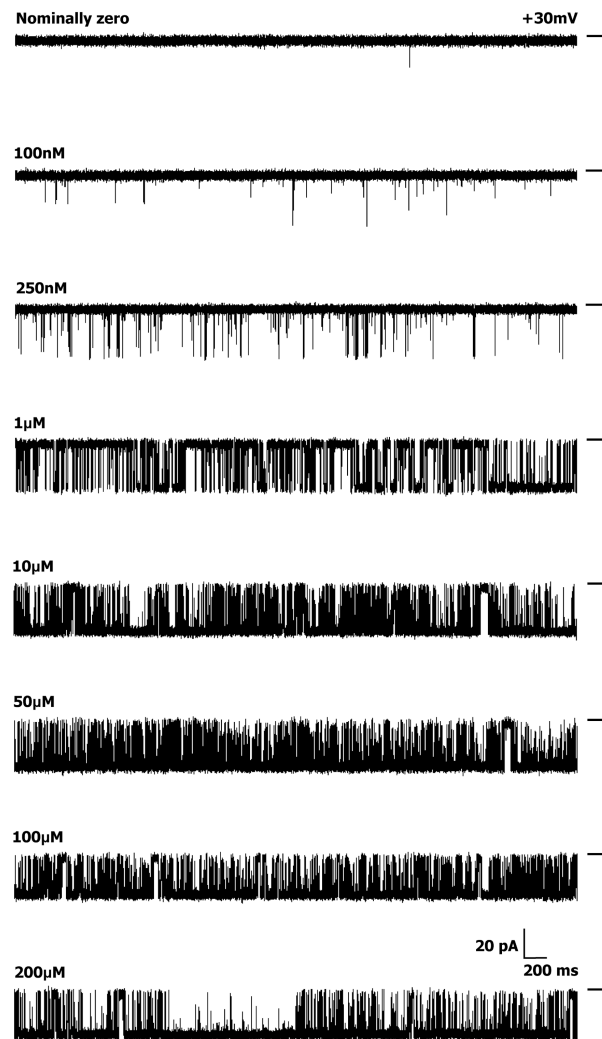


**Figure 5.3. A single WT hRyR2 channel activation by  $[Ca^{2+}]_{cyt}$ .** Representative current traces demonstrate the progressive activation of a single representative channel by  $[Ca^{2+}]_{cyt}$  from nominally zero to 200  $\mu M$ . Luminal  $Ca^{2+}$  was fixed at 50 nM and the bilayer was voltage clamped at +30 mV for all experiments. The permeant ion was  $K^+$  with both chambers having symmetrical solutions (210mM KCl). The short bars to the right of each trace represent the closed level of the channel and opening events are downward deflections from the baseline.

Pooled data for all twelve channels are shown in **Fig 5.4**, colour coded as in **Fig 5.2** (red: channels which were analysed for building the kinetic model, blue; channels which were not analysed further (see below), black; channels where additional intermediate  $[Ca^{2+}]_{cyt}$  were included were also analysed for the kinetic model). The data were fitted with a log [agonist] vs. response curve, which gave an  $EC_{50}$  of  $1.65 \pm 0.43 \mu M$  ( $n=12$ ). Closed times ( $T_c$ ) show a decreasing trend with increasing  $P_o$  (**Fig 5.4 B**), whereas the open times ( $T_o$ ) in **Fig 5.4 C** do not show a significant change with increasing channel open probability except in a few cases where the  $P_o$  is nearing 1.0. This is because on



occasions (in 3 of the 12 channels studied, see **Fig 5.2**, channels 8-10), very high open probabilities at high  $[Ca^{2+}]_{cyt}$  were observed which resulted in data points (coloured blue) where  $T_o \geq 12$  ms (**Fig 5.4 C**). The portions of traces representing these long channel openings were not included in subsequent analysis (see example data in **A2, Appendix I**) as the aim was to describe the typical gating behaviour of the RyR2 that is predominantly observed in the single channel current recordings for various  $[Ca^{2+}]_{cyt}$ . Also, due to the paucity of such long opening events, it is not feasible to analyse them in probabilistic terms in the present study. The closed and open times suggest that  $[Ca^{2+}]_{cyt}$  binds to the closed channel and increases its open probability by increasing the frequency of openings. The channels were at first incorporated in 210 mM symmetrical KCl solutions where they were being activated by contaminant  $[Ca^{2+}]_{cyt}$  which was then buffered to nominally zero using EGTA, HEDTA and NTA (thereby closing the channels) before being progressively activated by the addition of  $CaCl_2$  aliquots. This process directly demonstrates the reversibility of the  $Ca^{2+}$ -dependent activation of purified recombinant hRyR2 channels.

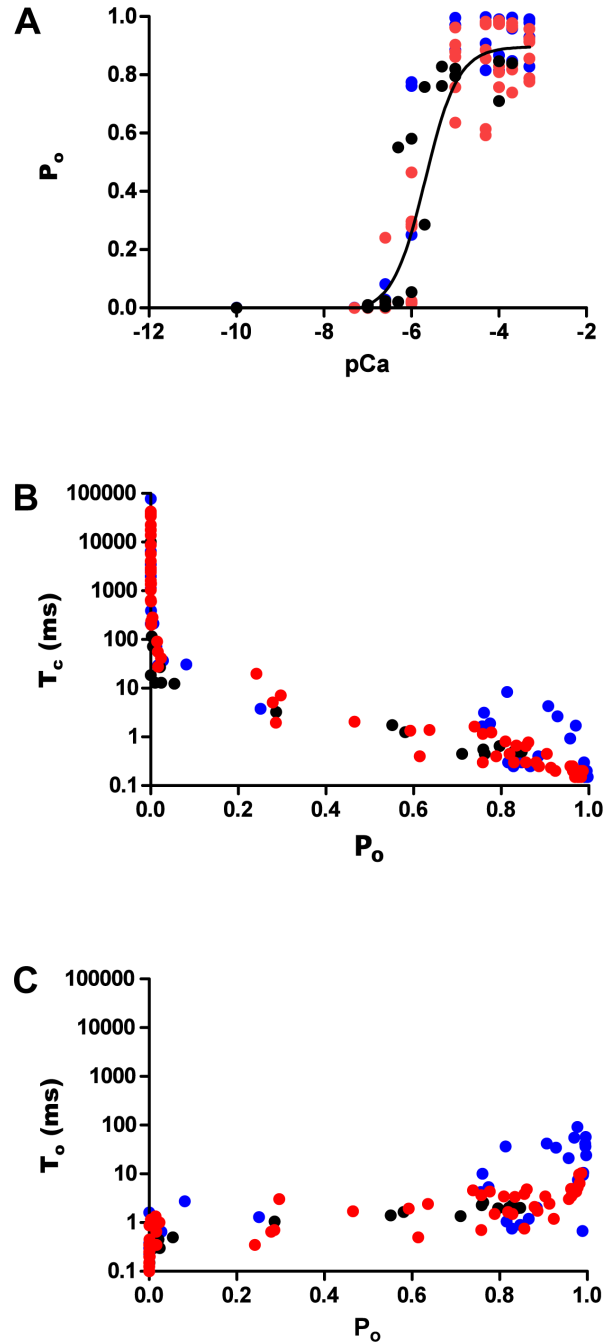


**Figure 5.4 Kinetic parameters of hRyR2 gating.** Data were obtained from the full range (0-500  $\mu\text{M}$ ) of  $\text{Ca}^{2+}$  activation for 12 individual channels. (A) Effect of  $[\text{Ca}^{2+}]_{\text{cyt}}$  on  $P_o$  where a sigmoidal relationship is observed upon fitting the pooled data points with a log [agonist] vs. response curve ( $\text{EC}_{50} = 1.65 \pm 0.43 \mu\text{M}$ , Hill coefficient =  $1.78 \pm 0.69$ ;  $n=12$  datasets) (B) Pooled data points from the 12 channels showing the relationship between  $P_o$  and  $T_c$ , (C) shows the relationship of  $P_o$  with  $T_o$ . The data points are colour coded according to their origin from the 12 individual channels as shown in Fig 5.2.

## 5.4.2 Dwell time distributions point towards underlying mechanisms

The aim of this work is to understand in simple terms, the predominant gating behaviour of the human cardiac ryanodine receptor when activated solely by its physiological ligand  $[Ca^{2+}]_{cyt}$ . In order to develop a putative gating model, the gating kinetics of 8 WT hRyR2 channels were studied over the whole range of  $[Ca^{2+}]_{cyt}$ . For recordings where the  $[Ca^{2+}]_{cyt}$  was below 250 nM, insufficient events were available for accurate fitting of dwell-time histograms due to the very low open probabilities. For this reason, I have shown fits of dwell-time sequences with sums of exponentials for data obtained at 250 nM  $Ca^{2+}$  and above (**Fig 5.5**, fits for one representative channel are shown). Robust maximum likelihood fitting described the data accurately using three exponential components each for open and closed time distributions at lower  $[Ca^{2+}]_{cyt}$  and three closed and four open components at  $[Ca^{2+}]_{cyt}$  of 10  $\mu$ M and above. Therefore, a minimum of three closed and three to four open states were required to be incorporated in the kinetic schemes for an accurate description of the single channel data.

The time constants ( $\tau$ ) and the relative areas (%) under each exponential component for both open and closed distributions for all 8 channels (presented as means  $\pm$  SEM, states are labelled in accordance with **Fig 5.6B**) were examined for shifts with increasing channel activity (**Table 5.3**). The duration and population of the longer closed states show a decreasing trend with an increase in channel  $P_o$ , while the population of the shortest closed state increases. The channel progressively occupies the longer open states ( $O_2$  and  $O_3$ ) rather than the shortest as  $[Ca^{2+}]_{cyt}$  increases from 250nM to 200 $\mu$ M, and an additional open state ( $O_4$ , longest) is required to describe gating towards saturating  $[Ca^{2+}]_{cyt}$ . This may occur due to stabilisation of the channel in various open states with longer dwell-times as more ligand ( $Ca^{2+}$ ) binds to the RyR2. Various candidate models with their corresponding transition rates generated simultaneously during the process of fitting the dwell-time sequences using MIL were considered and the top four schemes were ranked according to their maximum likelihood values. The models with the highest ranking were the same for each of the 8 channels analysed and therefore most likely provide the best description of the single channel data (see section 4.4.8.1, **Chapter 4** for details). The top ranked models for one representative channel are shown in **Table 5.4**. The likelihood values for the various individual models change with increasing  $[Ca^{2+}]_{cyt}$  and channel  $P_o$  since more events were detected for similar durations of channel activity (see **Fig 5.3**).

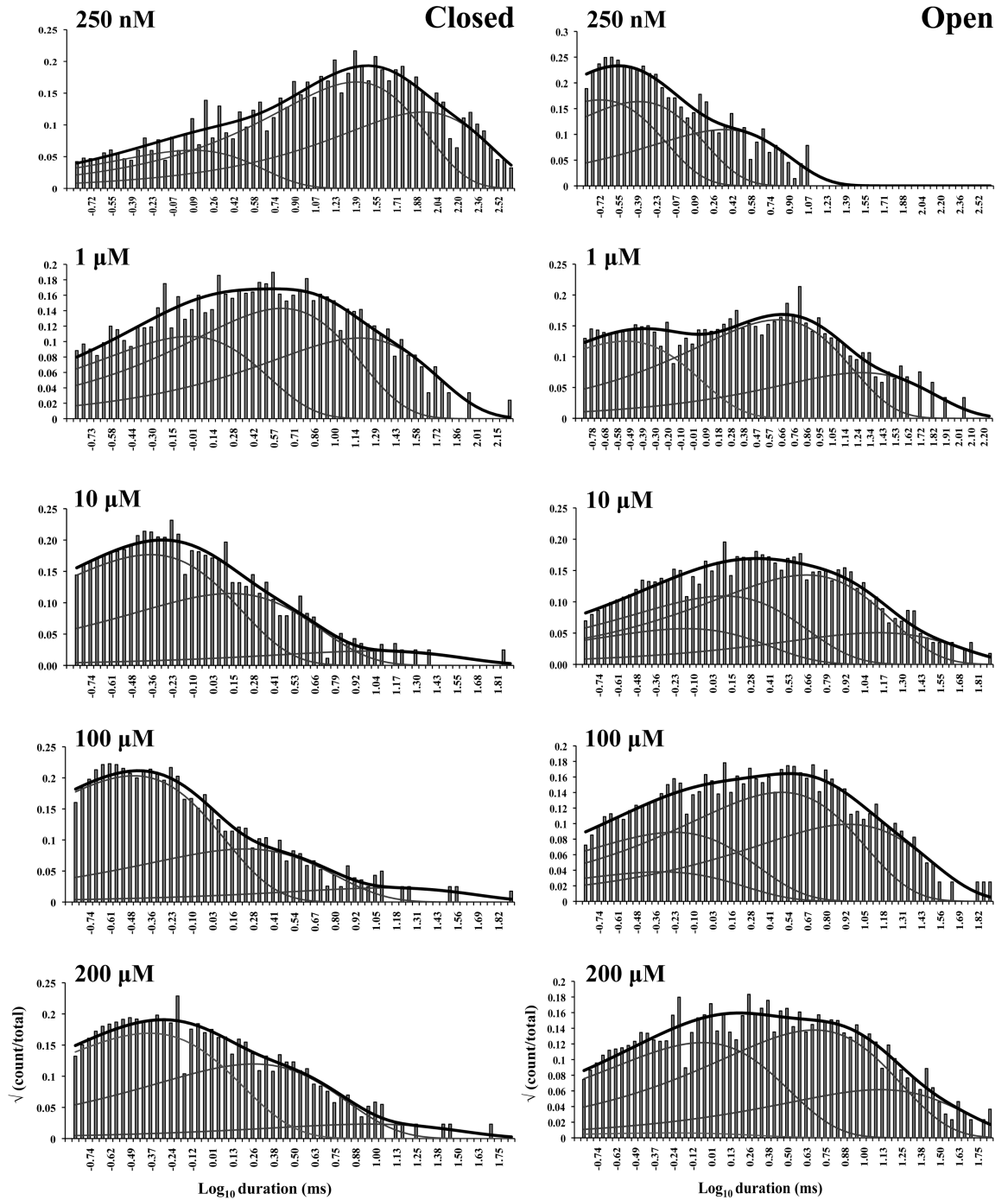


**Figure 5.5.** Closed and open dwell-time histograms from a single representative channel recorded at various activating  $[Ca^{2+}]_{\text{cyt}}$ , fitted with sums of exponential curves. The black curve on each histogram represents the overall fit and the three or four grey curves underneath show the individual fits. The activating  $[Ca^{2+}]_{\text{cyt}}$  are shown on the top left corner of each histogram.

**TABLE 5.3**

*Time constants and relative areas for exponential fits of dwell-time distributions*

Channel Activity		CLOSED		OPEN		
		$\tau$ (ms)	Area (%)	$\tau$ (ms)	Area (%)	
Sub-activating $P_o < 0.1$ (0.25-1 $\mu\text{M}$ )	$C_I$	$1.55 \pm 0.93$	$16.08 \pm 4.67$	$O_{UL}$	$0.19 \pm 0.04$	$42.50 \pm 7.82$
	$C_R$	$29.21 \pm 13.37$	$70.65 \pm 8.13$	$O_1$	$0.72 \pm 0.26$	$49.00 \pm 0.82$
	$C_{NR}$	$51.23 \pm 25.60$	$15.15 \pm 6.71$	$O_2$	$10.4 \pm 10.4$	$13.33 \pm 13.03$
Activating $P_o 0.1-0.6$ (1-5 $\mu\text{M}$ )	$C_F$	$0.92 \pm 0.40$	$13.74 \pm 5.41$	$O_1$	$0.40 \pm 0.06$	$36.04 \pm 7.30$
	$C_R$	$8.71 \pm 1.82$	$45.34 \pm 6.82$	$O_2$	$2.27 \pm 0.33$	$43.73 \pm 0.33$
	$C_{NR}$	$35.81 \pm 7.97$	$37.56 \pm 9.84$	$O_3$	$9.69 \pm 1.72$	$11.80 \pm 1.81$
Low saturating $P_o > 0.65$ (2-10 $\mu\text{M}$ )	$C_F$	$0.41 \pm 0.03$	$50.4 \pm 5.97$	$O_1$	$1.02 \pm 0.28$	$15.12 \pm 6.87$
	$C_R$	$0.94 \pm 0.27$	$47.11 \pm 6.17$	$O_2$	$1.53 \pm 0.61$	$28.70 \pm 6.15$
	$C_{NR}$	$30.27 \pm 16.09$	$1.73 \pm 0.55$	$O_3$	$5.67 \pm 1.09$	$38.91 \pm 3.32$
				$O_4$	$28.09 \pm 11.56$	$9.91 \pm 4.07$
High saturation $P_o > 0.8$ (100-200 $\mu\text{M}$ )	$C_F$	$0.36 \pm 0.03$	$54.21 \pm 3.96$	$O_1$	$1.53 \pm 0.36$	$17.68 \pm 4.87$
	$C_R$	$0.83 \pm 0.15$	$41.90 \pm 3.82$	$O_2$	$2.08 \pm 0.50$	$33.44 \pm 3.76$
	$C_{NR}$	$12.23 \pm 3.80$	$1.02 \pm 0.15$	$O_3$	$10.93 \pm 1.19$	$40.39 \pm 5.94$
				$O_4$	$64.14 \pm 33.92$	$6.08 \pm 3.53$

### 5.4.3 Model-based description of RyR2 activation by cytosolic Ca<sup>2+</sup>

The top-ranked kinetic schemes provide a description of the behaviour of hRyR2 when activated solely by [Ca<sup>2+</sup>]<sub>cyt</sub>. However, no single model directly derived by fitting of the single channel data can describe the gating behaviour of the channel across the whole activation range, this was found to be the case for all 8 channels studied. Drastic shifts in RyR2 gating kinetics during channel activation by increasing [Ca<sup>2+</sup>]<sub>cyt</sub> are evident in the dwell-time histograms (**Fig 5.5**), which show abrupt changes particularly from 250 nM to 10 μM [Ca<sup>2+</sup>]<sub>cyt</sub>. This makes it impossible to fit single channel data simultaneously across the whole range of [Ca<sup>2+</sup>]<sub>cyt</sub> with a single mechanistic scheme. While one particular [Ca<sup>2+</sup>]<sub>cyt</sub> stabilises certain closed and open conformations, not all of these are observed as discrete states at other Ca<sup>2+</sup> concentrations. Furthermore, it was not possible to observe dwell-time distributions from further intermediate Pos due to the inherent steep dependence of the channel on activating [Ca<sup>2+</sup>]<sub>cyt</sub>. However, the similar single channel kinetics and shape of dwell-time histograms at 10 μM [Ca<sup>2+</sup>]<sub>cyt</sub> and above permit global fitting which gives a common scheme and set of rate constants that can describe RyR2 gating kinetics in that range of [Ca<sup>2+</sup>]<sub>cyt</sub>.

**TABLE 5.4**  
*Kinetic schemes ranked according to maximum likelihood values*

Rank	[Ca <sup>2+</sup> ] <sub>cyt</sub> (μM)			
	0.25	1	10	200
1	$\begin{array}{c} C_1 \leftrightarrow C_2 \leftrightarrow C_3 \leftrightarrow O_2 \leftrightarrow O_3 \\ \downarrow \\ O_1 \end{array}$	$\begin{array}{c} C_1 \leftrightarrow C_2 \leftrightarrow O_1 \leftrightarrow O_2 \leftrightarrow O_3 \\ \downarrow \\ C_3 \end{array}$	$\begin{array}{c} C_2 \leftrightarrow O_1 \leftrightarrow O_2 \leftrightarrow O_3 \leftrightarrow O_4 \\ \downarrow \quad \downarrow \\ C_1 \quad C_3 \end{array}$	$\begin{array}{c} C_2 \leftrightarrow O_1 \leftrightarrow O_2 \leftrightarrow O_3 \leftrightarrow O_4 \\ \downarrow \quad \downarrow \\ C_1 \quad C_3 \end{array}$
	4238.86	7784.72	17918.27	19859.37
2	$\begin{array}{c} C_1 \leftrightarrow C_2 \leftrightarrow O_2 \leftrightarrow O_3 \\ \downarrow \quad \downarrow \\ O_1 \quad C_3 \end{array}$	$\begin{array}{c} C_1 \leftrightarrow C_2 \leftrightarrow O_1 \leftrightarrow O_2 \leftrightarrow O_3 \\ \downarrow \\ C_3 \end{array}$	$\begin{array}{c} C_2 \leftrightarrow O_1 \leftrightarrow O_2 \leftrightarrow O_3 \leftrightarrow O_4 \\ \downarrow \quad \downarrow \\ C_1 \quad C_3 \end{array}$	$\begin{array}{c} C_2 \leftrightarrow O_1 \leftrightarrow O_2 \leftrightarrow O_3 \leftrightarrow O_4 \\ \downarrow \quad \downarrow \\ C_1 \quad C_3 \end{array}$
	4236.06	7774.30	17903.58	19845.04
3	$\begin{array}{c} C_1 \leftrightarrow C_2 \leftrightarrow O_1 \leftrightarrow O_2 \leftrightarrow O_3 \\ \downarrow \\ C_3 \end{array}$	$\begin{array}{c} C_1 \leftrightarrow C_2 \leftrightarrow C_3 \leftrightarrow O_1 \leftrightarrow O_2 \\ \downarrow \\ O_3 \end{array}$	$\begin{array}{c} C_2 \leftrightarrow C_3 \leftrightarrow O_1 \leftrightarrow O_2 \leftrightarrow O_3 \\ \downarrow \quad \downarrow \\ C_1 \quad O_4 \end{array}$	$\begin{array}{c} C_2 \leftrightarrow C_3 \leftrightarrow O_1 \leftrightarrow O_2 \leftrightarrow O_3 \\ \downarrow \quad \downarrow \\ C_1 \quad O_4 \end{array}$
	4236.06	7268.40	17875.44	19819.38
4	$\begin{array}{c} C_1 \leftrightarrow C_2 \leftrightarrow C_3 \leftrightarrow O_2 \leftrightarrow O_3 \\ \downarrow \\ O_1 \end{array}$	$\begin{array}{c} C_1 \leftrightarrow C_2 \leftrightarrow O_1 \leftrightarrow O_2 \leftrightarrow O_3 \\ \downarrow \\ C_3 \end{array}$	$\begin{array}{c} C_2 \leftrightarrow O_1 \leftrightarrow O_2 \leftrightarrow O_3 \leftrightarrow O_4 \\ \downarrow \quad \downarrow \\ C_1 \quad C_3 \end{array}$	$\begin{array}{c} C_2 \leftrightarrow O_1 \leftrightarrow O_2 \leftrightarrow O_3 \leftrightarrow O_4 \\ \downarrow \quad \downarrow \\ C_1 \quad C_3 \end{array}$
	4230.08	7765.82	17874.50	19819.15

**Fig 5.6A** shows kinetic schemes that provide snapshot descriptions of WT hRyR2 gating behaviour during the three stages of channel activation by  $[Ca^{2+}]_{\text{cyt}}$ . At low, or sub-activating levels of  $Ca^{2+}$ , channel activity is dominated by low  $P_o$  and long closed times (as seen in **Fig 5.4B**) and is represented by a scheme with three closed and three open states (light blue panel, corresponding to the top-ranked scheme in **Table 5.4**, 0.25  $\mu\text{M}$ ). Further increase in  $[Ca^{2+}]_{\text{cyt}}$  causes a sudden increase in  $P_o$  with significantly shorter closed times and this is represented by a different scheme with three closed and three open states (green panel, corresponding to **Table 5.4**, 1  $\mu\text{M}$ ). Finally at higher  $[Ca^{2+}]_{\text{cyt}}$  the channel exhibits a very high  $P_o$  with short closed times. For a description of gating at this range of  $[Ca^{2+}]_{\text{cyt}}$  ( $\geq 10 \mu\text{M}$ ), three closed and four open states are required to be incorporated into the kinetic scheme (red panel, corresponding to **Table 5.4**, 10-200  $\mu\text{M}$ ). However, in this study I attempt to understand the gating behaviour of hRyR2 not only in terms of open and closed states in kinetic schemes but also in terms of actual physical mechanisms underlying those states. Hence, these kinetic snapshots along with the time constants and their relative areas (**Table 5.3**) as well as the transition rates (shown for one representative channel in **Table 5.5**) allowed us to model channel activity in terms of conformational states at the three stages of activation (shown in **Fig 5.6B**, **schemes I-III**). The stochastic single channel activity of RyR2, like other ion channels, is prone to intermolecular variability as illustrated through variability in  $EC_{50}$  and Hill coefficient (**Fig 5.2**). While these slight differences in channel activity between the single RyR2s studied at given  $[Ca^{2+}]_{\text{cyt}}$  were reflected in the rate constants of state transitions in the gating models, gating data from all eight channels examined best fitted the gating schemes derived (**Fig 5.6B**), and the variability present is evident in the standard errors of **Table 5.3**.

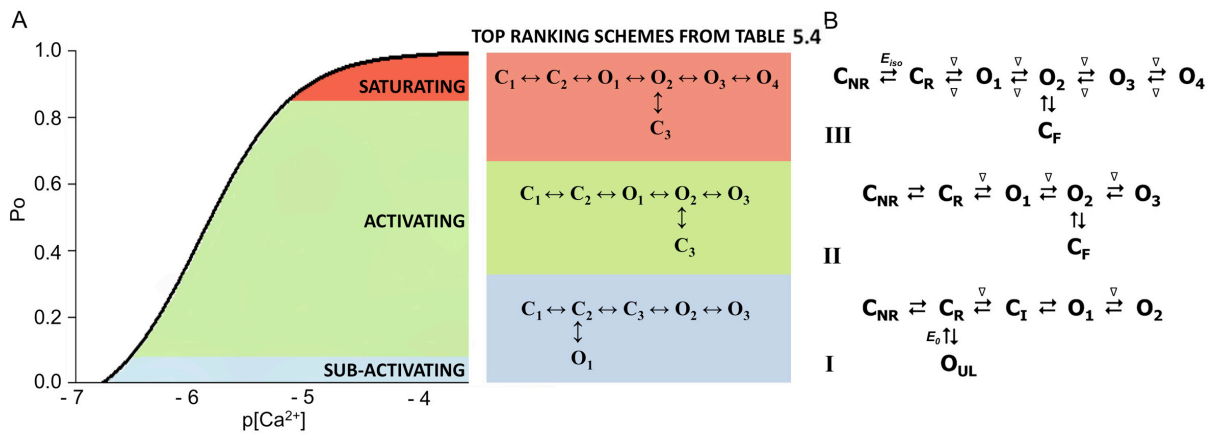


**Figure 5.6. Kinetic schemes to describe hRyR2 gating behaviour during activation by  $[Ca^{2+}]_{cyt}$ .** Fig 5.6A shows the three stages of activation of RyR2 namely, the subactivation, activation and near saturation/saturation phases designated along a sigmoidal dose response curve as light blue, green and red respectively. The top-ranking kinetic schemes (from Table 5.4) that best describe the gating behaviour of the channel at those corresponding stages of activation are shown in the coloured panels. Fig 5.6B gives a mechanistic perspective to the various closed and open states as interpreted from the results (schemes I, II and III). Here  $C_{NR}$  and  $C_R$  are the  $Ca^{2+}$  non-responsive and responsive closed states respectively while  $C_F$  is the flicker closing state from  $Ca^{2+}$  bound open states  $O_1$ ,  $O_2$ ,  $O_3$ , and  $O_4$  etc. The unliganded open state is represented by  $O_{UL}$  while the subscripts 1, 2, 3, 4 etc. depict open states of the channel with increasing amounts of  $Ca^{2+}$  bound, though it should be noted that the numbers in the subscript do not in any way refer to the actual number of  $Ca^{2+}$  ions bound to the channel. The  $[Ca^{2+}]_{cyt}$  dependent transitions are labelled by  $\nabla$  above and below the arrows.  $E_{iso}$  is the equilibrium constant of the transition between  $C_{NR}$  and  $C_R$  while  $E_0$  is that for constitutive channel activation.

#### 5.4.4 Observed state transitions in terms of putative mechanisms

Ion channels are known to open spontaneously without binding to agonist molecules. This phenomenon is known as constitutive or unliganded gating, and probably occurs due to intrinsic thermodynamic fluctuations in the protein molecule (Monod et al. 1965; Jackson 1984; Tibbs et al. 1997; Grosman and Auerbach 2000; Talukder and Aldrich 2000). In the single channel recordings at nominally zero  $[Ca^{2+}]_{cyt}$ , very brief openings have been observed but are rare ( $P_o = 8.42 \times 10^{-5} \pm 0.6 \times 10^{-5}$ ;  $n = 11$  channels) and last  $0.14 \pm 0.03$  ms ( $n=11$  channels). The population of open duration with the smallest  $\tau$  is the most likely candidate that represents the unliganded opening activity of RyR2 and is represented in the gating model for sub-activating  $[Ca^{2+}]_{cyt}$  as the  $C_2 \leftrightarrow O_1$  transition (light blue panel, Fig 5.6A), and assigned  $O_{UL}$  in the corresponding scheme (I, Fig 5.6B). However, with increasing  $P_o$  (i.e. increasing  $[Ca^{2+}]_{cyt}$ ) it becomes more unlikely that all the  $Ca^{2+}$  binding sites in RyR2 remain unoccupied at any given time, making constitutive



gating a very rare occurrence. Hence, this component cannot be resolved in gating schemes at  $[Ca^{2+}]_{cyt} \geq 1 \mu M$  (models in green and red panels of **Fig 5.6A**, schemes II and III of **Fig 5.6B**). In addition, it should be noted that the area under the exponential component fitting the shortest open duration will also include some longer dwell times due to overlapping with the adjacent distribution, hence the  $\tau$  and relative area values will be slightly overestimated for  $O_{UL}$ .

The first closed state  $C_1$  is not directly linked to any open states (very low likelihood) in any of the models and the channel needs to pass through at least one more closed state before it can open constitutively or when ligand-bound (all schemes, **Fig 5.6A**). For this reason, it is described as a putative non-responsive closed state ( $C_{NR}$ , **Fig 5.6B**). The non-responsive nature of this closed state to activation is characterised by the fact that it is discretely resolved and has a long duration ( $\tau = 12.23 \pm 3.8$  ms;  $n=8$  channels) even at saturating  $[Ca^{2+}]_{cyt}$  (100-200  $\mu M$ ), where the channel is assumed to be maximally activated and ligand-bound.

The much shorter duration second closed state ( $C_2$ ; all schemes **Fig 5.6A**), has been designated as responsive ( $C_R$ ; schemes I-III, **Fig 5.6B**), since from here the channel can move to an open state, be that unliganded ( $O_{UL}$ , **Fig 5.6B** scheme I) at subactivating  $[Ca^{2+}]_{cyt}$ , or ligand-bound ( $O_1$ ; **Fig 5.6B** schemes II and III) at higher  $[Ca^{2+}]_{cyt}$ . At low  $[Ca^{2+}]_{cyt}$ , there is a third pre-opening closed state  $C_3$  ( $C_2 \leftrightarrow C_3 \leftrightarrow O_2$ , light blue panel of **Fig 5.6A**), that could correspond to an intermediate ligand-bound closed state (first described by (del Castillo et al. 1957)) which then changes conformation to the open state  $O_2$ . This intermediate conformation (represented by  $C_1$  in scheme I of **Fig 5.6B**) is not resolved as a discrete state at higher  $[Ca^{2+}]_{cyt}$  due to the rapid increase in the channel  $P_o$  and frequency of transitions to the open states. At higher  $[Ca^{2+}]_{cyt}$ , (**Fig 5.6A**, green and red panels, schemes II and III of **Fig 5.6B**), the channel appears to open directly from the second closed state  $C_R$  and then sequentially moves between different open channel states ( $O_1 \leftrightarrow O_2 \leftrightarrow O_3 \leftrightarrow O_4$ ) generated by variable occupancy of its  $Ca^{2+}$  binding sites. It should be noted that the numbers in subscript only serve to designate the different open states and have no bearing on the actual number of  $Ca^{2+}$  binding sites, as this is as yet unknown.

The recordings show brief flicker closings from the open state and these are more evident at higher  $[Ca^{2+}]_{cyt}$  ( $\geq 10 \mu M$ ) where more such events are observed due to higher open probability of the channel (see **Fig 5.3**, 200  $\mu M$  trace). The  $O_2 \leftrightarrow C_3$  transition in the gating schemes (**Fig 5.6A**, green and red panels, labelled  $C_F$  in schemes II and III of **Fig 5.6B**) illustrate this form of gating where the mean times ( $\tau$ ) of this closed state show

little change with increasing (10-500  $\mu\text{M}$ )  $[\text{Ca}^{2+}]_{\text{cyt}}$  ( $0.36 \pm 0.03$  ms;  $n = 8$  channels) indicating that it is a  $\text{Ca}^{2+}$ -independent process. Flicker closings are not discretely resolved at sub-activating and activating  $[\text{Ca}^{2+}]_{\text{cyt}}$ , as such transitions are infrequent compared to longer closings at these lower open probabilities. Thus the  $\tau$  for  $C_F$  at activating  $[\text{Ca}^{2+}]_{\text{cyt}}$  in **Table 5.3** is somewhat overestimated due to significant overlap with the adjacent longer closed time distribution ( $C_R$ ). The kinetic schemes (I-III) described in **Fig 5.6B** are composed of the minimum number of conformational states that are stable enough to be discretely resolvable from the single channel data and can adequately explain in mechanistic terms, the channel gating behaviour during its activation by  $[\text{Ca}^{2+}]_{\text{cyt}}$ .

#### **5.4.5 Transition rate constants and simulated data analysis: characterising $\text{Ca}^{2+}$ binding**

Rates of transitions between the various states in the kinetic models representing the three stages of channel activation (shown in **Fig 5.6A**) for a representative single channel are presented in **Table 5.5**. The rates are shown for 0.25, 1, 10, 200  $\mu\text{M}$  and 10-500  $\mu\text{M}$   $[\text{Ca}^{2+}]_{\text{cyt}}$  (for the latter, single channel data were simultaneously fitted to mechanisms across the near-saturation/saturation range). Each hRyR2 channel is a single functional molecule and a degree of stochastic variability is expected in their activation kinetics, thus variation in  $\text{EC}_{50}$  value from channel to channel translates into variation in the rates of transition, as a consequence results for one representative channel are shown here. However, all single channel data examined in this study show comparable changes in the dwell-time distributions and the estimated parameters from the schemes with increasing  $[\text{Ca}^{2+}]_{\text{cyt}}$ . The dwell-time distributions and the rates of transitions between states in the kinetic schemes along with a Hill coefficient of  $1.78 \pm 0.69$  ( $n=12$ , **Fig 5.4A**) suggest some degree of cooperativity. However the increase in the rates is not proportional to the increase in  $[\text{Ca}^{2+}]_{\text{cyt}}$  as would be expected from the laws of mass action with identical ligand binding sites on each subunit of hRyR2. Hence it is possible that each subunit contains multiple binding sites, each having a different affinity for  $\text{Ca}^{2+}$ , producing different levels of channel activation or indeed inhibition.

**TABLE 5.5**  
*Transition rates between states at different  $[Ca^{2+}]_{cyt}$*

Transitions	$[Ca^{2+}]_{cyt}$ ( $\mu M$ )				
	0.25	1	10	200	10-500*
C1 $\rightarrow$ C2	16	92	99	115	117
C2 $\rightarrow$ C1	7	38	23	13	34
C2 $\rightarrow$ O1	20 <sup>§</sup>	222	792	613	713
O1 $\rightarrow$ C2	5760 <sup>§</sup>	1674	634	834	842
C2 $\rightarrow$ C3	154	---	---	---	---
C3 $\rightarrow$ C2	550	---	---	---	---
C2 $\rightarrow$ O2	---	---	---	---	---
O2 $\rightarrow$ C2	---	---	---	---	---
O1 $\rightarrow$ O2	---	1665	277	632	522
O2 $\rightarrow$ O1	---	281	124	247	147
O2 $\rightarrow$ C3	2235	87	651 <sup>#</sup>	616 <sup>#</sup>	629
C3 $\rightarrow$ O2	156	1133	2599 <sup>#</sup>	2654 <sup>#</sup>	2976 <sup>#</sup>
O2 $\rightarrow$ O3	521	26	523	638	606
O3 $\rightarrow$ O2	627	65	521	505	574
O3 $\rightarrow$ O4	---	---	20	22	38
O4 $\rightarrow$ O3	---	---	84	92	94

\* Global fitting across the high  $[Ca^{2+}]_{cyt}$  range (10-500  $\mu M$ ).

<sup>§</sup> Indicates rates for unliganded gating transitions.

<sup>#</sup> Denotes flicker transitions from the  $Ca^{2+}$ -bound open state.

Units are  $s^{-1}$  or  $\mu M^{-1}s^{-1}$  as appropriate.

This idea was further examined by the analysis of single channel data simulated at various  $[Ca^{2+}]_{cyt}$  from the kinetic model obtained at 10  $\mu M$  from individual channels by optimising the rate constants to be either dependent or independent of ligand concentration (see section 5.3.2). The kinetic parameters were then compared with the actual data obtained from individual channels for validity of the operation, and were found to match the experimental data at  $\geq 1 \mu M [Ca^{2+}]_{cyt}$  when both the forwards and the backward rates were constrained to be linearly dependent on ligand concentration. At lower  $[Ca^{2+}]_{cyt}$  only the forward rates appeared to be ligand-dependent (**Fig 5.6B**, schemes I-III, see also **A3** in **Appendix I**). This apparent leftward shift in the equilibrium due to perturbation of the backward rates of  $Ca^{2+}$ -dependent transitions (at  $\geq 1 \mu M$ ) could indicate the presence of an inhibitory site. The presence of an inactivation site on the cytosolic domain has been previously proposed ( $I_2$ ; 1.2  $\mu M$  affinity; (Laver 2007)) which could be responsible for the inhibitory effect at high  $[Ca^{2+}]_{cyt}$ . If there was only one independent activating  $Ca^{2+}$  binding site on each monomer, it would have resulted in the stabilisation of only one open conformation at saturating  $[Ca^{2+}]_{cyt}$  where all such binding sites would be expected to be occupied. This would mean that only one exponential component is required for fitting the open-time histograms, which is clearly not the case in our analysis where channel does not primarily dwell in the open state  $O_4$  (**Table 5.3**) at saturating  $[Ca^{2+}]_{cyt}$ . The existence of multiple open states at saturating  $[Ca^{2+}]_{cyt}$  could be due to channel inactivation as explained above or the presence of more than one type of interacting  $Ca^{2+}$  binding site which could activate the channel to different levels. These two possible factors could exist concomitantly, however evidence of any putative  $Ca^{2+}$  binding site(s) can only be confirmed by accurate structural information which, to date is not available.

#### 5.4.6 Validation of kinetic schemes using model-based simulations

As well as providing information regarding the inhibitory role of  $[Ca^{2+}]_{cyt} \geq 1 \mu M$  on channel gating (see **A3** in **Appendix I**), simulation of data from the kinetic schemes was also used to validate the models and transitions rates derived (see **Chapter 4** for detailed technique). The traces obtained using the SIM module of QuB resemble the actual recordings (**Fig 5.7**) obtained during experiments and were analysed after idealisation using the same criteria as previously used for experimental recordings. Po exhibits a sigmoidal relationship with  $[Ca^{2+}]_{cyt}$  with a comparable  $EC_{50}$  ( $1.75 \pm 0.59 \mu M$ ,  $n = 8$ ; **Fig 5.8A**) where saturation is reached at  $\sim 10 \mu M Ca^{2+}$ . The closed times decrease and the open times do not show any significant change with rising  $[Ca^{2+}]_{cyt}$  (**Figure 5.8B** and **C**).

These results validate the proposed kinetic schemes as *bona fide* descriptions of RyR2 gating kinetics when activated by cytosolic  $\text{Ca}^{2+}$  alone.

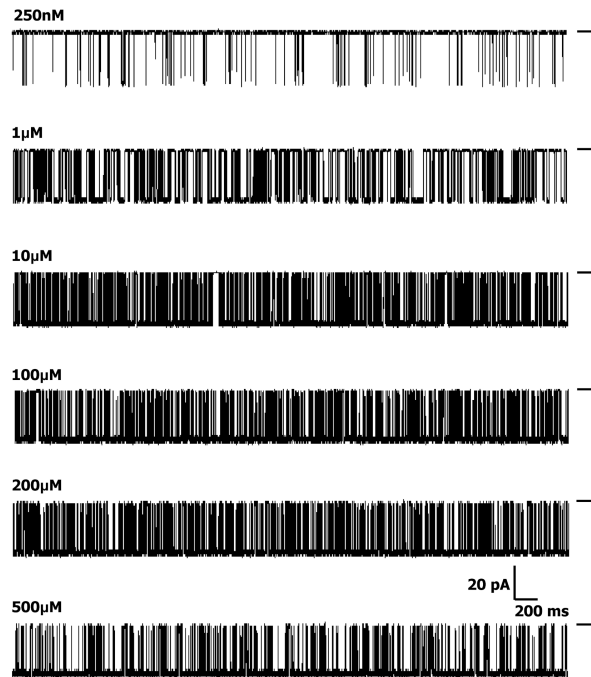


**Figure 5.7. Representative traces showing single channel data simulated using the kinetic model at various  $[\text{Ca}^{2+}]_{\text{cyt}}$ .** The closed level is labelled by solid bars on the right of the traces and the opening events are downward deflections from the closed level.

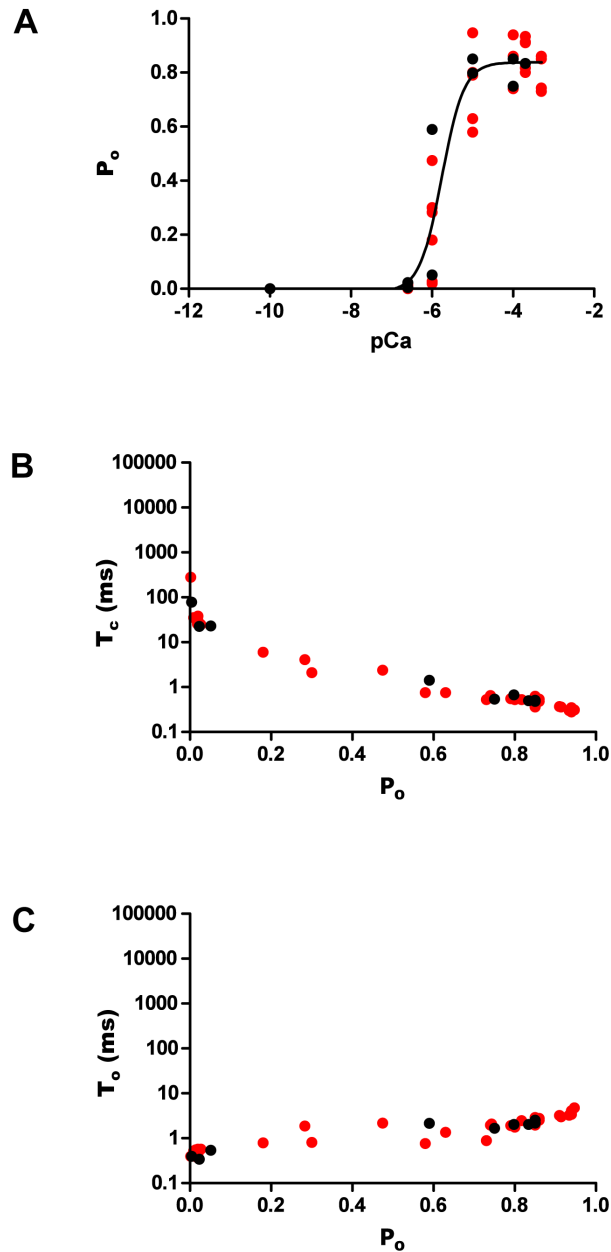


**Figure 5.8. Kinetic parameters of simulated data.** (A) Pooled  $P_o$  values obtained from analysis of simulated single channel data from all 8 individual channels exhibit a sigmoidal relationship with increasing  $[Ca^{2+}]_{cyt}$  when fitted with a log [agonist] vs. response curve where the  $EC_{50}$  was  $1.75 \pm 0.59 \mu M$ , and Hill coefficient was  $1.52 \pm 0.84$ ;  $n=8$ . Simulated data were obtained from models derived at  $0.25 \mu M$ ,  $1 \mu M$ ,  $10 \mu M$ ,  $100 \mu M$  and  $200 \mu M$   $[Ca^{2+}]_{cyt}$ . (B) and (C) shows the relationships of closed ( $T_c$ ) and open times ( $T_o$ ) respectively when activated by  $[Ca^{2+}]_{cyt}$ . The data points are colour coded according to the single channels used to derive the models (**Fig 5.2**). For clarity these data are displayed on the same axes as **Fig 5.4**.

### 5.4.7 Study of bursts of RyR2 channel openings: examining ligand-bound kinetics

The gating activity of many types of ion channels has been shown to contain bursts of rapid openings and closings separated by relatively longer interburst closings (Colquhoun and Hawkes 1982; Magleby and Pallotta 1983; Patlak and Ortiz 1989; Kwan et al. 2006; Chakrapani et al. 2007). In the recordings, hRyR2 exhibits bursting behaviour in response to activating  $[Ca^{2+}]_{\text{cyt}}$  (**Fig 5.9**). Bursts are known to occur when the channel oscillates rapidly between open and closed states in which the ligand is still presumed to be associated with the channel before dissociating to give rise to a longer interburst closed state. Therefore bursts are relevant markers of  $Ca^{2+}$ -bound RyR2 behaviour.

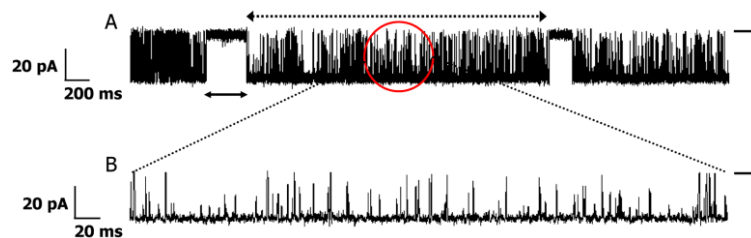


**Figure 5.9. Single channel burst analysis.** (A) Single channel current trace showing bursts where the dotted double-headed arrow on top shows the burst length while the solid double-headed arrow below shows the interburst interval. The solid bar on the right shows the closed level and the open events are downward deflections from it. The red circle encompasses a portion of a burst and is shown in (B) where the time base has been expanded by a factor of 10. The brief closing events, most of which do not reach the fully closed level in the current trace represent the flicker gating events.

To define sufficient quantities of bursts unambiguously for feasible statistical analysis, I limited the analyses to recordings at  $1 \mu\text{M } Ca^{2+}$  and higher. Analysis of bursts alone revealed that only two exponential components were necessary for adequate fitting of the closed duration histograms at these concentrations while those for the open-time distributions remained unchanged (**Fig 5.1**). The longest closed state  $C_{NR}$  was found to be responsible for the inter-burst gaps as this was the missing component in the closed-time distributions for bursts. The shaded region in **Fig 5.11** represents the transitions of the RyR2 within bursts that are resolved in the model where the channel shifts between various open conformations ( $O_1 \leftrightarrow O_2 \leftrightarrow O_3 \leftrightarrow O_4$ ) depending on the number of binding

sites occupied by  $\text{Ca}^{2+}$ . The channel closes by brief flicker transitions to the closed state  $C_F$  and also to the closed state  $C_R$ . The nature of  $\tau_{\text{crit}}$  calculation (used for defining bursts, see **Chapter 4**) means that the distribution of the longest closed period that represents the inter-burst interval ( $C_{\text{NR}}$ ) overlaps slightly with the second longest closed state  $C_R$ . Therefore, a minor fraction of the  $C_R$  closings events might be included in the calculation of the inter-burst interval and conversely, a small proportion of intra-burst closing events might seem to be due to the dissociation of  $\text{Ca}^{2+}$  from the RyR2 – this however does not alter the final outcome of the analysis.

Close scrutiny of burst parameters for each  $[\text{Ca}^{2+}]_{\text{cyt}}$  (colour coded for  $[\text{Ca}^{2+}]_{\text{cyt}}$  in **Fig 5.12**) reveals the nature of RyR2 gating kinetics when  $\text{Ca}^{2+}$  is bound. The closed durations within each burst decreases with increasing burst  $P_o$  and  $[\text{Ca}^{2+}]_{\text{cyt}}$  (**Fig 5.12A**) while the open durations show no significant change (**Fig 5.12B**). The duration of the bursts (burst length) tends to increase with increasing  $P_o$  and  $[\text{Ca}^{2+}]_{\text{cyt}}$  (**Fig 5.12C**). At high  $[\text{Ca}^{2+}]_{\text{cyt}}$  the channel has a low probability of visiting the closed state  $C_R$  as the equilibrium is maximally shifted to the right and therefore the closed time within burst decreases. The burst length increases as the channel has a higher probability of being in a ligand-bound state with rising  $[\text{Ca}^{2+}]_{\text{cyt}}$ . Interburst intervals show a decrease in duration with increasing  $P_o$  and  $[\text{Ca}^{2+}]_{\text{cyt}}$  (**Fig 5.12D**) but are not completely eliminated even at saturating levels of ligand (blue and black bars). This supports the existence of a closed state ( $C_{\text{NR}}$ ) which is not as responsive to activation by  $[\text{Ca}^{2+}]_{\text{cyt}}$  as  $C_R$ .



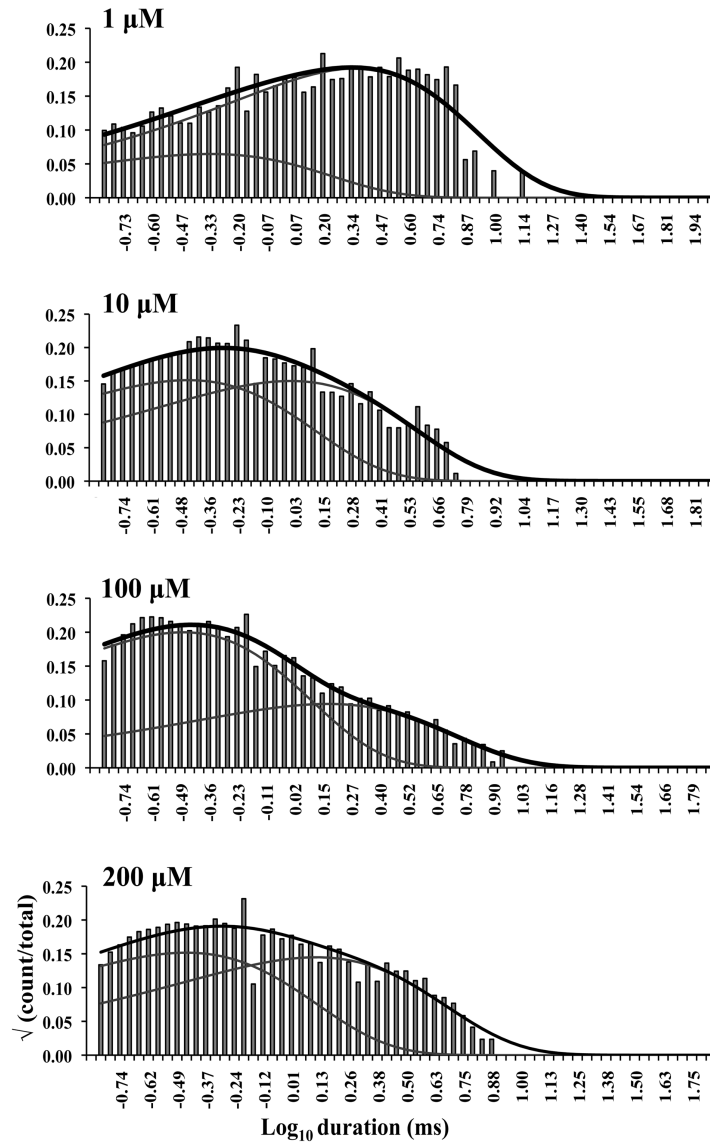


**Figure 5.10. Closed dwell-time histograms of single channel bursts at various activating  $[Ca^{2+}]_{cyt}$ .** Here the inter-burst intervals were removed from the idealised traces and the bursts were spliced together before creating the histograms. These were then fitted with sums of exponential curves. The overall exponential fit of each histogram is represented by the solid black curve while the individual components are shown by grey lines. Only two exponential components were required for fitting all closed-time histograms while the fits for the open-time histograms remained unchanged. The activating  $Ca^{2+}$  concentrations are shown on the top left corner of each histogram.

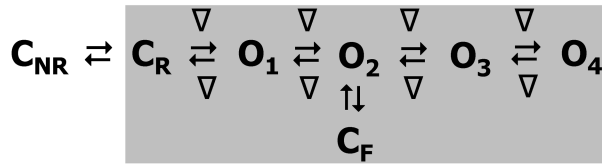


**Figure 5.11. Kinetic scheme describing the ligand-bound gating behaviour (bursts).** The shaded region in the scheme accounts for the state transitions seen within single channel bursts. Here the kinetic scheme represents RyR2 activity at high  $[\text{Ca}^{2+}]_{\text{cyt}}$  (Fig 5.6B, scheme III) where the bursts are longer in duration and are better resolved. The symbols and labels are the same as in Fig 5.6B.

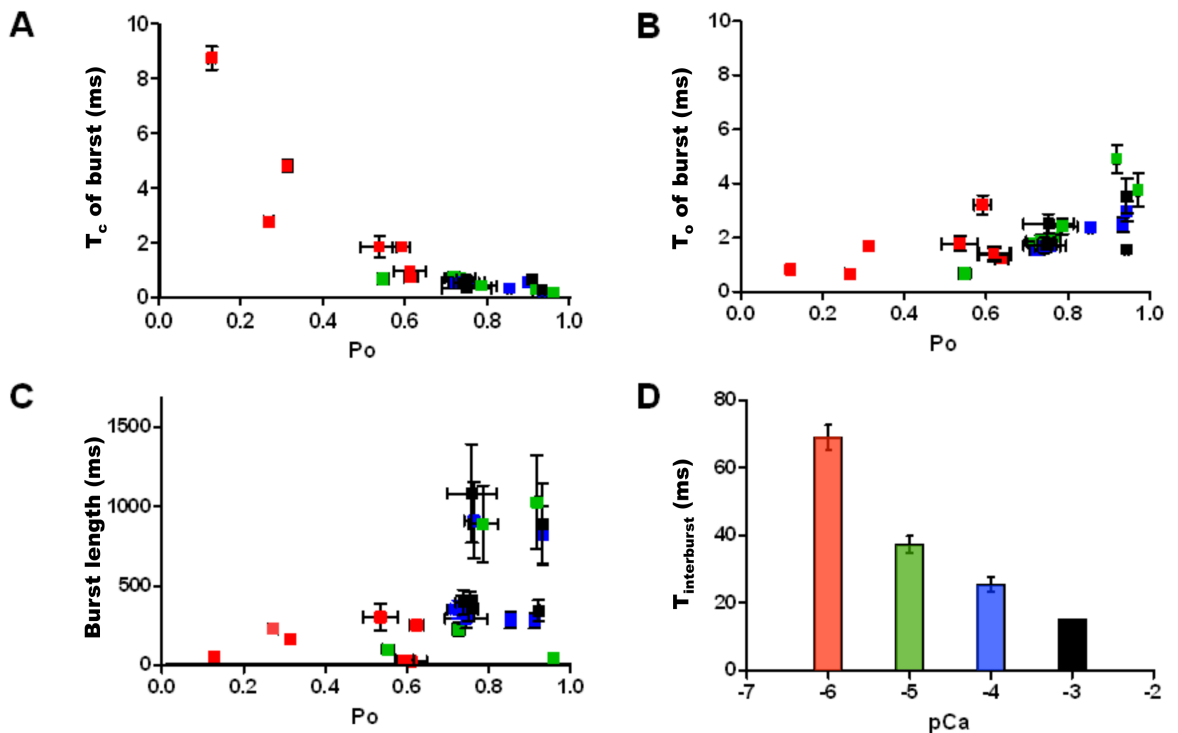


**Figure 5.12. Kinetic parameters of burst activity of WT hRyR2 at various activating  $[\text{Ca}^{2+}]_{\text{cyt}}$**  These are plotted as a scatter of means  $\pm$  SEM (A-C) for individual channels and mean  $\pm$  SEM for data points from all channels (D). Bursts were analysed from 7 individual single channel recordings at 1 ( $\square$ ), 10 ( $\square$ ), 100 ( $\square$ ) and 200  $\mu\text{M}$  ( $\square$ )  $\text{Ca}^{2+}$ . As the duration of bursts increases with increasing  $[\text{Ca}^{2+}]_{\text{cyt}}$ , for a given duration of recording, the total number of detected bursts decreases. For this analysis, 20 to 190 bursts were used for each channel at every  $[\text{Ca}^{2+}]_{\text{cyt}}$  (A-C) and for (D) a total of 300 to 720 interburst intervals for each  $[\text{Ca}^{2+}]_{\text{cyt}}$  were detected and analysed. (A) and (B) shows the relationship between  $P_o$  within bursts and intraburst  $T_c$  and  $T_o$  respectively with increasing  $[\text{Ca}^{2+}]_{\text{cyt}}$ . (C) Relationship of burst length and intraburst  $P_o$  with increasing  $[\text{Ca}^{2+}]_{\text{cyt}}$ . (D) A bar chart shows the effect of increasing  $[\text{Ca}^{2+}]_{\text{cyt}}$  on interburst intervals ( $T_{\text{interburst}}$ ). Error bars, where not visible are included within the dimensions of the squares (A-C) or bars (D).

#### 5.4.8 Putative mechanisms underlying the preopening isomerisation

At saturating  $[Ca^{2+}]_{cyt}$ , it can be assumed that almost all the ligand binding sites on the channel are occupied by  $Ca^{2+}$  and the channel is least likely to be in the preopening closed state  $C_R$  as the equilibrium will be maximally shifted right towards the  $Ca^{2+}$ -bound open states. However, as previously stated the channel is still able to isomerise to the non-responsive state  $C_{NR}$ . The presence of a closed state in which the channel is not in a suitable conformation to undergo activation (whether that be because ligand binding sites are not in a suitable conformation to bind  $Ca^{2+}$ , or for some other reason) could have functional implications, and as such the tendency of the channel to isomerise from  $C_R$  to  $C_{NR}$  at saturating  $[Ca^{2+}]_{cyt}$  needs to be quantified. The net tendency of channel transition between  $C_{NR}$  and  $C_R$  is denoted by the constant  $E_{iso}$  (equilibrium of isomerisation; **Fig 5.6B**, Scheme III), which is given by  $k_{C_R-C_{NR}}/k_{C_{NR}-C_R}$  at saturation. Using the parameters from the global fit of single channel data from 10 – 500  $\mu M$   $[Ca^{2+}]_{cyt}$  ( $C_R$  to  $C_{NR}$ ;  $27.7 \pm 3.8$   $s^{-1}$  and  $C_{NR}$  to  $C_R$ ;  $122.3 \pm 7.4$   $s^{-1}$ ,  $n=4$ ), the  $E_{iso}$  for WT hRyR2 in high  $[Ca^{2+}]_{cyt}$  was found to be  $0.23 \pm 0.026$  ( $n=4$ ) under minimal conditions. It is possible that various modifiers of RyR2 channel activity might affect this equilibrium to bring about channel activation or inactivation by favouring the stabilisation of conformations  $C_R$  or  $C_{NR}$  respectively.

#### 5.5 Discussion

The objective of this study was to identify putative gating models that could best describe the kinetic behaviour of single purified hRyR2 in response to  $[Ca^{2+}]_{cyt}$  and crucially, under strictly regulated ‘minimal’ and defined conditions where the channel has been isolated from possible external modulators. Although the process of solubilisation (low  $Ca^{2+}$  buffer) should strip the channel of external accessory proteins like calmodulin, any potential interaction with this cytosolic protein however, cannot be ruled out with certainty. The Western blot signals of hRyR2 in purified protein fractions are weak (**Fig. 2.6 A**) and it will be even more difficult to detect any signal from other associated proteins even if they are present (e.g. mAKAPs, protein kinases). Future studies of the purified protein fractions using mass spectrometry could be used to confirm the presence/absence of other interacting proteins. Instead of merely fitting the data adequately, the mathematical description of state transitions seeks an insight into the

actual physical reality of gating in order to assign possible conformations to the states in the kinetic schemes. In reality a channel can pass through numerous conformations during gating, all of which are in a continuum. However, for practical purposes only those states that represent the lowest points in the energy profile can be considered as discrete states stable enough to be deduced from single channel data. Although it is possible to fit many different kinetic models onto single channel data, kinetic schemes should provide an insight into the actual physical mechanisms involved in the gating behaviour of the channel. Many models were considered during the search but most were discarded as either they fitted the data poorly (with low maximum likelihood, these included cyclical models with loops) or were impossible to explain in terms of channel conformations and made little mechanistic sense. The top ranked models in **Table 5.4** at various  $[Ca^{2+}]_{cyt}$  are of the linear-branched type and the most logical model (in terms of physical gating mechanisms) was arrived at, which explained the data from all eight channels examined (including flicker and unliganded gating transitions) and yet retained its simplicity. However, it should be noted that while the possible mechanisms of RyR2 activation described in this work in terms of various channel conformations provide a logical explanation for the observed gating behaviour, their accuracy remains to be validated by structural information.

Unlike in previous studies, this study used a combination of  $Ca^{2+}$  buffers to accurately control free  $Ca^{2+}$  levels and  $[Ca^{2+}]_{cyt}$  points were chosen carefully to lie within the 'good buffering' ranges of the chelators used at the experimental ionic and pH conditions. Also, one has to bear in mind that precise buffering is also subject to the purity of the reagents and this study assumes that the purity levels are as claimed by the manufacturer (Sigma-Aldrich) is correct although there is some anecdotal evidence that batch purity is variable (Sitsapesan, personal communication). The very sharp activating nature of RyR2 in response to cytosolic  $Ca^{2+}$  is physiologically essential for the initiation of cardiomyocyte contraction. However, this meant that in single channel experiments, no more than two Po data points could be achieved on the rising phase of the  $Ca^{2+}$  activation curve despite the inclusion of further intermediate  $Ca^{2+}$  concentrations (**Fig 5.2**). Although this means that some very short-lived intermediate state topologies may not be resolved during activation by  $[Ca^{2+}]_{cyt}$ , the current study is the most comprehensive account of hRyR2 single channel behaviour so far available. The drastic changes in the dwell-time distributions (see **Fig 5.5**) due to rapid increase in Po from the sub-activating (100-250 nM) to the activating (1-10  $\mu$ M)  $[Ca^{2+}]_{cyt}$  range prevents the global fitting of dwell-time histograms derived from single channel data simultaneously across the whole range of

$[Ca^{2+}]_{cyt}$ , and as a result I have described hRyR2 gating behaviour in terms of three kinetic schemes, one for each phase of activation (**Fig 5.6**). These are represented as a phenomenological composite kinetic scheme in **Fig 5.13** where the discrete states resolved during analyses of single channel data could be a subset of a larger mechanistic network.

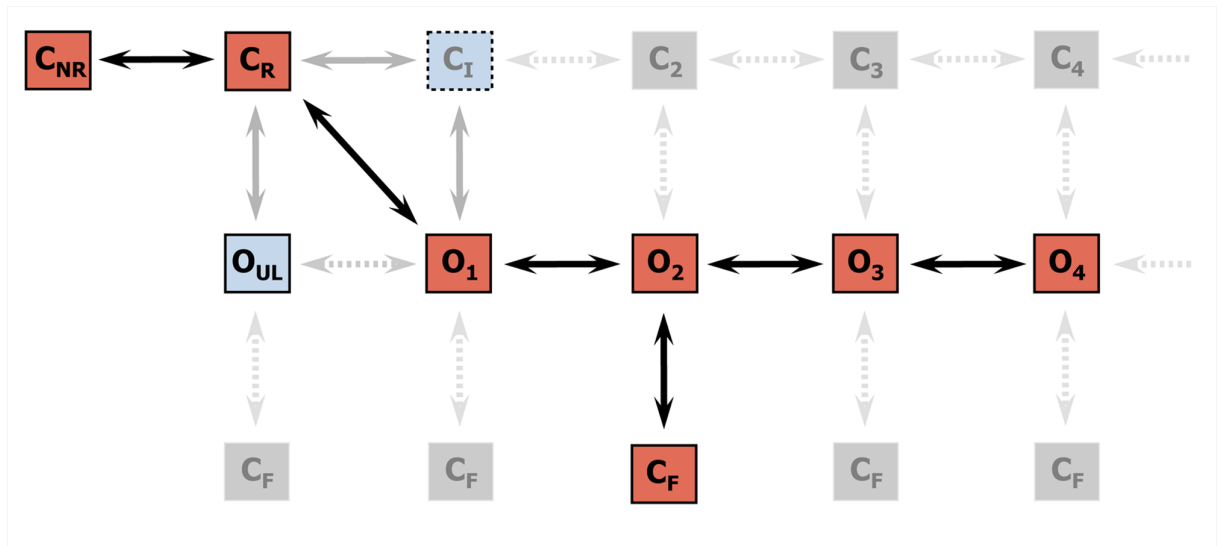


**Figure 5.13. Composite gating scheme proposed for hRyR2 activation by  $[Ca^{2+}]_{cyt}$  represented as part of a larger mechanistic network.** The red boxes represent the discretely resolved states in the model with solid black arrows showing the transitions between the states. At very low  $[Ca^{2+}]_{cyt}$  the unliganded open state  $O_{UL}$  and an intermediate  $Ca^{2+}$ -bound preopening closed state  $C_I$  are also resolved (shown in light blue boxes). Solid grey arrows represent the transitions to and from these states. The states and the transitions represented by grey boxes and light grey dotted arrows are not discretely resolved from single channel data analysis. These extrapolations show how the linear kinetic schemes (**Fig 5.6B**) could form a subset of a larger network (which could be interpreted as a phenomenological MWC-type model). Transitions to flicker closed states  $C_F$  could occur from any of the  $Ca^{2+}$ -bound open states and those that are not resolved directly from the data are represented by grey boxes and light grey dotted arrows.

### 5.5.1 Physical interpretation of the kinetic scheme: novel insights into RyR2 gating

**Fig 5.13** shows states and transitions that can be resolved from the single channel data at activating and high  $[Ca^{2+}]_{\text{cyt}}$  (red squares with transitions shown in black solid arrows, i.e. schemes I and II from **Fig 5.6B**), those seen only at very low  $[Ca^{2+}]_{\text{cyt}}$  (light blue squares with transitions shown in grey solid arrows, i.e. scheme I from **Fig 5.6B**), and those states extrapolated (possible states that could not be directly resolved from my data, shown in a lighter shade of grey with dotted arrows). The  $Ca^{2+}$ -bound closed states  $C_2$ ,  $C_3$  etc. are not discretely resolved possibly due to a very low likelihood of them being visited by the channel at higher  $[Ca^{2+}]_{\text{cyt}}$ . In this putative scheme,  $Ca^{2+}$ -independent flicker closings can occur from any of the open conformations but in practice are resolved from only one open state  $O_2$ . While there is evidence from this data that single channel gating behaviour of hRyR2 exhibits cooperativity (Hill coefficient =  $1.78 \pm 0.69$ ;  $n=12$ ), it is known that absolute cooperativity does not exist in any system. Although RyR2 is a homotetramer, a Hill coefficient of  $\sim 2$  (and not  $\sim 4$ ) suggests that there are partially saturated intermediate channel conformations which are evident from the gating schemes and there are a minimum of 2 binding sites for  $Ca^{2+}$ . The results of the detailed analysis allows us to present a modified MWC-type model network (**Fig 5.13**) as a possible phenomenological description of single hRyR2 channel gating behaviour in response to  $[Ca^{2+}]_{\text{cyt}}$ , however this cannot be confirmed until all the conformational states in the proposed kinetic network can be discretely resolved.

The observation of unliganded channel activity, the lack of sufficient  $Ca^{2+}$ -bound pre-opening closed channel conformations (a minimum of four for a tetramer) before the open state, and the Hill coefficients which indicate cooperativity and concerted motion of subunits point away from a sequential KNF (Koshland-Némethy-Filmer) type model (Koshland et al. 1966) of activation but towards a MWC-type (Monod-Wyman-Changeux) of gating behaviour (Monod et al. 1965; Changeux and Edelstein 2005). Preliminary cryo-EM studies have shown significant structural rearrangement in the cytoplasmic region of RyR during closed to open transition which further supports the allosteric nature of channel gating (Samsó et al. 2009; Van Petegem 2012; Van Petegem 2014).

### 5.5.2 Unliganded channel activity: constitutive gating in RyR2

The RyR2 can open from the non-conducting state in the absence of ligand, indicating that conformational changes during the gating process are possibly allosteric in nature with concerted transitions of all subunits, suggesting that RyR2 gating could be explained in terms of a MWC-type model (Auerbach 2012). Analyses of ligand-independent channel activity in other types of channels have shown an increase in spontaneous channel activity induced by certain disease causing mutations (Milone et al. 1997; M. Zhou et al. 1999; Grosman and Auerbach 2000; Purohit and Auerbach 2009). The study of constitutive channel activity provides a valuable experimental tool by which the process of channel gating could be isolated from the ligand binding process and the existence of various ligand-independent conformations can be verified. Therefore, this aspect of gating could be used as a marker of the functional perturbation of RyR2 due to arrhythmogenic mutation where a gain of function could manifest as increased constitutive activity. In a recent study on PKA phosphorylated sheep RyR2, it was found that removal of activating  $[Ca^{2+}]_{\text{cyt}}$  led to constitutive channel openings events characterised by long open times (Carter et al. 2011). This is an interesting finding and may arise due to a right-shift of equilibrium between the two pre-opening closed states leading to a change in  $E_{\text{iso}}$  (see section 5.4.8).

### 5.5.3 Gating independent of $[Ca^{2+}]_{\text{cyt}}$ : significance of flicker closing events

Flicker closings have been previously described in other types of channels such as BK, MthK and KcsA (Talukder and Aldrich 2000; Piskorowski and Aldrich 2006; Zadek and Nimigean 2006; Cuello et al. 2010). This phenomenon has been attributed to the metastable nature of the selectivity filter acting as a gate by rapid switching between conducting and non-conducting states and is distinct from gating at the helix-bundle crossover (Yellen 2002). These brief closing events are different from the longer typical C-type inactivation selectivity filter gating events seen in the KcsA  $K^+$  channel (Chakrapani et al. 2010). Structural modelling studies propose that RyR has a similar pore structure to that of  $K^+$  channels (Williams 2002; Welch et al. 2004; Ramachandran et al. 2013; W. Chen et al. 2014) hence it is quite possible that the flicker transitions in RyR2 occur due to gating at the selectivity filter through a similar mechanism.

Investigations into gating at the selectivity filter of BK channels (Piskorowski and Aldrich 2006) suggest that its flexible nature allows it to adopt two different

conformations that could account for the large conductance of this channel and that the flicker transitions might be a by-product of this phenomenon. RyR has a unitary conductance even greater than the BK channel (Williams et al. 2001) and modelling studies suggest that the putative selectivity filter is both wider and more flexible (**Fig 5.14**) than the equivalent region in  $K^+$  channels (Welch et al. 2004). Therefore, it is possible that the flicker transitions in RyR2 are symptomatic of a flexible selectivity filter during ion permeation. Further investigations into the role of the putative selectivity filter in the RyR2 pore model are likely to provide useful information on flicker gating transitions.

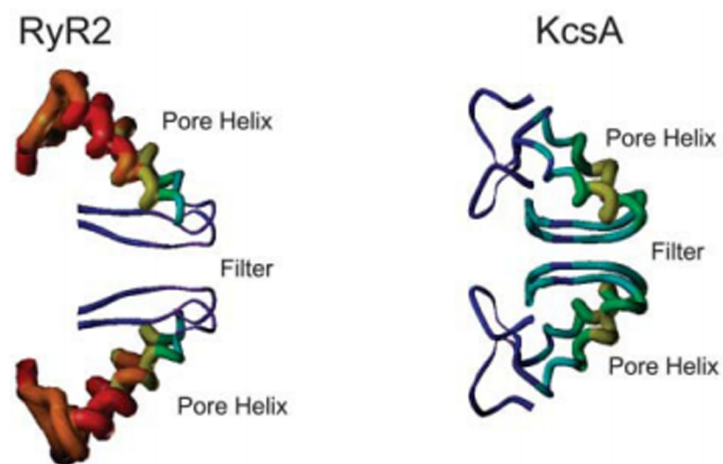


**Figure 5.14 Comparison of the putative selectivity filter region of RyR2 with that of the KcsA.** Here the statistical energy functions of RyR2 pore model is compared with KcsA where the width of the selectivity filter of RyR2 is significantly larger than in KcsA. Red and purple areas represent energetically least and most favourable regions respectively (Welch et al. 2004).

#### 5.5.4 Pathophysiological relevance of RyR2 gating mechanism

An understanding of the basic mechanisms underlying the gating behaviour of WT hRyR2 is essential if the modulatory functions of the accessory proteins and pathophysiology of the diseases caused by mutations in the channel are to be understood. Peptide studies have indicated that CPVT1-linked mutations in RyR2 are likely to disrupt intra-molecular interactions within the channel (Yamamoto et al. 2000; George et al. 2004; Uchinoumi et al. 2010), leading to mechanical instability, perturbed gating and an aberrant  $Ca^{2+}$  response/release. This suggests that these interactions are essential in maintaining channel closure, and may be involved in the conformational changes involved in  $Ca^{2+}$  release. If the mutant channels are studied under the minimal conditions



described here, the resulting data will provide a clue to establish if the mutation itself is sufficient to cause  $\text{Ca}^{2+}$  leak which could trigger the arrhythmia or if some other cellular component is an essential player in the pathophysiology of the disease. This information will come from quantitative changes in the gating model and the perturbed state transitions will point towards likely mechanisms underlying channel instability.

This would be of interest since other components of the macromolecular complex have been implicated in CPVT1-related channel dysfunction, most prominently the dissociation of FKBP12.6 (Marx et al. 2000; Wehrens et al. 2003). However, the relevance of this accessory protein and how big a role it plays in the regulation of WT or mutant channel function has been the subject of much controversy in recent years (see **Chapter 1** for details), with many groups concluding that it plays no part in RyR2 mediated arrhythmia. The aim of this study is to analyse hRyR2 gating in the absence of the modulatory effects of accessory proteins therefore, and in contrast to some other studies, FKBP12.6 was not included in my channel protein preparations (see **Chapter 3**). Notably, unlike some previous reports (Marx et al. 2000; Wehrens et al. 2003) sub-conductance states were not observed in the single channel recordings in the present study. Recent reports (Guo et al. 2010) suggest that 80% of RyR2 channels present in ventricular myocytes are not endogenously associated with FKBP12.6 and that the channel activity is unaffected in FKBP12.6 knockout mice. This agrees well with the data where the channel function does not appear to be abnormal in the absence of FKBP12.6, indeed my  $\text{EC}_{50}$  for  $\text{Ca}^{2+}$  activation ( $1.65 \pm 0.43 \mu\text{M}$ ;  $n=12$ ) is similar to that for unphosphorylated WT hRyR2 from HEK293 microsomal vesicles co-expressing FKBP12.6 ( $946 \pm 23 \text{ nM}$ ;  $n=4$  (Tester et al. 2007)). Importantly, the sequence of human recombinant RyR2 used in the study of Tester et al. is unknown. Further work is needed to analyse the function of this accessory protein in the regulation of RyR2 gating in the context of the kinetic model. Native sheep RyR2 derived from heavy SR preparations could only be maximally activated by  $[\text{Ca}^{2+}]_{\text{cyt}}$  up to a  $\text{Po}$  of  $\sim 0.5$  (Ashley and Williams 1990; Sitsapesan and Williams 1994a) and yielded an  $\text{EC}_{50}$  of approximately  $30\mu\text{M}$ , substantially higher than that obtained with hRyR2 in this thesis. These data point to a possible modulatory role of accessory proteins that may remain associated with the native channel.

Luminal  $\text{Ca}^{2+}$  *per se* has been shown to be a modulator of single RyR2 channel activity (Sitsapesan and Williams 1994b). It has also been shown to be indispensable in the regulation of RyR2 in physiological as well as pathological conditions (D. Jiang et al. 2004) and has been implicated as the primary trigger in the activation of RyR2 in the

$\text{Ca}^{2+}$  'feed-through' model (Laver 2007). However, it is generally accepted that  $\text{Ca}^{2+}$  entering the cytosol of the cardiac myocyte through the voltage-gated calcium channels provide the first signal for RyR2 to release  $\text{Ca}^{2+}$  from the SR by CICR. Although the luminal  $\text{Ca}^{2+}$  concentration was buffered to a very low level (50nM) in my experiments, the channels still exhibited the maximal activation by cytosolic  $\text{Ca}^{2+}$ . In the myocyte however, RyR2 activity is known to be regulated by luminal  $\text{Ca}^{2+}$  through its interaction with luminal accessory proteins like calsequestrin, junctin and triadin (S. Györke and Terentyev 2008). As these modulators are absent in this experimental system, it may also serve as an important tool for dissecting the effect of these regulatory proteins and luminal  $\text{Ca}^{2+}$  on channel gating. This kinetic framework describing the behaviour of hRyR2 in a controlled minimal environment will serve as a mechanistic benchmark against which more complex experimental outcomes involving various physiological modulators, disease causing mutations and therapeutic compounds can be studied and modelled.

## **Chapter 6.0**

**Mechanistic basis of modified RyR2 gating behaviour: a zero  $\text{Ca}^{2+}$  approach**

## 6.1 Introduction

A detailed functional study of the hRyR2 at the single molecule level when activated solely by its physiological ligand  $[Ca^{2+}]_{cyt}$  has provided important clues regarding the possible determinants of gating (**Chapter 5**). It has revealed that the channel gating behaviour is possibly controlled by two components that are most likely to reside in the channel pore (Mukherjee et al. 2012). While vital information regarding gating behaviour of RyR can be obtained by studying its response to  $Ca^{2+}$ , the scope for further inferences is stifled by the unavailability of any detailed structural information regarding the number, location and nature of binding sites for  $[Ca^{2+}]_{cyt}$ . A novel approach would be to study the RyR2 gating behaviour in the absence of activating  $[Ca^{2+}]_{cyt}$  in order to reveal the properties of the gates. However, it is known that in the absence of activating  $Ca^{2+}$ , the channel very rarely visits the open state ( $P_o \sim 8 \times 10^{-5}$ ) (Mukherjee et al. 2012), which makes it impossible to make inferences about its gating behaviour. The following experiments employ the archetypal ligand ryanodine, which has enabled the molecular characterisation and pharmacological profiling of RyRs, to modify and activate the channel in the complete absence of  $Ca^{2+}$ . The single channel data derived could be mathematically modelled to provide an accurate description of modified RyR2 gating behaviour. Although the modified channel cannot be directly compared with the unmodified in terms of gating behaviour, the results of this study could be useful for our understanding of the nature of gates involved.

Interaction of the plant alkaloid ryanodine with individual RyR channels results in very profound alterations in channel function (**Chapter 1**); unitary conductance of the channel is reduced while open probability ( $P_o$ ) is increased dramatically (Tinker and Williams 1993; Lindsay et al. 1994). Ryanodine binds to open RyRs and ‘locks’ the channel open ( $P_o \sim 1$ ) in a modified open subconductance state ( $\sim 60\%$  fractional conductance). The very slow dissociation rate of ryanodine makes the pharmacological effect on RyRs essentially irreversible in the time-scale of single channel experiments. The mechanisms underlying ryanodine-dependent altered rates of ion translocation in RyR have been described and the structural components of the ryanodine molecule that determine the ryanodine-modified fractional conductance have been investigated (Williams et al. 2001; Welch 2002) but the mechanisms involved in the elevation of  $P_o$  that results from ryanodine’s interaction are poorly understood. Data obtained from single channel experiments when subjected to sophisticated and sensitive methods of analyses could provide key mechanistic insights into the nature of the ryanodine-modified RyR2 gating.

A set of cell-penetrating toxins found in scorpion venoms display a high affinity (nM) and exquisite selectivity against RyRs and are collectively known as *calcins* (see **Chapter 1**). The hallmark of calcins is their ability to stabilise RyR openings in a long lasting, subconductance state that is analogous to the effect of ryanodine. However, unlike ryanodine, calcins bind rapidly to RyRs and freely dissociate from their binding site on the channel (reversible). Imperatoxin A (IpTxa) was the first calcin to be isolated (**Fig. 6.1**) from the venom of *Pandinus imperator* (Emperor Scorpion) and is a small (3.7 kDa), highly basic peptide (33 a.a) with a high affinity for RyR (~5-10 nM). IpTxa binds to open RyR and stabilises the channel in a subconductance state that exhibits a slight rectification (~30% fractional conductance at positive holding potentials and ~40% at negative; **Fig 6.2**). In this study, I will also try to ascertain if the mechanism of action of IpTxa on RyR2 is analogous to that of ryanodine as proposed in earlier reports (Schwartz et al. 2009). The appearance of a high  $P_o$  subconductance states due to possible alterations in the conformation of the channel pore is a hallmark of both ryanoids and calcins.

The  $P_o$  of any species of channel is a manifestation of the conformation of its conduction pathway, or more precisely, specific gate regions of the pathway that either prevent, or allow, ions to flow down their electrochemical gradient. The physical identities of gating regions have been established for many  $K^+$  channels from data obtained from combinations of high-resolution crystallographic structural investigations and detailed functional studies (Doyle et al. 1998; Hille 2001; Roux 2005). These channels contain two gating regions, one formed by the inner-helix bundle crossover at the cytosolic entrance to the pore and a second within the selectivity filter. The enormous size of the RyR channel, its location in an intracellular membrane and the lack of a prokaryotic analogue mean that no equivalent structural data is available for RyR, though molecular modelling indicates structural similarities between the overall architecture of the pore regions of RyR and  $K^+$  channels (Williams 2002; Welch et al. 2004; Ramachandran et al. 2013). In addition, an in depth study of channel gating suggested that  $Ca^{2+}$  sensitive and insensitive closing transitions could be explained by the presence of two different gates, similar to those found in  $K^+$  channels, in the conduction pathway of RyR (**Chapter 5**). In this chapter, detailed analysis of single channel gating and mathematical modelling was done to reveal novel information about the gating of ryanodine-modified RyR2, which is influenced by different ligands and holding potentials. The outcome of these experiments emphasises the consequences of ligand interaction on the conformational stability of RyR gating and I discuss how this could influence the structure of the conduction pathway.

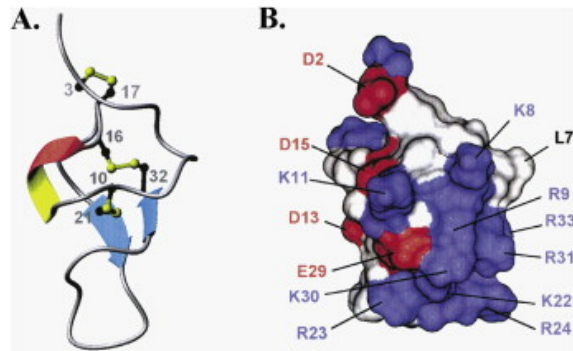


**Figure 6.1. Structure of IpTxa.** (A) Cartoon diagram of IpTxa illustrating the position of the  $\beta$  strands (blue), the 310 helical turn (red), and the disulphide bridges (yellow). (B) Profile of surfaces, negatively charged residues (acid) are shown in red, positively charged residues (basic) are shown in blue, and the uncharged and hydrophobic residues are in white (Lee et al. 2004).

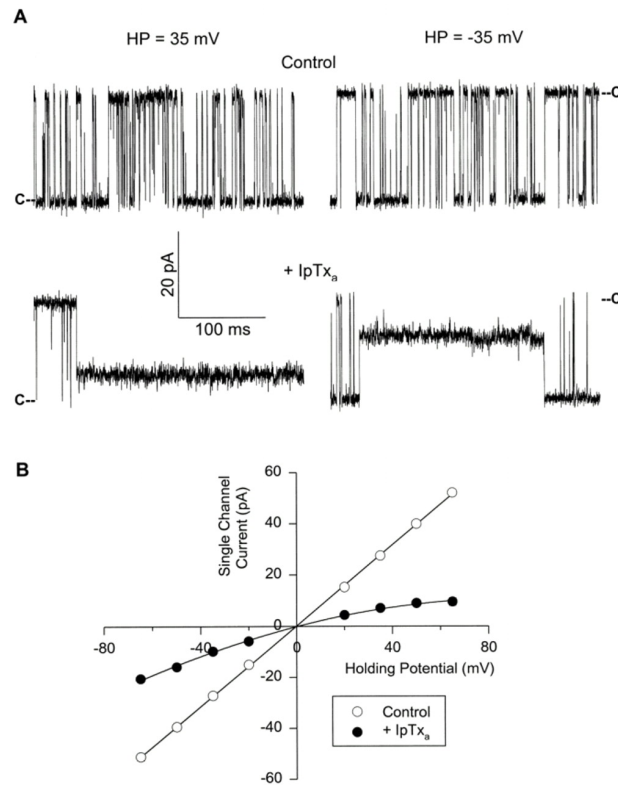


**Figure 6.2. Conduction and gating of IpTxa-modified RyR2.** (A) Shown are four recordings from one experiment at indicated holding potentials. Single channel currents, shown as downward or upward deflections from closed levels (-c), were re- recorded in symmetrical 0.25 M KCl, 20 mM HEPES, pH 7.4. The *cis* and *trans* chamber solutions contained contaminant free  $\text{Ca}^{2+}$ . The top recordings were obtained under control conditions and the bottom recordings after addition of 15 nM native IpTxa to the *cis* solution. (B) Mean current values of the full conductance (open circles) and IpTxa-induced subconductance (closed circles) states vs. holding potential. This figure is from (Tripathy et al. 1998).

## 6.2 Key Objectives

1. Accurate description of single channel gating behaviour of ryanodine-modified RyR2 in the presence and absence of  $[Ca^{2+}]_{cyt}$  for a mechanistic understanding of the action of ryanodine using mathematical modelling and energetic evaluation of state transitions. Apart from unravelling of the mechanism of channel modification leading to an increase in  $P_o$ , it may also provide important clues regarding the nature of the gates involved.
2. Establish whether the determinants of gating in the unmodified RyR2 when activated by  $[Ca^{2+}]_{cyt}$  remain intact in the modified channel in the absence of  $[Ca^{2+}]_{cyt}$ .
3. Ascertain if the proposed analogous mechanism of action of ryanodine and IpTxa is correct. It would serve to establish if ryanodine brings about a conformational change in the pore using mechanisms similar to those of the toxin.

### 6.3 Experimental procedures

All experiments in this chapter involve the incorporation of single purified recombinant hRyR2 channels into planar phospholipid bilayers. Protocols for these experiments were described in detail in **Chapter 2**. The experiments were carried out with symmetrical 210 mM KCl bathing solutions with  $K^+$  as the major permeant ion for better resolution of single channel currents. The RyR2 was activated by  $\sim 1 \mu\text{M}$   $\text{Ca}^{2+}$  which was present as ‘contaminant’ in 210 mM KCl. This was determined by comparing single channel data accumulated from 17 experiments ( $P_o = 0.21 \pm 0.06$ ) against the hRyR2  $\text{Ca}^{2+}$  activation curve obtained (**Fig. 6.3**) in **Chapter 5** and further verified using a calcium probe (Orion, Thermo Scientific).

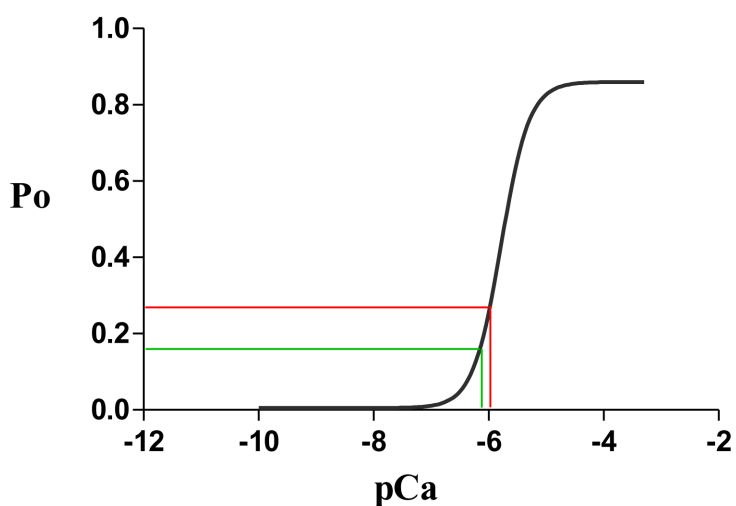


**Figure 6.3. Projection of  $P_o$  values on  $\text{Ca}^{2+}$  activation curve.** The lower and upper limits of open probabilities obtained from 17 single channel experiments (0.15-0.27) where RyR2 was activated by contaminant levels of  $[\text{Ca}^{2+}]_{\text{cyt}}$  were projected on to the  $\text{Ca}^{2+}$  activation curve shown in Chapter 5 (using green and red lines respectively). The corresponding vertical projections from the curve to the abscissa give a mean  $\text{Ca}^{2+}$  concentration of  $\sim 1 \mu\text{M}$ . This  $\text{Ca}^{2+}$  activation curve has been previously published (Mukherjee et al. 2012).

In the single channel experiments the RyR2 were modified using  $1 \mu\text{M}$  ryanodine (Abcam Biochemicals, UK) and  $20 \text{ nM}$  synthetic Imperatoxin A (Alomone Labs, Israel) on the cis side. The gating behaviour of the modified channels was examined under contaminant or nominally zero  $\text{Ca}^{2+}$  conditions (conditions extrapolated to  $\sim 20 \text{ pM}$  free  $\text{Ca}^{2+}$  as per <http://maxchelator.stanford.edu>) using  $3.5 \text{ mM}$  EGTA on both *cis/trans* sides. In some experiments  $2$  and  $4 \text{ mM}$   $\text{Ba}^{2+}$  was added to the cytosolic (cis) side and the



effects on channel gating was observed. As high cytosolic  $\text{Ba}^{2+}$  could potentially displace the buffer-bound  $\text{Ca}^{2+}$  and increase the  $[\text{Ca}^{2+}]$  level, this effect was quantified using MaxChelator program (<http://www.stanford.edu/~cpatton/webmaxcS.htm>). Although on addition of 2 and 4 mM  $\text{Ba}^{2+}$ , the  $[\text{Ca}^{2+}]$  increased to 45 pM and 530 pM respectively, these levels are still too low to cause any discernible activation of the modified RyR2. The *trans* chamber was held at virtual ground as in previous experiments while the *cis* chamber was voltage-clamped at  $\pm 40$  mV in all experiments except when studying voltage dependence where a range of holding potentials were applied. The ambient temperature was  $21 \pm 2^\circ\text{C}$  in all experiments. The incorporation of only a single channel in the bilayer was verified in each experiment by modification with ryanodine.

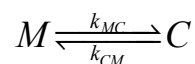
### 6.3.1. Analysis of single channel data

Single channel current traces of 2-3 minutes duration were idealised using the Segmental K-means (SKM) algorithm based on HMM found in the QuB suite of programs (version 2.0.0.7). This was found to be more suitable in detection of events from the modified channel subconductance level than the iterative HMM-based Baum-Welch expectation maximization algorithm (see **Chapter 4** for details) that was used previously for unmodified channel currents (**Chapter 5**). As described previously, a dead time of 75-120  $\mu\text{s}$  was imposed during idealisation and an initial two state  $\text{C} \leftrightarrow \text{O}$  scheme was used. The open and closed dwell time histograms generated by the initial idealisation were fitted with a mixture of exponential probability density functions using the Maximum Interval Likelihood (MIL) function of QuB. The kinetic schemes with their respective estimated rates of transitions were used for stochastic simulation of single channel data using the SIM interface of the QuB suite. The simulated data were idealised as described above to confirm the validity of the gating schemes. The Boltzmann equation was used to fit the activity–voltage relationships:  $P_o(V) = 1 / (1 + \exp(z_g F (V - V_{1/2}) / RT))$ , where  $P_o(V)$  is the voltage-dependent probability of the voltage sensing element assuming the activated state.  $V$  is the bilayer holding potential (in volts),  $V_{1/2}$  is the voltage of half-maximal voltage sensor activation,  $z_g$  is the number of elementary charges involved in gating that respond to the voltage drop across the membrane,  $R$  is the gas constant (in Joules per Kelvin per mole), and  $F$  is the Faraday constant (in Coulombs per mole).

### 6.3.2 Rate-equilibrium free energy relationship (REFER) and $\Phi$ value measurement

During gating transitions between various open and closed states, the RyR2 passes through a myriad of conformations, some of which are more energetically favoured than the others. These thermodynamically stable ground states can be resolved from single channel recordings but the mechanisms of transition between these states remain unknown. Energetic evaluations of channel kinetics could reveal novel information about the short-lived intermediate transition states. Linear free-energy relationships have been used to understand the nature of conformational changes during state transitions in proteins such as enzymes and ligand-gated ion channels (Fersht and Sato 2004). It provides clues about the temporal sequence of events that underlie the gating transition between the stable open and closed states (Auerbach 2007). The free energy of the intermediate transition state between the most stable open and closed ground states is prone to perturbation by changes in the immediate environment of the channel protein e.g. ligand concentration, voltage etc.

In this study, I examine the effects of various perturbations on the gating behaviour of the ryanodine-modified RyR2, which in turn altered the free energy barrier of the reaction. These included 1) completely eliminating the effect of the physiological activating ligand  $\text{Ca}^{2+}$  on channel gating and 2) switching the membrane potential experienced by the channel between positive and negative values. Let us consider the simple two state reaction scheme:



M is the ryanodine-modified open state and C is the closed state in equilibrium where  $k_{MC}$  and  $k_{CM}$  are the forward and backward rate constants respectively. This can be represented as an energy landscape diagram where the free energy (y-axis) is plotted against the reaction coordinate (x-axis) as shown in **Fig. 6.4** (black curve).

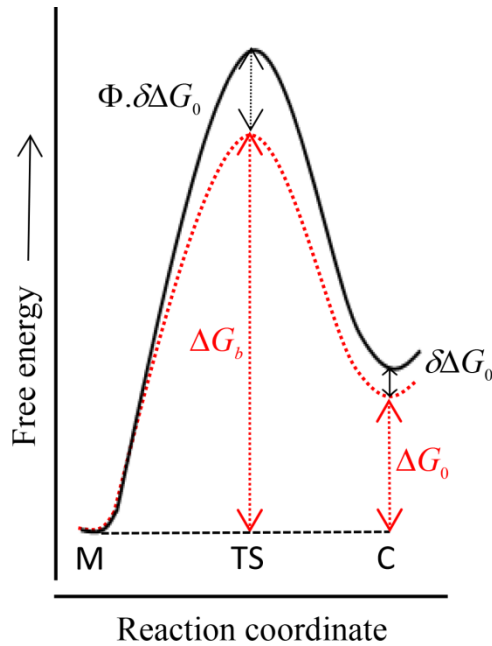


**Figure 6.4 Energy landscape diagram.**

When a structural perturbation of RyR2 changes the free energy of the closed ground state (C) by  $\delta\Delta G_0$  relative to the ryanodine-modified open ground state (M), the free energy of the transition state TS changes by  $\Phi \cdot \delta\Delta G_0$  as shown in **Fig. 6.4** (red dotted curve). Again, from the Arrhenius relationship the following could be derived:

$$\text{Reaction rate } k = A \cdot e^{-\frac{\Delta G_b}{RT}}$$

Where  $\Delta G_b$  (activation energy of the transition) represents the free energy barrier height in the energy landscape. Thus for the logarithms of the rate constants in Scheme I, a change of  $-\Phi \cdot \delta\Delta G_0/RT$  is seen for the forward rate ( $k_{MC}$ ) and  $-(\Phi - 1) \delta\Delta G_0/RT$  for backward rate ( $k_{CM}$ ) respectively. The slope obtained from a log-log plot of the forward rate constants against the equilibrium constants is the  $\Phi$  value (Cymes et al. 2002). In this study the  $\Phi$  values could provide strong empirical clues regarding the temporal aspect of the structural changes leading to the transition from one ground state to another (M and C) through the TS. The value of  $\Phi$  ranges between 0 to 1 and a high value ( $\sim 1$ ) points to a closed-like nature of TS structure and a value near 0 would indicate that the TS resembles the open modified state M. As the channel molecule moves through a spectrum of intermediate conformations in the transition region between M and C, the  $\Phi$  value offers a snapshot of the M vs. C nature of the global protein structure.

## 6.4 Results

### 6.4.1 Gating kinetics of ryanodine-modified RyR2 in the presence and absence of $\text{Ca}^{2+}$

Single channels currents were recorded after incorporation of RyR2 in planar lipid bilayers at  $\pm 40\text{mV}$  holding potential. The channels were activated by  $\sim 1\mu\text{M}$  contaminant  $\text{Ca}^{2+}$  present in  $210\text{mM}$  KCl solution (pH 7.4) on both sides (cytosolic and luminal). The channels exhibited typical gating behaviour ( $P_o = 0.21 \pm 0.06$ ;  $n=17$ ) under these conditions (**Fig. 6.5, A&B**). The channels were subsequently modified to an open subconductance state ( $\sim 60\%$  of full open level) using  $1\mu\text{M}$  ryanodine on the cytosolic (*cis*) side at  $+40\text{mV}$  holding potential (**Fig. 6.5 C**). The ryanodine-modified channels had a very high  $P_o$  ( $\sim 1$ ) with only a few brief transitions to the closed state while transitions to the fully open state never occurred (**Fig. 6.5, D&E**). On removal of  $\text{Ca}^{2+}$  from the cytosolic and luminal side using  $3.5\text{ mM}$  EGTA (*cis/trans*), the frequency of brief closing events from the modified open state increased dramatically. However, this increased propensity of channel closure in the absence of  $\text{Ca}^{2+}$  had an asymmetric response to voltage.

#### 6.4.1.1 Unique voltage-dependence of ryanodine-modified RyR2

The increase in the frequency of closing events due to the removal of  $\text{Ca}^{2+}$  was much more pronounced at  $+40\text{mV}$  than at  $-40\text{mV}$  as seen in the representative traces (**Fig. 6.5, F&G**). These results are summarised in the form of bar graphs in **Fig. 6.6**. The  $P_o$  for ryanodine-modified channels activated by contaminant  $\text{Ca}^{2+}$  at  $+40\text{mV}$  was  $0.99 \pm 0.002$  ( $n=9$ ) and decreased to  $0.75 \pm 0.05$  ( $n=9$ ) at zero  $\text{Ca}^{2+}$  (**Fig. 6.6 A**) while no significant changes were observed at  $-40\text{mV}$  ( $P_o = 0.99 \pm 0.001$  at contaminant and  $0.98 \pm 0.009$  at zero  $\text{Ca}^{2+}$ ;  $n=9$ ). This decrease in open probability is due to an increased frequency of brief closing events ( $\sim 170$  fold increase at  $+40\text{mV}$ ; **Fig. 6.6 D**) without a change in closed times (a mean of  $0.41\text{ ms}$ ; **Fig. 6.6 B**), leading to a decrease in open times (**Fig. 6.6 C**). However, due to a paucity of idealised events at contaminant  $\text{Ca}^{2+}$  with  $-40\text{mV}$  holding potential, the closed times are underestimated and reflected as an apparent decrease ( $0.26 \pm 0.02\text{ ms}$ ;  $n=9$ ) in **Fig. 6.6 B**. On an average, 15 closing events were detected per second in single channel data traces at  $-40\text{ mV}$  as opposed to a mean of 370 events at  $+40\text{ mV}$  in the absence of  $\text{Ca}^{2+}$  (more events result in better estimation of kinetic parameters). A portion of the current trace **F** in **Fig. 6.5** is shown again on an

expanded time-scale (**Fig. 6.5 H**) to reiterate that the character of the closing events does not change; only their frequency.

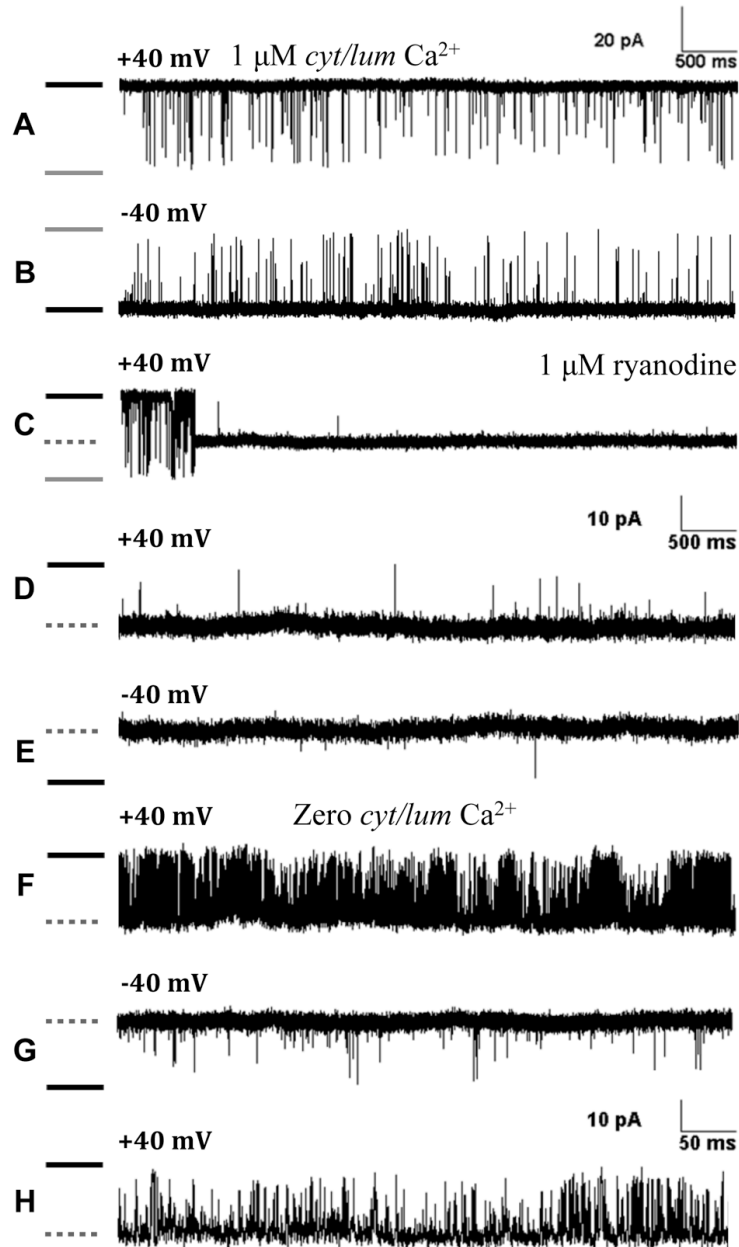


**Figure 6.5. Gating behaviour of ryanodine-modified RyR2 at zero  $\text{Ca}^{2+}$ .** Representative single channel traces are shown in (A-H). Black bars indicate closed levels; grey bars fully open levels and dotted bars modified levels. An unmodified channel activated by 1  $\mu\text{M}$  (contaminant) cytosolic and luminal  $\text{Ca}^{2+}$  at + (A) and -40 mV (B), subsequently modified with 1  $\mu\text{M}$  ryanodine at +40 mV (C). Under these conditions, the  $P_o$  of the modified channel is high, with only brief closings at both + (D) and -40 mV (E). Chelation of  $\text{Ca}^{2+}$  to nominally zero increases the frequency of closing events to a greater degree at +40 (F) than -40 mV (G). These closing events are brief in nature, as shown (H – x10 expanded section of trace F).

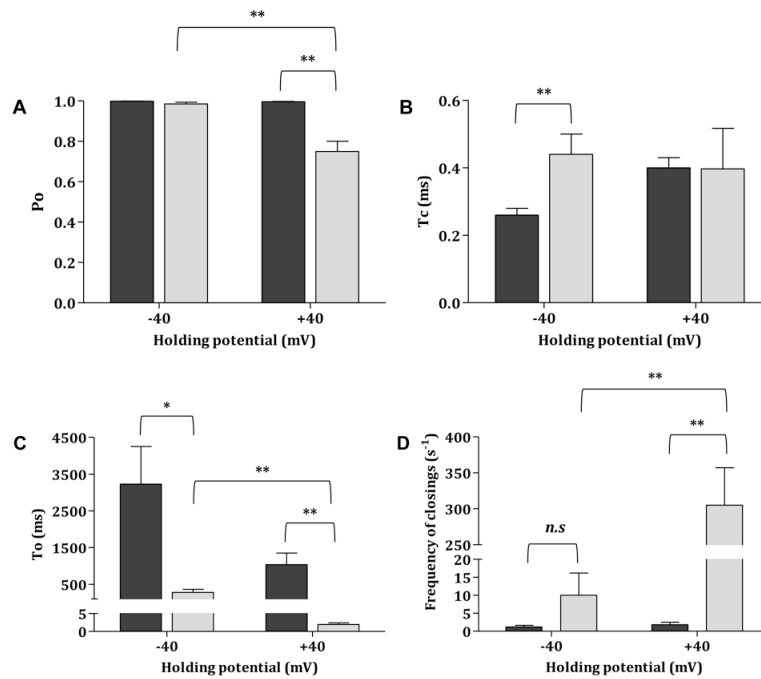


**Figure 6.6. Kinetic parameters of ryanodine-modified RyR2 gating (A-D)** are represented by black bars (1 μM Ca<sup>2+</sup>) and grey bars (nominally zero Ca<sup>2+</sup>). Data are shown as mean ± S.E.M for n=9. \* = p<0.05; \*\* = p<0.005; n.s= not significant. (A) Po is significantly reduced on removal of Ca<sup>2+</sup> at +40 mV compared to -40 mV. (B) Altered Po is not due to a change in Tc (difficulty in resolving events at -40 mV in the presence of 1 μM Ca<sup>2+</sup> means that Tc was underestimated – see text for details), but instead, (C) due to a decrease in To, which despite occurring at both + and -40 mV, only translates into a significant change in (D) the frequency of closings at +40 mV.

This dependence of channel activity on membrane potential was a manifestation of the removal of cytosolic Ca<sup>2+</sup> as experiments performed with 1 μM Ca<sup>2+</sup> only on the luminal side gave the same results (Po = 0.8 ± 0.06 at +40 mV and 0.99 ± 0.002 at -40 mV; n = 4). The interaction of ryanodine dramatically decreases the probability of RyR2 channel closing in the presence of activating Ca<sup>2+</sup>; nevertheless channel gating remains, to some degree, sensitive to [Ca<sup>2+</sup>]<sub>cyt</sub>. The asymmetric response of the ryanodine-modified RyR2 to voltage in the absence of Ca<sup>2+</sup> was unexpected, as the channel is not known to possess typical voltage sensor domains as seen in other voltage-gated channels (Bezannilla 2008; Catterall 2010). Therefore, this voltage dependence of channel gating was explored in detail.

### 6.4.1.2 A detailed examination of the voltage dependence

The next set of experiments were done under similar conditions where the ryanodine-modified RyR2 gating was examined at a range of holding potentials (from -80 mV to +80 mV) in the absence of  $\text{Ca}^{2+}$ . The voltage steps were in 10 mV increments but the modified channel current amplitudes were too small for the events to be reliably detected at holding potentials below  $\pm 20$  mV. The results are summarised in **Fig. 6.7** where the kinetic parameters of  $P_o$ ,  $T_c$ ,  $T_o$  and frequency of closing events have been examined. **Fig. 6.7 A** shows a steep dependence of channel activity on membrane potential when switched between positive and negative holding potentials. The voltage dependence quickly ‘saturates’ once the polarity is switched between negative (increased  $P_o$ ) and positive (reduced  $P_o$ ). **Fig. 6.7 D** shows that the decrease in channel activity at positive membrane potentials is due to the drastically increased frequency of brief closing events.

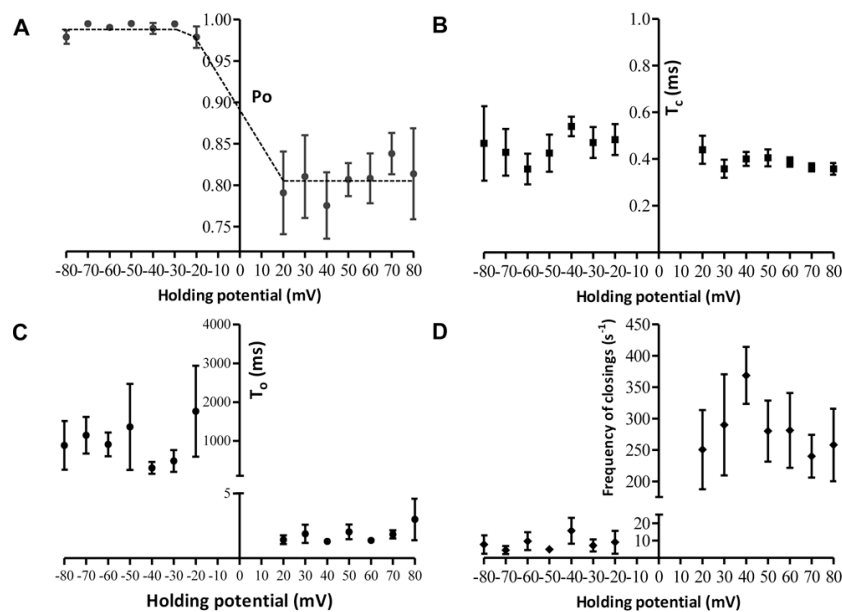


**Figure 6.7. Study of ryanodine-modified RyR2 gating in the absence of activating  $\text{Ca}^{2+}$  at various holding potentials reveals steep voltage dependence.** (A) A sharp decrease in channel activity ( $P_o$ ) is seen when holding potential is switched from negative to positive. The data points (closed circles) were then fitted with a Boltzmann equation (dotted line). Due to low signal-to-noise, it is not possible to accurately record single channel currents from ryanodine-modified RyR2 below  $\pm 20$  mV holding potential. (B) Closed times ( $T_c$ ) plotted against holding potentials (black squares) do not show significant variation indicating that the character of closing events remain unchanged. (C) Modified channel open times ( $T_o$ ) decreased sharply at positive holding potentials when switched from negative but don't show much variation at different voltages with the same polarity. (D) The frequency of closing events increases at positive voltages and is the basis for the decrease in modified channel  $P_o$  in response to voltage change. Data presented as mean  $\pm$  S.E.M with  $n = 6-9$  single channel experiments for each data point. Error bars, where not visible, are included within the symbol.

The data points on the Po-voltage plot were fitted with the Boltzmann function (see section 6.4.1) gives the ‘apparent gating valence’,  $z_g$  of  $\sim -32$  ( $\sim 8$  negative charges per subunit). Although the RyR2 does not have a known voltage sensor domain, the dependence of channel activity on voltage may be due to the movement of pockets of negatively charged residues along the potential drop, which in turn is transmitted to the channel gate. The steepness of the plot suggests that this mechanism is very fast and is global in nature.

#### 6.4.1.3 Observed changes in channel activity: a true voltage dependent phenomenon

Changing the bilayer holding potential between positive and negative voltages also changes the direction of ionic flux through the channel pore. However, the RyR is known to behave as an ‘Ohmic’ conductor where the observed current through the channel changes proportionately to the change in membrane potential and there is no rectification. Nevertheless, experiments with asymmetrical KCl solutions (ion gradient) were conducted to discount the possibility of the direction of net  $K^+$  flux being responsible for change in channel activity at zero  $Ca^{2+}$ . Fig. 6.8 shows representative traces from experiments where a x4 cytosolic to luminal ionic gradient (840 mM KCl *cis*; 210 mM KCl *trans*) was employed and channel activity observed at various holding potentials as previously described (Fig. 6.7). There is a significant increase in the frequency of closing events when the holding potential is increased from 0 mV to +20 mV. At negative holding potentials, the channel Po was high whether the direction of  $K^+$  flux through the RyR2 was from *cis* to *trans* (-10 mV and -20 mV) or from *trans* to *cis* (-40 mV and -60 mV). This is in agreement with earlier experiments where no ionic gradient was used (Fig. 6.5). No current was resolved when holding potential was close to the reversal potential for this particular ionic gradient pair (around -30 mV). As expected from an ‘Ohmic’ channel, the current-voltage plot derived from experiments where symmetrical KCl was used passes through the origin (Fig. 6.9B, red squares) whereas it is shifted in a parallel manner in the presence of a *cis* to *trans* gradient (Fig. 6.9B; green squares). It is evident from data presented in Fig. 6.9A that the activity of modified RyR2 in the absence of  $Ca^{2+}$  is influenced by membrane potential and not by the direction of flow of ions through the channel. Under symmetric conditions, the ryanodine-modified current level was too small to be accurately estimated (no net ionic flux) around 0 mV holding potential and around  $\sim -31$  mV (reversal potential) in the presence of a *cis* to *trans* gradient (asymmetric condition). Linear regressions through



the data points give the conductances under each condition. In the absence of a gradient, the slope conductance was  $442.5 \pm 1.25$  pS (n=5) and  $458 \pm 7.5$  pS (n=4) with a reversal potential of  $\sim -31$  mV in the presence of a x4 cytosolic to luminal gradient.

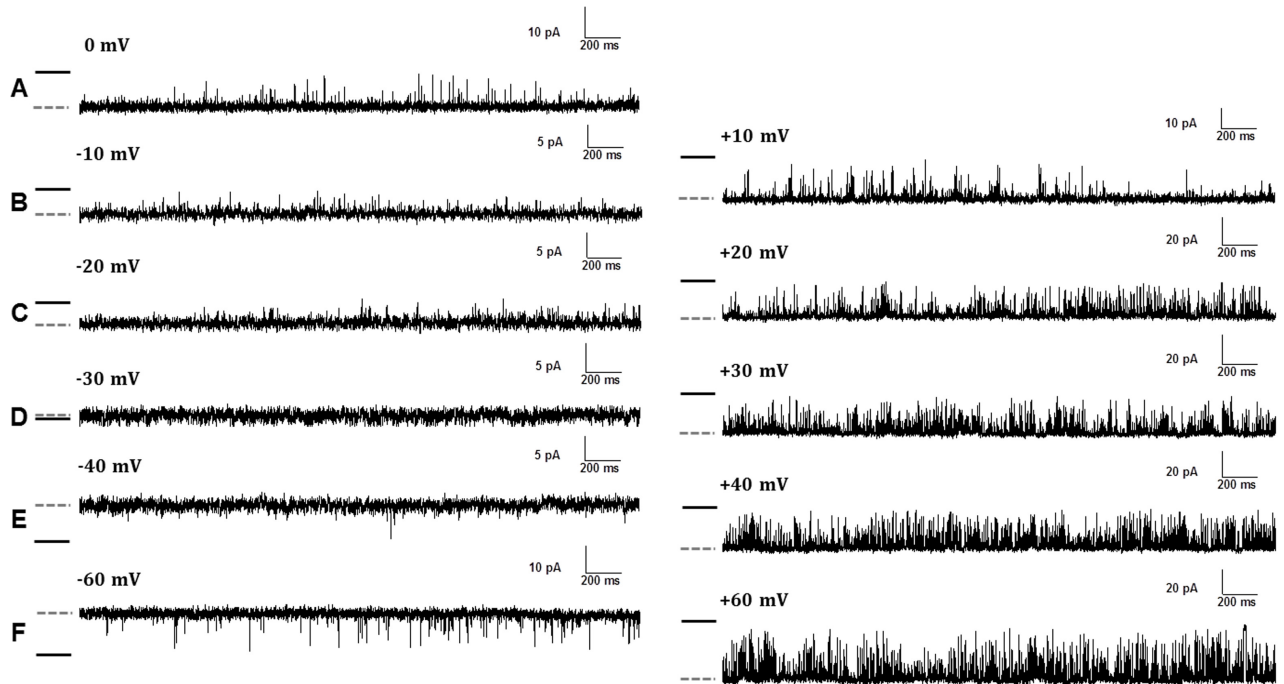


**Figure 6.8 (A-F) are representative single channel current traces showing the influence of membrane holding potential on ryanodine-modified RyR2 gating under asymmetric ionic conditions. A *cis* to *trans* K<sup>+</sup> gradient was employed (810 mM KCl *cis*; 210 mM KCl *trans*) to record channel activity at various positive and negative holding potentials in order to rule out the direction of ionic flux as the determinant of modified channel gating behaviour in the virtual absence of Ca<sup>2+</sup>. The closed levels are indicated by black bars and modified open levels are shown using grey dashed bars.**

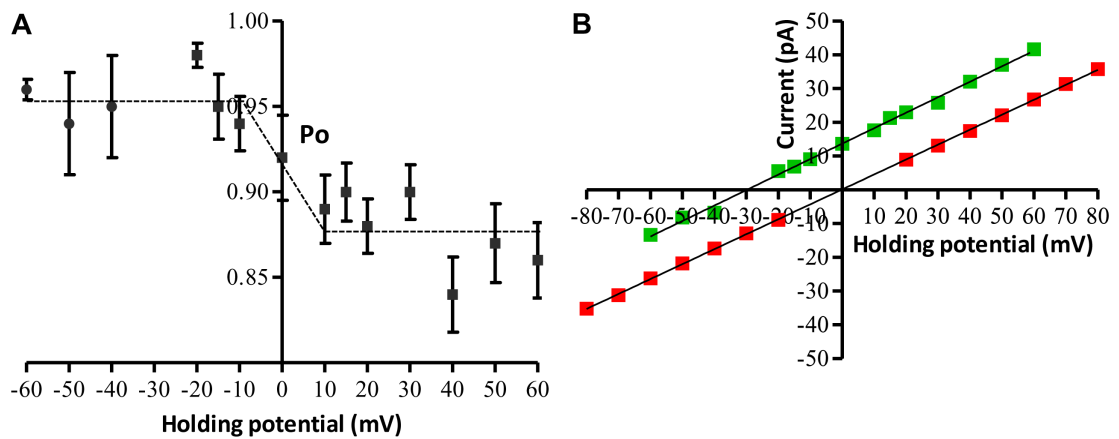


**Figure 6.9. Voltage dependence of ryanodine-modified RyR2 gating and direction of ionic flux. (A)** Shows channel  $P_o$  at different holding potentials in the presence of a *cytosolic* to *luminal* ionic gradient (840 mM KCl *cis* and 210 mM KCl *trans*). The voltages where the net ionic flux was from cytosolic to luminal side are represented as squares whereas where the direction of net flux was reversed (luminal to cytosolic) are shown using circles (at -40, -50 and -60 mV). As before, the modified RyR2 shows higher  $P_o$  (less closing events) at negative holding potentials irrespective of the direction of ionic flux through the channel. These data points were fitted using a Boltzmann equation (as done previously in **Fig. 6.7A**) whose outcome suggests the possible role of negatively charged residues in the sensing of voltage drop across the membrane. The Boltzmann fit is shown by the dotted line and data are presented as mean  $\pm$  S.E.M with  $n = 4-6$  single channel experiments for each data point. **(B)** Compares the current-voltage relationship of ryanodine-modified RyR2 under symmetrical (210 mM KCl *cis/trans*) ionic condition shown by red data points and when under an ionic gradient (840 mM KCl *cis* and 210 mM KCl *trans*) shown by green squares. Error bars, where not visible, are included within the dimensions of the red and green squares in the plot. All data are shown as mean  $\pm$  S.E.M.

#### 6.4.1.4 Mode-shifting of the ryanodine-modified channel

The phenomenon of modal shifts in gating kinetics in RyR has been described in previous studies (Zahradníková and Zahradník 1995; Armisen et al. 1996; Saftenku et al. 2001) where the channel is shown to spontaneously shift between high and low  $P_o$  modes (Fill et al. 2000). In these studies, modal shifting was attributed to sudden changes in  $[Ca^{2+}]_{cyt}$  and was also dependent on which mode the RyR was in during the change in ligand concentration.

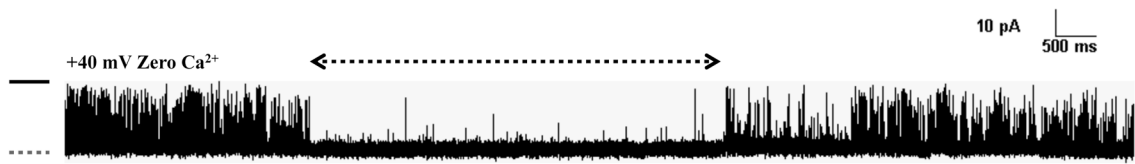


**Figure 6.10. Spontaneous modal gating behaviour of ryanodine-modified RyR2 in the absence of Ca<sup>2+</sup>.** A single channel trace recorded at +40 mV in nominally zero Ca<sup>2+</sup> shows shifting of gating from typical to a high Po mode (dotted double arrow on top) with few closing events and back to typical mode. The fully closed level is indicated by the black solid bar on the left and the modified open level by the grey dotted bar.

In this current study, modal shifts in modified-RyR2 gating behaviour were observed in the complete absence of Ca<sup>2+</sup> that occurred randomly in time without any obvious triggers (no ligand binding/unbinding). This stochastic nature of mode shifting implies that it is an intrinsic property of the channel molecule, probably the result of random thermodynamic fluctuations within the channel and not triggered by [Ca<sup>2+</sup>]<sub>cyt</sub>. For the purposes of describing modified RyR2 gating behaviour in terms of mathematical models, these rare periods of very high Po demonstrated in **Fig. 6.10** (<5% of total length of recording) were ignored and the typical gating behaviour was studied in detail.

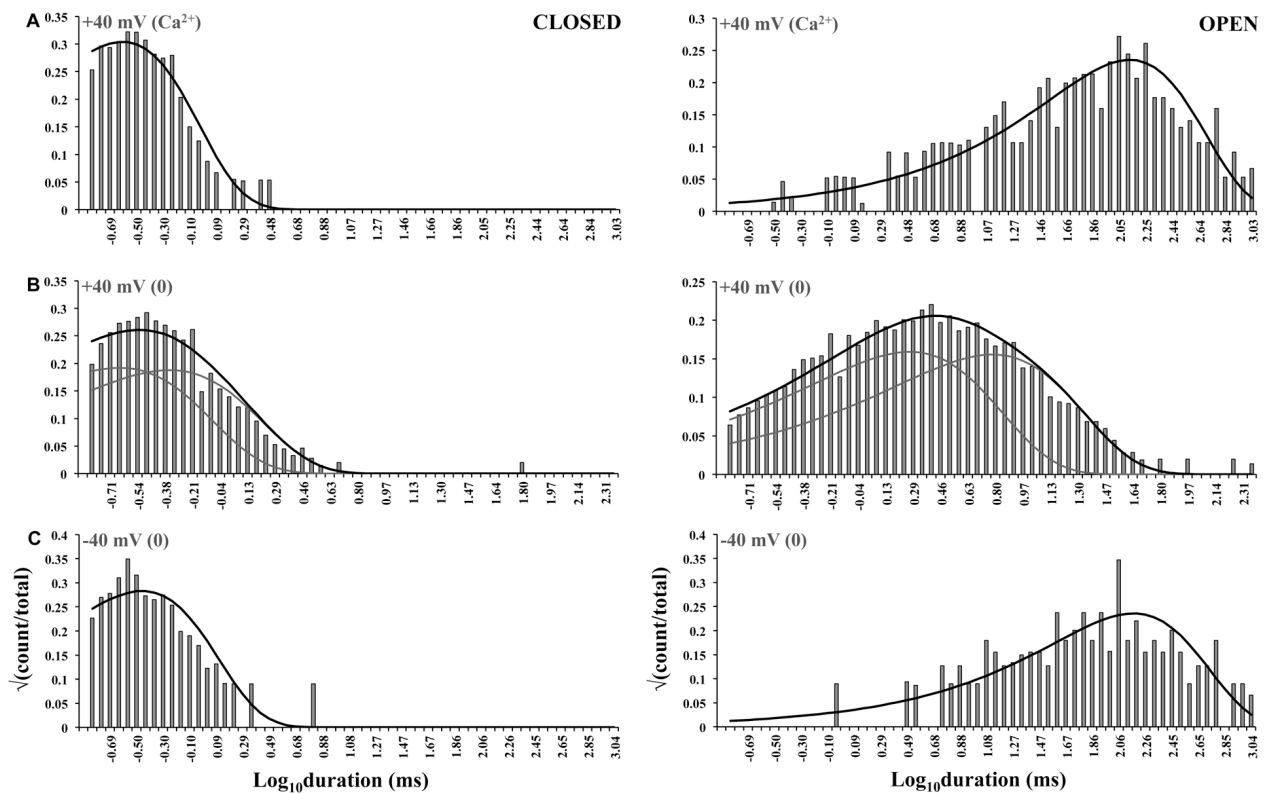


**Figure 6.11. Fitting of closed and open dwell-time histograms with exponentials allow mechanistic interpretation of single channel data.** Representative closed (left) and open (right) time distributions plotted as histograms from a single channel experiment are shown along with their overall fits (solid black curves) and exponential components underneath (grey curves). The membrane potential ( $\pm 40$  mV) and presence/absence of  $\text{Ca}^{2+}$  is indicated above the distribution. **(A)** The dwell-time distribution of the modified channel in the presence of  $1 \mu\text{M}$   $\text{Ca}^{2+}$  at  $+40$  mV was fitted using a single exponential. An insufficient number of events were obtained at  $-40$  mV for an accurate fit. **(B)** At nominally zero  $\text{Ca}^{2+}$ , two exponential components each were required for fitting closed and open time histograms when the membrane potential was  $+40$  mV. **(C)** In the absence of  $\text{Ca}^{2+}$  at  $-40$  mV, only one exponential component each was required for fitting closed and open time histograms. These exponential fits were then associated with corresponding closed and open states in gating models at various conditions of  $\text{Ca}^{2+}$  and voltage (**Schemes 1, 2 and 3**). The parameters of fits from many single channel experiments are shown in **Table 6.1**.

**TABLE 6.1**

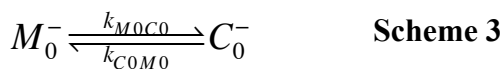
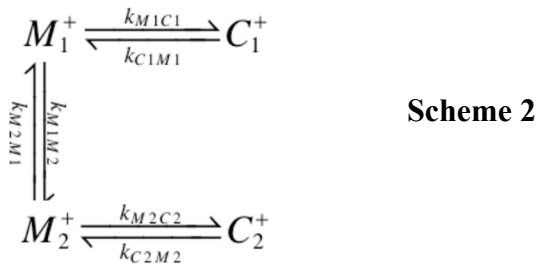
The parameters of the exponential components (time constants  $\tau$  and area A) used in fitting of the open and closed time histograms (see **Fig. 6.11**) while simultaneously building kinetic schemes (1, 2 and 3) are shown in the table. Each probability density function used in fitting corresponds to a modified open or closed state. Data presented as mean  $\pm$  S.E.M.

Conditions	CLOSED			OPEN		
		$\tau$ (ms)	Area (%)		$\tau$ (ms)	Area (%)
+40 mV, Scheme 1 (n=9) 1 $\mu$ M Ca <sup>2+</sup>	<b>C<sub>Ca</sub></b>	0.33 $\pm$ 0.05	100	<b>M<sub>Ca</sub></b>	440 $\pm$ 91	100
+40 mV, Scheme 2 (n=9) Zero Ca <sup>2+</sup>	<b>C<sub>1</sub></b>	0.32 $\pm$ 0.05	33 $\pm$ 7.8	<b>M<sub>1</sub></b>	7.8 $\pm$ 2	34 $\pm$ 5
	<b>C<sub>2</sub></b>	0.34 $\pm$ 0.04	67 $\pm$ 7.8	<b>M<sub>2</sub></b>	3.4 $\pm$ 0.8	66 $\pm$ 5
-40 mV, Scheme 3 (n=6) Zero Ca <sup>2+</sup>	<b>C<sub>0</sub></b>	0.38 $\pm$ 0.04	100	<b>M<sub>0</sub></b>	247 $\pm$ 63	100

#### 6.4.2 Mechanistic basis of ryanodine-modified channel gating

Dwell-time histograms generated using the idealised ryanodine-modified single channel data were fitted with exponential probability density functions to generate kinetic schemes that provide accurate descriptions of gating behaviour (see **Chapter 4**, section 4.4.8.1). The time constants and areas under fitted exponentials are shown in **Table 6.1**. Modified open- and closed-time histograms for single channels activated by 1  $\mu$ M Ca<sup>2+</sup> (+40 mV) could be fitted best using one exponential component each (**Fig. 6.11A**). The channel therefore visits at least one modified open state (M) and a closed state (C) for the majority of the time i.e. only two most energetically favourable states are resolved (**Scheme 1**, annotated as superscript '+' and subscript 'Ca'). The rate constants for the transitions are shown in **Table 6.2**. The lack of sufficient idealised events at -40 mV (1  $\mu$ M Ca<sup>2+</sup>) prevented accurate fitting of dwell time histograms, hence a kinetic scheme for channel gating under these conditions is not available. After removal of Ca<sup>2+</sup> the frequency of closing events increases, particularly at +40 mV. The fitted dwell time histograms for single channel recordings at +40 mV are shown in **Fig. 6.11 B** where a minimum of two exponential components each is required for the fit. **Scheme 2** below shows the best fit model for an accurate description of gating behaviour where the channel moves between two discrete modified open states M1 and M2 and from these,

makes brief but frequent sojourns to corresponding closed states C1 and C2. The dwell time histograms for single channel data at -40 mV in the absence of Ca<sup>2+</sup> (**Fig. 6.11 C**) were fitted with one exponential each for open and closed times suggesting a two state mechanism with transitions between a single modified and closed state (**Scheme 3**).



The experimental conditions of zero Ca<sup>2+</sup> and negative holding potentials are denoted in the scheme as superscript ‘-’ and subscript ‘0’ respectively. Although the ryanodine-modified RyR2 passes through a spectrum of possible conformations, only the most thermodynamically stable conformations are visited often enough to be resolved in single channel recordings. These states constitute the kinetic schemes 1, 2 and 3, which have the maximum likelihood of being able to describe the gating behaviour of the channel under different conditions of activating Ca<sup>2+</sup> and membrane potential. The ryanodine-modified RyR2 gating transitions (seen under different conditions of activating Ca<sup>2+</sup> and membrane potential) are distinct from those that describe channel gating in the absence of ryanodine modification. Previous studies modelling the gating behaviour of RyR2 when activated by Ca<sup>2+</sup><sub>cyt</sub> alone revealed transitions between several different stable conformations (**Chapter 5**), some of which are Ca<sup>2+</sup>-dependent and are presumed to be due to the helix-bundle crossover in the channel pore, and one Ca<sup>2+</sup>-independent transition (flicker closing) thought to be due to fluctuations in the putative selectivity filter region (Mukherjee et al. 2012). The change in Po in an unmodified channel in response to Ca<sup>2+</sup><sub>cyt</sub> was largely due to changes in closed times while open times mostly remained unchanged (**Chapter 5**), while in the case of the ryanodine-modified RyR2 the

mechanism is reversed (closed times remain unaltered). These important differences do not lend support to the previously published reports that ryanodine modification sensitises the RyR2 to  $\text{Ca}^{2+}$  (Masumiya et al. 2001; Du et al. 2001).

**TABLE 6.2**

Rate constants optimized during fitting of dwell-time histograms and model building.

Gating Schemes and conditions	Rates	Rate constants# (mean $\pm$ S.E.M)
<b>Scheme 1</b> Contaminant ( $\sim 1 \mu\text{M}$ ) $\text{Ca}^{2+}$ at +40 mV (n=9)	* $k_{\text{MC}}$	$5.4 \pm 0.9$
	$k_{\text{CM}}$	$3437 \pm 396$
	$k_{\text{M1M2}}$	$42 \pm 12.7$
	$k_{\text{M2M1}}$	$32 \pm 6.5$
<b>Scheme 2</b> Zero $\text{Ca}^{2+}$ at +40 mV (n=9)	* $k_{\text{M1C1}}$	$408 \pm 146$
	$k_{\text{C1M1}}$	$3722 \pm 386$
	* $k_{\text{M2C2}}$	$558 \pm 88$
	$k_{\text{C2M2}}$	$3492 \pm 413$
<b>Scheme 3</b> Zero $\text{Ca}^{2+}$ at -40 mV (n=6)	* $k_{\text{M0C0}}$	$10.3 \pm 3.8$
	$k_{\text{C0M0}}$	$2764 \pm 247$

# The units are  $\text{s}^{-1}$  or  $\mu\text{M}^{-1}.\text{s}^{-1}$  as appropriate.

\* Forward rate constants that were used in REFER analysis (**Fig. 6.13**).

### 6.4.3 Model-based simulations to validate kinetic schemes

The validity of the gating schemes (**1, 2 and 3**) obtained by the fitting of dwell time histograms and rate constant optimisation were verified by simulation of single channel data. Rate constants from kinetic schemes obtained from individual channels (summarised in **Table 6.2**) were used for stochastic simulation using the SIM module of the QuB interface (see **Chapter 4**, section 4.4.8.3). The representative traces shown in **Fig. 6.12A** are in good agreement with the experimental data traces in **Figure 6.5**. The change in  $P_o$  ( $0.99 \pm 0.0006$  at +40 mV,  $1 \mu\text{M Ca}^{2+}$ ;  $0.8 \pm 0.03$  at +40 mV, nominally zero  $\text{Ca}^{2+}$ ) is due to a decrease in open durations (**Fig. 6.12 D**) and an increase in the frequency of closings, while the closed durations remained unaltered (**Fig. 6.12 C**). Therefore, the gating models incorporating the minimum number of states necessary for an accurate description of RyR2 behaviour are valid for the experimental conditions used.

### 6.4.4 Modified RyR2 state transitions: from an energetics perspective

The kinetic schemes derived from modelling of single channel data describe only the most stable conformations (wells along the energy landscape) that RyR2 adopts during gating. As insufficient structural data are available to elucidate the mechanisms of state transition in RyR, energetic evaluation of gating could yield valuable information regarding the nature of intermediate transition states. REFER analyses (Grosman 2002; Y. Zhou et al. 2005) (see **section 6.4.2**) were carried out where the equilibrium was perturbed by the complete removal of ligand ( $\text{Ca}^{2+}$ ) or by changing the polarity of the membrane potential. At nominally zero  $\text{Ca}^{2+}$  the transitions involve a pure gating step as no binding or unbinding of ligand takes place (**Schemes 2, 3**). Likewise, with  $1 \mu\text{M Ca}^{2+}$  at +40 mV, the channel activity is saturated ( $P_o \sim 1$ ), therefore, these transitions can also be assumed to be gating steps for all practical purposes (**Scheme 1**). The measurement of pure gating steps is important in this analysis because the inclusion of intermediate binding steps would complicate interpretation of the data as various binding energies would then have to be considered. This would be impossible to accurately quantify in the case of RyR as structural information regarding the binding sites for  $\text{Ca}^{2+}$  and ryanodine is not available.



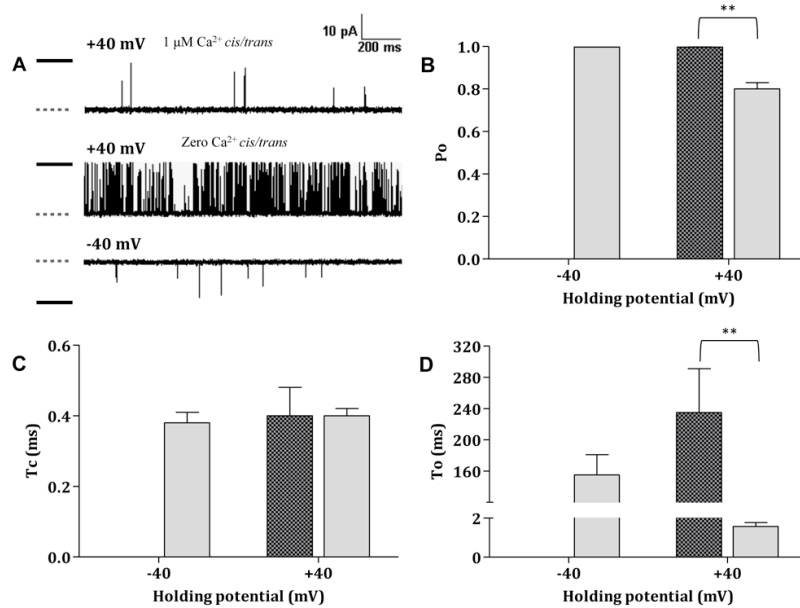


**Figure 6.12. Kinetic parameters from simulated single channel data validate gating models.**

(A) Representative traces of simulated single channel data generated from the gating schemes. Black solid bars on the left represent the closed level while the grey dotted bars denote the ryanodine-modified open level of RyR2. These simulated traces look similar to their actual experimental counterparts (Fig. 6.4 D, F, G). As fitted dwell-time distributions and corresponding gating schemes were unavailable for experiments conducted at -40 mV with 1 μM Ca<sup>2+</sup> (see Results), simulated traces could not be generated. Analysis of simulated single channel data shows that the results are in agreement with those obtained from experimental data (see Fig. 6.6 for experimental data). The kinetic parameters are plotted for holding potentials of ±40 mV (hatched dark grey bars, 1 μM Ca<sup>2+</sup>; light grey bars, nominally zero Ca<sup>2+</sup>). All data are shown as mean ± S.E.M for n=5 channels. (B) Open probabilities at +40 mV at zero Ca<sup>2+</sup> are significantly lower than when Ca<sup>2+</sup> is present, or at -40 mV with zero Ca<sup>2+</sup>. (C) Closed times do not show any variation with changes in Ca<sup>2+</sup> or holding potential. (D) The reduction in P<sub>o</sub> at +40 mV in the absence of Ca<sup>2+</sup> is due to a significant decrease in open times (1.57 ± 0.2 ms; n=5) compared to when Ca<sup>2+</sup> is present (235 ± 56 ms; n=5). Significant differences are indicated (\*\* = p<0.005).

As I'm interested in the properties of transitions to the closed states in both types of perturbations, the modified open states (M, M1 and M2) were chosen as starting states and the closed states (C, C1 and C2) as end states for convenience.

As there are two such transitions in Scheme 2 with similar characteristics (see Table 6.1 and Table 6.2), they were considered as two reactions. The log-log plots of the forward rate constants against the equilibrium constants (shown in Fig. 6.13) provide structural clues about the transition state (TS) during the conformational wave from one stable state

to another (see section 6.4.2). The  $\Phi$  value for the perturbation due to  $\text{Ca}^{2+}$  removal ( $\Phi_L$ ) is close to 1 (Fig. 6.13 A), as is that for perturbation of gating equilibrium by a voltage ( $V_m$ ) switch from -40 to + 40 mV ( $\Phi_{\Delta V}$ , Fig. 6.13 B). The  $\Phi$  value indicates the structural and temporal nature of the TS relative to the ground states (Auerbach 2007). A value close to zero would suggest that the structure of TS is similar to the starting ground state (modified state) and that the transition is slow. The results from this study ( $\Phi$  values close to 1) suggest that the conformation of TS is similar to that of the closed end state in both cases and that it occurs early during the course of the reaction (i.e. the transition is fast).

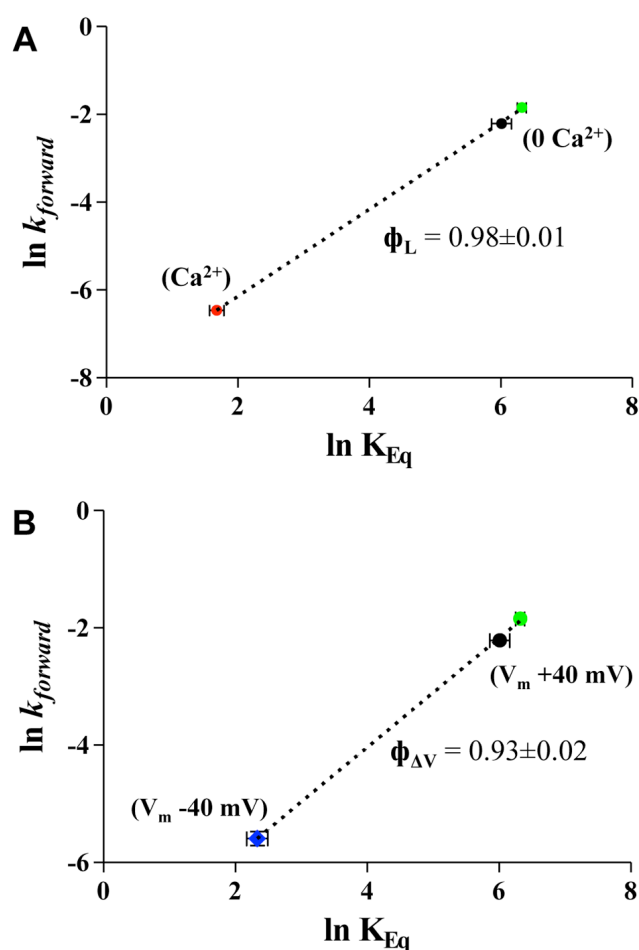


**Figure 6.13. REFER analysis and  $\Phi$  (Phi)-value estimation from state transitions provides structural insights into mechanisms.** The forward rate constants of the state transitions are plotted against the equilibrium constants on a log-log scale (see section 6.4.2 and Fig. 6.4 for details). The rate constants used and the gating schemes they are derived from are shown in Table 2 and are asterisked. **(A)** In the presence of activating  $\text{Ca}^{2+}$  at +40 mV when the channel has a  $P_o \sim 1$ , the forward rate constant is represented by  $k_{\text{MC}}$  (from Scheme I, red circle in the plot). When  $\text{Ca}^{2+}$  is removed the perturbation results in decreased  $P_o$  with two similar forward rate constants  $k_{\text{M1C1}}$  &  $k_{\text{M2C2}}$  from Scheme 2 (Black and green circles respectively). The slope of this plot (dotted line) gives the Phi value for ligand-induced perturbation of gating ( $\Phi_L$ ) =  $0.98 \pm 0.01$  ( $n=6$ ). **(B)** At -40 mV, in the absence of  $\text{Ca}^{2+}$ , the  $P_o$  is high and the forward rate constant is  $k_{\text{M0C0}}$  from Scheme 3 (blue square). When the holding potential is switched to +40 mV, the  $P_o$  decreases and the forward rate constants used are the same as in (A) with  $k_{\text{M1C1}}$  &  $k_{\text{M2C2}}$  from Scheme 2 represented by black and green circles respectively. The resulting Phi-value on perturbation of gating due to voltage change ( $\Phi_{\Delta V}$ ) =  $0.93 \pm 0.02$  ( $n=6$ ). Error bars, where not visible, are included within the dimensions of the closed circles in the plot. All data are shown as mean  $\pm$  S.E.M.

#### 6.4.5 Effect of cytosolic $Ba^{2+}$ on ryanodine-modified RyR2 gating

High cytosolic (mM)  $Ca^{2+}$  and  $Ba^{2+}$  are known to inhibit RyR2 channel gating, probably by acting on low affinity inhibitory sites on the cytoplasmic domain (Laver 2007, Diaz-Sylvester et al. 2011).  $Ba^{2+}$  was used as a tool to further investigate the gating of ryanodine-modified channels in nominally zero  $Ca^{2+}$  conditions.  $Ba^{2+}$  (2 and 4 mM) was added to the cytosolic side of the channel while holding at -40 mV to prevent any of the divalent from moving to the luminal side. Gating behaviour at +40 mV was subsequently studied. The representative traces in **Fig. 6.14**, show the progressive reduction of modified channel  $P_o$  brought about by the action of increasing concentrations of  $Ba^{2+}$ . Interestingly, with mM  $Ba^{2+}$  present at the cytosolic face of the channel,  $P_o$  is no longer voltage dependent (**Figs. 6.14, C-F**) with kinetic parameters similar at positive and negative holding potentials (**Figs. 6.14, G-I**).  $P_o$  decreases due to both an increase in closed times and a decrease in open times (**Figs. 6.14 H and I**). Fitting of dwell-time histograms using these idealised events reveals the presence two populations of closed events at both positive and negative potentials (**Fig. 6.15**); a long closed component ( $\tau = 3.33 \pm 0.9$  ms; Area =  $22 \pm 9\%$ ;  $n = 4$  at +40 and  $\tau = 3.35 \pm 0.7$  ms; Area =  $27 \pm 6\%$ ;  $n = 4$  at -40 mV) and a population of shorter closing events ( $\tau = 0.56 \pm 0.09$  ms; Area =  $78 \pm 9\%$   $n = 4$  at +40 and  $\tau = 0.88 \pm 0.13$  ms; Amp =  $73 \pm 6\%$ ;  $n = 4$  at -40 mV). These data demonstrate that mM concentrations of cytosolic  $Ba^{2+}$  can significantly reduce the  $P_o$  of ryanodine-modified RyR2 channels. While with ryanodine bound the likelihood of RyR2 channel closing is dramatically reduced, even in the absence of activating levels of cytosolic  $Ca^{2+}$ ,  $Ba^{2+}$  can still interact with the channel and significantly increase the probability of channel closing.

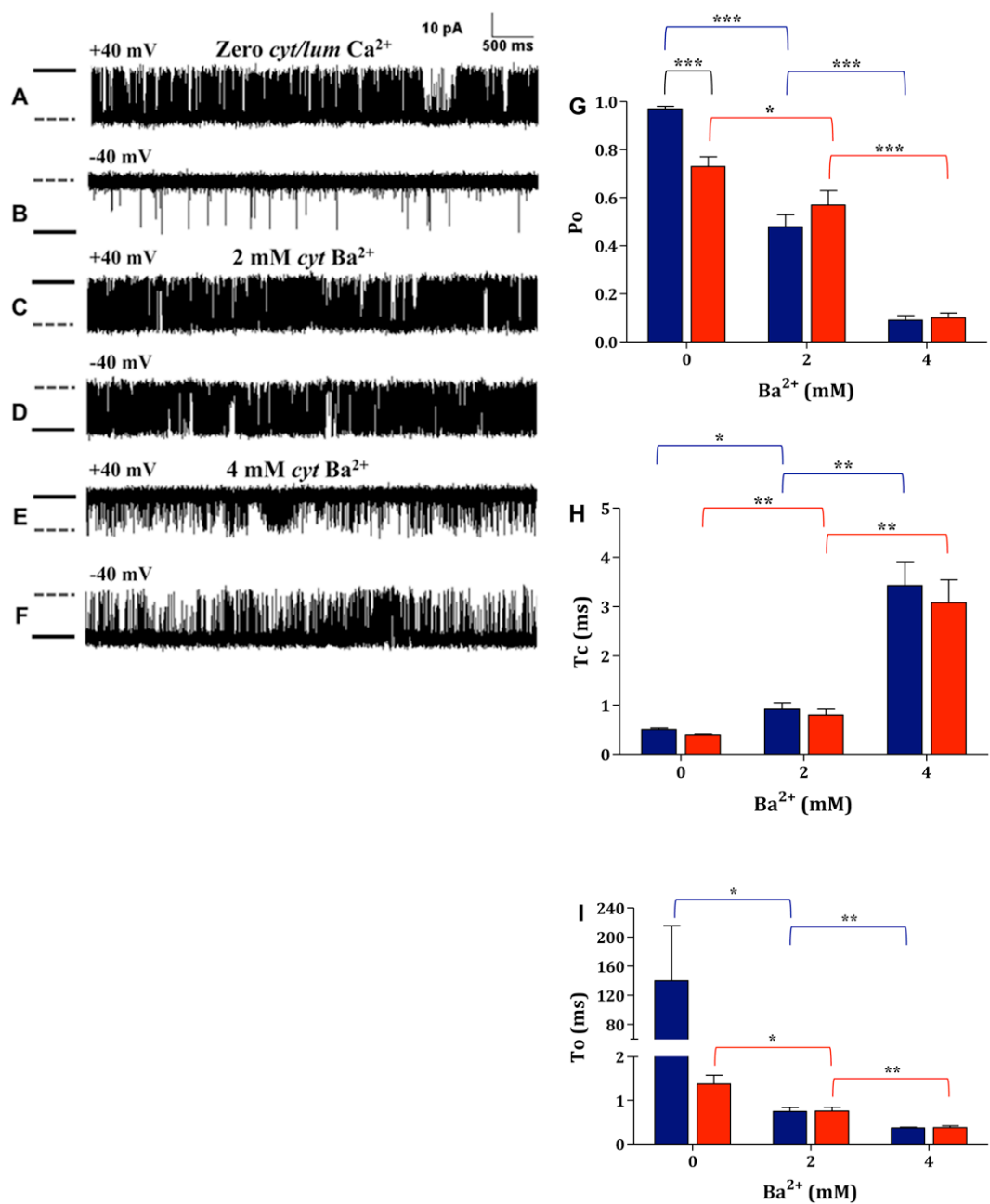


**Figure 6.14. Cytosolic Ba<sup>2+</sup> inhibition of ryanodine-modified channel Po also abolishes voltage dependence.** Representative single channel traces are shown in (A-F). Black bars - closed; grey dotted bars - modified. Modified gating at nominally zero Ca<sup>2+</sup> at + (A) and -40 mV (B) (see also Fig. 1F and 1G). With 2 mM cytosolic Ba<sup>2+</sup>, Po is decreased at +40 mV (C) and -40 mV (D). Increasing Ba<sup>2+</sup> to 4 mM further decreases Po at both + (E) and -40 mV (F). Current amplitude is slightly decreased at +40 mV due to the higher permeability but lower conductance of Ba<sup>2+</sup> compared with K<sup>+</sup>. Parameters from single channel analyses are shown in (G-I); blue and red bars represent data at - and +40 mV, respectively. Data are shown as mean ± S.E.M of n = 4-6 channels. Symbols denote significant differences (\* = p<0.05, \*\* = p<0.005 and \*\*\* = p<0.0001). (G) Voltage dependence of Po is abolished with increasing concentrations of Ba<sup>2+</sup>, which decrease Po at both + and -40 mV. (H) Ba<sup>2+</sup>-induced decrease in Po results from an increase in closed times at both +40 and -40 mV. This is in contrast to experiments in the absence of Ba<sup>2+</sup> where closed times remain the same (Fig. 6.7 B). (I) Open times also decrease significantly with Ba<sup>2+</sup>-induced inhibition of Po to a similar extent at both +40 and -40 mV.

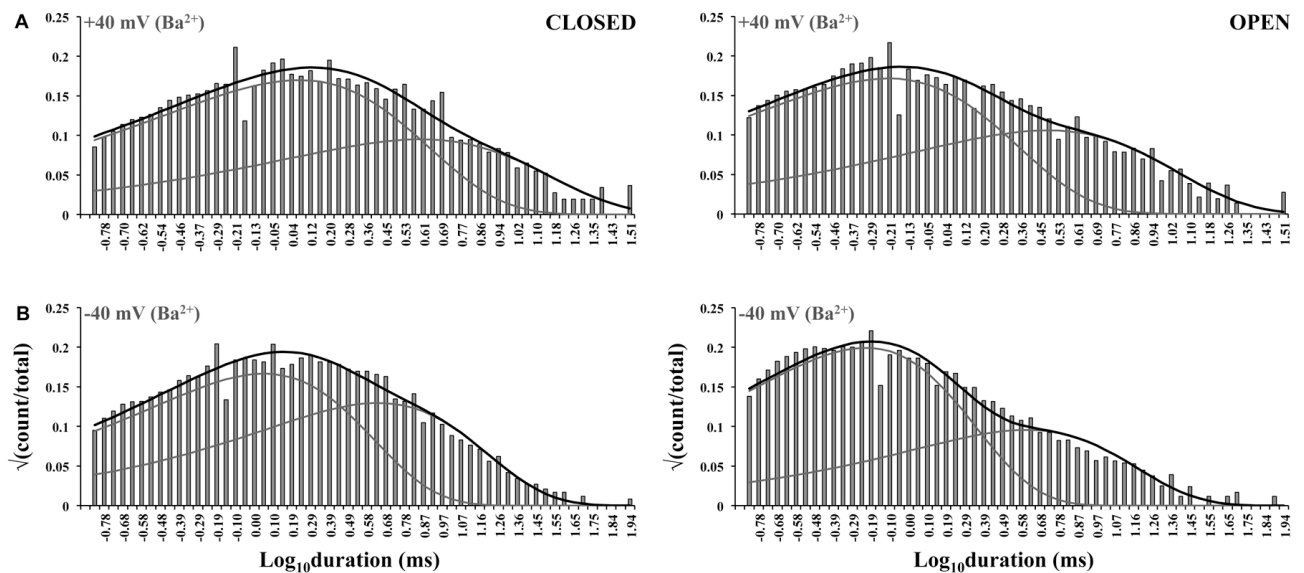


**Figure 6.15.** Fitting of dwell-time histograms from single channel data reveal mechanisms of modified channel inhibition by cytosolic  $\text{Ba}^{2+}$ . **(A)** Representative closed and open time distributions from data recorded at +40 mV and 2 mM cytosolic  $\text{Ba}^{2+}$  (in the absence of  $\text{Ca}^{2+}$ ) shows that each could be fitted accurately with two exponential components. **(B)** At -40 mV, the channel kinetics is not significantly altered and the dwell-time histograms could still be fitted with two exponentials each. In the presence of high cytosolic  $\text{Ba}^{2+}$ , two distinct distributions of closing events are revealed as opposed to only brief events when  $\text{Ba}^{2+}$  is absent.

#### 6.4.6 Mechanism of action of Imperatoxin A: is it analogous to ryanodine?

The scorpion venom toxin Imperatoxin A ( $\text{IpTx}_a$ ) stabilizes an open subconductance state of RyR (Tripathy et al. 1998) and it has been proposed that the mechanism of action of  $\text{IpTx}_a$  is similar to that of ryanodine (Schwartz et al. 2009). The following experiments were conducted to test this hypothesis. An example of  $\text{IpTx}_a$  interaction with a  $\text{Ca}^{2+}$ -activated RyR2 channel is shown in **Fig. 6.16**. With  $\text{IpTx}_a$  bound, the channel resides in a high  $P_o$ , reduced conductance state. At positive holding potentials the amplitude of the subconductance state is  $\sim 30\%$  of the full open state (**Fig. 6.16 B**), while at negative potentials it is  $\sim 40\%$  (**Fig. 6.16 C**), thereby exhibiting a slight rectification as has been reported previously (Quintero-Hernández et al. 2013).  $\text{IpTx}_a$  is a reversible modifier of the RyR2 channel, which binds in an activity ( $P_o$ )-dependent manner. Therefore, the removal of  $\text{Ca}^{2+}$  after binding of  $\text{IpTx}_a$  results in permanent channel closure once the toxin unbinds (**Fig. 6.16 D**), eliminating the probability of further interaction. It is noticeable that following the removal of  $\text{Ca}^{2+}$  at +40 mV (conditions that produce a

significant reduction  $P_o$  of the ryanodine-modified channel (**Fig. 6.4 F**), the  $P_o$  of the IpTx<sub>a</sub>-modified RyR2 does not change (**Fig. 6.16 D**). While this observation provides a qualitative indication that the mechanisms governing altered  $P_o$  in the ryanodine- and IpTx<sub>a</sub>-modified channels differ, the very limited amounts of data that can be gathered under these conditions before the channel shuts down precludes a more detailed description of the dependence of IpTx<sub>a</sub>-modified gating on  $[Ca^{2+}]_{cyt}$ . To obtain this information, I monitored gating parameters in IpTx<sub>a</sub>-modified states of ryanodine-modified channels. A representative experiment is shown in **Fig. 6.17**.

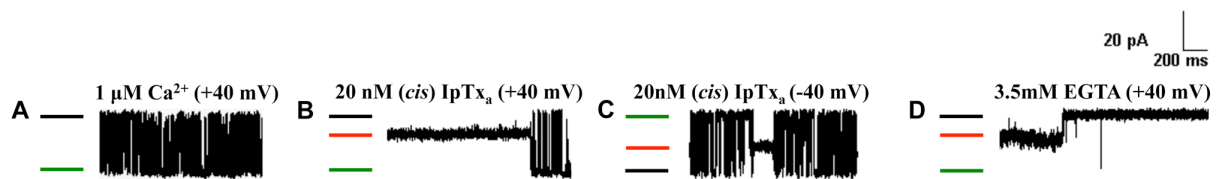


**Figure 6.16. Modification of RyR2 with Imperatoxin A in the presence and absence of activating  $Ca^{2+}$ .** (A) Shows a representative single channel trace where RyR2 is activated with 1  $\mu M$   $Ca^{2+}$  at +40 mV holding potential. The black bar on the left indicates the fully closed level and the green bar the fully open level. (B) The channel was modified using 20 nM IpTx<sub>a</sub> (cytosolic) at +40 mV. The red bar on the left shows the modified channel subconductance level (~30%). The  $P_o$  of the modified RyR2 is very high with almost no closing events and the modification is reversible as the channel is seen to revert back to unmodified gating after the toxin unbinds. (C) On switching to a negative holding potential, the probability of modification decreases (voltage dependence) and the subconductance is slightly higher (~40%) than at +40 mV due to rectification. (D) On removal of  $Ca^{2+}$  from the cytosolic side by adding 3.5 mM EGTA at +40 mV, the channel enters the fully closed state from the modified state once the IpTx<sub>a</sub> unbinds. The very low open probability of RyR2 in the absence of activating cytosolic  $Ca^{2+}$  prevents further binding and modification of the channel by the toxin.

As in earlier experiments, channels were modified with 1  $\mu M$  ryanodine and  $Ca^{2+}$  removed, before being further modified with 20 nM synthetic IpTx<sub>a</sub> added to the cytosolic side (**Figs. 6.17 A, B and C**). Note that the ryanodine-modified subconductance level is distinctly different from that of the IpTx<sub>a</sub>-modified level of the ryanodine-modified channel. However the IpTx<sub>a</sub>-modified state observed for the ryanodine-modified RyR2 retains features characteristic of the state prior to ryanodine modification, including a degree of rectification (subconductance of ~30% at +40 mV and ~40% at -40 mV) (**Figs. 6.16 B, 6.16 C, 6.17 C and 6.17 D**).

It is evident from the channel traces that once IpTx<sub>a</sub> binds, RyR2 ceases to exhibit the gating transitions to the closed state brought about by the complete removal of  $Ca^{2+}$  in

the ryanodine-modified state at positive holding potentials (**Fig. 6.17 C**). **Figs. 6.17 E** and **F** demonstrate that gating of the IpTx<sub>a</sub>-modified state is also insensitive to the inhibitory effect of mM Ba<sup>2+</sup> that occurs in the ryanodine-modified state of RyR2. The marked difference in the gating patterns of the ryanodine- and the IpTx<sub>a</sub>-modified states seen in these experiments confirms the earlier observation of a lack of influence of ligands on the IpTx<sub>a</sub>-modified state.



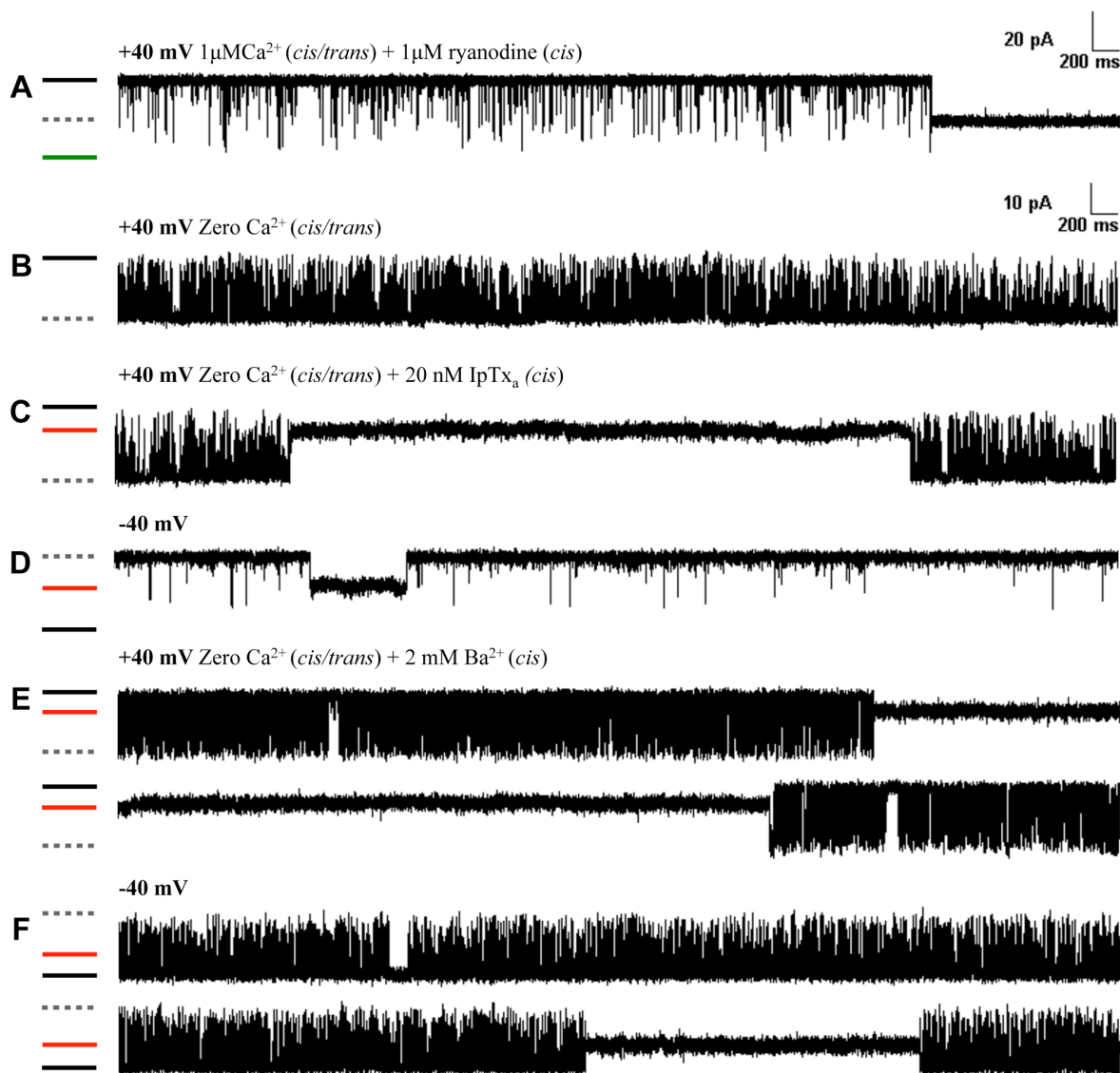


**Figure 6.17. Double modification of RyR2 with ryanodine and IpTx<sub>a</sub> in the absence of Ca<sup>2+</sup> reveals mechanistic differences.** (A) Representative single channel current trace showing RyR2 being activated by 1  $\mu\text{M}$  Ca<sup>2+</sup> at +40 mV that was then modified with 1  $\mu\text{M}$  ryanodine (cytosolic). The fully closed level is denoted by black bar on the left and the fully open level by the green bar. The ryanodine-modified subconductance level is indicated by the grey dotted bar. (B) Ca<sup>2+</sup> was removed from the cytosolic and luminal sides to nominally zero levels using 3.5 mM EGTA (*cis/trans*). As in previous experiments, numerous brief closing events appear at +40 mV. (C) The ryanodine-modified RyR2 was further modified with IpTx<sub>a</sub> (20 nM) at +40 mV. The IpTx<sub>a</sub>-modified subconductance level of the ryanodine-modified RyR2 was readily observed (red bar) in the absence of Ca<sup>2+</sup> as Po was maintained at a high level by ryanodine. Note that brief closings observed from the ryanodine-modified level are completely absent when the channel binds the toxin. (D) IpTx<sub>a</sub> binds to and modifies the ryanodine-modified channel at -40 mV less frequently than at +40 mV as the on and off rates are voltage sensitive (Tripathy et al. 1998). (E) and (F) show the effect of adding 2 mM Ba<sup>2+</sup> to the cytosolic side of the ryanodine- and IpTx<sub>a</sub>-modified channel at +40 and -40 mV holding potentials respectively in the absence of Ca<sup>2+</sup>. Please note that the closing events due to the inhibitory effect of Ba<sup>2+</sup> on the ryanodine-modified RyR2 observed previously (Figs. 6.14 C and D) disappear completely upon IpTx<sub>a</sub> modification of the ryanodine-modified channel. The lack of closing events due to Ca<sup>2+</sup> removal and Ba<sup>2+</sup>-induced inhibition from the IpTx<sub>a</sub>-modified state suggests that the mechanisms maintaining the stability of RyR2 in the ryanodine- and IpTx<sub>a</sub>-modified states are different.

## 6.5 Discussion

This approach of studying the mechanistic aspects of gating of the ryanodine-modified hRyR2 using a  $\text{Ca}^{2+}$  free environment is novel. Interaction of ryanodine with a single RyR2 channel induces profound changes in function. Unitary conductance is reduced and  $P_o$  of the reduced-conductance state is increased dramatically. This irreversible action of ryanodine on the channel was utilised to keep it open in the absence of activating  $[\text{Ca}^{2+}]_{\text{cyt}}$ .

In the presence of activating  $[\text{Ca}^{2+}]_{\text{cyt}}$   $P_o$  approaches 1.0 at positive and negative holding potentials. Removal of  $\text{Ca}^{2+}_{\text{cyt}}$  reveals a marked dependence of ryanodine-modified channel  $P_o$  on voltage, leading to a significant decrease in  $P_o$  at positive but not negative potentials.

Earlier studies proposed that mechanisms underlying ryanodine-induced elevated  $P_o$  involved an increase in the sensitivity of the channel to  $[\text{Ca}^{2+}]_{\text{cyt}}$  (Masumiya et al. 2001; Du et al. 2001). The data presented here indicate that this is not the case. In the absence of ryanodine, gating of RyR2 at  $1 \mu\text{M} \text{Ca}^{2+}_{\text{cyt}}$  is best described by a scheme incorporating multiple open and closed states (Mukherjee et al. 2012). Variations in  $P_o$  induced by changing  $[\text{Ca}^{2+}]_{\text{cyt}}$  result from alterations in closed times, with little change in open times. In contrast, gating of the ryanodine-modified RyR2 can be described by simpler schemes in which the relatively small  $\text{Ca}^{2+}$ -dependent changes in  $P_o$  that occur result from variations in open times, while closed times remain constant. Rather than sensitising RyR2 to activating  $\text{Ca}^{2+}$ , the ryanodine-bound channel adopts an extremely stable modified-open conformation. The stability of this conformation precludes transitions to the full open state and presents a significant energy barrier to closing.

In the presence of activating  $[\text{Ca}^{2+}]_{\text{cyt}}$ ,  $P_o$  approaches 1.0 indicating that all potential mechanisms by which the channel can close are disfavoured by the presence of ryanodine. Removal of  $\text{Ca}^{2+}_{\text{cyt}}$  partially destabilises the open conformation resulting in the occurrence of closing events at positive potentials. The brief duration of these closings demonstrates that, even at sub-activating  $[\text{Ca}^{2+}]_{\text{cyt}}$ , the energetically preferred conformation of the ryanodine-bound channel is open. Evidence in support of such a conformational change comes from earlier characterisations of the ion-handling properties of ryanodine-modified RyR2 channels (Tinker and Williams 1993; Lindsay et al. 1994; Mead and Williams 2002b; Mason et al. 2012). In all cases altered function is consistent with changes in the conformation, stability and rigidity of the channel's conduction pathway.

Removal of  $\text{Ca}^{2+}_{\text{cyt}}$  from the ryanodine-modified RyR2 reveals an underlying dependence of gating on holding potential. A similar effect has been noted previously (Du et al. 2001) and these authors proposed that luminal to cytosolic cation flux might, in some undefined way, increase  $P_o$ . As the experiments with ionic gradients show that the direction of net cation flux through the ryanodine-modified RyR2 channel unlikely to affect its gating (**Figs 6.8 & 6.9**), true voltage dependence is a more plausible explanation for the observed phenomenon. Fitting of the Boltzmann equation to the  $P_o$ -voltage relationship predicts the presence of negatively charged residues that sense the potential drop across the ryanodine-modified channel.

Like most ion channels, RyR could visit a number of very short-lived channel conformations that are not stable enough to be detected under most experimental conditions. I propose that ryanodine modification of the channel preferentially stabilises one of those rarely visited conformations where the channel exhibits subconductance. In these conformations, negatively charged motifs are aligned together in a region that can sense the voltage drop across the membrane. By analogy with conventional voltage-sensitive channels (Bezannila 2008), movements of these residues in response to changing potential are transmitted to the gating machinery to alter  $P_o$ , favouring the open state at negative potentials with transitions to the closed state more likely at positive potentials. Along the RyR2 protein sequence there are indeed series of consecutive negatively charged amino acids (Aspartate and Glutamate) that could constitute a crude voltage-sensing element when the channel visits a favourable global conformation (**Fig 6.18**).

The increased tendency for closing at positive potentials is overridden by the interaction of  $\text{Ca}^{2+}_{\text{cyt}}$  with the channel. The  $P_o$  of the ryanodine-modified conformation is determined by the influence of both trans-membrane potential and  $[\text{Ca}^{2+}]_{\text{cyt}}$ . This dependence of channel activity on membrane potential at low  $\text{Ca}^{2+}_{\text{cyt}}$  is not limited to ryanodine-modified RyR: interaction of sulmazole and ATP produce similar effects (Sitsapesan and Williams 1994b). The ryanodine-dependent simplification of RyR2 gating, with transitions between modified-open and closed states, has enabled us to use REFER analysis to provide novel insights into the nature of the transition state between these stable, resolvable, gating states.

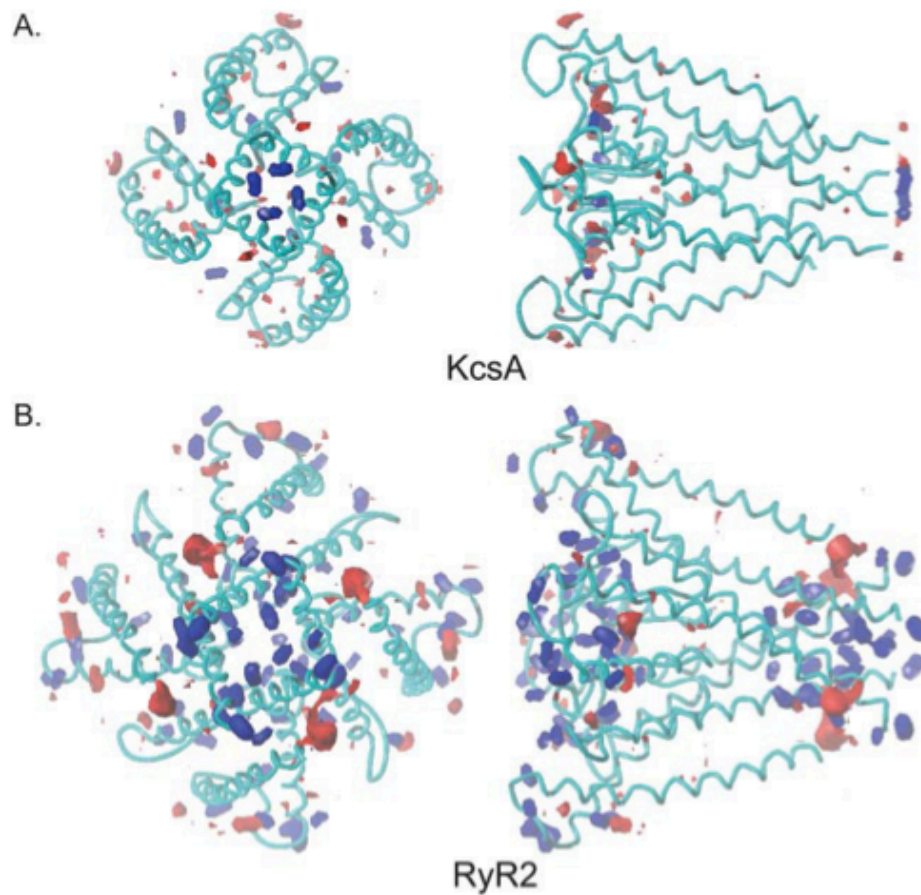


**Figure 6.18. The distribution of acidic and basic residues in the pore-forming region of RyR2 compared with KcsA.** The cartoons demonstrate the condition and distribution of amino acid residues at pH 7.0. Acidic residues (negatively charged) are contoured blue. The left-hand panels of **(A)** and **(B)** are oriented such that the structures are viewed from the cytosol. In the right-hand panels, the cytosolic ends of the structures are on the right. The negatively charged residues that are positioned within the voltage-drop could be responsible for charge sensing during change in membrane potential (Welch et al. 2004).

It has been proposed that the cytosolic domain of the RyR2 channel contains three classes of binding site for  $\text{Ca}^{2+}$  (Laver 2007). High affinity ( $\mu\text{M}$ ) sites are responsible for both increasing ( $\text{I}_1$ ) and decreasing ( $\text{I}_2$ )  $\text{Po}$ , while binding of  $\text{Ca}^{2+}$ , or other divalent cations, to a low affinity ( $\text{mM}$ ) site ( $\text{I}_3$ ) leads to a reduction in  $\text{Po}$ . In the absence of ryanodine, millimolar concentrations of  $\text{Ba}^{2+}$  added to the cytosolic face of the RyR2 reduce  $\text{Po}$  (Diaz-Sylvester et al. 2011). This prompted us to use equivalent  $[\text{Ba}^{2+}]$  to further investigate gating of the ryanodine-modified RyR2 in the absence of  $\text{Ca}^{2+}_{\text{cyt}}$ . The key observations arising from these experiments are that cytosolic  $\text{Ba}^{2+}$ , a) at positive holding potentials, exacerbates the reduction in  $\text{Po}$  of the ryanodine-modified RyR2 initiated by the removal of  $\text{Ca}^{2+}_{\text{cyt}}$  and b) eliminates the voltage dependence in the absence of  $\text{Ca}^{2+}_{\text{cyt}}$ , so that the  $\text{Po}$  of channels is comparable at + and -40 mV. Lifetime analysis and mathematical modelling indicate that the interaction of  $\text{Ba}^{2+}$  gives rise to two populations of closed events with equivalent characteristics at both positive and negative potentials.

Reduction in  $\text{Po}$  of the ryanodine-modified state that results from the interaction of  $\text{Ba}^{2+}$  is significantly greater than that occurring on removal of activating  $[\text{Ca}^{2+}]$ . In the absence of  $\text{Ca}^{2+}_{\text{cyt}}$  all three activation/inhibitory binding sites will be available.  $\text{Ba}^{2+}_{\text{cyt}}$  does not activate RyR2 at concentrations between 1  $\mu\text{M}$  and 1  $\text{mM}$  (Ashley and Williams 1990; Diaz-Sylvester et al. 2011) and my observation of two  $\text{Ba}^{2+}$ -dependent closed states indicates that these are likely to result from the binding of  $\text{Ba}^{2+}$  to the inhibitory sites ( $\text{I}_1$  and  $\text{I}_2$ ). The marked increase in mean closed time associated with the increase in cytosolic  $\text{Ba}^{2+}$  from 2 to 4  $\text{mM}$  suggests that the population of long closings is dependent upon the interaction of  $\text{Ba}^{2+}$  with the low affinity ( $\text{I}_1$ ) divalent site. Occupancy of the inhibitory sites by  $\text{Ba}^{2+}$  significantly destabilises the otherwise stable, rigid, conformation of the ryanodine-modified pore. It should also be noted that  $\text{Ba}^{2+}$ -dependent closings cannot merely be superimposed onto the closings seen at +40 mV prior to the addition of  $\text{Ba}^{2+}$ , rather the voltage-dependent closings are replaced by  $\text{Ba}^{2+}$ -dependent closings and the characteristics of these closings are not influenced by holding potential. I envisage two possible mechanisms for this behaviour. The first is that the presence of  $\text{mM}$  cytosolic  $\text{Ba}^{2+}$  effectively removes the voltage-sensing component of the ryanodine-modified conformation of the channel by screening the acidic residues postulated to respond to changing voltage. Under these conditions the voltage-dependent component of gating is eliminated and  $\text{Ba}^{2+}$ -dependent closings are equivalent at positive and negative potentials. In the second mechanism the closed states resulting from the interaction of  $\text{Ba}^{2+}$  with inhibitory sites on RyR2 override the voltage dependence of the

ryanodine-modified conformation. This would be analogous to the proposal that the tendency of the ryanodine-modified channel to close at positive potentials is overridden by activating  $[Ca^{2+}]_{cyt}$ .

The interaction of IpTx<sub>a</sub> with RyR2 has functional consequences that appear, superficially, to be analogous to those of ryanodine. However, I highlight important differences between the two modified forms of RyR2. The relatively short residence times of IpTx<sub>a</sub> on RyR2 and the dependence of IpTx<sub>a</sub> interaction on channel Po make quantification of gating of the IpTx<sub>a</sub>-modified channel following the removal of  $Ca^{2+}_{cyt}$  extremely difficult. Nevertheless, the data indicates that the Po of the IpTx<sub>a</sub>-modified RyR2 is not influenced by  $[Ca^{2+}]_{cyt}$ . I have obtained additional information on the properties of the IpTx<sub>a</sub>-modified state by monitoring these in ryanodine-bound RyR2 channels. Under these conditions the extremely high Po of the IpTx<sub>a</sub>-modified state is unaffected by trans-membrane potential, the removal of  $Ca^{2+}_{cyt}$ , or the presence of cytosolic  $Ba^{2+}$ . These data indicate that, as is the case with ryanodine, the interaction of IpTx<sub>a</sub> with the RyR2 channel stabilises a modified conformation of the pore-forming region of the channel. However the insensitivity of the IpTx<sub>a</sub>-bound conformation to factors that alter the stability of the ryanodine-modified channel indicates that the stability of the IpTx<sub>a</sub>-bound conformation exceeds that of the ryanodine-bound analogue.

### 6.5.1 Study limitations

The absence of detailed crystal structures of the ligand binding and gating regions in the RyR limits the scope of energetics-based interpretations about the structure-activity relationships. This also prevents an informed approach to site-directed mutagenesis of charged elements within the channel responsible for the voltage sensing and response, as well as the residues directly involved in the movements of the gating elements. The interpretations from the mathematical models are limited by the sensitivity and response of the single channel data acquisition systems and I present here the minimal gating schemes that could best explain the data. The lack of sufficient idealised events detected at -40mV with  $1\mu M Ca^{2+}$  prevented the modelling and further quantitative interpretation of channel behaviour under this condition. Due to low signal-to-noise, it is not possible to accurately record single channel currents from ryanodine-modified RyR2 below  $\pm 20$  mV holding potential. The fit of the Boltzmann function was therefore forced to go through the data points near the maximum and minimum levels due to paucity of

intermediate data points. This may limit the scope of interpretation from the parameters derived from the fit.

## **6.6 Implications of this study**

In addition to providing novel insights into the mechanisms underlying the profound changes in function associated with the interaction of ryanodine and IpTx<sub>a</sub> with the RyR2 channel (summarised in **Fig. 6.19**), energetic analysis was used to reveal new information on the mechanism of state transition during gating of the ryanodine-modified channel. Analysis of this kind could prove useful in investigating the effects of various RyR agonists and modifiers of function (e.g. phosphorylation, CPVT-linked mutation and RyR-targeted drugs) on the structural stability of the channel as any instability introduced would manifest as a difference in the relationship between ground and transition states in the gating energy landscape, thereby altering the energy barrier. Future studies will determine if these differences can be revealed using this experimental platform as the ryanodine-modified channel offers a much simpler gating model where perturbations can be easily detected and quantified. The possibility of the presence of a negatively charged voltage-sensing domain in RyR should be further explored for a better understanding of the nature of voltage dependence of channel activity.

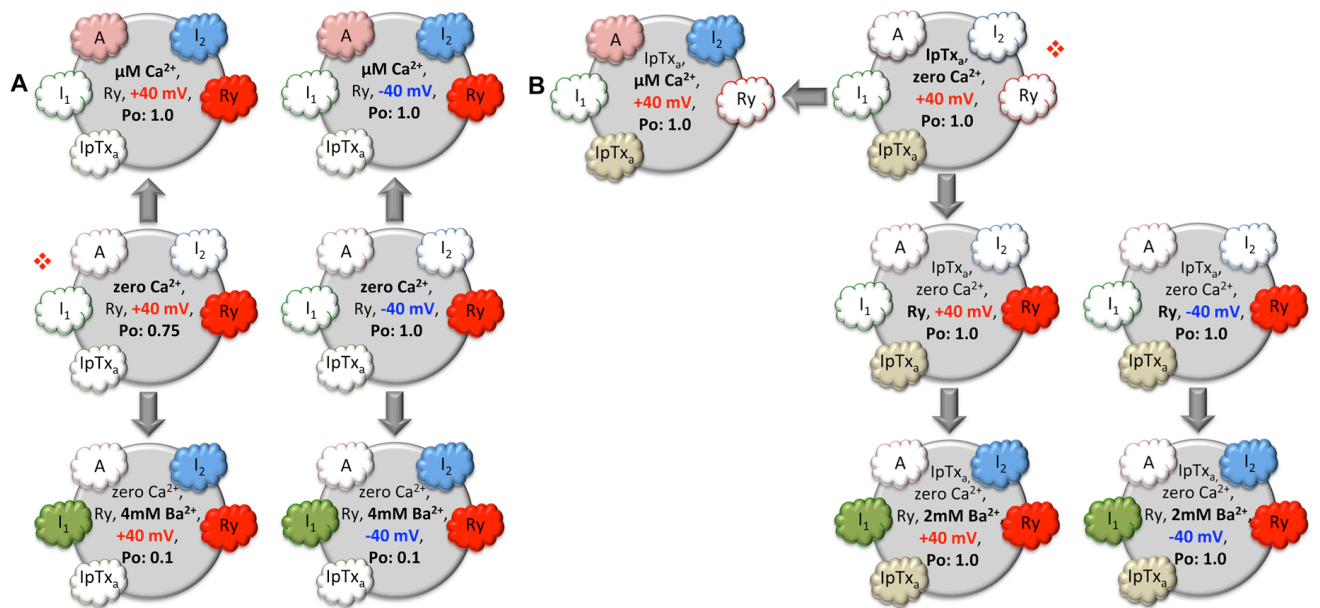


**Figure 6.19. Schematic recapitulation of RyR2 gating behaviour under different experimental conditions.** The circular cartoon blocks represent the molecular state of the channel: they indicate the channel activity (Po), the ligands interacting with the RyR2 (viz.  $\text{Ca}^{2+}$ ,  $\text{Ba}^{2+}$ , ryanodine and  $\text{IpTx}_a$ ) and the holding potential ( $\pm 40$  mV). Putative binding sites of various interacting ligands are shown as cartoon clouds along the circumference of the blocks; they are either empty (white) or occupied (coloured) by the respective ligand. **(A)** For an easier interpretation, the schematic begins at the block with the simplest experimental condition and is marked with a red shamrock. Ryanodine-modified RyR2 in the absence of  $\text{Ca}^{2+}$  ( $\text{Ca}^{2+}$  binding sites A,  $I_1$  and  $I_2$  are unoccupied) has a lower Po due to an increased frequency of brief closing events at +40 mV when compared to -40 mV. In the presence of  $1 \mu\text{M Ca}^{2+}$  (top row blocks), the putative high affinity activation (A) and inhibition sites ( $I_2$ ) on the modified RyR2 are occupied which increases the channel Po to  $\sim 1$  both at +40 mV and -40 mV with the disappearance of closing events. However, if the ryanodine-modified channel is instead exposed to high cytosolic  $\text{Ba}^{2+}$  (4 mM) in the absence of  $\text{Ca}^{2+}$  (arrows pointing downwards in the scheme), the channel is strongly inhibited due to  $\text{Ba}^{2+}$  occupying both high affinity ( $I_2$ ) and low affinity ( $I_1$ ) inhibition sites on the RyR2 (bottom row blocks). Under the influence of  $\text{Ba}^{2+}$ , voltage dependence of the modified channel gating is abolished (see **6.6 Discussion** for possible mechanisms). **(B)** The starting block is marked with a red shamrock as above to represent the simplest experimental scenario describing the interaction of  $\text{IpTx}_a$  with the channel. In the absence of  $\text{Ca}^{2+}$ , the  $\text{IpTx}_a$ -modified RyR2 has a very high Po (1.0) with few discernible closing events but once the toxin unbinds, the channel closes, preventing further binding (**Fig. 6.16 D**). The kinetics of the  $\text{IpTx}_a$ -modified state in the presence of  $\text{Ca}^{2+}$  does not change and the Po remains  $\sim 1.0$  (top row left block). Downward arrows from the starting point towards conditions where the RyR2 is modified concomitantly with  $\text{IpTx}_a$  and ryanodine in the absence of  $\text{Ca}^{2+}$  at  $\pm 40$  mV (as seen in **Figs. 6.17 C, D**). The Po when  $\text{IpTx}_a$  is bound to the ryanodine-modified channel still remains at 1.0 with no noticeable change in the kinetics. In contrast, the ryanodine-modified state exhibits voltage dependence of gating as seen in **(A)**. When the above conditions are further modified by the addition of mM  $\text{Ba}^{2+}$  (bottom row blocks), the  $\text{IpTx}_a$ -modified state of the ryanodine-modified channel remains immune (Po  $\sim 1.0$ ) to the inhibitory action of the divalent, whereas the Po of the ryanodine-modified state is drastically reduced at both  $\pm 40$  mV under these conditions.



## **Chapter 7.0**

**A summary of findings: their implications and future directions**

## 7.1 Background

The aim of this work was to understand the mechanism of activation of human RyR2 (hRyR2) by  $\text{Ca}^{2+}_{\text{cyt}}$  in the absence of other modulatory effects of factors external to the channel molecule. This fundamental knowledge is vital for unravelling the effects of disease causing mutations, the role of accessory regulatory proteins along with channel modifications such as phosphorylation; oxidation etc., for all of them must be studied in the context of  $\text{Ca}^{2+}$ -induced  $\text{Ca}^{2+}$  release through RyR2. However, the lack of detailed information about the architecture of channel gating machinery prevents a complete understanding of the actual physical basis of state transitions. The unique nature of modifications of RyR2 single channel behaviour by ligands such as ryanodine and IpTx potentially offers valuable insights into the characteristics of the putative elements involved in channel gating. A robust single channel experimental platform for studying purified hRyR2 is therefore required, incorporating sophisticated analysis techniques for accurate quantification of channel gating behaviour.

## 7.2 Overcoming issues with channel solubilisation and purification

Accurate assessment of hRyR2 gating behaviour in response to  $\text{Ca}^{2+}_{\text{cyt}}$  requires multiple single channel experiments after incorporation into planar phospholipid bilayers and this demands a sufficient and consistent yield of purified channel protein. Unfortunately, the process of solubilisation of hRyR2 from mixed membrane microsomal preparation resulted in the loss of a major proportion of the channel protein leading to a sub-optimal yield of purified channels making regular single channel experiments unfeasible. The experiments described in **Chapter 3** were designed to systematically dissect the various crucial steps of the detergent induced solubilisation process in order to identify the conditions responsible for low channel yield. A 0.6%w/v concentration of CHAPS in the solubilisation buffer was found to be optimal for the extraction of functional hRyR2 recombinantly expressed in HEK293 cells and was verified by biochemical and functional assays (**Figures 3.3-3.8**). Interestingly, the major portion of the RyR2 protein was found in the pellet fraction after the high-speed centrifugation (110,000 g) post solubilisation instead of its expected location in the supernatant. This suggests that even after detergent solubilisation, the hRyR2 protein is not completely soluble and comes out of the supernatant into the pellet which was usually otherwise discarded. The massive

size of RyR2 (~2.2 MDa) with its putative insoluble domains might result in aggregation of channel protein molecules leading to an overall anomalous solubility and its eventual loss in the pellets. This issue was remedied by employing a low speed spin (15,000 g) after solubilisation to prevent the majority of the channels from coming down in the pellet. The subsequent purification using sucrose density gradient ultracentrifugation resulted in higher yields of single channels, ensuring the consistent incorporation of functional hRyR2 in lipid bilayers. An investigation into the nature of the channel protein molecules after solubilisation and centrifugation is necessary to determine the reason behind this anomalous solubility but such studies are beyond the scope of this current work. Cryo-EM studies of the RyR2 molecules present in the supernatant and pellet fractions to visualise their physical state after centrifugation using both high and low speeds could represent a starting point for such an investigation. Recent advancements in molecular biology have led to the use of induced-pluripotent stem cells (iPSCs) as a patient-specific cell based system to study the nature of cardiovascular disease states due to RyR2 mutations (Di Pasquale et al. 2013). Use of these reprogrammed cells could facilitate disease modelling and screening of potentially therapeutic molecules in future studies of CPVT1.

### **7.3 Resolving mechanisms from single channel data: HMM based analysis**

The routinely employed method of half-amplitude threshold crossing for the detection and idealisation of single channel events (**Fig. 4.1**) when used for analysis of data from hRyR2 experiments produced inaccurate results (**Figures 4.3A and C**). HMM based single channel analysis programs (QuB; <http://www.qub.buffalo.edu/>) were found to be suitable in terms of speed and precision for the accurate description of single purified hRyR2 channel gating behaviour. Single channel traces from experiments on RyR contain a wealth of information about state transitions and the possible underlying mechanisms. In order to glean this information, the analysis programs in QuB required a series of customisations of parameter settings to fully exploit the power and sophistication of HMM based algorithms. **Chapter 4** describes an iterative exercise aimed at finding the optimal algorithms that would provide the best possible descriptions at various levels of RyR2 activity. Single channel data at very low and high levels of channel activity where there are fewer opening and closing events respectively, was best idealised using the Baum-Welch algorithm employing re-estimation formulae (**Table 4.3, Chapter 4**). This was also useful where the majority of the events being idealised were

brief or the data had a low signal-to-noise ratio. However, at intermediate levels of RyR2 activity with the majority of events showing clear transitions between closed and open levels, the significantly faster segmental K-means (SKM) algorithm based idealisation program gives the best results. Accurate fitting of idealised data using the MIL program enables the building of putative gating schemes that would ultimately provide a mechanistic description of single channel gating behaviour of RyR2 when acted upon by various ligands. The closed and open states in the gating models along with the rate constants of state transitions should be interpreted in terms of possible molecular mechanisms that give an idea about the actual physical basis of RyR2 gating. This study has utilised the power and accuracy of HMM based analysis programs along with a robust fitting of single channel data from RyR2 for the first time with an aim to identify actual gating mechanisms involved in the state transitions.

#### **7.4 Mechanism of activation of hRyR2 by $\text{Ca}^{2+}_{\text{cyt}}$ : kinetics reveal putative gates**

A detailed study of hRyR2 single channel behaviour when activated exclusively by cytosolic  $\text{Ca}^{2+}$  in a minimal environment was conducted where all other external modulatory factors were probably absent (**Chapter 5**). The steep activation along with the provision for unliganded openings pointed towards a modified MWC-type gating scheme where the mechanism is allosteric in nature. Single channel data from  $\text{Ca}^{2+}$  activation of RyR2 and the gating schemes derived were interpreted in the light of structural models of the RyR2 pore region based on  $\text{K}^+$  channel crystal structures (Williams 2002; Welch et al. 2004; Ramachandran et al. 2013). The similarities between the structural elements of gating (between RyR2 and  $\text{K}^+$  channels) suggests that  $\text{Ca}^{2+}$  dependent transitions are manifestations of gating at the putative inner helix bundle crossover and the  $\text{Ca}^{2+}$  independent flicker closing events are possibly due to movements in the selectivity filter region of the RyR2 pore (**Fig. 5.14**). A schematic summary of the various putative conformational species resolved in the kinetic schemes are shown in **Fig 7.1**. The ligand-operated gate generated by a helix-bundle crossover is shown at the entrance to the cytoplasmic vestibule of the channel and the ligand-independent gate made by a flexible selectivity filter towards the luminal end of the channel pore. Only when both gates are open at the same time can ions flow through the pore to generate a current (shown by orange double arrows). The gating schemes indicate that discrete open conformations of hRyR2 (shown in yellow) are progressively stabilised with increasing  $[\text{Ca}^{2+}]_{\text{cyt}}$ , probably due to the occupancy of its activating  $\text{Ca}^{2+}$  binding sites. However, it

should be noted that the  $\text{Ca}^{2+}$  binding sites shown on the two representative subunits are only indicative and have no bearing on the actual number or type of binding site(s) present on the RyR2.

Future experiments can now be designed to further characterise the nature of these gates in RyR2. Also, the unliganded openings of RyR2 can act as a measure of its inherent instability, allowing the quantification of the effects of disease causing mutations, phosphorylation and potentially therapeutic compounds in future experiments.

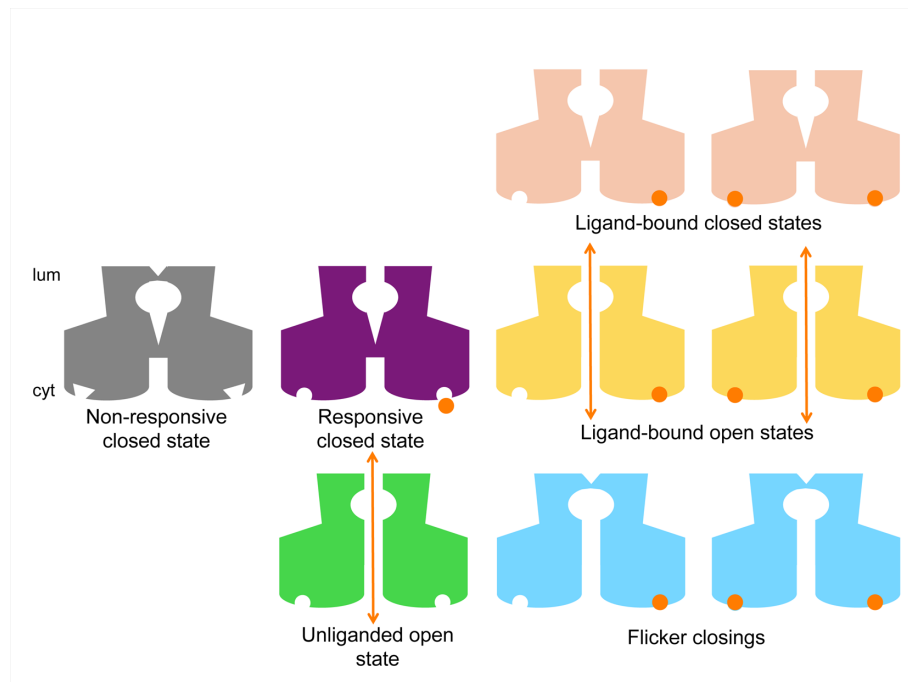
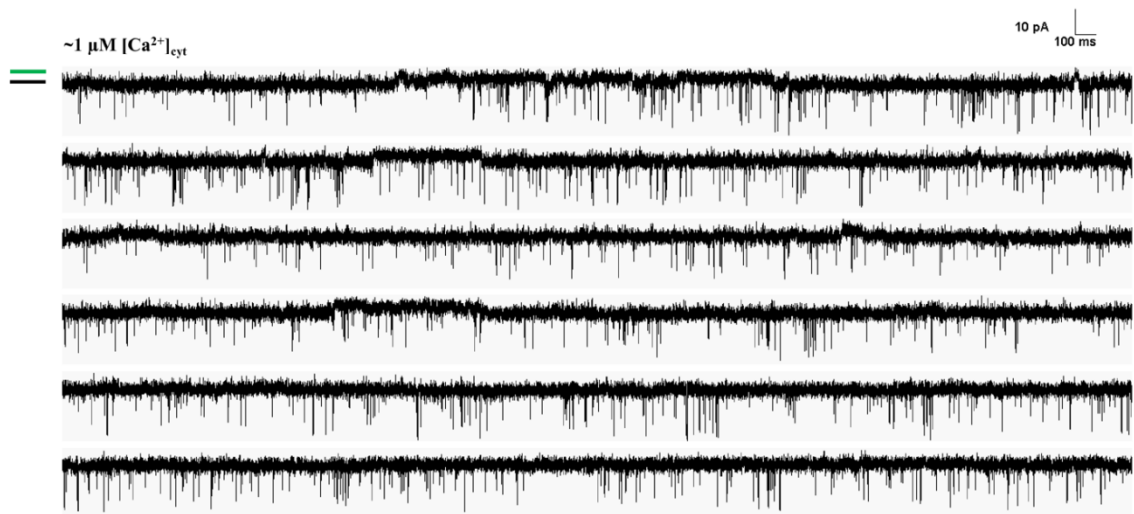


**Figure 7.1. Cartoons figures summarising the putative channel conformations in the gating model for hRyR2.** The diagrams are not meant to depict the actual structure of the channel or of the ligand binding sites and are purely schematic in nature. The non-responsive closed state ( $C_{NR}$ ; grey), is represented with binding sites that are not receptive to the ligand, though it should be noted that this conformation cannot activate to the unliganded open (green) state either. This can only happen from the responsive closed state ( $C_R$ ; purple), which is able to bind the ligand ( $\text{Ca}^{2+}$ - shown as orange circles), and undergo a conformational change to ligand bound open states (yellow). The channel can also move into intermediate closed conformations where its putative ligand-dependent gate towards the cytoplasmic side (cyt) is shut while  $\text{Ca}^{2+}$ -bound as shown (pink), this was resolved at very low  $[\text{Ca}^{2+}]_{\text{cyt}}$  as  $C_I$  in the kinetic schemes. Flicker closing events ( $C_F$ ; light blue) can occur for the  $\text{Ca}^{2+}$ -bound open states where the channel is non-conducting probably due the collapse of its selectivity filter near the luminal face of the channel (lum). Orange arrows denote the open (conducting) states of the channel where the putative gates at the selectivity filter region and at the helix-bundle cross over are open simultaneously (Mukherjee et al. 2012).

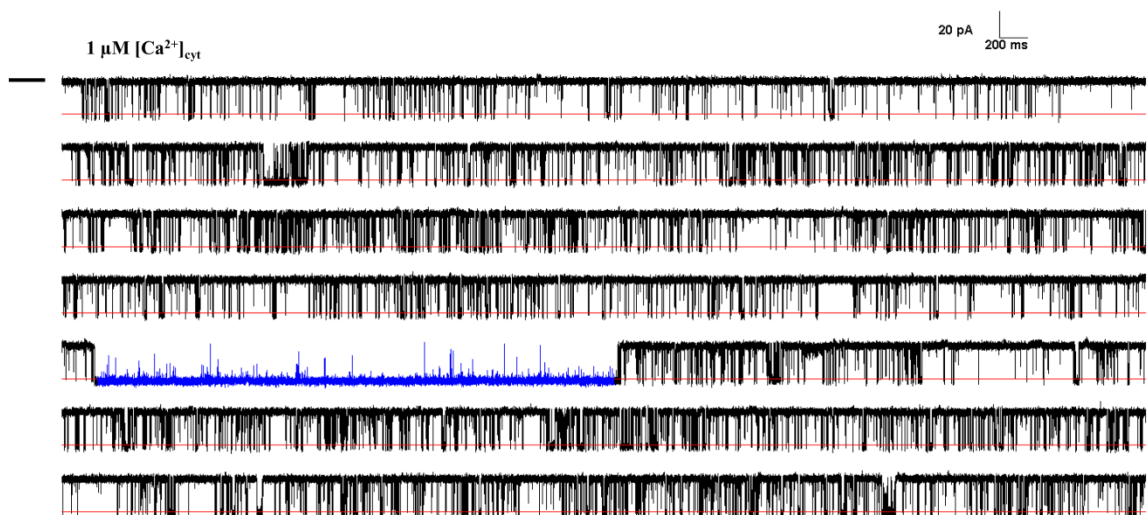
## 7.5 Ryanodine-modified channel conformation: new revelations

The RyR is identified by its ability to specifically interact with its quintessential ligand ryanodine and many previous studies have looked at the effects of such interactions in single channel experiments (see **Chapter 1**). Although the phenomenon of decreased conductance through the modified channel pore has been described, the mechanistic basis of the effect of ryanodine on channel gating leading to very high  $P_o$  is poorly understood. The experiments on ryanodine modified hRyR2 channels in the presence and virtual absence of  $Ca^{2+}$  (**Chapter 6**) has revealed two important traits: a) the modified open state is very stable with only brief transitions to the closed state even in the complete absence of  $Ca^{2+}$  and b) the gating kinetics of the modified conformation are voltage dependent especially in low  $Ca^{2+}$  or in its absence. Thus ryanodine doesn't act simply by sensitising the channel to  $Ca^{2+}$  as previously reported (Masumiya et al. 2001; Du et al. 2001) but instead results in the RyR2 adopting an extremely stable open conformation with only very brief sojourns to the closed state. The voltage dependence of ryanodine channel gating in the absence of activating  $Ca^{2+}$  is a real phenomenon and is probably due to voltage sensing domains (formed by negatively charged residues) being stabilised in the ryanodine modified conformation. However, this voltage sensitive conformation is not stable enough to be resolved in the unmodified RyR2. The ryanodine modified gating behaviour is explained by relatively simpler kinetic models compared to that of the unmodified channel (**Schemes 1, 2 and 3; Chapter 6**) and energetic evaluation of state transitions using REFER analysis suggests a fast change in modified RyR2 conformations when perturbed by voltage or ligand ( $Ca^{2+}$ ) changes. The novel phenomenon of voltage dependence was abolished by mM  $[Ba^{2+}]_{cyt}$  and channel open probability was drastically reduced. Experiments with ryanodine-modified channels co-modified using IpTx<sub>a</sub> suggest that these two ligands act via different mechanisms to bring about changes in channel conductance and  $P_o$  whereas their actions were previously thought to be analogous. The much simpler gating model of the ryanodine bound RyR2 in the absence of  $Ca^{2+}$  (no ligand binding/unbinding reactions) can be used as an experimental platform for unambiguous mechanistic interpretations of the action of therapeutic compounds with an aim to extrapolate the findings to the unmodified channel.

## Appendix I



**A1. Representative hRyR2 single channel traces from experiments using mixed membrane microsomal preparations.** RyR2 single channel activity seen in contaminant  $[Ca^{2+}]_{cyt}$  ( $\sim 1 \mu M$ ) at +30 mV (210 mM KCl, *cis/trans*), the actual baseline (closed level) is shown by the green bar. Unlike purified protein preparations, mixed membrane preparations also contain other channels like TRIC  $K^+$  channels (see Chapter 1) which may distort the baseline when they gate concomitantly with hRyR2 (black bar). This figure refers to section 3.4 in Chapter 3.



**A2. Atypical gating behaviour of hRyR2.** Representative single channel traces showing abrupt increases hRyR2  $P_o$  (from  $\sim 0.2$  to  $\sim 0.99$ ) due to the phenomenon of modal gating. These short ( $\leq 10\%$ ) periods of atypical activity (highlighted in blue) were not considered in further analyses and only the typical gating activity were used for generating gating schemes (see section 5.4, Chapter 5). The  $[Ca^{2+}]_{cyt}$  was buffered to  $1 \mu M$  with +30 mV holding potential and 210 mM KCl (symmetrical). The black bar shows the closed level and the red lines mark the fully open channel current levels.

A		B	
[Ca <sup>2+</sup> ] <sub>cyt</sub>	Actual data	Model demonstrating ligand-dependent rates	Simulated data
200 μM	P <sub>o</sub>	C <sub>NR</sub> ⇌ C <sub>R</sub> ⇌ O <sub>1</sub> ⇌ O <sub>2</sub> ⇌ O <sub>3</sub> ⇌ O <sub>4</sub> C <sub>F</sub>	P <sub>o</sub>
	T <sub>o</sub>		T <sub>o</sub>
	T <sub>c</sub>		T <sub>c</sub>
100 μM	P <sub>o</sub>	C <sub>NR</sub> ⇌ C <sub>R</sub> ⇌ O <sub>1</sub> ⇌ O <sub>2</sub> ⇌ O <sub>3</sub> ⇌ O <sub>4</sub> C <sub>F</sub>	P <sub>o</sub>
	T <sub>o</sub>		T <sub>o</sub>
	T <sub>c</sub>		T <sub>c</sub>
1 μM	P <sub>o</sub>	C <sub>NR</sub> ⇌ C <sub>R</sub> ⇌ O <sub>1</sub> ⇌ O <sub>2</sub> ⇌ O <sub>3</sub> ⇌ O <sub>4</sub> C <sub>F</sub>	P <sub>o</sub>
	T <sub>o</sub>		T <sub>o</sub>
	T <sub>c</sub>		T <sub>c</sub>
0.25 μM	P <sub>o</sub>	C <sub>NR</sub> ⇌ C <sub>R</sub> ⇌ O <sub>1</sub> ⇌ O <sub>2</sub> ⇌ O <sub>3</sub> ⇌ O <sub>4</sub> C <sub>F</sub> O <sub>UL</sub>	P <sub>o</sub>
	T <sub>o</sub>		T <sub>o</sub>
	T <sub>c</sub>		T <sub>c</sub>

C		D	
[Ca <sup>2+</sup> ] <sub>cyt</sub>	Actual data	Model demonstrating ligand-dependent rates	Simulated data
200 μM	P <sub>o</sub>	C <sub>NR</sub> ⇌ C <sub>R</sub> ⇌ O <sub>1</sub> ⇌ O <sub>2</sub> ⇌ O <sub>3</sub> C <sub>F</sub>	P <sub>o</sub>
	T <sub>o</sub>		No data
	T <sub>c</sub>		T <sub>c</sub>
100 μM	P <sub>o</sub>	C <sub>NR</sub> ⇌ C <sub>R</sub> ⇌ O <sub>1</sub> ⇌ O <sub>2</sub> ⇌ O <sub>3</sub> C <sub>F</sub>	P <sub>o</sub>
	T <sub>o</sub>		T <sub>o</sub>
	T <sub>c</sub>		T <sub>c</sub>
1 μM	P <sub>o</sub>	C <sub>NR</sub> ⇌ C <sub>R</sub> ⇌ O <sub>1</sub> ⇌ O <sub>2</sub> ⇌ O <sub>3</sub> C <sub>F</sub>	P <sub>o</sub>
	T <sub>o</sub>		T <sub>o</sub>
	T <sub>c</sub>		T <sub>c</sub>
0.25 μM	P <sub>o</sub>	C <sub>NR</sub> ⇌ C <sub>R</sub> ⇌ O <sub>1</sub> ⇌ O <sub>2</sub> ⇌ O <sub>3</sub> C <sub>F</sub> O <sub>UL</sub>	P <sub>o</sub>
	T <sub>o</sub>		T <sub>o</sub>
	T <sub>c</sub>		T <sub>c</sub>

**A3. Dependence of backward as well as forward rates on ligand concentration suggests the possibility of ligand-dependent inhibition at high [Ca<sup>2+</sup>]<sub>cyt</sub>.** Tables show P<sub>o</sub>, T<sub>o</sub> and T<sub>c</sub> from actual and simulated data. Simulations were carried out using the 10 μM model for four channels from **Fig 5.3 (Chapter 5)**: channel 1 (**A**), 2 (**B**), 11 (**C**) and 12 (**D** – where data at 200 μM [Ca<sup>2+</sup>]<sub>cyt</sub> was not available). All models apart from that in **C** achieve four ligand-bound open states. Rates shown in bold were made ligand dependent while the others remained fixed. At high [Ca<sup>2+</sup>]<sub>cyt</sub> (100 to 200 μM) making both forward (binding) and backward (unbinding) rates from C<sub>R</sub> to O<sub>3</sub> or O<sub>4</sub> ligand-dependent simulates data comparable to that acquired, suggesting inhibition at these concentrations. At intermediate [Ca<sup>2+</sup>]<sub>cyt</sub> (1 μM) ligand-dependency of forward (from C<sub>R</sub> to O<sub>3</sub> or O<sub>4</sub>) and backward rates between open states only (i.e. from O<sub>1</sub> to O<sub>3</sub> or O<sub>4</sub>) simulates data similar to that obtained in practice. At low (0.25 μM) [Ca<sup>2+</sup>]<sub>cyt</sub>, ligand dependence of forward rates (from C<sub>R</sub> to O<sub>3</sub> or O<sub>4</sub>) only simulates data comparable to that recorded. At this [Ca<sup>2+</sup>]<sub>cyt</sub> the addition of O<sub>UL</sub> (with rates from the individual channel, if this state was resolved, as in **A**, **C** and **D**), and removal of C<sub>F</sub> further improved the match between actual and simulated data (see **sections 5.4.5** and **5.4.6**).



#### A4. Protocol for accurate buffering of $\text{Ca}^{2+}$ in single channel studies of hRyR2

Buffer stock solutions were prepared in 210 mM KCl and pH adjusted to 7.4 at 22°C. The buffer ranges and free  $[\text{Ca}^{2+}]$  were estimated using the MaxChelator and the amounts of  $\text{CaCl}_2$  required to be added as cumulative aliquots to the *cis* chamber were calculated. The free  $[\text{Ca}^{2+}]$  in the *trans* chamber (1000  $\mu\text{l}$ ) was buffered to  $\sim 50$  nM using 5 mM EGTA stock (25  $\mu\text{M}$ ; 1:200 (v/v) of 5mM EGTA; 5  $\mu\text{l}$  added) in all experiments.

After channel incorporation, the free  $[\text{Ca}^{2+}]$  in the *cis* chamber (500  $\mu\text{l}$ ) was first buffered to nominally zero ( $\sim 0.7$  nM) using 5.5  $\mu\text{l}$  of 90 mM EGTA stock and 5.5  $\mu\text{l}$  of 90 mM HEDTA/NTA stock such that the final concentration of all buffers was 1 mM. After stirring the *cis* chamber, 11  $\mu\text{l}$  of solution was removed to bring back its volume to 500  $\mu\text{l}$ . The hRyR2 channel shuts down due to the absence of activating  $[\text{Ca}^{2+}]$  after which it is progressively activated using cumulative additions (no volume corrections needed) of  $\text{CaCl}_2$  aliquots to the *cis* chamber (500  $\mu\text{l}$ ) from a 20 mM stock prepared in 210 mM KCl (pH 7.4) (See Table below). All values were obtained from MaxChelator (**Chapter 5.3.1**).

The calculated amounts of  $\text{CaCl}_2$  needed in the *cis* chamber for the different levels of free  $[\text{Ca}^{2+}]$  are shown in the table below. All experiments were conducted at  $\sim 22^\circ\text{C}$  to maintain the buffering accuracy.

pCa	$[\text{Ca}^{2+}]$	$\mu\text{M CaCl}_2$ required in <i>cis</i> chamber	Vol. ( $\mu\text{l}$ ) of 20 mM $\text{CaCl}_2$ stock added to <i>cis</i> chamber
7.3	50 nM	415 $\mu\text{M}$	10.4 $\mu\text{l}$
7	100 nM	600 $\mu\text{M}$	4.9 $\mu\text{l}$
6.6	250 nM	825 $\mu\text{M}$	5.9 $\mu\text{l}$
6.3	500 nM	970 $\mu\text{M}$	3.8 $\mu\text{l}$
6	1 $\mu\text{M}$	1125 $\mu\text{M}$	4.1 $\mu\text{l}$
5.7	2 $\mu\text{M}$	1270 $\mu\text{M}$	3.8 $\mu\text{l}$
5.3	5 $\mu\text{M}$	1530 $\mu\text{M}$	6.9 $\mu\text{l}$
5	10 $\mu\text{M}$	1750 $\mu\text{M}$	5.9 $\mu\text{l}$
4.3	50 $\mu\text{M}$	2220 $\mu\text{M}$	12.8 $\mu\text{l}$
4	100 $\mu\text{M}$	2465 $\mu\text{M}$	6.8 $\mu\text{l}$
3.7	200 $\mu\text{M}$	2760 $\mu\text{M}$	6.9 $\mu\text{l}$
3.3	500 $\mu\text{M}$	3270 $\mu\text{M}$	14.3 $\mu\text{l}$

## References

- Ahern, G.P., Junankar, P.R. and Dulhunty, A.F. 1994. Single channel activity of the ryanodine receptor calcium release channel is modulated by FK-506. *FEBS letters* 352(3), pp. 369–374.
- Ahern, G.P., Junankar, P.R. and Dulhunty, A.F. 1997. Subconductance states in single-channel activity of skeletal muscle ryanodine receptors after removal of FKBP12. *Biophysj* 72(1), pp. 146–162.
- Anderson, K., Lai, F.A., Liu, Q.Y., Rousseau, E., Erickson, H.P. and Meissner, G. 1989. Structural and functional characterization of the purified cardiac ryanodine receptor-Ca<sup>2+</sup> release channel complex. *The Journal of biological chemistry* 264(2), pp. 1329–1335.
- Armisen, R., Sierralta, J., Vélez, P., Naranjo, D. and Suárez-Isla, B.A. 1996. Modal gating in neuronal and skeletal muscle ryanodine-sensitive Ca<sup>2+</sup> release channels. *The American journal of physiology* 271(1 Pt 1), pp. C144–53.
- Ashley, R.H. and Williams, A.J. 1990. Divalent cation activation and inhibition of single calcium release channels from sheep cardiac sarcoplasmic reticulum. *The Journal of General Physiology* 95(5), pp. 981–1005.
- Auerbach, A. 2007. How to Turn the Reaction Coordinate into Time. *The Journal of General Physiology* 130(6), pp. 543–546.
- Auerbach, A. 2012. Thinking in cycles: MWC is a good model for acetylcholine receptor-channels. *The Journal of physiology* 590(Pt 1), pp. 93–98.
- Baddeley, D., Jayasinghe, I.D., Lam, L., Rossberger, S., Cannell, M.B. and Soeller, C. 2009. Optical single-channel resolution imaging of the ryanodine receptor distribution in rat cardiac myocytes. *Proceedings of the National Academy of Sciences* 106(52), pp. 22275–22280.
- Baird, D.C. 1962. *Experimentation. An Introduction to Measurement Theory and Experiment Design*. Englewood Cliffs.
- Balshaw, D., Gao, L. and Meissner, G. 1999. Luminal loop of the ryanodine receptor: a pore-forming segment? *Proceedings of the National Academy of Sciences* 96(7), pp. 3345–3347.
- Balshaw, D.M., Xu, L., Yamaguchi, N., Pasek, D.A. and Meissner, G. 2001. Calmodulin Binding and Inhibition of Cardiac Muscle Calcium Release Channel (Ryanodine Receptor). *Journal of Biological Chemistry* 276(23), pp. 20144–20153.
- Baum, L.E., Petrie, T., Soules, G. and Weiss, N. 1970. A Maximization Technique Occurring in Statistical Analysis of Probabilistic Functions of Markov Chains. *Annals of Mathematical Statistics* 41(1), pp. 164–171.
- Beard, N.A., Laver, D.R. and Dulhunty, A.F. 2004. Calsequestrin and the calcium release channel of skeletal and cardiac muscle. *Progress in Biophysics and Molecular Biology* 85(1), pp. 33–69.

- Belevych, A.E., Radwanski, P.B., Carnes, C.A. and Györke, S. 2013. 'Ryanopathy': causes and manifestations of RyR2 dysfunction in heart failure. *Cardiovascular research* 98(2), pp. 240-247.
- Bellinger, A.M., Reiken, S., Dura, M., Murphy, P.W., Deng, S.X., Landry, D.W., Nieman, D., et al. 2008. Remodeling of ryanodine receptor complex causes 'leaky' channels: a molecular mechanism for decreased exercise capacity. *Proceedings of the National Academy of Sciences of the United States of America* 105(6), pp. 2198–2202.
- Benkusky, N.A., Weber, C.S., Scherman, J.A., Farrell, E.F., Hacker, T.A., John, M.C., Powers, P.A., et al. 2007. Intact  $\beta$ -Adrenergic Response and Unmodified Progression Toward Heart Failure in Mice With Genetic Ablation of a Major Protein Kinase A Phosphorylation Site in the Cardiac Ryanodine Receptor. *Circulation research* 101(8), pp. 819–829.
- Berridge, M.J., Lipp, P. and Bootman, M.D. 2000. The versatility and universality of calcium signalling. *Nature reviews. Molecular cell biology* 1(1), pp. 11–21.
- Bers, D.M. 2008. Calcium Cycling and Signaling in Cardiac Myocytes. *Annual Review of Physiology* 70(1), pp. 23–49.
- Bers, D.M. 2002. Cardiac excitation-contraction coupling. *Nature* 415(6868), pp. 198–205.
- Bers, D.M. 2004. Macromolecular complexes regulating cardiac ryanodine receptor function. *Journal of molecular and cellular cardiology* 37(2), pp. 417–429.
- Bezannilla, F. 2008. How membrane proteins sense voltage. *Nature reviews. Molecular cell biology* 9(4), pp. 323–332.
- Blatter, L.A. and McGuigan, J.A. 1986. Free intracellular magnesium concentration in ferret ventricular muscle measured with ion selective micro-electrodes. *Quarterly journal of experimental physiology (Cambridge, England)* 71(3), pp. 467–473.
- Blayney, L.M. and Lai, F.A. 2009. Ryanodine receptor-mediated arrhythmias and sudden cardiac death. *Pharmacology & therapeutics* 123(2), pp. 151–177.
- Brochet, D.X.P., Yang, D., Cheng, H. and Lederer, W.J. 2012. Elementary Calcium Release Events from the Sarcoplasmic Reticulum in the Heart. In: *Advances in Experimental Medicine and Biology*. Advances in Experimental Medicine and Biology. Dordrecht: Springer Netherlands, pp. 499–509.
- Callaway, C., Seryshev, A., Wang, J.P., Slavik, K.J., Needleman, D.H., Cantu, C., Wu, Y., et al. 1994. Localization of the high and low affinity [<sup>3</sup>H]ryanodine binding sites on the skeletal muscle Ca<sup>2+</sup> release channel. *The Journal of biological chemistry* 269(22), pp. 15876–15884.
- Carney, J., Mason, S.A., Viero, C. and Williams, A.J. 2010. *The Ryanodine Receptor Pore: Is There a Consensus View?* Serysheva, I. I. ed. Academic Press.
- Carter, S., Pitt, S.J., Colyer, J. and Sitsapesan, R. 2011. Ca<sup>2+</sup>-Dependent Phosphorylation of RyR2 Can Uncouple Channel Gating from Direct Cytosolic Ca<sup>2+</sup> Regulation. *The Journal of Membrane Biology* 240(1), pp. 21-33.

- Catterall, W.A. 2010. Ion Channel Voltage Sensors: Structure, Function, and Pathophysiology. *Neuron* 67(6), pp. 915–928.
- Catterall, W.A. 2000. Structure and regulation of voltage-gated Ca<sup>2+</sup> channels. *Annual review of cell and developmental biology* 16, pp. 521–555.
- Chakrapani, S., Cordero-Morales, J.F. and Perozo, E. 2007. A quantitative description of KcsA gating II: single-channel currents. *The Journal of General Physiology* 130(5), pp. 479–496.
- Chakrapani, S., Cordero-Morales, J.F., Jogini, V., Cortes, D.M., and Perozo, E. 2010. On the structural basis of modal gating behavior in K<sup>+</sup> channels. *Nature structural & molecular biology* 18(1), pp. 67–74.
- Chakroborty, S., Goussakov, I., Miller, M.B. and Stutzmann, G.E. 2009. Deviant Ryanodine Receptor-Mediated Calcium Release Resets Synaptic Homeostasis in Presymptomatic 3xTg-AD Mice. *The Journal of neuroscience : the official journal of the Society for Neuroscience* 29(30), pp. 9458–9470.
- Changeux, J.P. and Edelstein, S.J. 2005. Allosteric mechanisms of signal transduction. *Science (New York, NY)* 308(5727), pp. 1424–1428.
- Chen, C. and Okayama, H. 1987. High-efficiency transformation of mammalian cells by plasmid DNA. *Molecular and cellular biology* 7(8), pp. 2745–2752.
- Chen, H., Valle, G., Furlan, S., Nani, A., Györke, S., Fill, M. and Volpe, P. 2013. Mechanism of calsequestrin regulation of single cardiac ryanodine receptor in normal and pathological conditions. *The Journal of General Physiology* 262(5), p. C614.
- Chen, S.R., Leong, P., Imredy, J.P., Bartlett, C., Zhang, L. and MacLennan, D.H. 1997a. Single-Channel Properties of the Recombinant. *Biophysj* 73(4), pp. 1904–1912.
- Chen, S.R.W., Li, X., Ebisawa, K. and Zhang, L. 1997b. Functional Characterization of the Recombinant Type 3 Ca<sup>2+</sup> Release Channel (Ryanodine Receptor) Expressed in HEK293 Cells. *Journal of Biological Chemistry* 272(39), pp. 24234–24246.
- Chen, W., Wang, R., Chen, B., Zhong, X., Kong, H., Bai, Y., Zhou, Q., et al. 2014. The ryanodine receptor store-sensing gate controls Ca. *Nature Publishing Group*, pp. 1–13.
- Cheng, H., Lederer, W.J. and Cannell, M.B. 1993. Calcium sparks: elementary events underlying excitation-contraction coupling in heart muscle. *Science (New York, NY)* 262(5134), pp. 740–744.
- Ching, L.L., Williams, A.J. and Sitsapesan, R. 2000. Evidence for Ca<sup>2+</sup> Activation and Inactivation Sites on the Luminal Side of the Cardiac Ryanodine Receptor Complex. *Circulation research* 87(3), pp. 201–206.
- Clapham, D.E. and Neher, E. 1984. Substance P reduces acetylcholine-induced currents in isolated bovine chromaffin cells. *The Journal of physiology* 347, pp. 255–277.
- Colquhoun, D., Dowsland, K.A., Beato, M. and Pledsted, A.J.R. 2004. How to Impose Microscopic Reversibility in Complex Reaction Mechanisms. *Biophysical Journal* 86(6), pp. 3510–3518.

- Colquhoun, D. and Hawkes, A. 1995. The Principles of the Stochastic Interpretation of Ion-Channel Mechanisms. In: Sakmann, B. and Neher, E. ed 2. *Single-Channel Recording*. Springer US, pp. 397–482.
- Colquhoun, D. and Hawkes, A.G. 1982. On the stochastic properties of bursts of single ion channel openings and of clusters of bursts. *Philosophical transactions of the Royal Society of London. Series B, Biological sciences* 300(1098), pp. 1–59.
- Colquhoun, D. and Hawkes, A.G. 1981. On the Stochastic Properties of Single Ion Channels. *Proceedings of the Royal Society B: Biological Sciences* 211(1183), pp. 205–235.
- Colquhoun, D. and Hawkes, A.G. 1994. Practical analysis of single channel records Ogden, D. C. ed. *Company of Biologists, Cambridge*, pp. 141–188.
- Colquhoun, D. and Hawkes, A.G. 1977. Relaxation and fluctuations of membrane currents that flow through drug-operated channels. *Proceedings of the Royal Society of London Series B, Containing papers of a Biological character Royal Society (Great Britain)* 199(1135), pp. 231–262.
- Colquhoun, D. and Sigworth, F.J. 1995. Fitting and Statistical Analysis of Single-Channel Records. In: Sakmann, B. and Neher, E. ed 2. *Single-Channel Recording*. Springer US, pp. 483–587.
- Cordero-Morales, J.F., Cuello, L.G., Zhao, Y., Jogini, V., Cortes, D.M., Roux, B. and Perozo, E. 2006. Molecular determinants of gating at the potassium-channel selectivity filter. *Nature structural & molecular biology* 13(4), pp. 311–318.
- Coronado, R., Morrissette, J., Sukhareva, M. and Vaughan, D.M. 1994. Structure and function of ryanodine receptors. *The American journal of physiology* 266(6 Pt 1), pp. C1485–504.
- Crotti, L., Johnson, C.N., Graf, E., De Ferrari, G.M., Cuneo, B.F., Ovadia, M., Papagiannis, J., et al. 2013. Calmodulin Mutations Associated With Recurrent Cardiac Arrest in Infants. *Circulation* 127(9), pp. 1009–1017.
- Cuello, L.G., Jogini, V., Cortes, D.M. and Perozo, E. 2010. Structural mechanism of C-type inactivation in K<sup>+</sup> channels. *Nature* 466(7303), pp. 203–208.
- Currie, S., Elliott, E.B., Smith, G.L. and Loughrey, C.M. 2011. Pharmacology & Therapeutics. *Pharmacology & therapeutics* 131(2), pp. 204–220.
- Cymes, G.D., Grosman, C. and Auerbach, A. 2002. Structure of the transition state of gating in the acetylcholine receptor channel pore: a phi-value analysis. *Biochemistry* 41(17), pp. 5548–5555.
- del Castillo, J. and Katz, B. 1957. Interaction at end-plate receptors between different choline derivatives. *Proceedings of the Royal Society of London Series B, Containing papers of a Biological character Royal Society (Great Britain)* 146(924), pp. 369–381.
- Dempster, A.P., Laird, N.M. and Rubin, D.B. 1977. Maximum likelihood from incomplete data via the EM algorithm. *Journal of the Royal Statistical Society. Series B (Methodological)*, pp. 1–38.

- di Barletta, M.R., Viatchenko-Karpinski, S., Nori, A., Memmi, M., Terentyev, D., Turcato, F., Valle, G., et al. 2006. Clinical Phenotype and Functional Characterization of CASQ2 Mutations Associated With Catecholaminergic Polymorphic Ventricular Tachycardia. *Circulation* 114(10), pp. 1012–1019.
- Di Pasquale, E., Lodola, F., Miragoli, M., Denegri, M., Avelino-Cruz, J.E., Buonocore, M., Nakahama, H., et al. 2013. cddis2013369a. 4(10), pp. e843–11.
- Diaz-Sylvester, P.L., Porta, M. and Copello, J.A. 2011. Modulation of cardiac ryanodine receptor channels by alkaline earth cations. *PLoS ONE* 6(10), p. e26693.
- Dobrev, D. and Wehrens, X.H.T. 2014. Role of RyR2 Phosphorylation in Heart Failure and Arrhythmias: Controversies Around Ryanodine Receptor Phosphorylation in Cardiac Disease. *Circulation research* 114(8), pp. 1311–1319.
- Doyle, D. 2004. Structural themes in ion channels. *European biophysics journal : EBJ* 33(3).
- Doyle, D.A., Morais Cabral, J., Pfuetzner, R.A., Kuo, A., Gulbis, J.M., Cohen, S.L., Chait, B.T., et al. 1998. The structure of the potassium channel: molecular basis of K<sup>+</sup> conduction and selectivity. *Science (New York, NY)* 280(5360), pp. 69–77.
- Driessen, H.E., Bourgonje, V.J.A., van Veen, T.A.B. and Vos, M.A. 2014. New antiarrhythmic targets to control intracellular calcium handling. *Netherlands Heart Journal* 22(5), pp. 198-213.
- Du, G.G. 1998. Characterization of Recombinant Rabbit Cardiac and Skeletal Muscle Ca<sup>2+</sup> Release Channels (Ryanodine Receptors) with a Novel [<sup>3</sup>H]Ryanodine Binding Assay. *Journal of Biological Chemistry* 273(50), pp. 33259–33266.
- Du, G.G. 2001. Functional Characterization of Mutants in the Predicted Pore Region of the Rabbit Cardiac Muscle Ca<sup>2+</sup> Release Channel (Ryanodine Receptor Isoform 2). *Journal of Biological Chemistry* 276(34), pp. 31760–31771.
- Du, G.G., Avila, G., Sharma, P., Khanna, V.K., Dirksen, R.T. and MacLennan, D.H. 2004. Role of the Sequence Surrounding Predicted Transmembrane Helix M4 in Membrane Association and Function of the Ca<sup>2+</sup> Release Channel of Skeletal Muscle Sarcoplasmic Reticulum (Ryanodine Receptor Isoform 1). *Journal of Biological Chemistry* 279(36), pp. 37566–37574.
- Du, G.G., Guo, X.H., Khanna, V.K. and MacLennan, D.H. 2001. Ryanodine sensitizes the cardiac Ca<sup>2+</sup> release channel (ryanodine receptor isoform 2) to Ca<sup>2+</sup> activation and dissociates as the channel is closed by Ca<sup>2+</sup> depletion. *Proceedings of the National Academy of Sciences of the United States of America* 98(24), pp. 13625–13630.
- Du, G.G., Sandhu, B., Khanna, V.K., Guo, X.H. and MacLennan, D.H. 2002. Topology of the Ca<sup>2+</sup> release channel of skeletal muscle sarcoplasmic reticulum (RyR1). *Proceedings of the National Academy of Sciences* 99(26), pp. 16725–16730.
- Eisner, D.A., Kashimura, T., Venetucci, L.A. and Trafford, A.W. 2009. From the ryanodine receptor to cardiac arrhythmias. *Circulation journal : official journal of the Japanese Circulation Society* 73(9), pp. 1561–1567.
- Elliott, R.J., Aggoun, L. and Moore, J.B. 1995. Hidden Markov Models: Estimation and

Control.

Euden, J., Mason, S.A., Viero, C., Thomas, N.L. and Williams, A.J. 2013. Investigations of the Contribution of a Putative Glycine Hinge to Ryanodine Receptor Channel Gating. *Journal of Biological Chemistry* 288(23), pp. 16671–16679.

Fabiato, A. 1983. Calcium-induced release of calcium from the cardiac sarcoplasmic reticulum. *The American journal of physiology* 245(1), pp. C1–14.

Farrell, E.F., Antaramian, A., Rueda, A., Gomez, A.M. and Valdivia, H.H. 2003. Sorcin Inhibits Calcium Release and Modulates Excitation-Contraction Coupling in the Heart. *Journal of Biological Chemistry* 278(36), pp. 34660–34666.

Fearnley, C.J., Roderick, H.L. and Bootman, M.D. 2011. Calcium Signaling in Cardiac Myocytes. *Cold Spring Harbor Perspectives in Biology* 3(11), pp. a004242–a004242.

Fersht, A.R. and Sato, S. 2004. Phi-value analysis and the nature of protein-folding transition states. *Proceedings of the National Academy of Sciences of the United States of America* 101(21), pp. 7976–7981.

Fill, M. and Copello, J.A. 2002. Ryanodine receptor calcium release channels. *Physiological reviews* 82(4), pp. 893–922.

Fill, M., Zahradníková, A., Villalba-Galea, C.A., Zahradník, I., Escobar, A.L. and Györke, S. 2000. Ryanodine receptor adaptation. *The Journal of General Physiology* 116(6), pp. 873–882.

Fischer, T., Herting, J., Tirilomis, T., Renner, A., Neef, S., Toischer, K., Ellenberger, D., et al. 2013. CaMKII and PKA Differentially Regulate SR Ca<sup>2+</sup>-Leak in Human Cardiac Pathology. *Circulation* 128(9), pp. 970-981.

Fleischer, S., Ogunbunmi, E.M., Dixon, M.C. and Fleer, E.A. 1985. Localization of Ca<sup>2+</sup> release channels with ryanodine in junctional terminal cisternae of sarcoplasmic reticulum of fast skeletal muscle. *Proceedings of the National Academy of Sciences of the United States of America* 82(21), pp. 7256–7259.

Fozzard, H.A. 1977. Heart: Excitation-Contraction Coupling. *Annual Review of Physiology* 39(1), pp. 201–220.

Franzini-Armstrong, C., Protasi, F. and Ramesh, V. 1999. Shape, Size, and Distribution of Ca. *Biophysj* 77(3), pp. 1528–1539.

Franzini-Armstrong, C., Protasi, F. and Tijssens, P. 2005. The Assembly of Calcium Release Units in Cardiac Muscle. *Annals of the New York Academy of Sciences* 1047(1), pp. 76–85.

Galfré, E., Pitt, S.J., Venturi, E., Sitsapesan, M., Zaccai, N.R., Tsaneva-Atanasova, K., O'Neill, S., et al. 2012. FKBP12 Activates the Cardiac Ryanodine Receptor Ca<sup>2+</sup>-Release Channel and Is Antagonised by FKBP12.6. *PLoS ONE* 7(2), p. e31956.

George, C.H. 2003. Ryanodine Receptor Mutations Associated With Stress-Induced Ventricular Tachycardia Mediate Increased Calcium Release in Stimulated Cardiomyocytes. *Circulation research* 93(6), pp. 531–540.

- George, C.H. 2008. Sarcoplasmic reticulum Ca<sup>2+</sup> leak in heart failure: mere observation or functional relevance? *Cardiovascular research* 77(2), pp. 302–314.
- George, C.H., Jundi, H., Thomas, N.L., Scoote, M., Walters, N., Williams, A.J. and Lai, F.A. 2004. Ryanodine receptor regulation by intramolecular interaction between cytoplasmic and transmembrane domains. *Molecular biology of the cell* 15(6), pp. 2627–2638.
- George, C.H., Sorathia, R., Bertrand, B.M.A. and Lai, F.A. 2003. In situ modulation of the human cardiac ryanodine receptor (hRyR2) by FKBP12.6. *The Biochemical journal* 370(Pt 2), pp. 579–589.
- Graham, F.L., Smiley, J., Russell, W.C. and Nairn, R. 1977. Characteristics of a Human Cell Line Transformed by DNA From Human Adenovirus Type-5. *Journal of General Virology* 36, pp. 59–72.
- Grosman, C. 2002. Linear free-energy relationships and the dynamics of gating in the acetylcholine receptor channel. *Journal of biological physics* 28(2), pp. 267–277.
- Grosman, C. and Auerbach, A. 2000. Kinetic, mechanistic, and structural aspects of unliganded gating of acetylcholine receptor channels: a single-channel study of second transmembrane segment 12' mutants. *The Journal of General Physiology* 115(5), pp. 621–635.
- Guo, T., Cornea, R.L., Huke, S., Camors, E., Yang, Y., Picht, E., Fruen, B.R., et al. 2010. Kinetics of FKBP12.6 Binding to Ryanodine Receptors in Permeabilized Cardiac Myocytes and Effects on Ca Sparks. *Circulation research* 106(11), pp. 1743–1752.
- Guo, T., Nani, A., Shonts, S., Perryman, M., Chen, H., Shannon, T., Gillespie, D., et al. 2013. Sarcoplasmic Reticulum K<sup>+</sup> (TRIC) Channel Does Not Carry Essential Countercurrent during Ca<sup>2+</sup> Release. *Biophysj* 105(5), pp. 1151–1160.
- Gusev, K. and Niggli, E. 2008. Modulation of the Local SR Ca<sup>2+</sup> Release by Intracellular Mg<sup>2+</sup> in Cardiac Myocytes. *The Journal of General Physiology* 132(6), pp. 721–730.
- Györke, I. and Györke, S. 1998. Regulation of the cardiac ryanodine receptor channel by luminal Ca<sup>2+</sup> involves luminal Ca<sup>2+</sup> sensing sites. *Biophysj* 75(6), pp. 2801–2810.
- Györke, I., Hester, N., Jones, L.R. and Györke, S. 2004. The Role of Calsequestrin, Triadin, and Junctin in Conferring Cardiac Ryanodine Receptor Responsiveness to Luminal Calcium. *Biophysj* 86(4), pp. 2121–2128.
- Györke, S. and Terentyev, D. 2008. Modulation of ryanodine receptor by luminal calcium and accessory proteins in health and cardiac disease. *Cardiovascular research* 77(2), pp. 245–255.
- Hamill, O.P., Marty, A., Neher, E., Sakmann, B. and Sigworth, F.J. 1981. Improved patch-clamp techniques for high-resolution current recording from cells and cell-free membrane patches. *Pflügers Archiv : European journal of physiology* 391(2), pp. 85–100.
- Hayashi, T., Martone, M.E., Yu, Z., Thor, A., Doi, M., Holst, M.J., Ellisman, M.H., et al. 2009. Three-dimensional electron microscopy reveals new details of membrane systems for Ca<sup>2+</sup> signaling in the heart. *Journal of cell science* 122(7), pp. 1005–1013.



- Hernandez, O.M., Housmans, P.R. and Potter, J.D. 2001. Invited review: pathophysiology of cardiac muscle contraction and relaxation as a result of alterations in thin filament regulation. *Journal of Applied Physiology* 90(3), pp. 1125–1136.
- Hess, P., Prod'Hom, B. and Pietrobon, D. 1989. Mechanisms of interaction of permeant ions and protons with dihydropyridine-sensitive calcium channels. *Annals of the New York Academy of Sciences* 560, pp. 80–93.
- Hilgemann, D.W., Collins, A. and Matsuoka, S. 1992. Steady-state and dynamic properties of cardiac sodium-calcium exchange. Secondary modulation by cytoplasmic calcium and ATP. *The Journal of General Physiology* 100(6), pp. 933–961.
- Hill, A.P. and Sitsapesan, R. 2002. DIDS Modifies the Conductance, Gating, and Inactivation Mechanisms of the Cardiac Ryanodine Receptor. *Biophysj* 82(6), pp. 3037–3047.
- Hille, B. 2001. *Ion Channels of Excitable Membranes*. Sinauer Associates.
- Hilliard, F.A., Steele, D.S., Laver, D., Yang, Z., Le Marchand, S.J., Chopra, N., Piston, D.W., et al. 2010. Journal of Molecular and Cellular Cardiology. *Journal of molecular and cellular cardiology* 48(2), pp. 293–301.
- Holmberg, S.R. and Williams, A.J. 1989. Single channel recordings from human cardiac sarcoplasmic reticulum. *Circulation research* 65(5), pp. 1445–1449.
- Huke, S. and Bers, D.M. 2008. Ryanodine receptor phosphorylation at Serine 2030, 2808 and 2814 in rat cardiomyocytes. *Biochemical and Biophysical Research Communications* 376(1), pp. 80–85.
- Imagawa, T., Takasago, T. and Shigekawa, M. 1989. Cardiac ryanodine receptor is absent in type I slow skeletal muscle fibers: immunochemical and ryanodine binding studies. *Journal of biochemistry* 106(2), pp. 342–348.
- Inui, M., Saito, A. and Fleischer, S. 1987. Purification of the ryanodine receptor and identity with feet structures of junctional terminal cisternae of sarcoplasmic reticulum from fast skeletal muscle. *The Journal of biological chemistry* 262(4), pp. 1740–1747.
- Jackson, M.B. 1984. Spontaneous openings of the acetylcholine receptor channel. *Proceedings of the National Academy of Sciences of the United States of America* 81(12), pp. 3901–3904.
- Jeyakumar, L.H., Ballester, L., Cheng, D.S., McIntyre, J.O., Chang, P., Olivey, H.E., Rollins-Smith, L., et al. 2001. FKBP Binding Characteristics of Cardiac Microsomes from Diverse Vertebrates. *Biochemical and Biophysical Research Communications* 281(4), pp. 979–986.
- Jiang, D. 2002. Enhanced Basal Activity of a Cardiac Ca<sup>2+</sup> Release Channel (Ryanodine Receptor) Mutant Associated With Ventricular Tachycardia and Sudden Death. *Circulation research* 91(3), pp. 218–225.
- Jiang, D. 2005. Enhanced Store Overload-Induced Ca<sup>2+</sup> Release and Channel Sensitivity to Luminal Ca<sup>2+</sup> Activation Are Common Defects of RyR2 Mutations Linked to Ventricular Tachycardia and Sudden Death. *Circulation research* 97(11), pp. 1173–1181.

- Jiang, D., Chen, W., Wang, R., Zhang, L. and Chen, S.R.W. 2007. Loss of luminal  $\text{Ca}^{2+}$  activation in the cardiac ryanodine receptor is associated with ventricular fibrillation and sudden death. *Proceedings of the National Academy of Sciences of the United States of America* 104(46), pp. 18309–18314.
- Jiang, D., Xiao, B., Yang, D., Wang, R., Choi, P., Zhang, L., Cheng, H., et al. 2004. RyR2 mutations linked to ventricular tachycardia and sudden death reduce the threshold for store-overload-induced  $\text{Ca}^{2+}$  release (SOICR). *Proceedings of the National Academy of Sciences of the United States of America* 101(35), pp. 13062–13067.
- Jiang, Y., Lee, A., Chen, J., Cadene, M., Chait, B.T. and MacKinnon, R. 2002. Crystal structure and mechanism of a calcium-gated potassium channel. *Nature* 417(6888), pp. 515–522.
- Juang, B.H. and Rabiner, L.R. 1991. Hidden Markov Models for Speech Recognition. *Technometrics* 33(3), pp. 251–272.
- Kaneko, N. 1994. New 1,4-Benzothiazepine Derivative, K201, Demonstrates Cardioprotective Effects Against Sudden Cardiac Cell-Death and Intracellular Calcium Blocking Action. *Drug Development Research* 33(4), pp. 429–438.
- Kermode, H., Williams, A.J. and Sitsapesan, R. 1998. The interactions of ATP, ADP, and inorganic phosphate with the sheep cardiac ryanodine receptor. *Biophysical Journal* 74(3), pp. 1296–1304.
- Kobayashi, T., Jin, L. and de Tombe, P.P. 2008. Cardiac thin filament regulation. *Pflügers Archiv : European journal of physiology* 457(1), pp. 37–46.
- Kontula, K., Laitinen, P., Lehtonen, A., Toivonen, L., Viitasalo, M. and Swan, H. 2005. Catecholaminergic polymorphic ventricular tachycardia: Recent mechanistic insights. *Cardiovascular research* 67(3), pp. 379–387.
- Koshland, D.E., Némethy, G. and Filmer, D. 1966. Comparison of experimental binding data and theoretical models in proteins containing subunits. *Biochemistry* 5(1), pp. 365–385.
- Kranias, E.G. and Hajjar, R.J. 2012. Modulation of Cardiac Contractility by the Phospholamban/SERCA2a Regulatome. *Circulation research* 110(12), pp. 1646–1660.
- Krishnamurthy, V. and Chung, S.H. 2007. Signal Processing Based on Hidden Markov Models for Extracting Small Channel Currents. In: Chung, S.H., Andersen, O., and Krishnamurthy, V. eds. *Biological And Medical Physics Biomedical Engineering*. Biological And Medical Physics Biomedical Engineering. New York, NY: Springer New York, pp. 623–650–650.
- Kuo, A., Domene, C., Johnson, L.N., Doyle, D.A. and Vénien-Bryan, C. 2005. Two Different Conformational States of the KirBac3.1 Potassium Channel Revealed by Electron Crystallography. *Structure* 13(10), pp. 1463–1472.
- Kwan, D.C.H., Fedida, D. and Kehl, S.J. 2006. Single Channel Analysis Reveals Different Modes of Kv1.5 Gating Behavior Regulated by Changes of External pH. *Biophysical Journal* 90(4), pp. 1212–1222.
- Laemmli, U.K. 1970. Cleavage of structural proteins during the assembly of the head of

bacteriophage T4. *Nature* 227(5259), pp. 680–685.

Lahat, H., Pras, E., Olender, T., Avidan, N., Ben-Asher, E., Man, O., Levy-Nissenbaum, E., et al. 2001. A missense mutation in a highly conserved region of CASQ2 is associated with autosomal recessive catecholamine-induced polymorphic ventricular tachycardia in Bedouin families from Israel. *The American Journal of Human Genetics* 69(6), pp. 1378–1384.

Lai, F.A., Erickson, H.P., Rousseau, E., Liu, Q.Y. and Meissner, G. 1988. Purification and reconstitution of the calcium release channel from skeletal muscle. *Nature* 331(6154), pp. 315–319.

Laitinen, P.J., Brown, K.M., Piippo, K., Swan, H., Devaney, J.M., Brahmbhatt, B., Donarum, E.A., et al. 2001. Mutations of the cardiac ryanodine receptor (RyR2) gene in familial polymorphic ventricular tachycardia. *Circulation* 103(4), pp. 485–490.

Lam, E., Martin, M.M., Timerman, A.P., Sabers, C., Fleischer, S., Lukas, T., Abraham, R.T., et al. 1995. A Novel FK506 Binding Protein Can Mediate the Immunosuppressive Effects of FK506 and Is Associated with the Cardiac Ryanodine Receptor. *Journal of Biological Chemistry* 270(44), pp. 26511–26522.

Lanner, J.T., Georgiou, D.K., Joshi, A.D. and Hamilton, S.L. 2010. Ryanodine Receptors: Structure, Expression, Molecular Details, and Function in Calcium Release. *Cold Spring Harbor Perspectives in Biology* 2(11), pp. a003996–a003996.

Laver, D. 2001. The power of single channel recording and analysis: its application to ryanodine receptors in lipid bilayers. *Clinical and experimental pharmacology & physiology* 28(8), pp. 675–686.

Laver, D.R. 2007.  $\text{Ca}^{2+}$  stores regulate ryanodine receptor  $\text{Ca}^{2+}$  release channels via luminal and cytosolic  $\text{Ca}^{2+}$  sites. *Biophysical Journal* 92(10), pp. 3541–3555.

Laver, D.R. 2009. Luminal  $\text{Ca}^{2+}$  activation of cardiac ryanodine receptors by luminal and cytoplasmic domains. *European biophysics journal : EBJ* 39(1), pp. 19–26.

Laver, D.R. and Honen, B.N. 2008. Luminal  $\text{Mg}^{2+}$ , A Key Factor Controlling RYR2-mediated  $\text{Ca}^{2+}$  Release: Cytoplasmic and Luminal Regulation Modeled in a Tetrameric Channel. *The Journal of General Physiology* 132(4), pp. 429–446.

Laver, D.R., Baynes, T.M. and Dulhunty, A.F. 1997. Magnesium inhibition of ryanodine-receptor calcium channels: evidence for two independent mechanisms. *The Journal of Membrane Biology* 156(3), pp. 213–229.

Laver, D.R., Roden, L.D., Ahern, G.P., Eager, K.R., Junankar, P.R. and Dulhunty, A.F. 1995. Cytoplasmic  $\text{Ca}^{2+}$  inhibits the ryanodine receptor from cardiac muscle. *The Journal of Membrane Biology* 147(1), pp. 7–22.

le Maire, M., Champeil, P. and Moller, J.V. 2000. Interaction of membrane proteins and lipids with solubilizing detergents. *Biochimica et biophysica acta* 1508(1-2), pp. 86–111.

Lederer, W.J., Bers, D.M. and Eisner, D.A. 2013. Journal of Molecular and Cellular Cardiology. *Journal of molecular and cellular cardiology* 58(C), pp. 3–4.

Lee, C.W., Lee, E.H., Takeuchi, K., Takahashi, H., Shimada, I., Sato, K., Shin, S.Y., et

- al. 2004. Molecular basis of the high-affinity activation of type 1 ryanodine receptors by imperatoxin A. *The Biochemical journal* 377(Pt 2), pp. 385–394.
- Leenhardt, A., Denjoy, I. and Guicheney, P. 2012. Catecholaminergic Polymorphic Ventricular Tachycardia. *Circulation: Arrhythmia and Electrophysiology* 5(5), pp. 1044–1052.
- Lehnart, S.E., Mongillo, M., Bellinger, A., Lindegger, N., Chen, B.X., Hsueh, W., Reiken, S., et al. 2008. Leaky Ca<sup>2+</sup> release channel/ryanodine receptor 2 causes seizures and sudden cardiac death in mice. *The Journal of clinical investigation* 118(6), pp. 2230–2245.
- Lehnart, S.E., Terrenoire, C., Reiken, S., Wehrens, X.H.T., Song, L.S., Tillman, E.J., Mancarella, S., et al. 2006. Stabilization of cardiac ryanodine receptor prevents intracellular calcium leak and arrhythmias. *Proceedings of the National Academy of Sciences* 103(20), pp. 7906–7910.
- Lewarchik, C.M., Orabi, A.I., Jin, S., Wang, D., Muili, K.A., Shah, A.U., Eisses, J.F., et al. 2014. The ryanodine receptor is expressed in human pancreatic acinar cells and contributes to acinar cell injury. *AJP: Gastrointestinal and Liver Physiology* 307(5), pp. G574–G581.
- Li, P. and Chen, S.R. 2001. Molecular basis of Ca<sup>2+</sup> activation of the mouse cardiac Ca<sup>2+</sup> release channel (ryanodine receptor). *The Journal of General Physiology* 118(1), pp. 33–44.
- Lichtenberg, D., Ahyayauch, H. and Goñi, F.M. 2013. The Mechanism of Detergent Solubilization of Lipid Bilayers. *Biophysj* 105(2), pp. 289–299.
- Lindsay, A.R., Manning, S.D. and Williams, A.J. 1991. Monovalent cation conductance in the ryanodine receptor-channel of sheep cardiac muscle sarcoplasmic reticulum. *The Journal of physiology* 439, pp. 463–480.
- Lindsay, A.R., Tinker, A. and Williams, A.J. 1994. How does ryanodine modify ion handling in the sheep cardiac sarcoplasmic reticulum Ca<sup>2+</sup>-release channel? *The Journal of General Physiology* 104(3), pp. 425–447.
- Liu, N. 2006. Arrhythmogenesis in Catecholaminergic Polymorphic Ventricular Tachycardia: Insights From a RyR2 R4496C Knock-In Mouse Model. *Circulation research* 99(3), pp. 292–298.
- Liu, N., Denegri, M., Ruan, Y., Avelino-Cruz, J.E., Perissi, A., Negri, S., Napolitano, C., et al. 2011. Short Communication: Flecainide Exerts an Antiarrhythmic Effect in a Mouse Model of Catecholaminergic Polymorphic Ventricular Tachycardia by Increasing the Threshold for Triggered Activity. *Circulation research* 109(3), pp. 291–295.
- Liu, W., Pasek, D.A. and Meissner, G. 1998. Modulation of Ca<sup>2+</sup>-gated cardiac muscle Ca<sup>2+</sup>-release channel (ryanodine receptor) by mono- and divalent ions. *The American journal of physiology* 274(1 Pt 1), pp. C120–8.
- Liu, Y., Kimlicka, L., Hiess, F., Tian, X., Wang, R., Zhang, L., Jones, P.P., et al. 2013. The CPVT-associated RyR2 mutation G230C enhances store overload induced Ca<sup>2+</sup> release and destabilizes the N-terminal domains. *The Biochemical journal* 454(1), pp. 123–131.

- Liu, Z. 2002. Three-dimensional Reconstruction of the Recombinant Type 2 Ryanodine Receptor and Localization of Its Divergent Region 1. *Journal of Biological Chemistry* 277(48), pp. 46712–46719.
- Lokuta, A.J., Meyers, M.B., Sander, P.R., Fishman, G.I. and Valdivia, H.H. 1997. Modulation of Cardiac Ryanodine Receptors by Sorcin. *Journal of Biological Chemistry* 272(40), pp. 25333–25338.
- Long, S.B., Tao, X., Campbell, E.B. and MacKinnon, R. 2007. Atomic structure of a voltage-dependent K<sup>+</sup> channel in a lipid membrane-like environment. *Nature* 450(7168), pp. 376–382.
- Ma, J. 1993. Block by ruthenium red of the ryanodine-activated calcium release channel of skeletal muscle. *The Journal of General Physiology* 102(6), pp. 1031–1056.
- Mackrill, J.J. 2010. Ryanodine receptor calcium channels and their partners as drug targets. *Biochemical pharmacology* 79(11), pp. 1535–1543.
- Magleby, K.L. and Pallotta, B.S. 1983. Burst kinetics of single calcium-activated potassium channels in cultured rat muscle. *The Journal of physiology* 344, pp. 605–623.
- Maier, L.S. 2003. Transgenic CaMKII $\delta$ C Overexpression Uniquely Alters Cardiac Myocyte Ca<sup>2+</sup> Handling: Reduced SR Ca<sup>2+</sup> Load and Activated SR Ca<sup>2+</sup> Release. *Circulation research* 92(8), pp. 904–911.
- Marjamaa, A., Laitinen-Forsblom, P., Wronska, A., Toivonen, L., Kontula, K. and Swan, H. 2011. Ryanodine receptor (RyR2) mutations in sudden cardiac death: studies in extended pedigrees and phenotypic characterization in vitro. *International Journal of Cardiology* 147(2), pp. 246–252.
- Marks, A.R. 2013. Calcium cycling proteins and heart failure: mechanisms and therapeutics. *The Journal of clinical investigation* 123(1), pp. 46–52.
- Marx, S.O. and Marks, A.R. 2013. Journal of Molecular and Cellular Cardiology. *Journal of molecular and cellular cardiology* 58(C), pp. 225–231.
- Marx, S.O., Gaburjakova, J., Gaburjakova, M., Henrikson, C., Ondrias, K. and Marks, A.R. 2001. Coupled Gating Between Cardiac Calcium Release Channels (Ryanodine Receptors). *Circulation research* 88(11), pp. 1151–1158.
- Marx, S.O., Reiken, S., Hisamatsu, Y., Jayaraman, T., Burkhoff, D., Rosemblyt, N. and Marks, A.R. 2000. PKA phosphorylation dissociates FKBP12.6 from the calcium release channel (ryanodine receptor): defective regulation in failing hearts. *Cell* 101(4), pp. 365–376.
- Mason, S.A., Viero, C., Euden, J., Bannister, M., West, D., Chen, S.R.W. and Williams, A.J. 2012. The contribution of hydrophobic residues in the pore-forming region of the ryanodine receptor channel to block by large tetraalkylammonium cations and Shaker B inactivation peptides. *The Journal of General Physiology* 140(3), pp. 325–339.
- Masumiya, H. 2002. Localization of the 12.6-kDa FK506-binding Protein (FKBP12.6) Binding Site to the NH<sub>2</sub>-terminal Domain of the Cardiac Ca<sup>2+</sup> Release Channel (Ryanodine Receptor). *Journal of Biological Chemistry* 278(6), pp. 3786–3792.

- Masumiya, H., Li, P., Zhang, L. and Chen, S.R. 2001. Ryanodine sensitizes the Ca<sup>2+</sup> release channel (ryanodine receptor) to Ca<sup>2+</sup> activation. *Journal of Biological Chemistry* 276(43), pp. 39727–39735.
- McCauley, M.D. and Wehrens, X.H.T. 2011. Targeting ryanodine receptors for anti-arrhythmic therapy. *Nature Publishing Group* 32(6), pp. 749–757.
- Mead, F. and Williams, A.J. 2002a. Block of the Ryanodine Receptor Channel by Neomycin Is Relieved at High Holding Potentials. *Biophysj* 82(4), pp. 1953–1963.
- Mead, F. and Williams, A.J. 2002b. Ryanodine-induced structural alterations in the RyR channel suggested by neomycin block. *Biophysical Journal* 82(4), pp. 1964–1974.
- Medeiros-Domingo, A., Bhuiyan, Z.A., Tester, D.J., Hofman, N., Bikker, H., van Tintelen, J.P., Mannens, M.M.A.M., et al. 2009. The RYR2-Encoded Ryanodine Receptor/Calcium Release Channel in Patients Diagnosed Previously With Either Catecholaminergic Polymorphic Ventricular Tachycardia or Genotype Negative, Exercise-Induced Long QT Syndrome. *JAC* 54(22), pp. 2065–2074.
- Meissner, G. 1994. Ryanodine receptor/Ca<sup>2+</sup> release channels and their regulation by endogenous effectors. *Annual Review of Physiology* 56, pp. 485–508.
- Meissner, G. and Henderson, J.S. 1987. Rapid calcium release from cardiac sarcoplasmic reticulum vesicles is dependent on Ca<sup>2+</sup> and is modulated by Mg<sup>2+</sup>, adenine nucleotide, and calmodulin. *The Journal of biological chemistry* 262(7), pp. 3065–3073.
- Meissner, G., Rios, E., Tripathy, A. and Pasek, D.A. 1997. Regulation of Skeletal Muscle Ca<sup>2+</sup> Release Channel (Ryanodine Receptor) by Ca<sup>2+</sup> and Monovalent Cations and Anions. *Journal of Biological Chemistry* 272(3), pp. 1628–1638.
- Meng, X., Wang, G., Viero, C., Wang, Q., Mi, W., Su, X.-D., Wagenknecht, T., et al. 2009. CLIC2-RyR1 Interaction and Structural Characterization by Cryo-electron Microscopy. *Journal of Molecular Biology* 387(2), pp. 320–334.
- Michailova, A., Edwards, A.G., Hake, J., Hoshijima, M. and McCulloch, A.D. 2014. Calcium Signaling in Cardiomyocyte Models With Realistic Geometries Zipes, D. P. and Jalife, J. eds. *Elsevier*, pp. 331–340.
- Milone, M., Wang, H.L., Ohno, K., Fukudome, T., Pruitt, J.N., Bren, N., Sine, S.M., et al. 1997. Slow-channel myasthenic syndrome caused by enhanced activation, desensitization, and agonist binding affinity attributable to mutation in the M2 domain of the acetylcholine receptor alpha subunit. *The Journal of neuroscience : the official journal of the Society for Neuroscience* 17(15), pp. 5651–5665.
- Monod, J., Wyman, J. and Changeux, J.P. 1965. On The Nature of Allosteric Transitions: A Plausible Model. *Journal of Molecular Biology* 12, pp. 88–118.
- Mueller, P., Rudin, D.O., Tien, H.T. and Wescott, W.C. 1962. Reconstitution of cell membrane structure in vitro and its transformation into an excitable system. *Nature* 194, pp. 979–980.
- Mukherjee, S., Thomas, N.L. and Williams, A.J. 2012. A mechanistic description of gating of the human cardiac ryanodine receptor in a regulated minimal environment. *The Journal of General Physiology* 140(2), pp. 139–158.

- Mukherjee, S., Thomas, N.L. and Williams, A.J. 2014. Insights into the Gating Mechanism of the Ryanodine-Modified Human Cardiac  $\text{Ca}^{2+}$ -Release Channel (Ryanodine Receptor 2). *Molecular pharmacology* 86(3), pp. 318–329.
- Nagle, J.F. and Tristram-Nagle, S. 2000. Structure of lipid bilayers. *Biochimica et biophysica acta* 1469(3), pp. 159–195.
- Nakai, J., Imagawa, T., Hakamat, Y., Shigekawa, M., Takeshima, H. and Numa, S. 1990. Primary structure and functional expression from cDNA of the cardiac ryanodine receptor/calcium release channel. *FEBS letters* 271(1-2), pp. 169–177.
- Nattel, S., Voigt, N. and Dobrev, D. 2014. The Molecular Pathophysiology of Atrial Fibrillation Zipes, D. P. and Jalife, J. eds. *Elsevier*, pp. 441–458.
- Neher, E. and Sakmann, B. 1976. Single-channel currents recorded from membrane of denervated frog muscle fibres. *Nature* 260(5554), pp. 799–802.
- Nyegaard, M., Overgaard, M.T., Søndergaard, M.T., Vranas, M., Behr, E.R., Hildebrandt, L.L., Lund, J., et al. 2012. Mutations in Calmodulin Cause Ventricular Tachycardia and Sudden Cardiac Death. *The American Journal of Human Genetics* 91(4), pp. 703–712.
- O'Mahoney, J.V. and Adams, T.E. 1994. Optimization of Experimental-Variables Influencing Reporter Gene-Expression in Hepatoma-Cells Following Calcium-Phosphate Transfection. *Dna and Cell Biology* 13(12), pp. 1227–1232.
- Oda, T. 2005. Defective Regulation of Interdomain Interactions Within the Ryanodine Receptor Plays a Key Role in the Pathogenesis of Heart Failure. *Circulation* 111(25), pp. 3400–3410.
- Ostmeyer, J., Chakrapani, S., Pan, A.C., Perozo, E. and Roux, B. 2013. *Nature* 501(7465), pp. 121–124.
- Otsu, K., Willard, H.F., Khanna, V.K., Zorzato, F., Green, N.M. and MacLennan, D.H. 1990. Molecular cloning of cDNA encoding the  $\text{Ca}^{2+}$  release channel (ryanodine receptor) of rabbit cardiac muscle sarcoplasmic reticulum. *The Journal of biological chemistry* 265(23), pp. 13472–13483.
- Park, H., Park, I.Y., Kim, E., Youn, B., Fields, K., Dunker, A.K. and Kang, C. 2004. Comparing Skeletal and Cardiac Calsequestrin Structures and Their Calcium Binding: A proposed mechanism for coupled calcium binding and protein polymerization. *Journal of Biological Chemistry* 279(17), pp. 18026–18033.
- Patlak, J.B. and Ortiz, M. 1989. Kinetic diversity of  $\text{Na}^{+}$  channel bursts in frog skeletal muscle. *The Journal of General Physiology* 94(2), pp. 279–301.
- Patton, C., Thompson, S. and Epel, D. 2004. Some precautions in using chelators to buffer metals in biological solutions. *Cell calcium* 35(5), pp. 427–431.
- Payandeh, J., El-Din, T.M.G., Scheuer, T., Zheng, N. and Catterall, W.A. 2012. Crystal structure of a voltage-gated sodium channel in two potentially inactivated states. *Nature* 486(7401), pp. 135–139.
- Pessah, I.N., Francini, A.O., Scales, D.J., Waterhouse, A.L. and Casida, J.E. 1986.

- Calcium-ryanodine receptor complex. Solubilization and partial characterization from skeletal muscle junctional sarcoplasmic reticulum vesicles. *The Journal of biological chemistry* 261(19), pp. 8643–8648.
- Picht, E., Zima, A.V., Shannon, T.R., Duncan, A.M., Blatter, L.A. and Bers, D.M. 2011. Dynamic Calcium Movement Inside Cardiac Sarcoplasmic Reticulum During Release. *Circulation research* 108(7), pp. 847–856.
- Piskorowski, R.A. and Aldrich, R.W. 2006. Relationship between pore occupancy and gating in BK potassium channels. *The Journal of General Physiology* 127(5), pp. 557–576.
- Pitt, S.J., Park, K.-H., Nishi, M., Urashima, T., Aoki, S., Yamazaki, D., Ma, J., et al. 2010. Charade of the SR K<sup>+</sup>-channel: two ion-channels, TRIC-A and TRIC-B, masquerade as a single K<sup>+</sup>-channel. *Biophysical Journal* 99(2), pp. 417–426.
- Priori, S.G. and Chen, S.R.W. 2011. Inherited Dysfunction of Sarcoplasmic Reticulum Ca<sup>2+</sup> Handling and Arrhythmogenesis. *Circulation research* 108(7), pp. 871–883.
- Prosser, B.L., Hernández-Ochoa, E.O. and Schneider, M.F. 2011. S100A1 and calmodulin regulation of ryanodine receptor in striated muscle. *Cell calcium* 50(4), pp. 323–331.
- Purohit, P. and Auerbach, A. 2009. Unliganded gating of acetylcholine receptor channels. *Proceedings of the National Academy of Sciences of the United States of America* 106(1), pp. 115–120.
- Qin, F. and Li, L. 2004. Model-Based Fitting of Single-Channel Dwell-Time Distributions. *Biophysj* 87(3), pp. 1657–1671.
- Qin, F., Auerbach, A. and Sachs, F. 1996. Estimating Single-Channel Kinetic. *Biophysj* 70(1), pp. 264–280.
- Quintero-Hernández, V., Jiménez-Vargas, J.M., Gurrola, G.B., Valdivia, H.H. and Possani, L.D. 2013. Scorpion venom components that affect ion-channels function. *Toxicon* 76, pp. 328-342.
- Rabiner, L. and Juang, B. 1986. An introduction to hidden Markov models. *IEEE ASSP Magazine* 3(1), pp. 4–16.
- Ramachandran, S., Chakraborty, A., Xu, L., Mei, Y., Samsó, M., Dokholyan, N.V. and Meissner, G. 2013. Structural determinants of skeletal muscle ryanodine receptor gating. *Journal of Biological Chemistry* 288(9), pp. 6154–6165.
- Respress, J.L., van Oort, R.J., Li, N., Rolim, N., Dixit, S.S., deAlmeida, A., Voigt, N., et al. 2012. Role of RyR2 Phosphorylation at S2814 During Heart Failure Progression. *Circulation research* 110(11), pp. 1474–1483.
- Ringer, S. 1883. A further Contribution regarding the influence of the different Constituents of the Blood on the Contraction of the Heart. *The Journal of physiology* 4(1), pp. 29–42.3.
- Rogers, E.F. and Koniuszy, F.R. 1948. Plant insecticides; ryanodine, a new alkaloid from *Ryania speciosa* Vahl. *Journal of the American Chemical Society* 70(9), pp. 3086–3088.



- Rosales, R.A., Fill, M. and Escobar, A.L. 2004. Calcium regulation of single ryanodine receptor channel gating analyzed using HMM/MCMC statistical methods. *The Journal of General Physiology* 123(5), pp. 533–553.
- Rosenberg, R.L., Hess, P. and Tsien, R.W. 1988. Cardiac calcium channels in planar lipid bilayers. L-type channels and calcium-permeable channels open at negative membrane potentials. *The Journal of General Physiology* 92(1), pp. 27–54.
- Rousseau, E. and Meissner, G. 1989. Single cardiac sarcoplasmic reticulum Ca<sup>2+</sup>-release channel: activation by caffeine. *The American journal of physiology* 256(2 Pt 2), pp. H328–33.
- Roux, B. 2005. Ion conduction and selectivity in K<sup>+</sup> channels. *Annual Review of Biophysics and Biomolecular Structure* 34(1), pp. 153–171.
- Ruknudin, A., He, S., Lederer, W.J. and Schulze, D.H. 2000. Functional differences between cardiac and renal isoforms of the rat Na<sup>+</sup>-Ca<sup>2+</sup> exchanger NCX1 expressed in *Xenopus* oocytes. *The Journal of physiology* 529 Pt 3, pp. 599–610.
- Saftenku, E., Williams, A.J. and Sitsapesan, R. 2001. Markovian models of low and high activity levels of cardiac ryanodine receptors. *Biophysj* 80(6), pp. 2727–2741.
- Samsó, M., Feng, W., Pessah, I.N. and Allen, P.D. 2009. Coordinated Movement of Cytoplasmic and Transmembrane Domains of RyR1 upon Gating Aldrich, R. W. ed. *PLoS Biology* 7(4), p. e85.
- Samsó, M., Shen, X. and Allen, P.D. 2006. Structural Characterization of the RyR1–FKBP12 Interaction. *Journal of Molecular Biology* 356(4), pp. 917–927.
- Samsó, M., Wagenknecht, T. and Allen, P.D. 2005. Internal structure and visualization of transmembrane domains of the RyR1 calcium release channel by cryo-EM. *Nature structural & molecular biology* 12(6), pp. 539–544.
- Sanchez, E.J., Lewis, K.M., Danna, B.R. and Kang, C. 2012. High-capacity Ca<sup>2+</sup> Binding of Human Skeletal Calsequestrin. *Journal of Biological Chemistry* 287(14), pp. 11592–11601.
- Saucerman, J.J. and Bers, D.M. 2012. Calmodulin binding proteins provide domains of local Ca<sup>2+</sup> signaling in cardiac myocytes. *Journal of molecular and cellular cardiology* 52(2), pp. 312–316.
- Schiefer, A., Meissner, G. and Isenberg, G. 1995. Ca<sup>2+</sup> activation and Ca<sup>2+</sup> inactivation of canine reconstituted cardiac sarcoplasmic reticulum Ca<sup>2+</sup>-release channels. *The Journal of physiology* 489 ( Pt 2), pp. 337–348.
- Schwartz, E.F., Capes, E.M., Diego-García, E., Zamudio, F.Z., Fuentes, O., Possani, L.D. and Valdivia, H.H. 2009. Characterization of hadrucalcin, a peptide from *Hadrurus gertschi* scorpion venom with pharmacological activity on ryanodine receptors. *British Journal of Pharmacology* 157(3), pp. 392–403.
- Seddon, A.M., Curnow, P. and Booth, P.J. 2004. Membrane proteins, lipids and detergents: not just a soap opera. *Biochimica et Biophysica Acta (BBA) - Biomembranes* 1666(1-2), pp. 105–117.

- Serysheva, I.I., Ludtke, S.J., Baker, M.L., Cong, Y., Topf, M., Eramian, D., Sali, A., et al. 2008. Subnanometer-resolution electron cryomicroscopy-based domain models for the cytoplasmic region of skeletal muscle RyR channel. *Proceedings of the National Academy of Sciences of the United States of America* 105(28), pp. 9610–9615.
- Shan, J., Xie, W., Betzenhauser, M., Reiken, S., Chen, B., Wronska, A. and Marks, A.R. 2012. Calcium Leak Through Ryanodine Receptors Leads to Atrial Fibrillation in Three Mouse Models of Catecholaminergic Polymorphic Ventricular Tachycardia. *Circulation research* 111(6), pp.708-717
- Shannon, T.R. and Bers, D.M. 1997. Assessment of intra-SR free [Ca] and buffering in rat heart. *Biophysj* 73(3), pp. 1524–1531.
- Sharma, M.R., Penczek, P., Grassucci, R., Xin, H.B., Fleischer, S. and Wagenknecht, T. 1998. Cryoelectron microscopy and image analysis of the cardiac ryanodine receptor. *The Journal of biological chemistry* 273(29), pp. 18429–18434.
- Shaw, R.M. and Colecraft, H.M. 2013. L-type calcium channel targeting and local signalling in cardiac myocytes. *Cardiovascular research* 98(2), pp. 177–186.
- Shelley, C. and Magleby, K.L. 2008. Linking Exponential Components to Kinetic States in Markov Models for Single-Channel Gating. *The Journal of General Physiology* 132(2), pp. 295–312.
- Sigalas, C., Bent, S., Kitmitto, A., O'Neill, S. and Sitsapesan, R. 2009. Ca<sup>2+</sup>-calmodulin can activate and inactivate cardiac ryanodine receptors. *British Journal of Pharmacology* 156(5), pp. 794–806.
- Sigworth, F.J. and Sine, S.M. 1987. Data transformations for improved display and fitting of single-channel dwell time histograms. *Biophysj* 52(6), pp. 1047–1054.
- Sitsapesan, R. and Williams, A.J. 1994a. Gating of the native and purified cardiac SR Ca<sup>2+</sup>-release channel with monovalent cations as permeant species. *Biophysical Journal* 67(4), pp. 1484–1494.
- Sitsapesan, R. and Williams, A.J. 1990. Mechanisms of caffeine activation of single calcium-release channels of sheep cardiac sarcoplasmic reticulum. *The Journal of physiology* 423(1), pp. 425–439.
- Sitsapesan, R. and Williams, A.J. 1994b. Regulation of the gating of the sheep cardiac sarcoplasmic reticulum Ca<sup>2+</sup>-release channel by luminal Ca<sup>2+</sup>. *The Journal of Membrane Biology* 137(3), pp. 215–226.
- Smith, J.S., Rousseau, E. and Meissner, G. 1989. Calmodulin modulation of single sarcoplasmic reticulum Ca<sup>2+</sup>-release channels from cardiac and skeletal muscle. *Circulation research* 64(2), pp. 352–359.
- Stewart, R., Song, L., Carter, S.M., Sigalas, C., Zaccari, N.R., Kanamarlapudi, V., Bhat, M.B., et al. 2008. Single-Channel Characterization of the Rabbit Recombinant RyR2 Reveals a Novel Inactivation Property of Physiological Concentrations of ATP. *The Journal of Membrane Biology* 222(2), pp. 65–77.
- Sutko, J.L., Ito, K. and Kenyon, J.L. 1985. Ryanodine: a modifier of sarcoplasmic reticulum calcium release in striated muscle. *Federation proceedings* 44(15), pp. 2984–

2988.

Takeshima, H., Nishimura, S., Matsumoto, T., Ishida, H., Kangawa, K., Minamino, N., Matsuo, H., et al. 1989. Primary structure and expression from complementary DNA of skeletal muscle ryanodine receptor. *Nature* 339(6224), pp. 439–445.

Talukder, G. and Aldrich, R.W. 2000. Complex voltage-dependent behavior of single unliganded calcium-sensitive potassium channels. *Biophysical Journal* 78(2), pp. 761–772.

Tang, W., Sencer, S. and Hamilton, S.L. 2002. Calmodulin modulation of proteins involved in excitation-contraction coupling. *Frontiers in bioscience : a journal and virtual library* 7, pp. d1583–9.

Tanskanen, A.J., Greenstein, J.L., Chen, A., Sun, S.X. and Winslow, R.L. 2007. Protein Geometry and Placement in the Cardiac Dyad Influence Macroscopic Properties of Calcium-Induced Calcium Release. *Biophysical Journal* 92(10), pp. 3379–3396.

Tao, X., Avalos, J.L., Chen, J. and MacKinnon, R. 2009. Crystal Structure of the Eukaryotic Strong Inward-Rectifier K<sup>+</sup> Channel Kir2.2 at 3.1 Å Resolution. *Science (New York, NY)* 326(5960), pp. 1668–1674.

Tencerova, B., Zahradníková, A., Gaburjakova, J. and Gaburjakova, M. 2012. Luminal Ca<sup>2+</sup> controls activation of the cardiac ryanodine receptor by ATP. *The Journal of General Physiology* 140(2), pp. 93–108.

Tester, D.J., Dura, M., Carturan, E., Reiken, S., Wronska, A., Marks, A.R. and Ackerman, M.J. 2007. A mechanism for sudden infant death syndrome (SIDS): stress-induced leak via ryanodine receptors. *Heart rhythm : the official journal of the Heart Rhythm Society* 4(6), pp. 733–739.

Thomas, N.L. and Williams, A.J. 2012. Pharmacology of ryanodine receptors and Ca<sup>2+</sup>-induced Ca<sup>2+</sup> release. *Wiley Interdisciplinary Reviews: Membrane Transport and Signaling* 1(4), pp. 383–397.

Thomas, N.L., George, C.H. and Lai, F.A. 2004. Functional heterogeneity of ryanodine receptor mutations associated with sudden cardiac death. *Cardiovascular research* 64(1), pp. 52–60.

Thomas, N.L., George, C.H., Williams, A.J. and Lai, F.A. 2007. Ryanodine receptor mutations in arrhythmias: advances in understanding the mechanisms of channel dysfunction. *Biochemical Society transactions* 35(Pt 5), pp. 946–951.

Thomas, N.L., Lai, F.A. and George, C.H. 2005. Differential Ca<sup>2+</sup> sensitivity of RyR2 mutations reveals distinct mechanisms of channel dysfunction in sudden cardiac death. *Biochemical and Biophysical Research Communications* 331(1), pp. 231–238.

Thomas, N.L., Maxwell, C., Mukherjee, S. and Williams, A.J. 2010. Ryanodine receptor mutations in arrhythmia: The continuing mystery of channel dysfunction. *FEBS letters* 584(10), pp. 2153–2160.

Tibbs, G.R., Goulding, E.H. and Siegelbaum, S.A. 1997. Allosteric activation and tuning of ligand efficacy in cyclic-nucleotide-gated channels. *Nature* 386(6625), pp. 612–615.

- Timerman, A.P., Onoue, H., Xin, H.B., Barg, S., Copello, J., Wiederrecht, G. and Fleischer, S. 1996. Selective Binding of FKBP12.6 by the Cardiac Ryanodine Receptor. *Journal of Biological Chemistry* 271(34), pp. 20385–20391.
- Tinker, A. and Williams, A.J. 1992. Divalent cation conduction in the ryanodine receptor channel of sheep cardiac muscle sarcoplasmic reticulum. *The Journal of General Physiology* 100(3), pp. 479–493.
- Tinker, A. and Williams, A.J. 1995. Measuring the Length of the Pore of the Sheep. *Biophysj* 68(1), pp. 111–120.
- Tinker, A. and Williams, A.J. 1993. Using large organic cations to probe the nature of ryanodine modification in the sheep cardiac sarcoplasmic reticulum calcium release channel. *Biophysical Journal* 65(4), pp. 1678–1683.
- Tinker, A., Lindsay, A.R. and Williams, A.J. 1992. A model for ionic conduction in the ryanodine receptor channel of sheep cardiac muscle sarcoplasmic reticulum. *The Journal of General Physiology* 100(3), pp. 495–517.
- Tinker, A., Sutko, J.L., Ruest, L., Deslongchamps, P., Welch, W., Airey, J.A., Gerzon, K., et al. 1996. Electrophysiological effects of ryanodine derivatives on the sheep cardiac sarcoplasmic reticulum calcium-release channel. *Biophysical Journal* 70(5), pp. 2110–2119.
- Tiso, N., Stephan, D.A., Nava, A., Bagattin, A., Devaney, J.M., Stanchi, F., Larderet, G., et al. 2001. Identification of mutations in the cardiac ryanodine receptor gene in families affected with arrhythmogenic right ventricular cardiomyopathy type 2 (ARVD2). *Human molecular genetics* 10(3), pp. 189–194.
- Tripathy, A., Resch, W., Xu, L., Valdivia, H.H. and Meissner, G. 1998. Imperatoxin A induces subconductance states in  $\text{Ca}^{2+}$  release channels (ryanodine receptors) of cardiac and skeletal muscle. *The Journal of General Physiology* 111(5), pp. 679–690.
- Uchinoumi, H., Yano, M., Suetomi, T., Ono, M., Xu, X., Tateishi, H., Oda, T., et al. 2010. Catecholaminergic polymorphic ventricular tachycardia is caused by mutation-linked defective conformational regulation of the ryanodine receptor. *Circulation Research* 106(8), pp. 1413–1424.
- Uehara, A., Yasukochi, M., Mejía-Alvarez, R., Fill, M. and Imanaga, I. 2002. Gating kinetics and ligand sensitivity modified by phosphorylation of cardiac ryanodine receptors. *Pflügers Archiv : European journal of physiology* 444(1-2), pp. 202–212.
- Valdivia, H.H. 2014. Structural and Molecular Bases of Sarcoplasmic Reticulum Ion Channel Function Zipes, D. P. and Jalife, J. eds. *Elsevier*, pp. 55–69.
- Valdivia, H.H., Fuentes, O., El-Hayek, R., Morrissette, J. and Coronado, R. 1991. Activation of the ryanodine receptor  $\text{Ca}^{2+}$  release channel of sarcoplasmic reticulum by a novel scorpion venom. *The Journal of biological chemistry* 266(29), pp. 19135–19138.
- van der Werf, C. and Wilde, A.A.M. 2013. Catecholaminergic polymorphic ventricular tachycardia: from bench to bedside. *Heart* 99, pp. 497-504.
- Van Petegem, F. 2014. Ryanodine Receptors: Allosteric Ion Channel Giants. *Journal of Molecular Biology*, pp. 1–23.

- Van Petegem, F. 2012. Ryanodine receptors: structure and function. *Journal of Biological Chemistry* 287(38), pp. 31624–31632.
- Venetucci, L., Denegri, M., Napolitano, C. and Priori, S.G. 2012. Inherited calcium channelopathies in the pathophysiology of arrhythmias. *Nature reviews. Cardiology* 9(10), pp. 561–575.
- Venturi, E., Galfré, E., O'Brien, F., Pitt, S.J., Bellamy, S., Sessions, R.B. and Sitsapesan, R. 2014. FKBP12.6 Activates RyR1: Investigating the Amino Acid Residues Critical for Channel Modulation. *Biophysj* 106(4), pp. 824–833.
- Venturi, E., Sitsapesan, R., Yamazaki, D. and Takeshima, H. 2013. TRIC channels supporting efficient Ca<sup>2+</sup> release from intracellular stores. *Pflügers Archiv : European journal of physiology* 465(2), pp. 187–195.
- Viterbi, A.J. 1967. Error bounds for convolutional codes and an asymptotically optimum decoding algorithm. *Information Theory, IEEE Transactions on* 13(2), pp. 260–269.
- Walweel, K., Li, J., Molenaar, P., Imtiaz, M.S., Quail, A., Remedios, dos, C.G., Beard, N.A., et al. 2014. Differences in the regulation of RyR2 from human, sheep, and rat by Ca<sup>2+</sup> and Mg<sup>2+</sup> in the cytoplasm and in the lumen of the sarcoplasmic reticulum. *The Journal of General Physiology* 144(3), pp. 263–271.
- Wang, R., Chen, W., Cai, S., Zhang, J., Bolstad, J., Wagenknecht, T., Liu, Z., et al. 2007. Localization of an NH2-terminal Disease-causing Mutation Hot Spot to the 'Clamp' Region in the Three-dimensional Structure of the Cardiac Ryanodine Receptor. *Journal of Biological Chemistry* 282(24), pp. 17785–17793.
- Watanabe, H., Chopra, N., Laver, D., Hwang, H.S., Davies, S.S., Roach, D.E., Duff, H.J., et al. 2009. Flecainide prevents catecholaminergic polymorphic ventricular tachycardia in mice and humans. *Nature Medicine* 15(4), pp. 380–383.
- Wehrens, X.H.T. 2004a. Ca<sup>2+</sup>/Calmodulin-Dependent Protein Kinase II Phosphorylation Regulates the Cardiac Ryanodine Receptor. *Circulation research* 94(6), pp. e61–e70.
- Wehrens, X.H.T. 2004b. Protection from Cardiac Arrhythmia Through Ryanodine Receptor-Stabilizing Protein Calstabin2. *Science (New York, NY)* 304(5668), pp. 292–296.
- Wehrens, X.H.T., Lehnart, S.E., Huang, F., Vest, J.A., Reiken, S.R., Mohler, P.J., Sun, J., et al. 2003. FKBP12.6 deficiency and defective calcium release channel (ryanodine receptor) function linked to exercise-induced sudden cardiac death. *Cell* 113(7), pp. 829–840.
- Wehrens, X.H.T., Lehnart, S.E., Reiken, S., Vest, J.A., Wronska, A. and Marks, A.R. 2006. Ryanodine receptor/calcium release channel PKA phosphorylation: a critical mediator of heart failure progression. *Proceedings of the National Academy of Sciences* 103(3), pp. 511–518.
- Welch, W. 2002. Quantitative relationships between ryanoids, receptor affinity and channel conductance. *Frontiers in bioscience : a journal and virtual library* 7, pp. d1727–42.
- Welch, W., Rheault, S., West, D.J. and Williams, A.J. 2004. A model of the putative pore

region of the cardiac ryanodine receptor channel. *Biophysj* 87(4), pp. 2335–2351.

Welch, W., Williams, A.J., Tinker, A., Mitchell, K.E., Deslongchamps, P., Lamothe, J., Gerzon, K., et al. 1997. Structural components of ryanodine responsible for modulation of sarcoplasmic reticulum calcium channel function. *Biochemistry* 36(10), pp. 2939–2950.

White, S. 1986. *The Physical Nature of Planar Bilayer Membranes*. Miller, C. ed. Plenum Publishing Corporation.

Williams, A.J. 1994. An introduction to the methods available for ion channel reconstitution Ogden, D. C. ed. *Company of Biologists, Cambridge*, pp. 79–99.

Williams, A.J. 2002. Ion conduction and selectivity in the ryanodine receptor channel. *Frontiers in Bioscience* 7, pp. d1223–30.

Williams, A.J., West, D.J. and Sitsapesan, R. 2001. Light at the end of the Ca<sup>2+</sup>-release channel tunnel: structures and mechanisms involved in ion translocation in ryanodine receptor channels. *Quarterly reviews of biophysics* 34(1), p. 61.

Witcher, D.R., Kovacs, R.J., Schulman, H., Cefali, D.C. and Jones, L.R. 1991. Unique phosphorylation site on the cardiac ryanodine receptor regulates calcium channel activity. *The Journal of biological chemistry* 266(17), pp. 11144–11152.

Wu, B., Yamaguchi, H., Lai, F.A. and Shen, J. 2013. Presenilins regulate calcium homeostasis and presynaptic function via ryanodine receptors in hippocampal neurons. *Proceedings of the National Academy of Sciences of the United States of America* 110(37), pp. 15091–15096.

Wu, Y., Dzhura, I., Colbran, R.J. and Anderson, M.E. 2001. Calmodulin kinase and a calmodulin-binding ‘IQ’ domain facilitate L-type Ca<sup>2+</sup> current in rabbit ventricular myocytes by a common mechanism. *The Journal of physiology* 535(Pt 3), pp. 679–687.

Xiao, B. 2005. Characterization of a Novel PKA Phosphorylation Site, Serine-2030, Reveals No PKA Hyperphosphorylation of the Cardiac Ryanodine Receptor in Canine Heart Failure. *Circulation research* 96(8), pp. 847–855.

Xiao, B. 2004. Protein Kinase A Phosphorylation at Serine-2808 of the Cardiac Ca<sup>2+</sup>-Release Channel (Ryanodine Receptor) Does Not Dissociate 12.6-kDa FK506-Binding Protein (FKBP12.6). *Circulation research* 94(4), pp. 487–495.

Xiao, B., Zhong, G., Obayashi, M., Yang, D., Chen, K., Walsh, M.P., Shimoni, Y., et al. 2006. Ser-2030, but not Ser-2808, is the major phosphorylation site in cardiac ryanodine receptors responding to protein kinase A activation upon  $\beta$ -adrenergic stimulation in normal and failing hearts. *The Biochemical journal* 396(1), p. 7.

Xu, L., Mann, G. and Meissner, G. 1996. Regulation of Cardiac Ca<sup>2+</sup> Release Channel (Ryanodine Receptor) by Ca<sup>2+</sup>, H<sup>+</sup>, Mg<sup>2+</sup>, and Adenine Nucleotides Under Normal and Simulated Ischemic Conditions. *Circulation research* 79(6), pp. 1100–1109.

Yamaguchi, N., Xu, L., Pasek, D.A., Evans, K.E. and Meissner, G. 2003. Molecular Basis of Calmodulin Binding to Cardiac Muscle Ca<sup>2+</sup> Release Channel (Ryanodine Receptor). *Journal of Biological Chemistry* 278(26), pp. 23480–23486.

- Yamamoto, T., El-Hayek, R. and Ikemoto, N. 2000. Postulated role of interdomain interaction within the ryanodine receptor in  $\text{Ca}^{2+}$  channel regulation. *The Journal of biological chemistry* 275(16), pp. 11618–11625.
- Yamamoto, T., Yano, M., Xu, X., Uchinoumi, H., Tateishi, H., Mochizuki, M., Oda, T., et al. 2008. Identification of Target Domains of the Cardiac Ryanodine Receptor to Correct Channel Disorder in Failing Hearts. *Circulation* 117(6), pp. 762–772.
- Yellen, G. 2002. The voltage-gated potassium channels and their relatives. *Nature* 419(6902), pp. 35–42.
- Yin, C.C., D’Cruz, L.G. and Lai, F.A. 2008. Ryanodine receptor arrays: not just a pretty pattern? *Trends in Cell Biology* 18(4), pp. 149–156.
- Zadek, B. and Nimigean, C.M. 2006. Calcium-dependent gating of MthK, a prokaryotic potassium channel. *The Journal of General Physiology* 127(6), pp. 673–685.
- Zahradník, I., Györke, S. and Zahradníková, A. 2005. Calcium activation of ryanodine receptor channels--reconciling RyR gating models with tetrameric channel structure. *The Journal of General Physiology* 126(5), pp. 515–527.
- Zahradníková, A. and Zahradník, I. 1995. Description of modal gating of the cardiac calcium release channel in planar lipid membranes. *Biophysical Journal* 69(5), pp. 1780–1788.
- Zahradníková, A., Dura, M., Györke, I., Escobar, A.L., Zahradník, I. and Györke, S. 2003. Regulation of dynamic behavior of cardiac ryanodine receptor by  $\text{Mg}^{2+}$  under simulated physiological conditions. *AJP: Cell Physiology* 285(5), pp. C1059–C1070.
- Zhao, M., Li, P., Li, X., Zhang, L., Winkfein, R.J. and Chen, S.R.W. 1999. Molecular Identification of the Ryanodine Receptor Pore-forming Segment. *Journal of Biological Chemistry* 274(37), pp. 25971–25974.
- Zhou, M., Engel, A.G. and Auerbach, A. 1999. Serum choline activates mutant acetylcholine receptors that cause slow channel congenital myasthenic syndromes. *Proceedings of the National Academy of Sciences of the United States of America* 96(18), pp. 10466–10471.
- Zhou, Q., Xiao, J., Jiang, D., Wang, R., Vembaiyan, K., Wang, A., Smith, C.D., et al. 2011. Carvedilol and its new analogs suppress arrhythmogenic store overload–induced Ca. *Nature Publishing Group* 17(8), pp. 1003–1009.
- Zhou, Y., Pearson, J.E. and Auerbach, A. 2005. Phi-value analysis of a linear, sequential reaction mechanism: theory and application to ion channel gating. *Biophysical Journal* 89(6), pp. 3680–3685.
- Zima, A.V., Picht, E., Bers, D.M. and Blatter, L.A. 2008. Termination of Cardiac  $\text{Ca}^{2+}$  Sparks: Role of Intra-SR  $[\text{Ca}^{2+}]$ , Release Flux, and Intra-SR  $\text{Ca}^{2+}$  Diffusion. *Circulation research* 103(8), pp. e105–e115.
- Zissimopoulos, S., Viero, C., Seidel, M., Cumbes, B., White, J., Cheung, I., Stewart, R., et al. 2013. N-terminus oligomerization regulates the function of cardiac ryanodine receptors. *Journal of cell science* 126(21), pp. 5042–5051.